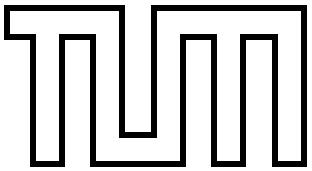

FAKULTÄT FÜR PHYSIK

DER TECHNISCHEN UNIVERSITÄT MÜNCHEN

# Dissertation

zur Erlangung der Doktorwürde

## Advanced Diffusion MR Methods to Study Human Brain

Eingereicht von Tim Sprenger

**2016**

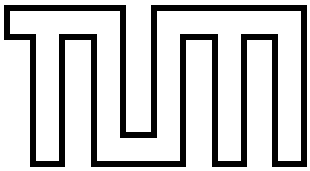


FAKULTÄT FÜR PHYSIK

Zentralinstitut für Medizintechnik


# Advanced Diffusion MR Methods to Study Human Brain


Tim Sprenger



Vollständiger Abdruck der von der Fakultät für Physik der Technischen Universität München zur Erlangung des akademischen Grades eines

Doktors der Naturwissenschaften

genehmigten Dissertation.

Vorsitzende(r): Prof. Dr. Martin Zacharias

Prüfer der Dissertation:

1. Prof. Dr. Axel Haase

2. Priv. Doz. Dr. Marion Menzel

Die Dissertation wurde am 15.03.2016 bei der Technischen Universität München eingereicht und durch die Fakultät für Physik am 24.03.2017 angenommen.

# Acknowledgements

First and foremost, I am indebted to everyone who has contributed to the successful completion of my dissertation. During my PhD, I have met so many new people, made so many new friends, that actually, this section appears to be one of the most difficult. From the beginning in February 2012, I felt extremely welcome, and I enjoyed your company, your guidance and help. The time was flying and honestly, I cannot believe that almost four years have passed by. Thank you all so much, I really hope that our paths will often cross in the future again. Before getting too emotional, I would like to express my special appreciation and thanks to

- you, **Prof. Haase** for academic supervision of this dissertation. You always helped when I asked for it.
- you, **Marion Menzel** for advising my thesis. Thank you for your enduring support - you were always there to fight my worries and concerns.
- you, **Jonathan Sperl** for advising my thesis. The discussions with you were extremely helpful and your feedback was always very accurate and clear. You really helped me a lot and everything I can say is thank you.
- you, **Benjamin Fürsich** for your great work as my master student. You did a tremendous job and you more than exceeded my expectations. I will always keep in mind our various meetings at the "Kicker" table and our snowboard adventures.
- you, **Ines Eidner** for all your help to run the multiples sclerosis study at the Max Planck institute. You took a big load of me so that I could focus on many other projects.
- you, **Philipp Sämann** for all your help in the organization and evaluation of the multiples sclerosis study.
- to the TUM Graduate School of Bioengineering, especially to **Katharina Lang, Petra Dorfner and Ursula Mühle** for your patience with me and my sometimes chaotic organization. Whenever I had a problem to organize my PhD, you helped solving it.
- to my girlfriend **Anabea** for her enduring support during my PhD and for proof reading every page of this thesis.
- to **Ulrich Köllisch, Markus Durst, Stephan Düwel, Benjamin Fürsich, Johannes Scholz, Nicolas Hehn, Miguel Molina, Eugen Kubala, Jonathan Sperl** and many others for the great meetings at the "Kicker" table.
- to all students and employees at GE Global Research Munich and at the Institute of Medical Engineering for the great working atmosphere.
- all my family and friends for supporting me and believing in me.

# Contents

# 1. Introduction

Magnetic Resonance Imaging (MRI) is a volumetric imaging technique that is widely used in radiology to examine the anatomy and physiology of the human body. Since its invention in 1971 by Peter Lauterbur [1], MRI has evolved to an indispensable technique for diagnosis and staging of a large variety of disorders. To acknowledge the fundamental importance of MRI in medicine, Peter Lauterbur and Peter Mansfield, who played a key role in the development of MRI, were awarded the 2003 Nobel Prize in Physiology or Medicine for their "discoveries concerning magnetic resonance imaging".

MRI is based on the principles of Nuclear Magnetic Resonance (NMR), which describes the absorption and dissipation of electromagnetic radiation by atomic nuclei under the presence of a static magnetic field. In NMR, a Radio Frequency Pulse (RF-pulse) is used to disrupt the equilibrium state of the nuclei. The measured signal, when the nuclei are returning to the equilibrium state, provides information about the molecular structure and the environment of the nuclei. NMR and also MRI, typically, operate in the Megahertz-regime. Thus, in contrary to other volumetric imaging techniques such as computer tomography or positron emission tomography, MRI avoids harmful ionizing radiation.

The great strength of MRI is its remarkable flexibility. A series of RF-pulses and magnetic field gradient pulses, also called pulse sequence, are used to manipulate the contrast. For example in neuroimaging, a $T_1$ weighted pulse sequence exhibits an excellent contrast between Gray Matter (GM) and White Matter (WM). In $T_2$ weighted images, Cerebrospinal Fluid (CSF) and many types of brain lesions appear hyperintense. Moreover, to differ between CSF and lesions, a Fluid Attenuated Inversion Recovery (FLAIR) contrast is typically employed that attenuates CSF while lesions remain hyperintense. The FLAIR contrast for example plays a key role in the diagnosis and staging of the autoimmune disease multiples sclerosis [2]. Apart from those, there are many more contrasts in MRI; to name but a few, proton density weighting is used for example to examine ligaments [3], susceptibility weighted imaging can be applied to detect hemorrhages [4], and Blood Oxygenation Level Dependent (BOLD) contrast is used for functional MRI [5].

The focus of this thesis lies on another special MRI technique, called Diffusion Weighted Imaging (DWI). DWI is the only noninvasive imaging method that enables estimating the molecular self-diffusion of water within the surrounding biological tissue [6, 7]. Magnetic field gradients are used to impart a phase shift to the NMR signal, which is only partially reversed by a second magnetic field gradient with opposite polarity, because the water molecules undergo Brownian motion or diffusion [8]. In a liquid, diffusion can be well described with a Gaussian Ensemble Average Propagator (EAP), which predicts the probability that a proton moves by a certain displacement in a certain time. However, in biological tissue, the motion of the protons is hindered or restricted by cell membranes and compartments of different size. Therefore, measuring diffusion allows for investigating the microstructural properties of tissues on micrometer scale, which is far below the imaging resolution of MRI.

The diffusion of water in biological tissue can be quantified by various diffusion models. Among the first of these models was Diffusion Tensor Imaging (DTI), which assumes non-restricted, Gaussian diffusion [9, 10]. Rotationally invariant diffusion metrics that are derived from the Diffusion Tensor (DT), such as Mean Diffusivity (MD) and Fractional Anisotropy (FA), are widely used in clinics, especially for the staging of acute stroke [11]. However, it has been reported that diffusion in the human brain is generally non-Gaussian [12–14]. Therefore, more sophisticated diffusion models were developed, for example Diffusion Kurtosis Imaging (DKI) [15] which is an extension of DTI and uses additional parameters to describe the non-Gaussianity of the EAP.

Apart from modeling the diffusion, DWI is also of special importance to study the organization of the central nervous system. The anisotropic diffusion of water in white matter is exploited to compute an atlas of the structural connectivity of the brain, the so called connectome. The human connectome project, that was recently launched by the National Institutes of Health (USA), focuses on this topic. Similarly, the European Union launched the human brain project, a large 10-year scientific research project with more than one billion euros of funding. These projects aim for a better understanding of the anatomical and functional connectivity of the human brain, which will hopefully also facilitate research in brain disorders such as dyslexia, autism, Alzheimer's disease, or schizophrenia [16–19].

Unfortunately, DWI is an intrinsically low Signal to Noise Ratio (SNR) imaging application for two reasons. On the one hand, the diffusion encoding requires a fairly long time, resulting in a prolonged Echo Time (TE) and a strong $T_2$ weighting. On the other hand, the diffusion weighting gradients themselves attenuate the signal. Moreover, all data processing in DWI is typically based on the magnitude of the complex MR signal, because the signal's phase is spoiled by motion encoding of the intracranial pulsatility [20], eddy currents and susceptibility induced phase. Magnitude processing, however, results in an unequal noise distribution with positive, nonzero mean. Therefore, if the DWI signals are close to the background noise level, the measured amplitude is significantly biased by the positive noise floor [21]. Such overestimations reduce the image contrast and yield distorted values for diffusion measures like the MD and FA derived from magnitude data.

The problem of the low SNR in DWI is addressed from several angles in this thesis. Initially, the impact of noise on the estimation accuracy and precision of the DKI model is systematically investigated in chapter 3. It is shown, that the effect of noise can be very heterogeneous and depends on many impact factors, such as the SNR but also the underlying tissue, the acquisition scheme and the reconstruction techniques. This is especially a problem for multi-center studies, where often different hardware and even different acquisition schemes are used and consequently, an accurate quantitative comparison is hampered by different noise induced biases.

However, these problems could be avoided when considering real-valued MR images which requires to determine the phase of the MR signal accurately. Therefore, in chapter 4, a novel phase correction technique is proposed which significantly reduces the signal bias and enhances the image contrast at low SNR.

A special characteristic of DWI is its motion sensitivity, which is why primarily single shot sequences are used. In neuroimaging, particularly the intracranial pulsatility [20] is encoded in the signal's phase causing phase variations that hamper segmented k-space readout techniques. The data acquisition in DWI is commonly based on a 2D single-shot EPI sequence with Stejskal-Tanner diffusion preparation, that only reaches relatively poor

SNR.

Recently, three novel DWI pulse sequences were reported, i.e. Simultaneous Multi-Slice Echo Planar Imaging (SMS-EPI) [22, 23], Multi-Slab Echo Planar Imaging (MS-EPI) [24] and Diffusion-Weighted Steady State Free Precession (DWSSFP) [25], which try to overcome the motion induced phase variations. Although these sequences provide an improved SNR efficiency over conventional 2D Echo Planar Imaging (EPI), they are also accompanied by certain artifacts or disadvantages, such as g-factor penalties in SNR [26], slab boundary artifacts [27] or signal loss due to remaining phase inconsistencies.

Therefore, in chapter 5, a framework is proposed to compare the SNR efficiencies of the new DWI pulse sequences to better weigh their pros and cons. An important prerequisite for the SNR efficiencies comparison is the accurate prediction of the diffusion weighted signal. Contrary to a Stejskal Tanner (ST) preparation, modeling the Diffusion-Weighted Steady State Free Precession (DWSSFP) signal is highly complex. Consequently, the accuracy of different analytical signal models for the pulsed DWSSFP are compared and a new accurate model is proposed.

In chapter 6, a new processing technique of the complex DWI signal is adopted which goes beyond the measurement of the diffusion induced signal attenuation. Whereas in the past, the aforementioned phase variations were considered as concomitant phenomena, it is shown here, that it is possible to quantify the intracranial pulsatility using a conventional DWI acquisition. This allows for a joint estimation of the brain microstructure and the brain pulsatility and may add valuable information for disorders such as peripheral vascular disease, dementia, brain tumor or traumatic brain injury [20].

In summary, this thesis aims for both, improving the data quality in DWI and increasing the information that is extracted from it. This includes work in the areas of data acquisition, data preprocessing and data quantification.

## Outline

This thesis is structured as follows:

- In **chapter 2**, the basics of NMR are described including the origin of the magnetic moment of atomic nuclei, the polarization in a static magnetic field, the interaction of the magnetic moments with an RF-pulse, and the Bloch equations. Thereafter, the influence of coherent and incoherent motion on the NMR signal is explained and different diffusion models are introduced. Finally, the principles of MRI are presented, starting with the spatial encoding, followed by a brief description of MRI pulse sequences in general and a more detailed explanation of Echo Planar Imaging (EPI) as it is the most commonly used readout technique in DWI. The chapter closes with the explanation of typical artifacts observed in EPI images.
- In **chapter 3**, the precision and bias of the DKI model estimation are systematically analyzed. A weighted linear least squares fitting algorithm is used as well as different acquisition schemes including several multi-shell schemes, a Diffusion Spectrum Imaging (DSI) , and a compressed sensing reconstruction of an undersampled DSI scheme. Monte Carlo simulations are performed to study the 3D distribution of the apparent kurtosis coefficient. Experimental data were acquired from one healthy volunteer with multiple repetitions using the same acquisition schemes as for the simulations.
- In **chapter 4**, a novel phase correction technique is proposed that yields real-valued diffusion data and maintains a Gaussian noise distribution. Simulations of the noise propagation in the echo planar imaging reconstruction chain are conducted to obtain the spatial noise correlation in the image. The resulting correlation patterns are used to determine optimized filter kernels to estimate the true phase of the signal in each voxel. Furthermore, an outlier detection technique is adopted to replace the real value by the magnitude in case of substantial signal loss due to incorrect phase correction. The benefits of the new method are demonstrated on Monte Carlo simulations, DWI data acquired from healthy volunteer experiments, estimated parameters of the diffusion kurtosis imaging model, and the model-free diffusion spectrum imaging technique.
- In **chapter 5**, a framework to compare different DWI sequences in terms of SNR and SNR efficiency is provided, and applied to a typical whole brain DWI scenario. The most widely used pulse sequence for DWI, based on 2D single-shot EPI readout with Stejskal–Tanner diffusion preparation, only reaches relative poor SNR. Modern pulse sequences try to overcome the limited SNR and SNR efficiency of this technique. On the one hand, simultaneous multi-slice sequences provide higher SNR efficiency. On the other hand, multi-shot techniques reach for higher SNR using a segmented k-space acquisition. Promising multi-shot DWI techniques are 3D multi-slab EPI sequence and 3D diffusion weighted steady state free precession sequence. In this chapter, the SNR efficiencies of all three new sequences are compared to conventional 2D EPI. Moreover, existing analytical models for pulsed diffusion weighted steady state free precession sequences are systematically analyzed and a new accurate model is presented.

- In **chapter 6**, a novel phase filtering method is proposed to extract a meaningful phase from DWIs, which allows for inferring information of the intracranial pulsatility of the brain. Initial results from phantom and volunteer experiments are shown and the repeatability of the new technique is investigated.
- In **chapter 7**, the results of this thesis are briefly summarized.

Each of the chapters 3 to 6 comprises a separate introduction and discussion, where existing literature and methods are introduced and compared with the results of this thesis, respectively.

# 2. Principles of Magnetic Resonance Imaging

In this chapter, the principles of MRI are described beginning the signal formation based on NMR. Thereafter the effects of coherent and incoherent motion on the NMR signal is shown. Finally the actual volumetric imaging technique MRI is introduced.

## 2.1. Nuclear Magnetic Resonance

Nuclear Magnetic Resonance (NMR) is describes the phenomenon that atomic nuclei in a static magnetic field can absorb or emit electromagnetic radiation at certain resonance frequencies. This effect was first discovered by Isidor Rabi [28] in 1938 and he was awarded the Nobel Prize in Physics "for his resonance method for recording the magnetic properties of atomic nuclei" in 1944.

### 2.1.1. Angular Momentum and Magnetic Moment

#### Classical Notion

Considering a point mass with a charge $q$ and mass $m$ rotating about an axis with the velocity $\vec{v}$. The angular momentum $\vec{L}$ of this charge is defined as the cross product of its position vector $\vec{r}$ and its momentum $m\vec{v}$.

$$\vec{L} = m\vec{r} \times \vec{v} \tag{2.1}$$

It will be shown now, that this rotating charge $q$ generates a magnetic moment (more precisely magnetic dipole moment) $\vec{\mu}$, which is a measure that determines the torque exerted on an object in a static magnetic field. It is defined as the volume integral over the cross product of $\vec{r}$ and the current density $\vec{j}$.

$$\vec{\mu} = \frac{1}{2} \iiint_V \vec{r} \times \vec{j}(\vec{r})\, dV \tag{2.2}$$

The current density $\vec{j}$ at a point $\vec{r}$ can be written as the product of the volume charge density $\rho$ and the velocity $\vec{v}$.

$$\vec{j} = \rho\vec{v} \tag{2.3}$$

Using 2.3 and the assumption of the point mass, 2.2 can an be simplified to:

$$\vec{\mu} = \frac{1}{2} q\vec{r} \times \vec{v}. \tag{2.4}$$

A comparison of 2.1 and 2.4 reveals that $\vec{\mu}$ can be expressed with the factor $\gamma = \frac{q}{2m}$ and $\vec{L}$.

$$\vec{\mu} = \frac{q}{2m}\vec{L} \tag{2.5}$$

The factor $\gamma$ is called the gyromagnetic ratio which links the angular momentum $\vec{L}$ of a charge with its magnetic moment $\vec{\mu}$. In conclusion, an angular momentum $\vec{L}$ of a charge is always associated with a magnetic moment $\vec{\mu}$ and vice versa.

**Quantum Mechanical Notion**

In this section quantum mechanical operators are printed in bold to differentiate them from the classical representation. In quantum mechanics two different types of angular momentum exist. First, the orbital angular momentum **L** as the quantum mechanical counterpart to the classical notion of angular momentum. Second, the spin **S** which is a intrinsic form of angular momentum of elementary particles, composite particles and atomic nuclei. Both add to the total angular momentum **J**.

$$\mathbf{J} = \mathbf{S} + \mathbf{L} \tag{2.6}$$

As in the classical case, the ratio between the total angular momentum of a charge and its magnetic dipole moment $\vec{\mu}$ is described by the gyromagnetic ratio $\gamma$.

$$\boldsymbol{\mu} = \gamma \mathbf{J} \tag{2.7}$$

However, in addition to the classical definition of $\gamma$ as given in 2.5, a dimensionless factor, the so called g-factor, needs to be introduced because the two types of angular momentum exhibit a different impact on $\vec{\mu}$.

$$\gamma = g\frac{q}{2m} \tag{2.8}$$

In the simple case of an electron the g-factor accounts for the different magnetic moments induced by the orbital angular momentum ($g = 1$) and the spin ($g \approx 2$). If both, **S** and **L** contribute to **J** the g-factor can be calculated following the formula of Landé [29].

**Magnetic Moments of Nuclei**

On the contrary to electrons, nuclei are no elementary particles. They consist of the protons and the neutrons which belong to the particle family of the baryons. As electrons, baryons have a spin of $\frac{1}{2}$. However, baryons are also no elementary particles. They exhibit an internal structure of quarks (which are elementary particles according to current knowledge) resulting in g-factors of 5.59 for the proton and -3.83 for the neutron. In addition, protons and neutrons are about 1800 times heavier than electrons which results, despite their higher g-factors, in a gyromagnetic ratio almost 3 magnitudes smaller.

Typically the total angular momentum of nuclei is termed **I**. There are nuclei with $\mathbf{I} = 0$ where all contributions of angular momentum cancel out. This is the case for all nuclei with even number of protons and neutrons, because the pairing of nucleons of the same type is energetically most favorable if their spins are oriented antiparallel. All other stable nuclei have a nonzero angular momentum **I** in the ground state and, hence, exhibit a magnetic moment $\vec{\mu}$. The gyromagnetic ratio of these nuclei depends on their atomic structure where positive and negative values are possible. Nuclei with high gyromagnetic ratios and thus with a strong NMR signal are for example: $^{1}\mathrm{H}$, $^{3}\mathrm{He}$, $^{7}\mathrm{Li}$, $^{13}\mathrm{C}$, $^{19}\mathrm{F}$, $^{23}\mathrm{Na}$, and $^{31}\mathrm{P}$.

By far the most important isotope for MRI is $^{1}\mathrm{H}$ because it is present in biological tissues in great abundance, mostly in form of water and fat. Additionally, $^{1}\mathrm{H}$ has the highest

gyromagnetic ratio ($\gamma = 2.675 \times 10^8\,\mathrm{J\,T^{-1}}$) of all stable nuclei. Appart from $^1\mathrm{H}$, $^{23}\mathrm{Na}$ and $^{31}\mathrm{P}$ are also naturally abundant in the human body. The feasibility of $^{23}\mathrm{N}a$ imaging on humans for stroke and tumor detection has been shown [30]. Moreover injectable solutions containing hyperpolarized $^{13}\mathrm{C}$ can be used to investigate the biochemical metabolism [31]. However, imaging of non hydrogen nuclei is primarily a research technique at present. This thesis focuses on $^1\mathrm{H}$ only and all examples and calculations given in the next sections refer to this specific case.

### 2.1.2. Macroscopic Magnetization in the Presence of a Static Magnetic Field

In the presence of a static magnetic field $\vec{B}_0$, the ground energy state of $^1\mathrm{H}$ splits into two levels due to the Zeeman effect [32]. The energy level $E_{\uparrow\uparrow}$, with parallel alignment of the proton's spin and $\vec{B}_0$, is energetically lower than the energy state $E_{\uparrow\downarrow}$ with antiparallel alignment. The energy difference $\Delta E$ between the two states can be described with the gyromagnetic ratio $\gamma$ and the absolute value of the static magnetic field $B_0$.

$$\Delta E = E_{\uparrow\downarrow} - E_{\uparrow\uparrow} = \hbar\gamma B_0 \tag{2.9}$$

The ratio between the number of protons occupying the parallel state and the antiparallel state can be described with a Boltzmann distribution

$$\frac{N_{\uparrow\uparrow}}{N_{\uparrow\downarrow}} = e^{\frac{-\Delta E}{k_B T}}\ , \tag{2.10}$$

$$\approx 1 + \frac{\Delta E}{k_B T} \qquad (\Delta E \ll k_B T)\ , \tag{2.11}$$

where $k_B T$ is the thermal energy of the proton. Assuming that $N_0$ is the total number of protons and $\Delta N$is the spin excess describing how many more spins populate the parallel state than the antiparallel state, Eq. 2.11 can then be rewritten to

$$\frac{1}{2}\frac{N_0 + \Delta N}{N_0 - \Delta N} = 1 + \frac{\Delta E}{k_B T}. \tag{2.12}$$

Under the the assumption of $\Delta E \ll k_B T$, Eq. 2.12 can be solved to $\Delta N$.

$$\Delta N = \frac{1}{2} N_0 \frac{\Delta E}{k_B T} \tag{2.13}$$

Recalling Eq. 2.7, the magnetic moment of one proton equals $\mu_i = \frac{1}{2}\hbar\gamma$. Finally the macroscopic magnetization $M_0$ can be calculated as the product of the spin excess and $\mu_i$.

$$M_0 = \frac{1}{2}\hbar\gamma\Delta N \tag{2.14}$$

$$= N\frac{\gamma^2\hbar^2}{4k_B T}B_0 \tag{2.15}$$

$M_0$ is identical to the sum of all magnetic moments $\mu_i$ of the spin ensemble. Since the energy difference $\Delta E$ is small compared to the thermal energy $k_B T$ the spin excess is very small. For a field strength of $1.5\,\mathrm{T}$ the spin excess is only about 5 out of a million. Nevertheless the huge amount of spins even within grams of matter creates a measurable macroscopic magnetization, which is the basis of all NMR experiments.

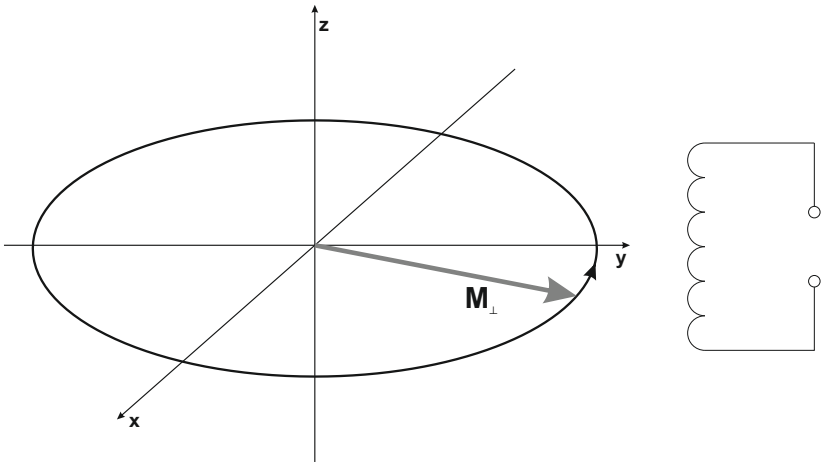


Figure 2.1.: Schematic illustration of the precessing transverse magnetization. The changing magnetic flux induces a voltage in the receive coil.

### 2.1.3. Dynamics of the Magnetic Moments

Without loss of generality, let the static magnetic field $\vec{B}_0$ point in the positive $z$ direction where the absolute value of $\vec{B}_0$ is denoted $B_0$.

$$\vec{B}_0 = B_0 \vec{e}_z. \tag{2.16}$$

Consequently also the macroscopic magnetization $\vec{M}$ in the equilibrium state, points in the positive z-direction. In agreement with Eq. 2.14. the absolute value of $\vec{M}$ is denoted $M_0$.

Unfortunately it is extremely difficult to measure $M_0$ in the equilibrium state because it is static and magnetometers usually lack the required sensitivity. Hence in NMR experiments $\vec{M}$ is tipped into the transverse plane where it is precessing around $\vec{B}_0$. The frequency of this precession is called Larmor frequency $\omega_0$ which is proportional to $B_0$ or, equivalently, the energy difference $\Delta E$ of the two spin states.

$$\omega_0 = \gamma B_0 \tag{2.17}$$

$$= \frac{\Delta E}{\hbar} \tag{2.18}$$

The transverse component $M_\perp$ of $\vec{M}$ creates a changing magnetic flux in a receive coil placed next to the measured object as illustrated in Fig. 2.1. This changing magnetic flux induces a voltage in the receive coil which represents the actual NMR signal. After $\vec{M}$ is tipped into the transverse plane, different relaxation processes start, which lead to a recovery of the equilibrium state. The dynamics of the $M_\perp$ will be described in detail in the next sections.

#### Rotating reference frame and $B_1$ field

Changing the orientation of the macroscopic magnetization $\vec{M}$, either away or towards the parallel alignment with $\vec{B}_0$, changes the internal energy of the protons because either

more or less spins occupy the favorable energy state (parallel orientation). The macroscopic magnetization $\vec{M}$ can be rotated using a RF-pulse with the Larmor frequency $\omega_0$. The physical mechanism to add energy is the stimulated absorption and to dissipate energy is the stimulated emission [33]. The quantum mechanical interaction of a two-level-system and the RF-pulse can be described by the Rabi cycle [34]. However, as most of the phenomena in NMR, classical physics can be used to described the rotation of $\vec{M}$.

Assuming a quadrature transmission coil, which creates a circular polarized magnetic field $\vec{B}_1$ with the frequency $\Omega$, the amplitude $B_1$ and the phase offset $\Phi$. The effective field $\vec{B}_{\text{eff}}$ including $\vec{B}_0$ and $\vec{B}_1$ can be defined as

$$\vec{B}_{\text{eff}} = B_0 \cdot \vec{e}_z + B_1[\cos(\Omega t + \Phi) \cdot \vec{e}_x - \sin(\Omega t + \Phi) \cdot \vec{e}_y] \ . \tag{2.19}$$

In the early days of NMR also a coil arrangement producing a linear polarized radio frequency field was used but it is less efficient and rarely used anymore. To understand the impact of the RF-pulse on $\vec{M}$ it is helpful to change in a rotating reference frame where $\vec{e}_x$ and $\vec{e}_y$ rotate around $\vec{e}_z$ with the frequency $\Omega$. All variables in the rotating reference frame are marked with a prime to distinguish from the system at rest. In the rotating reference the effective magnetic field $\vec{B}'_{\text{eff}}$ changes to

$$\vec{B}'_{\text{eff}} = B_0(1 - \frac{\Omega}{\omega_0}) \cdot \vec{e}'_z + B_1[\cos(\Phi) \cdot \vec{e}'_x - \sin(\Phi) \cdot \vec{e}'_y] \ . \tag{2.20}$$

In the rotating reference frame, the transverse component of $\vec{B}'_{\text{eff}}$ is at rest and its orientation only depends on the constant phase offset $\Omega$ which is typically called RF phase. Moreover there is a fictitious magnetic field term $-\frac{\Omega}{\omega_0}B_0 \cdot \vec{e}_z$ which counteracts $B_0 \cdot \vec{e}_z$. The derivation of this term can be found for example in [35]. In favor of clarity, $\Phi$ is set to zero in the following equations because it corresponds to a simple rotation of the coordinate system. In the case of resonance $\Omega = \omega_0$, the effective field $\vec{B}'_{\text{eff}}$ can be simplified to:

$$\vec{B}'_{\text{eff}} = B_1 \vec{e}'_y. \tag{2.21}$$

Each magnetic moment $\vec{\mu}$, which is oriented perpendicular to $\vec{B}'_{\text{eff}}$, experiences a torque, resulting in the following equation of motion

$$\frac{d\vec{M}}{dt} = \gamma \vec{M} \times \vec{B}'_{\text{eff}} \ . \tag{2.22}$$

Assuming a rectangular RF-pulse with amplitude $B_1$ and duration $\tau_{\text{RF}}$, the differential equation 2.22 can be solved to:

$$\vec{M}(B_1, \tau_{\text{RF}}) = M_0[\sin(\gamma B_1 \tau_{\text{RF}}) \cdot \vec{e}'_x + \cos(\gamma B_1 \tau_{\text{RF}}) \cdot \vec{e}'_z] \ . \tag{2.23}$$

It can be seen from Equation 2.23, that the RF-pulse rotates $\vec{M}$ around $\vec{e}'_y$. The amount of rotation is described by the so called flip angle $\alpha$.

$$\alpha = \gamma B_1 \tau_{\text{RF}} \tag{2.24}$$

Especially in MRI, the frequency spectrum of a RF-pulse is very important, either for spatial selectivity RF-pulse (see section 2.3.1) or chemical (spectral) selectivity. In the case of

small flip angles, the excitation profile of a RF-pulse can be well described by the Fourier transform of the pulse shape in time. For instance, the previous example of a rectangular pulse results in a sinc function in the frequency space. Such a rectangular RF-pulse is also called hard pulse and exhibits a broad frequency spectrum around $\omega_0$. However, for higher flip angles (i.e. over the range of 30°-180°) the Fourier relationship between the pulse shape and the excitation profile begins to fail [36, p. 43] due to nonlinear effects in the Bloch equations (see section 2.1.3). Thus, higher flip angles require iterative algorithms, like the Shinnar Le Roux algorithm (SLR), to determine the shape of the RF-pulse [37].

**Relaxation of the Magnetization**

After the application of a RF-pulse on $\vec{M}$, the spin ensemble relaxes back to the equilibrium state. There are two fundamental relaxation mechanisms in NMR. First, the recovery of the longitudinal magnetization $M_z$ to $M_0 \cdot \vec{e}_z$. Usually the spin ensemble is in an energetically higher state and needs to dissipate energy which occurs by stimulated emission. The transition is induced by magnetic field fluctuations due to thermal motion of neighbouring nuclei in the lattice. Therefore the relaxation of $M_z$ is also called spin-lattice relaxation. The rate of growth $\frac{dM_z}{dt}$ is proportional to the difference of the equilibrium value $M_0$ and $M_z$.

$$\frac{dM_z}{dt} = \frac{1}{T_1}(M_0 - M_z) \tag{2.25}$$

The differential equation 2.25 can be solved to

$$M_z(t) = M_z(0)e^{\frac{-t}{T_1}} + M_0(1 - e^{\frac{-t}{T_1}}) \ , \tag{2.26}$$

where $M_z(0)$ is the initial value of $M_z$ and $T_1$ is a tissue or material parameter which describes the time until $M_z(t)$ recovered to about $0.63M_0$ assuming $M_z(0) = 0$.

The second relaxation mechanism describes the decay of the transverse magnetization $M_\perp$ towards the equilibrium value zero. This decay is caused by little field inhomogeneities on the micro- and nanoscale. Thermal motion within the spin ensemble leads to an individual phase accumulation of each spin, resulting in destructive interference. The decay does not involve energetic transitions and no energy is transferred to the lattice. Thus, the relaxation of $M_\perp$ is called spin-spin relaxation. The following equation for the exponential decay of $M_\perp$ can be derived analogous to 2.25.

$$M_\perp(t) = M_\perp(0)e^{\frac{-t}{T_2}}. \tag{2.27}$$

The tissue or material parameter $T_2$ describes the time in which $M_\perp(t)$ decays to approximately $0.37M_\perp(0)$. The spin-spin relaxation involves those field fluctuations which meet resonance condition and, thus, cause a spin flip, as well as those field fluctuations which do not meet this condition. Consequently, the spin-lattice relaxation cannot be faster than the spin-spin relaxation, or with respect to the relaxation times, $T_2 \leq T_1$.

In addition to microscopic magnetic field fluctuations, there is a second effect causing a decay of $M_\perp$. A static background field also causes dephasing of the spin ensemble, and thus increase the decay of $M_\perp$. This additional relaxation mechanism is described by

another exponential decay constant $T_2'$. Although there is no guarantee that a inhomogeneous magnetic field results in an exponential decay of $M_\perp$, in most cases it is a sufficient model [35, p. 57]. The overall decay of $M_\perp$ is called Free Induction Decay (FID) and involves both effects $T_2$ and $T_2'$. The corresponding overall decay time is called $T_2^*$.

$$\frac{1}{T_2^*} = \frac{1}{T_2} + \frac{1}{T_2'} \tag{2.28}$$

It will be shown later that the dephasing effect due to $T_2'$ can be reversed using a so called Spin Echo (SE). However, the decay due to $T_2$ is a thermodynamical process and is irreversible.

### Bloch Equations

The dynamics of $\vec{M}$ can be described with the Bloch equations [38]. They describe the interaction of the spin ensemble with the magnetic fields $\vec{B}_0(t)$ and $\vec{B}_1(t)$ as well as the relaxation of the longitudinal and the relaxation magnetization, $M_z$ and $M_\perp$.

$$\frac{d\vec{M}}{dt} = \gamma\vec{M} \times \vec{B(t)} + \frac{1}{T_1}(M_0 - M_z) \cdot \vec{e}_z - \frac{1}{T_2}(M_x \cdot \vec{e}_x + M_y \cdot \vec{e}_y) \tag{2.29}$$

There exists no complete analytical solution for the Bloch equations. However, in MRI the duration of a RF-pulse is usually short compared to the relaxation times $T_1$ and $T_2$. That is why a separate treatment of RF-pulse and relaxation is sufficient in many cases. Corresponding analytical solutions for the effect of an RF-pulse and for the relaxation of the spin ensemble were shown in the previous two sections. However, an accurate prediction of $\vec{M}$ can only be achieved by numerically solving the Bloch equations.

### The Spin Echo

A NMR sample or a voxel in MRI typically exhibits a spectrum of different Larmor frequencies because of background $B_0$ inhomogeneity, susceptibility differences or chemical shifts. Consequently the local field $B_{\text{local}}(\vec{r})$ of each spin can deviate by the off-resonance $\Delta B_0$ from the constant field $B_0$.

$$B_{\text{local}}(\vec{r}) = B_0 + \Delta B_0(\vec{r}) \tag{2.30}$$

The off-resonance $\Delta B_0$ is typically dependent on the position $\vec{r}$ of the spin. The dephasing effect of $\Delta B_0$ can be reversed using a refocusing pulse. Following the excitation pulse (Fig. 2.2b) each spin accumulates phase according to its local Larmor frequency $\gamma B_{local}$ (Fig. 2.2c). After the time $\tau$, a refocusing pulse is applied, which rotates the spins by $180°$ around $\vec{B}_1$ (Fig. 2.2d) such that the "faster" spins are now behind the "slower" spins (Fig. 2.2e). As a result, after the time $2\tau$ all spins have the same phase again as illustrated in 2.2f. This effect was first reported by Hahn and Maxwell and is called Spin Echo (SE) [39, 40]. It is also possible to create an echo with more than two RF-pulses, for example using three subsequent $90°$ pulses which is called Stimulated Echo (STE) [41].

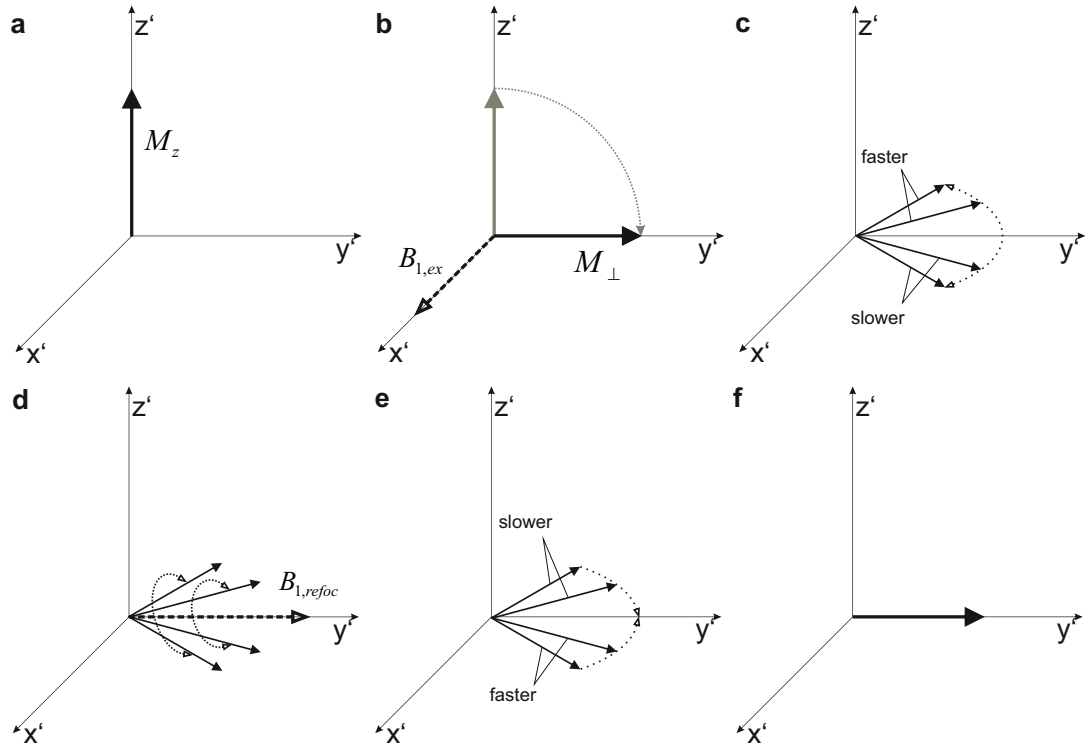


Figure 2.2.: Schematic illustration of the creation of a spin echo: a) equilibrium state, b) excitation pulse flipping $M_z$ into transverse plane, c) dephasing of the spins due to static background field, d) the refocusing pulse is mirroring the magnetization about the $y\prime$ axis, e) the "slow" spins are now in front of the "fast" spins f) formation of the spin echo.

## 2.2. Motion in NMR

In the previous section 2.1.3, it was shown that the dephasing of the spins due to a static backround field can be reversed using a SE. This, however, requires the spins to be at rest with respect to the static $B_{local}(\vec{r})$, which is generally not the case. On the one hand, all particles undergo Brownian motion which is a random process of particles that depends on their thermal energy and their mobility [8]. There is no correlation between the Brownian motion trajectory of different particles, which is why this type of motion is called incoherent or diffusion. On the other hand, all spins or parts of them can follow the same motion trajectory, which is called coherent motion. Types of coherent motion are, for example, translation, rotation or pulsation.

If a spin moves through an inhomogeneous magnetic field during a SE preparation, the spin will accumulate a net phase shift compared to another spin which is at rest. The reason is that the field $\Delta B_0(\vec{r})$, which the spin experiences before and after the refocusing pulse, is not identical. In the case of coherent motion, all spins experience the same phase shift, and therefore the phase of the NMR signal is shifted by the same amount. However, in the case of incoherent motion, all spins accumulate a different phase shift,

resulting in destructive interference and attenuation of the signal's amplitude. To counter this effect, the use of a train of refocusing pulses with short spacing in between each other was suggest by Carr and Purcell [6] and further improved by Meiboom and Gill [42]. This train of refocusing pulses is widely used in MRI, and is named after the inventors, CPMG sequence.

Although modern NMR spectrometers or MRI scanners offer a very homogenous background field, there are some cases where susceptibility differences in the scanned object, e.g. between different tissue types, can induce field gradients that cause diffusion attenuation of the SE signal. Solid–air interfaces can lead to significant signal attenuation in porous media NMR. Also in the case of in-vivo MRI, diffusion effects can predominate over $T_2^*$, for instance in regions around small vessels, particularly at high field [43]. However, most often, diffusion effects due to background gradients can be neglected in MRI. Instead, artificial magnetic field gradients, which are induced by additional coils, are applied to the spins and the resulting signal attenuation is analyzed to obtain insights about the microstructure of the underlying object or tissue.

### 2.2.1. Self Diffusion

Classical Diffusion is defined as net movement of atoms or molecules from regions with high concentration to regions with low concentration. According to Fick's first law the molar flux $\vec{J}$ is proportional to the gradient of the molar concentration $c_i(\vec{r})$

$$\vec{J} = D\nabla c_i(\vec{r}), \tag{2.31}$$

where $D$ is the diffusion coefficient [44]. Further, Fick's second law predicts the change of the concentration $c_i(\vec{r}, t)$ in time.

$$\frac{\partial M(\vec{r}, t)}{\partial t} = D\nabla^2 c_i(\vec{r}, t) \tag{2.32}$$

In the notion of Fick's law, $D$ describes the diffusivity of a certain solute (e.g. ethanol) in a certain solvent (e.g. water). However, the focus of this thesis is the so called self diffusion where no macroscopic gradient of $c_i(\vec{r})$ exists. In this case $D$ is called the self diffusion coefficient describing the diffusion of a certain substance in itself. Einstein derived an expression for $D$ by introducing the conditional probability $P(\vec{r}\,|\vec{r}\,', t)$ that a particle starting at position $\vec{r}$ will move to position $\vec{r}\,'$ after the time $t$ [33]. Einstein solved the partial differential equation of Fick's second law 2.32 using $P(\vec{r}\,|\vec{r}\,', t)$ instead of $c_i(\vec{r}, t)$ leading to a Gaussian probability distribution.

$$P(\vec{r}\,|\vec{r}\,', t) = (4\pi Dt)^{-3/2} \exp(-\frac{(\vec{r}\,' - \vec{r}\,)^2}{4Dt}) \tag{2.33}$$

Unfortunately the conditional probability $P(\vec{r}\,|\vec{r}\,', t)$ is extremely difficult to measure because diffusion lengths within typical NMR relaxation times are very small and far below the resolution limit of MRI. A more useful definition is the average probability $\overline{P}(\vec{R}, t)$ of all protons within the sample to move by the displacement $\vec{R} = \vec{r}\,' - \vec{r}$. $\overline{P}(\vec{R}, t)$ can be calculated by substituting $\vec{r}\,' = \vec{r} + \vec{R}$ in 2.33, multiplying with the probability $P(\vec{r})$ to find

a proton at location $\vec{r}$, and integrating over all possible start positions $\vec{r}$.

$$\overline{P}(\vec{R},t) = \int_V P(\vec{r}\,|\vec{r}+\vec{R},t)P(\vec{r})\,d\vec{r} \tag{2.34}$$

The definition of $\overline{P}(\vec{R},t)$ given in 2.34 is called the EAP, and is widely used in diffusion weighted NMR and DWI. It is important to note, that the EAP definition is valid for any arbitrary conditional probability $P(\vec{r}\,|\vec{r}\,',t)$ and it is not limited to the Gaussian shape in 2.33. However, when assuming a Gaussian $P(\vec{r}\,|\vec{r}\,',t)$ the Mean Squared Displacement (MSD) $\langle\vec{R}^2\rangle$ after the time $t$ can be used as a measure of the diffusivity D of the particles.

$$\langle\vec{R}^2\rangle = \int_{-\infty}^{\infty} \overline{P}(\vec{R},t)\vec{R}^2\,d\vec{R} \tag{2.35}$$

$$= 6Dt \tag{2.36}$$

### 2.2.2. The Bloch Torrey Equations

A more general approach to describe the time dependent behavior of the magnetization $\vec{M}$ was made by Torrey [45]. The effect of free Gaussian diffusion was accounted for by introducing additional terms in the Bloch equations (see section 2.1.3, Eq. 2.29).

$$\frac{d\vec{M}}{dt} = \gamma\vec{M}\times\vec{B(t)} + \frac{1}{T_1}(M_0 - M_z)\cdot\vec{e}_z - \frac{1}{T_2}(M_x\cdot\vec{e}_x + M_y\cdot\vec{e}_y) + D\nabla^2\vec{M} \tag{2.37}$$

Equation 2.37 is called Bloch-Torrey equation where $D$ is the diffusion coefficient. Unfortunately there is no general analytic solution of 2.37. However, an important special case is the signal evolution of $M_\perp(t)$ which was tipped into the transverse plane by an excitation pulse. In that case, the longitudinal magnitization can be neglected. Following this approach, equation 2.37 is evaluated using the rotating reference frame and the following assumptions are made:

- **1:** There are no $B_1$ fields except for a perfect, instantaneous $90°$ excitation pulse and a arbitrary number of perfect, instantaneous $180°$ refocusing pulses which keep all magnetization in the transverse plane.
- **2:** The magnetic field $\vec{B}'$ in the rotating reference frame is approximated by a constant magnetic field offset $\Delta B_0$ and a time varying magnetic field gradient $\vec{G}^*(t)$in $z$ direction. $\vec{G}^*(t)$ is generated by special gradient coils, which can create an arbitrary gradient in space of the $z$-component of the magnetic field, to encode diffusion (the gradient coils are also used for the spatial encoding, see chapter 2.3). The star in $\vec{G}^*(t)$ indicates the "effective gradient" that the spins experience, as the polarity has to be flipped each time a refocusing pulse is applied.

$$\vec{B}' = (\Delta B_0 + \vec{G}^*(t)\cdot\vec{r}\,)\cdot\vec{e}_z' \tag{2.38}$$

- **3:** The transverse magnetization is expressed with a complex number where the real part corresponds to the $\vec{e}_x'$ axis and the imaginary part corresponds to the $\vec{e}_y'$ axis.

$$M_\perp = M_x + iM_y \tag{2.39}$$

- **4:** The trajectory $\vec{r}(t)$ describes the coherent motion of the spin ensemble.

Rewriting 2.37 with the given assumptions yields:

$$\frac{dM_\perp}{dt} = -i\gamma M_\perp(\Delta B_0 + \vec{G}^*(t)\cdot\vec{r}(t)\,) - \frac{M_\perp}{T_2} + D\nabla^2 M_\perp\,. \tag{2.40}$$

The ansatz to solve the partial differential equation 2.40 can be found in [45–47]. Here only the solution is shown

$$M_\perp(t) = e^{(-t/T_2)}e^{(-i\gamma\Delta B_0 t)}e^{(-i\phi_g(t,\vec{r}(t)))}e^{(-bD)}\;, \tag{2.41}$$

where the first term describes the signal attenuation due to spin-spin relaxation, the second term describes the phase shift due to the constant magnetic field offset $\Delta B_0$, the third term describes a phase shift $\phi_g(t,\vec{r}(t))$ due to the gradient field and coherent motion, and the fourth term describes the signal attenuation due to incoherent motion or diffusion, where the coefficient $b$ is called b-value and will be described in detail later.

The phase $\phi_g(t,\vec{r}(t))$ can be written as the sum of all phase contributions the spin ensemble has experienced along the trajectory $\vec{r}(t)$.

$$\phi_g(t,\vec{r}(t)) = \gamma\int_0^t \vec{G}^*(t')\vec{r}(t')\,dt' \tag{2.42}$$

Expanding the trajectory $\vec{r}(t')$ in a Taylor series yields

$$\phi_c(t) = \gamma\sum_{i=0}^{n}\frac{\vec{r}^{(n)}}{n!}\int_0^t \vec{G}^*(t')(t')^n\,dt'\,, \tag{2.43}$$

where $\vec{r}^{(n)}$ corresponds to the moments of the trajectory, the starting position $\vec{r}^{(0)}$, the velocity $\vec{r}^{(1)}$, the acceleration $\vec{r}^{(2)}$ and higher order moments. For each moment of the trajectory a so called gradient moment $\vec{M}_n$ can be defined.

$$\vec{M}_n = \frac{\gamma}{n!}\int_0^t \vec{G}^*(t')(t')^n\,dt' \tag{2.44}$$

The phase shift of the spin ensemble can now be simply written as the sum of the moments of the trajectory multiplied by the corresponding gradient moment.

$$\phi_g(t) = \sum_{i=0}^{n}\vec{r}^{(n)}\vec{M}_n \tag{2.45}$$

The zero order gradient moment $\vec{M}_0$, also called gradient area, is simply the integral of the gradient field over time and the resulting phase shift only depends on the starting position $\vec{r}_0$. Usually $\vec{G}^*(t')$ is chosen such that $\vec{M}_0 = 0$ at the TE when the NMR signal is sampled. Otherwise there would be an additional signal attenuation because not all spins exhibit the same phase. Let $\phi_c(t)$ be the phase shift caused only by coherent motion described by all nonzero moments.

$$\phi_c(t) = \sum_{i=1}^{n}\vec{r}^{(n)}\vec{M}_n \tag{2.46}$$

Often $\phi_c(t)$ is only a concomitant phenomenon of the spatial or diffusion encoding but it can also be used to investigate the motion trajectory that the spin ensemble has taken. For example, comparing the phase of the NMR signal with and without the application of a bipolar gradients can reveal the velocity of the spins, assuming that higher order moments are negligible. This technique is called velocity or flow encoding.

The solution of the Bloch-Torrey equation 2.41 also describes the attenuation of the signal's amplitude due to incoherent motion. The exponential decay is defined by the diffusion constant D and the b-value $b$. The b-value can be calculated for an arbitrary sequence of effective magnetic field gradients $\vec{G}^*(t)$ [45–47] which is typically called diffusion encoding scheme.

$$b = \gamma^2 \int_0^t \left( \int_0^{t'} \vec{G}^*(t'')\, dt'' \right)^2 dt' \tag{2.47}$$

A diffusion encoding schemes can be used to investigate microstructural features of the underlying tissue or sample. For example, a bipolar gradient with certain b-value is applied after the excitation pulse and the corresponding signal attenuation of $S(b)$ is derived by a comparison with the non-diffusion weighted signal $S(b = 0)$. Assuming that diffusion is truly Gaussian, the diffusion coefficient D can be calculated, using both the b-value and signal attenuation.

$$D = \frac{1}{b} \ln \left( \frac{S(b=0)}{S(b)} \right) \tag{2.48}$$

In conclusion, diffusion encoding schemes can be employed to quantitatively investigate the diffusion behavior of NMR active nuclei.

### 2.2.3. The Stejskal Tanner Pulse Preparation

In the beginning of diffusion weighted NMR [6, 39] constant magnetic field gradients in combination with a SE were used to obtain a diffusion weighted signal. Although this method is very time efficient, the presence of a constant gradient during signal acquisition is not compatible with spatial encoding in MRI (see section 2.3.1), and it introduces a strong $T_2^*$ decay before and after the SE. Thus, only pulsed diffusion weighted gradients are used in DWI. By far the most widely used diffusion encoding scheme is the so called ST preparation [48]. The ST preparation uses two pulsed diffusion weighting gradients with the same polarity, separated by a $180°$ refocusing pulse as illustrated in Figure 2.3. In principle, also bipolar gradients can be used for diffusion encoding but the advantage of using a SE is a typically higher SNR because the signal only decays with $T_2$ instead of $T_2^*$. To determine the expected signal attenuation of the ST preparation, the b-value has to be calculated according to equation 2.47. Assuming two rectangular gradient pulses in an arbitrary direction with the gradient strength G, the duration $\delta$ and the temporal spacing $\Delta$ (typically called the diffusion time or the mixing time) as illustrated in Figure 2.3, the b-value of the ST preparation is given by

$$\begin{aligned} b &= \gamma^2 G^2 \left[ \int_0^{\delta} (t')^2 dt' + \int_{\delta}^{\Delta} \delta^2 dt' + \int_{\Delta}^{\Delta+\delta} (\delta + \Delta - t')^2 dt' \right] , && (2.49) \\ &= \gamma^2 G^2 (\Delta - \delta/3) . && (2.50) \end{aligned}$$

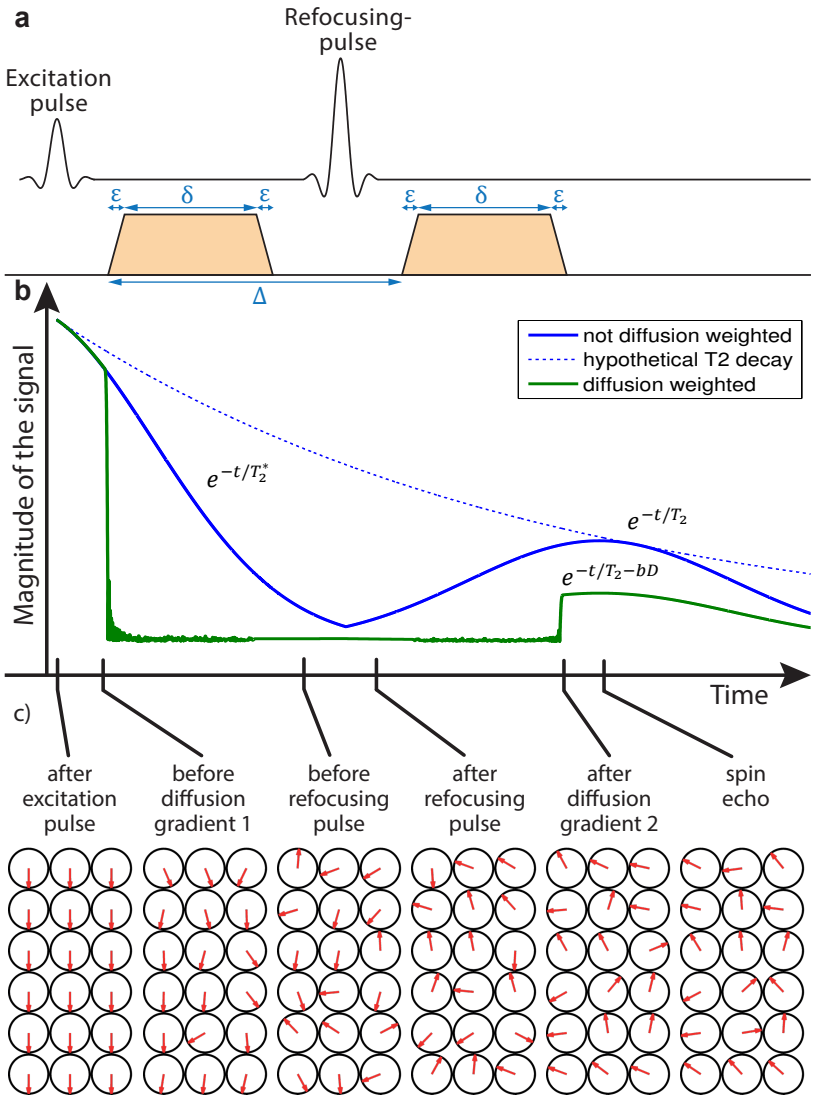


Figure 2.3.: Schematic illustration of the Stejskal Tanner (ST) diffusion encoding scheme. a) Chronological order of RF-pulses and diffusion encoding gradients. b) Exemplary simulated signal curves with and without diffusion preparation, including $T_2^*$ effects. The refocusing pulse is assumed to work instantaneous. In addition the pure $T_2$ signal decay is plotted to highlight the effect of the spin echo. c) Phase diagrams for 18 exemplary spins at 6 different time points of the ST sequence: Firstly, directly after the excitation pulse where all spins are coherent, secondly prior to the first diffusion gradient where the static background field causes initial dephasing, thirdly prior to refocusing pulse where the spins are completely dephased due to the first diffusion weighting gradient, fourthly after the refocusing pulse where spins have been flipped around the x-axis, fifthly after the second diffusion gradient where the first gradient moment is zero again, and finally, at the time of the spin echo, where the spins exhibit incomplete phase reversal due to incoherent motion.

Under realistic conditions, the gradient amplitude cannot be ramped up instantaneously and equation 2.49 is only an approximate solution. Assuming a linear ramp of the gradient amplitude over the time $\epsilon$ yields [49]:

$$b = \gamma^2 G^2 (\Delta - \delta/3 + \epsilon^3/30 - \delta\epsilon^2/6) \,. \tag{2.51}$$

### 2.2.4. Non Gaussian diffusion

The analytical solution of the Bloch–Torrey equation to describe the effect of diffusion in the presence of magnetic field gradients, which was shown in the previous sections 2.2.2 and 2.2.3, presumes the EAP to be Gaussian. Hence, the diffusion-weighted signal for a distinct diffusion encoding direction is expected to decay mono-exponentially with the b-value.

This is in general not the case for biological tissue [12–15] because the motion of the water molecules is restricted by cell membranes and compartments of different size. In the field of DWI two concepts have been introduced to describe the interaction of diffusing atoms or molecules with obstacles, namely hindered diffusion and restricted diffusion. The former assumes that diffusion of a substance, e.g. water, is slowed down by a variety of obstacles but still exhibits a Gaussian EAP and thus the NMR signal still decays exponentially with $b$ [14, 50]. The extra-axonal space of WM is a typical example for hindered diffusion as it is mostly connected and diffusion is approximately Gaussian [51]. On the other hand, restricted diffusion means that the motion of the atoms or molecules is limited to a certain volume due to boundaries in the medium [52]. In this case, the shape EAP becomes constant at long diffusion times $\Delta$ because the maximum displacement is intrinsically limited by the restricting volume. On the contrary, the displacement predicted by the Gaussian model exceeds the size of the restricting volume. A typical example of restricted diffusion is the intra-axonal space in WM as the axon's myelin sheath can be considered impermeable to water over typical diffusion times $\Delta$ [14, 53]. Examples of the EAP for free, hindered and restricted diffusion are depicted in Figure 2.4 assuming mixing times ranging from $5\,\mathrm{ms}$ to $30\,\mathrm{ms}$ and a diameter of the restricting volume of $10\,\mu\mathrm{m}$. The EAP of free and hindered diffusion broadens with increasing $\Delta$ maintaining the Gaussian shape while the EAP of restricted diffusion exhibits a constant triangular shape for high $\Delta$. Consequently, in case of restricted diffusion, the attenuation of the NMR signal due to diffusion does not steadily increase with $\Delta$ but reaches plateau.

In MRI the imaging volume is split into multiple small volumes, called voxel, where the NMR signal from each voxel can be measured separately (see section 2.3). As the following descriptions are closely related to Diffusion Weighted Imaging (DWI) rather than NMR, the term voxel is used instead of sample. The voxel size in DWI is typically in the millimeter range or slightly below while the molecular displacement within realistic mixing times is in the micrometer range. Thus the diffusion signal measured in DWI is the ensemble average of a large variety of microstructural features, potentially exhibiting free and hindered diffusion as well as the highly non-gaussian restricted diffusion. Which of the three diffusion types dominates can also depend on the diffusion encoding scheme, e.g. in case of a ST preparation the mixing time $\Delta$ and the b-value. Moreover multiple tissue types can contribute to the same voxel which is called partial volume effect.

In conclusion a mono exponential decay with b and D is a highly simplified concept but

it can be very useful to roughly quantify diffusion. However, to account for the complexity of biological tissue, in DWI, the term Apparent Diffusion Coefficient (ADC) is often used for the exponential decay constant instead of $D$. Thus, the ADC is the diffusion coefficient one would calculate if the EAP were Gaussian.

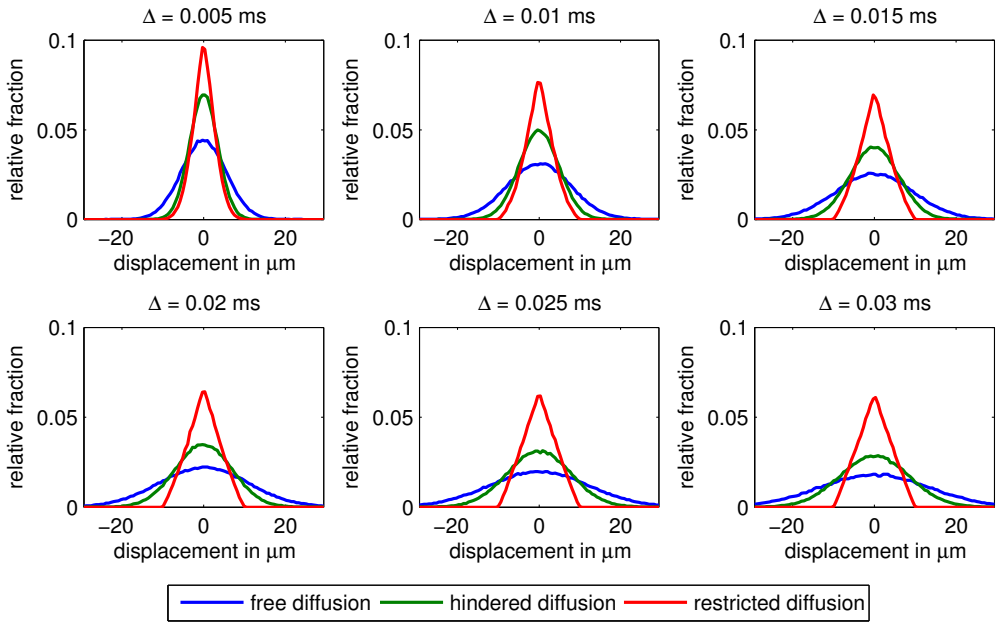


Figure 2.4.: Simulation comparing the EAP for free diffusion, hindered diffusion and restricted diffusion using different mixing times $\Delta$. The following parameter were chosen for the simulation: free diffusion, $D = 3 \times 10^{-9}\,\mathrm{m^2 s^{-1}}$ corresponding to diffusion coefficient of water at body temperature [54, p. 43]; hindered diffusion, $D = 1.2 \times 10^{-9}\,\mathrm{m^2 s^{-1}}$; restricted diffusion $D = 3 \times 10^{-9}\,\mathrm{m^2 s^{-1}}$ and diameter of the restricting volume was $10\,\mu\mathrm{m}$.

### 2.2.5. Diffusion Models

By far the most widely used model to quantify diffusion in the human brain is the DTI model [9]. This technique uses a three-dimensional (3D) second order diffusion tensor with 6 independent parameters to describe the directional dependence of the ADC as an ellipsoid. However, as pointed out in the previous section (2.2.4) the neuronal tissue architecture is highly complex and thus the DTI model may be oversimplifying [55]. Consequently newer diffusion models extend beyond the concept of the ADC trying to describe also non-Gaussian diffusion.

Multi-tensor fitting is a simple extension of DTI to handle crossing fibers in WM. The measured signal is assumed to originate from different compartments, e.g. two crossing fiber bundles, where each compartment is characterized by one DT respectively [56, 57]. In some implementations a third compartment with isotropic diffusion is added to allow partial volume fractions of GM or CSF [57]. However, as discussed before, the ADC concept is incapable of accurately modeling the diffusion signal of the highly restricted intra-

axonal space [53]. Therefore, the Composite Hindered and Restricted Model of Diffusion (CHARMED) model only uses a DT to describe the diffusion weighted signal from extra-axonal space [58]. In contrary to multi-tensor fitting, the diffusion weighted signal of each fiber population is modeled assuming restricted diffusion within cylindrically bounded volumes. While the multi-tensor approach only requires a single shell High Angular Resolution Diffusion-weighted Imaging (HARDI) acquisition [56], CHARMED requires diffusion encoding schemes with multiple b-values. An expansion of CHARMED is used in the AxCaliber model for estimation of the axon diameter distribution [59]. In AxCaliber, only single fiber population is assumed and restricted diffusion is modeled assuming axons (cylinders) with multiple diameters. The population fraction of the axon diameter is approximated by a gamma distribution. Since AxCaliber requires DWIs with multiple b-values and multiple mixing times $\Delta$, typically only one diffusion encoding direction is measured which is aligned perpendicular to the fiber orientation [59].

In Neurite Orientation Dispersion and Density Imaging (NODDI) [60], the axons are modeled as one-dimensional (1D) sticks with Gaussian diffusion parallel to the sticks and no diffusion perpendicular to the sticks. However, the orientation of the sticks is dispersed, following a Watson distribution, where the orientation dispersion index characterizes the the amount of dispersion. Consequently, only the component of the diffusion encoding gradient aligned parallel to a stick causes Gaussian diffusion attenuation (see Eq. 2.47 or 2.49). The signal of the intra-axonal volume fraction corresponds to the sum over all sticks and therefore equals a multiexponential decay in the b-value. Further, the extra-axonal volume fraction is modeled by hindered diffusion, using again a DT and CSF contamination is addressed by a third component with isotropic Gaussian diffusion.

Modeling the diffusion signal of WM is a very active field of research and many more multi-compartment models do exist. A contemporary comparison of the performance of multi-compartment diffusion models can be found in Ferizi et al. [61].

Recently Jensen et al. introduced DKI [15], which extends the DTI model by a second order Taylor expansion in the b-value to characterize the non-Gaussian fraction of diffusion. This additional term can be described by a 3D 4th order Diffusion Kurtosis Tensor (DKT), adding 15 further independent coefficients to the DTI model. Therefore the DKI model is parametrized by altogether 22 elements: the non-diffusion-weighted signal, the 6 independent elements of the DT and the 15 independent elements of the DKT.

Finally, there exist q-space methods, which estimate the EAP by exploiting its Fourier relationship with the so called q-space [62] (see section 2.2.5). In Diffusion Spectrum Imaging (DSI) altogether 6-dimensional data is acquired, three image dimensions and three q-space dimensions, to reconstruct the EAP for each voxel respectively [63]. As there is no explicit diffusion model assumed, q-space methods are often considered to be "model-free" [55].

In the following sections, the DTI and DKI model as well as the DSI technique are described in more detail as they are extensively used in this thesis.

### Diffusion Tensor Imaging

The DTI model is an elegant way to describe anisotropic diffusion using a 3D second order diffusion tensor **D**. The diffusion weighted signal $S(b, \vec{n}, \mathbf{D})$ equals

$$S(b, \vec{n}, \mathbf{D}) = S_0 \exp\left( -b \sum_{i,j=1}^{3} n_i n_j \mathrm{D}_{i,j} \right) , \tag{2.52}$$

where $S_0$ is the non-diffusion-weighted signal, $\mathrm{D}_{i,j}$ is a coefficient of the diffusion tensor **D**, $b$ is the b-value and $n_i$, $n_j$ are coefficients of an arbitrary unit vector $\vec{n}$. The diffusion tensor **D** is symmetric because the signal attenuation is independent of the polarity of the diffusion encoding gradient.

$$\mathbf{D} = \begin{bmatrix} \mathrm{D}_{xx} & \mathrm{D}_{xy} & \mathrm{D}_{xz} \\ \mathrm{D}_{yx} & \mathrm{D}_{yy} & \mathrm{D}_{xz} \\ \mathrm{D}_{zx} & \mathrm{D}_{zy} & \mathrm{D}_{zz} \end{bmatrix} \tag{2.53}$$

The ADC in the direction $\vec{n}$ is given by

$$\mathrm{ADC}(\vec{n}, \mathbf{D}) = \sum_{i,j=1}^{3} n_i n_j \mathrm{D}_{i,j} \ . \tag{2.54}$$

Several rotationally invariant diffusion metrics can be derived from the DT, including MD and FA, which are used extensively to analyze structural integrity of neuronal tissue [64–66]. MD is used to characterize average diffusivity within a voxel and has the same unit as $D$ or ADC. It is given by the trace of **D** divided by three

$$\mathrm{MD} = \frac{1}{3} \sum_{i=1}^{3} \mathrm{D}_{i,i} \ , \tag{2.55}$$

which is equivalent to the average of the eigenvalues ($\lambda_1$, $\lambda_2$, $\lambda_3$) of **D**. On the other hand, FA is a dimensionless quantity to describe the anisotropy of diffusion, ranging from zero to one.

$$\mathrm{FA} = \sqrt{\frac{3}{2}} \sqrt{\frac{(\lambda_1 - \mathrm{MD})^2 + (\lambda_2 - \mathrm{MD})^2 + (\lambda_3 - \mathrm{MD})^2}{(\lambda_1^2 + \lambda_2^2 + \lambda_3^2)}} \ . \tag{2.56}$$

Fig. 2.5 depicts 3D-plots surface plots of the ADC for four different DTs with the corresponding eigenvalues $\lambda_1$, $\lambda_2$ and $\lambda_3$. All four examples exhibit a very similar value for MD, although the shape of the ADC is very different. A comparison of Fig. 2.5b and c demonstrates, that also FA is not an unambiguous metric to describe the DT. Although the MD and FA values are very similar, the ADC plot in Fig. 2.5b and c look very different. Therefore, it has been reported, that the eigenvalues itself or combinations of eigenvalues, such as radial diffusivity

$$D_{\perp} = \frac{\lambda_2 + \lambda_3}{2} \ , \tag{2.57}$$

or axial diffusivity

$$D_{||} = \lambda_1 \ , \tag{2.58}$$

may be more specific to WM pathology [50, 67].

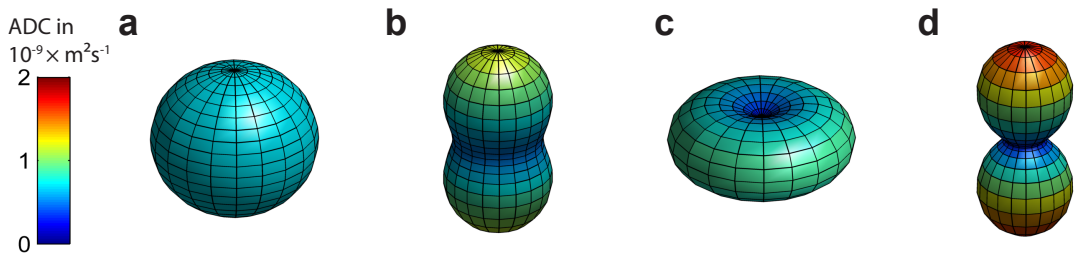


| FA | 0 | 0.5 | 0.5 | 0.8 |
|---|---|---|---|---|
| MD | 0.70 × $10^{-9}$ m²s$^{-1}$ | 0.73 × $10^{-9}$ m²s$^{-1}$ | 0.68 × $10^{-9}$ m²s$^{-1}$ | 0.77 × $10^{-9}$ m²s$^{-1}$ |
| $\lambda_1$ | 0.70 × $10^{-9}$ m²s$^{-1}$ | 0.50 × $10^{-9}$ m²s$^{-1}$ | 0.90 × $10^{-9}$ m²s$^{-1}$ | 0.30 × $10^{-9}$ m²s$^{-1}$ |
| $\lambda_2$ | 0.70 × $10^{-9}$ m²s$^{-1}$ | 0.50 × $10^{-9}$ m²s$^{-1}$ | 0.90 × $10^{-9}$ m²s$^{-1}$ | 0.30 × $10^{-9}$ m²s$^{-1}$ |
| $\lambda_3$ | 0.70 × $10^{-9}$ m²s$^{-1}$ | 1.20 × $10^{-9}$ m²s$^{-1}$ | 0.25 × $10^{-9}$ m²s$^{-1}$ | 1.70 × $10^{-9}$ m²s$^{-1}$ |

Figure 2.5.: **a-d**: Surface plots of the ADC for four different DTs. The corresponding eigenvalues of the DTs as well as MD and FA values are given in the table below.

### Diffusional kurtosis imaging

The DKI model parametrizes the MR signal $S(b, \vec{n})$ with the non-weighted signal $S_0$, the symmetric second-order diffusion tensor $\mathbf{D_{DKI}}$ and the symmetric 4th order kurtosis tensor $\mathbf{W}$

$$S(b, \vec{n}, \mathbf{D}, \mathbf{W}) = S_0 \exp\left( -b \sum_{i,j=1}^{3} n_i n_j \mathrm{D}_{i,j} + \frac{b^2}{6} \left( \sum_{i=1}^{3} \frac{\mathrm{D}_{i,i}}{3} \right)^2 \sum_{i,j,k,l=1}^{3} n_i n_j n_k n_l \mathbf{W}_{ijkl} \right), \quad (2.59)$$

where $\vec{n}$ is an arbitrary unit vector. Because both tensors are fully symmetric, $\mathbf{D}$ and $\mathbf{W}$ have 6 and 15 independent coefficients respectively. Basically all metrics of the DTI model can be derived from $\mathbf{D_{DKI}}$. However, they should not be directly compared as they belong to two different models. Therefor, to avoid confusion in the notation, the index "DKI" is added to DTI metrics related to a DKI fit. The Apparent Kurtosis Coefficient (AKC) of the DKI model is defined similarly to ADC, and is used to quantify the non-Gaussianity of diffusion in direction $\vec{n}$.

$$\mathrm{AKC}(\vec{n}) = \left( \frac{\mathrm{MD_{DKI}}}{\mathrm{ADC_{DKI}}(\vec{n})} \right)^2 \sum_{i,j,k,l=1}^{3} n_i n_j n_k n_l \mathbf{W}_{ijkl} \quad (2.60)$$

To increase accuracy and precision of the $\mathrm{DT_{DKI}}$ and DKT estimation, several constraints have been proposed to ensure that $\mathrm{ADC_{DKI}}$ and AKC lie within a physically acceptable range [68–70]. Particularly negative values of the $\mathrm{ADC_{DKI}}$ and AKC are considered as physically not plausible (a negative ADC is also not plausible for the DTI model). Furthermore, a third constraint has been proposed by Veraart et al. [68] enforcing the MR signal $S(b, \vec{n}, \mathbf{D}, \mathbf{W})$ to monotonically decrease with b. The mathematical formulations of

the contraints are given by

$$1. \quad \mathrm{ADC}_{\mathrm{DKI}}(\vec{n}, \mathbf{D}) \geq 0 \quad \forall\, |\vec{n}| = 1\,, \tag{2.61}$$

$$2. \quad \mathrm{AKC}(\vec{n}, \mathbf{D}, \mathbf{W}) \geq 0 \quad \forall\, |\vec{n}| = 1\,, \tag{2.62}$$

$$3. \quad \mathrm{AKC}(b, \vec{n}, \mathbf{D}, \mathbf{W}) \leq \frac{3}{\mathrm{ADC}_{\mathrm{DKI}}(b, \vec{n}, \mathbf{D}) b} \quad \forall\, 0 \leq b \leq b_{max},\ |\vec{n}| = 1\,, \tag{2.63}$$

where $b_{max}$ is the highest b-value in the diffusion encoding scheme. Basically, constraints #1 and #2 can be fulfilled by enforcing positive definiteness of the DT and DKT using nonlinear fitting methods [70]. Unfortunately the commonly used Linear Least Squares (LLS) and Weighted Linear Least Squares (WLLS) fitting techniques are not capable to implicitly impose positive definiteness of the DT and DKT. However, explicit constrains of $\mathrm{ADC}_{\mathrm{DKI}}$ and AKC for a finite number of directions can be used for LLS or WLLS fitting instead [69, 71].

Several rotationally invariant, scalar metrics for DKI exist, including different kinds of mean values such as MK (spherical average AKC), ME (ellipsoidal average AKC), MZ (average AKC in the scaled inherent coordinate system) [72], directional metrics such as radial kurtosis ($\mathrm{AKC}_{\perp}$) and axial kurtosis ($\mathrm{AKC}_{||}$) [73] as well as extreme values like maximum kurtosis ($\mathrm{AKC}_{\mathrm{max}}$) and minimum kurtosis ($\mathrm{AKC}_{\mathrm{min}}$) [72]. While MK and ME can only be computed numerically [72], there exist a simple closed form solution for MZ. To calculate MZ, $\mathbf{W}$ must be transformed into the eigenspace of $\mathbf{D}$ yielding $\hat{\mathbf{W}}$. Assuming that the columns of the orthogonal matrix $\mathbf{P}$ correspond to the eigenvectors of $\mathbf{D}$, the coefficients of $\hat{\mathbf{W}}$ can be calculated as

$$\hat{\mathrm{W}}_{ijkl} = \sum_{i',j',k',l'}^{3} \mathrm{W}_{i',j',k',l'} \mathrm{P}_{i'i} \mathrm{P}_{j'j} \mathrm{P}_{k'k} \mathrm{P}_{l'l}\ . \tag{2.64}$$

It is shown in Qi et al. [72] that MZ is given by

$$\mathrm{MZ} = \frac{(\mathrm{MD}_{\mathrm{DKI}})^2}{5} \left( \frac{\hat{\mathrm{W}}_{1111}}{\lambda_1^2} + \frac{\hat{\mathrm{W}}_{2222}}{\lambda_2^2} + \frac{\hat{\mathrm{W}}_{3333}}{\lambda_3^2} + \frac{\hat{\mathrm{W}}_{1122}}{\lambda_1 \lambda_2} + \frac{\hat{\mathrm{W}}_{1133}}{\lambda_1 \lambda_3} + \frac{\hat{\mathrm{W}}_{2233}}{\lambda_2 \lambda_3} \right)\ . \tag{2.65}$$

where $\lambda_1$, $\lambda_2$, $\lambda_3$ correspond to the eigenvalues of $\mathbf{D}$. Since $\hat{\mathbf{W}}$ is already transformed into the eigenspace of $\mathbf{D}$, $\mathrm{AKC}_{||}$ and $\mathrm{AKC}_{\perp}$ can be defined similarly to the DTI model (see Eqs. 2.57, 2.58) [73].

$$\mathrm{AKC}_{||} = \frac{(\mathrm{MD}_{\mathrm{DKI}})^2}{\lambda_1^2} \hat{\mathrm{W}}_{1111} \tag{2.66}$$

$$\mathrm{AKC}_{\perp} = \frac{(\mathrm{MD}_{\mathrm{DKI}})^2}{2} \left( \frac{\hat{\mathrm{W}}_{2222}}{\lambda_2^2} + \frac{\hat{\mathrm{W}}_{3333}}{\lambda_3^2} \right) \tag{2.67}$$

The accurate extreme values $\mathrm{AKC}_{\mathrm{max}}$ and ($\mathrm{AKC}_{\mathrm{min}}$) can be calculated using the D-eigenvalues of $\mathbf{W}$ [74]. However, as the calculation of the D-eigenvalues is computationally very demanding, Kelvin-eigenvalues [74] of $\mathbf{W}$ are a computationally simple alternative to derive an upper and lower bounds for $\mathrm{AKC}_{\mathrm{max}}$ and $\mathrm{AKC}_{\mathrm{min}}$.

### Diffusion Spectrum Imaging and the Narrow Gradient Pulse Approximation

In the previous sections, certain assumptions were made to model the diffusion-weighted signal. While empirical models like DTI or DKI (see sections 2.2.5 and 2.2.5) assume that the signal can be described by a higher order polynomial, multi compartment models such as CHARMED, AxCaliber or NODDI assume a certain tissue composition (see section 2.2.4). However, it is unlikely that any of these models can accurately describe the diffusion weighted signal originating from biological tissue because of its high complexity. Ferizi et al. noted that "even in regions of tissue with supposedly the simplest geometry the models required to explain the data are surprisingly complex" [61]. An alternative approach to address this problem are "model-free" q-space methods which try to directly estimate the EAP.

All q-space methods have in common that the diffusion encoding gradient pulses are assumed to be instantaneous $\delta \ll \Delta$ which is typically called the "narrow pulse approximation" [47]. Now a ST preparation is assumed where both gradient pulses are separated by the mixing time $\Delta$. Each gradient pulse points in direction $\vec{G}$ with the gradient amplitude $|\vec{G}|$ and the duration $\delta$. The first gradient pulse imparts to each spin at position $\vec{r}$ the phase shift $\gamma\delta(\vec{G}\cdot\vec{r})$. A spin that moves from position $\vec{r}$ to $\vec{r}\,'$ at the time of the second gradient pulse $\Delta$ will experience a phase shift of $\gamma\delta\vec{G}\cdot(\vec{r}-\vec{r}\,')$.

Analogous to section 2.2.1, $P(\vec{r})$ is the probability to find a spin at position $\vec{r}$ and $P(\vec{r}\,|\vec{r}\,',t)$ is the conditional probability of a spin to move from $\vec{r}$ to $\vec{r}\,'$. Using the phase shift $\gamma\delta\vec{G}\cdot(\vec{r}-\vec{r}\,')$ given in the previous paragraph, the diffusion weighted signal $S(\vec{G},\delta,\Delta)$ can be calculated as

$$S(\vec{G},\delta,\Delta) = S_0 \int_V \int_{-\infty}^{\infty} P(\vec{r}) P(\vec{r}\,|\vec{r}\,',\Delta) \exp\left(i\gamma\delta\vec{G}\cdot[\vec{r}-\vec{r}\,']\right) d\vec{r}\,' d\vec{r}\ , \tag{2.68}$$

where $S_0$ is the non-diffusion-weighted signal. The bound of the first integral in Eq. 2.68 is the sample volume (or voxel volume) and the bound of the second integral is infinite since there is no limit assumed for the displacement (from a mathematical point of view, there are of course practical limits). Recalling the definition of the EAP

$$\overline{P}(\vec{R},t) = \int_V P(\vec{r}\,|\vec{r}+\vec{R},t) P(\vec{r})\, d\vec{r} \tag{2.69}$$

with $\vec{R} = \vec{r}\,' - \vec{r}$, Eq. 2.68 can be rewritten to

$$S(\vec{G},\delta,\Delta) = S_0 \int_{-\infty}^{\infty} \overline{P}(\vec{R},t) \exp\left(i\gamma\delta\vec{G}\cdot\vec{R}\right) d\vec{R}\ . \tag{2.70}$$

Eq. 2.70 is equivalent to a Fourier transform of $\overline{P}(\vec{R},t)$ where

$$\vec{q} = \frac{1}{2\pi}\gamma\delta\vec{G} \tag{2.71}$$

can be defined to describe the reciprocal q-space, given by

$$S(\vec{q},\Delta) = S_0 \mathcal{F}^{-1}[\overline{P}(\vec{R},\Delta)] = S_0 \int_{-\infty}^{\infty} \overline{P}(\vec{R},t) \exp\left(i2\pi\vec{q}\cdot\vec{R}\right) d\vec{R}\ . \tag{2.72}$$

It is important to note that both $\overline{P}(\vec{R}, t)$ and the Fourier transform of $\overline{P}(\vec{R}, t)$ are positive, real valued functions [63]. However, $S_0$ is generally complex valued, and more important, coherent motion can result in significant phase shifts in $S(\vec{q}, \Delta)$. Consequently, the inverse operation to obtain the EAP from the sampled DWI data usually requires the magnitudes of $S_0$ and $S(\vec{q}, \Delta)$.

$$\overline{P}(\vec{R}, \Delta) = \frac{1}{|S_0|} \int_{-\infty}^{\infty} |S(\vec{q}, \Delta)| \exp\left(i2\pi\vec{q} \cdot \vec{R}\right) d\vec{q} \ . \tag{2.73}$$

A typical q-space method is the DSI technique where discrete values of $S(\vec{q}, \Delta)$ are sampled on a 3D Cartesian grid and the EAP is computed using a discretized version of Eq. 2.73 [63]. However, there are several problems which hamper an accurate estimation of the EAP. First of all, it is very challenging to satisfy $\delta \ll \Delta$ because the available gradient amplitude and slew rate of MRI systems is limited [55, 75]. If the narrow gradient pulse approximation is violated, the measured displacement reflects only the differences between the average position of the spins during the first and the second gradient pulse respectively [76]. Consequently, the measured displacement of restricted diffusion seems underestimated [77]. However, it has been shown, that longer gradient pulses do not necessarily affect the measured fiber orientation [63]. A second issue of DSI is the limited support of the discrete q-space signal which results in truncation artifacts, namely a convolution of the true EAP with the Fourier transform of the windowing function (typically a rectangular window) [78, 79]. These truncation artifacts can be addressed for example using filter functions, e.g. a Hanning window, or deconvolution algorithms [80]. Finally, a general problem, that not only applies to DSI, is the absolute value operation in Eq. 2.73, which causes a positive signal bias as the Gaussian noise distribution is changed to an unequal noise distribution with nonzero mean. Consequently, the accuracy of the estimated EAP is reduced. An alternative real valued reconstruction technique which can significantly reduce the noise induced bias is proposed in section 4.

## 2.3. Magnetic Resonance Imaging

Magnetic Resonance Imaging (MRI) is a volumetric imaging technique that is based on NMR. The imaging volume is split into many sub-volumes, called voxel, which are arranged on a regular grid in 3D space. In MRI the principles of NMR are used to create a certain tissue contrast and a spatial encoding technique is applied to determine the NMR signal for each voxel separately. The advantage of MRI compared to other volumetric imaging techniques, such as computer tomography, is the excellent soft tissue contrast and the avoidance of ionizing radiation.

### 2.3.1. Spatial Encoding

The wavelength in air, corresponding to the Larmor frequency of protons at $3\,\mathrm{T}$, is about $2.35\,\mathrm{m}$. Spatially resolved sensor arrays, which are for example used in computer tomography or positron emission tomography, are inapplicable in MRI. Instead, each MRI scanner is equipped with three gradient coils to create an arbitrary magnetic field gradient $\vec{G}$ of the

$B_z$ component of the magnetic field $\vec{B}$. The components of the gradient $\vec{G}$ are denoted $G_x$, $G_y$ and $G_z$. If such a gradient field is applied, $B_z$ can be calculated as

$$B_z = \vec{r} \cdot \vec{G} \ , \tag{2.74}$$

$$= xG_x + yG_y + zG_z \ , \tag{2.75}$$

where $x$, $y$, $z$ are the spatial coordinates and $G_x$, $G_y$ and $G_z$ are the gradient amplitudes of the three coils (these gradient coils are the same being used for the diffusion encoding). As a result, the local Larmor frequency $\omega(\vec{r})$ is spatially dependent.

$$\omega(\vec{r}) = \omega_0 + \gamma \vec{G} \vec{r} \tag{2.76}$$

Note that in the above equation the local off-resonance $\gamma \Delta B_0(\vec{r})$ is assumed to be zero. There are two different approaches for spatial encoding in MRI. On the one hand, magnetic field gradients in combination with spatially selective RF-pulses are used to excite only a certain volume, e.g. a single slice, which is typically called slice encoding. On the other hand, the NMR signal can be Fourier encoded using the magnetic field gradients and the image is reconstructed by an inverse Fourier transform. Both techniques are explained in detail in the following sections.

**Slice encoding**

According to Eq. 2.76, $\omega(\vec{r})$ is constant in all planes perpendicular to $\vec{G}$ if a magnetic field gradient is applied. On the other hand $\omega(\vec{r})$ increases linearly with $|\vec{G}|$ in the direction parallel to $\vec{G}$. Let $w_{RF}$ be the carrier frequency and $\Delta w_{RF}$ the bandwidth of a rectangular RF-pulse in the frequency domain. If a slice encoding gradient $\vec{G}_s$ is applied all spins which are located in the slice given by Eq. 2.77 are on-resonant with the RF-pulse.

$$w_{RF} - \frac{\Delta w_{RF}}{2} \leq \omega_0 + \gamma(\vec{G}_s \cdot \vec{r}\,) \leq w_{RF} + \frac{\Delta w_{RF}}{2} \tag{2.77}$$

The position and orientation of the slice is dependent on $\vec{G}_s$ and $w_{RF}$, and the slice thickness $\Delta s$ depends on $|\vec{G}_s|$ and $\Delta w_{RF}$.

$$\Delta s = \frac{\Delta \omega}{\gamma \left| \vec{G}_s \right|} \tag{2.78}$$

However, in reality a perfectly rectangular shaped RF-pulse in the frequency domain is unrealistic because it requires a sinc-shaped envelope of (theoretically) infinite length in the time domain (see section 2.1.3). Apart from practical considerations such as the duration of the RF-pulse there are other limitations including the maximum amplitude or the duty cycle of the RF-amplifier and more important Specific Absorption Rate (SAR) restrictions. The latter describes the energy absorption by the scanned subject as it leads to heating of the underlying tissue [81]. There are certain restrictions, depending on the scanned body region, to avoid potential tissue damage. Moreover, the computation of RF-pulses with a certain slice profile and with higher flip angles is nontrivial as the nonlinearity of the Bloch equations needs to be taken into account (see section 2.1.3) [37]. Therefore, the slice profile of an RF-pulse is always a compromise between several impact factors and it is never exactly rectangular.

**Fourier encoding**

In the previous section 2.3.1 it was described how a single slice can be excited by a RF-pulse. In this section, the in-plane spatial encoding is explained. Assuming the slice encoding direction is $z$ and $S(x, y)$ is the NMR signal originating from spins located at position (x,y) in the excited slice. The signal induced in a nearby coil is the integral of $S(x, y)$ over all $x$ and $y$ (the spatial sensitivity profile of the receive coil is neglected).

$$S = \int \int_{-\infty}^{+\infty} S(x, y)\, dxdy \tag{2.79}$$

Now, a first gradient pulse is applied in $x$ direction with the amplitude $G_x$ and the duration $\tau_x$ and a second gradient pulse is applied in $y$ direction with the amplitude $G_y$ and the duration $\tau_y$. The two gradient pulses impart a phase shift $\phi(x, y)$ onto $S(x, y)$

$$\phi(x, y) = \gamma(G_x\tau_x x + G_y\tau_y y) \ . \tag{2.80}$$

The signal $S(G_x, \tau_x, G_y, \tau_y)$, induced in the nearby coil, now depends on the amplitude and duration of the applied gradient pulses.

$$S(G_x, \tau_x, G_y, \tau_y) = \int \int_{-\infty}^{+\infty} S(x, y) \exp(-i\gamma[G_x\tau_x x + G_y\tau_y y])\, dxdy \tag{2.81}$$

In fact, Eq. 2.81 bears a close resemblance to Eq. 2.70 which was used to describe the connection between q-space and EAP. In this sense, the k-space $S(k_x, k_y)$ can be defined as the reciprocal space of $S(x, y)$ with

$$k_x = \frac{1}{2\pi}\gamma G_x\tau_x \ , \tag{2.82}$$

$$k_y = \frac{1}{2\pi}\gamma G_y\tau_y \ . \tag{2.83}$$

The signal induced in the nearby coil $S(k_x, k_y)$ can be calculated as the Fourier transform of $S(x, y)$.

$$S(k_x, k_y) = \mathcal{F}[S(x, y)] = \int \int_{-\infty}^{+\infty} S(x, y) e^{-i2\pi(k_x x + k_y y)}\, dxdy \tag{2.84}$$

However, in a MRI experiment $S(k_x, k_y)$ is sampled and an inverse Fourier transform is applied to obtain $S(x, y)$.

$$S(x, y) = \mathcal{F}^{-1}[S(k_x, k_y)] = \int \int_{-\infty}^{+\infty} S(k_x, k_y) e^{i2\pi[(k_x x + k_y y)}\, dk_x dk_y \tag{2.85}$$

It is important to note, that Fourier encoding is not restricted to two dimensions. There exist plenty of 3D sequences where the RF-pulse excites the whole imaging volume and the third dimension is Fourier encoded too.

**Discretization**

Because during a MRI scan only a finite number of $S(k_x, k_y)$ can be sampled, a discretized version of the Fourier transform is needed in Eq. 2.85. The definition of the discrete Fourier transform can be found in many signal processing or MRI books, e.g. in Bracewell et al. [78] or Bernstein et al. [36]. Here, only the 1D case is described because the approach is identical for higher dimensions. Let $J$ and $K$ be the indices for $N$ discrete coefficients $S_J$ in image space and $N$ discrete coefficients $S_K$ in k-space. The $K$th element of the Discrete forward Fourier Transformation (DFT) is defined as

$$S_K = \sum_{J=0}^{N-1} S_J e^{\frac{-i2\pi JK}{N}} \quad K = 0, 1, 2, ..., N-1 \ , \tag{2.86}$$

and the $J$th element of the Inverse Discrete forward Fourier Transformation (IDFT) is given by

$$S_J = \frac{1}{N} \sum_{K=0}^{N-1} S_K e^{\frac{i2\pi JK}{N}} \quad J = 0, 1, 2, ..., N-1 \quad . \tag{2.87}$$

The normalization factor $1/N$ is needed to ensure that a consecutive application of a DFT and a IDFT result in the same values as before. However, the factor $1/N$ can be arbitrarily distributed to DFT and IDFT as long as the product of both fractions yields $1/N$. The Eqs. 2.86 and 2.87 still lack a relation to physical units, namely the grid size in image space $\Delta x$ and in k-space $\Delta k$. To determine the relation for $\Delta x$ and $\Delta k$, the integrals of the continuous Fourier transform, given in Eqs. 2.84 and 2.85 are directly discretized for the 1D case. The continuous variables $x$ and $k$ are replaced by their discrete representations $x_J$ and $k_K$.

$$x_J = J\Delta x \tag{2.88}$$
$$k_K = K\Delta k \tag{2.89}$$

To maintain the symmetry of the integral, the number of discrete values $N$ is chosen to be odd with

$$N = 2M + 1 \quad M \in \mathbb{N} \ . \tag{2.90}$$

Discretizing the continuous Fourier transform, given in Eq. 2.84, for the 1D case yields

$$S(K\Delta k) = \sum_{J=-M}^{M} S(J\Delta x) e^{-i2\pi J\Delta x K\Delta k} \Delta x \ , \tag{2.91}$$

and analogously, the continuous inverse Fourier transform, given in Eq. 2.85, results in

$$S(J\Delta x) = \sum_{K=-M}^{M} S(K\Delta k) e^{i2\pi J\Delta x K\Delta k} \Delta k \ . \tag{2.92}$$

A comparison of Eqs. 2.91 and 2.92 with the definition of DFT and IDFT in Eqs. 2.86 and 2.87 reveals

$$\Delta x \Delta k = \frac{1}{N} \ . \tag{2.93}$$

Based on Eq. 2.93, two important conclusions can be drawn. The resolution $\Delta x$ in a Fourier encoded dimension depends on the highest k-value $\Delta k N$. Therefore, an increase in resolution requires longer gradient pulses or higher gradient amplitudes. Also the coverage $\Delta x N$ in a Fourier encoded dimension, typically called Field Of View (FOV), is inverse proportional to the grid size in k-space $\Delta k$.

**Frequency and Phase Encoding**

In the previous section, the IDFT was introduced to transform the discrete k-space signal, which is regularly sampled on a Cartesian grid into the image space. Although there are many non-Cartesian readout techniques such as spiral, radial or propeller [82–84], Cartesian sampling schemes are by far the most common, mainly due to the computationally simple reconstruction.

If a two-dimensional (2D) Cartesian readout is used, two perpendicular directions that span the FOV are defined, the Frequency Encoding (FE) direction and the Phase Encoding (PE) direction. Now, a combination of gradients in PE and FE direction are used to sample one line in k-space as illustrated in Fig. 2.6. After the excitation pulse, a dephasing gradient in FE direction is applied to shift the position in k-space from the center to the edge. The purpose of the prephasing gradient is to prepare the magnetization such that the whole FE line in k-space can be sampled in the subsequent readout. At the same time a PE gradient is applied to select one line k-space. Next, the FE gradient, also called readout gradient, is applied while the Analog-Digital-Converter (A/D) samples the selected line in k-space. This method is repeated with different PE gradients until the full 2D k-space is covered. As already mentioned, Fourier encoding is also possible in all three dimensions, simply by adding a second PE axis. Next, the gradient amplitude and duration of the PE and readout gradients are calculated. Let $\Delta x$ be the isotropic voxel size and $N = 2M + 1,\ M \in \mathbb{N}$ the matrix size assuming a quadratic FOV with edge length $N\Delta x$. According to Eq. 2.93 the grid size in k-space $\Delta k$ is given by

$$\Delta k = \frac{1}{N\Delta x} \ . \tag{2.94}$$

For practical reasons, the duration $\tau_{\text{PE}}$ of all PE gradients is typically set to a constant value and the gradient area is scaled by the amplitude. Using the definition of the k-space given in Eq. 2.82 the, amplitude $G_{\text{PE}}(n)$ of the PE gradient that encodes the $n$th k-space line, can be calculated as

$$G_{\text{PE}}(n) = \frac{2\pi n}{\gamma N \Delta x \tau_{\text{PE}}} \quad n = -M, -M+1, ..., M-1, M \quad . \tag{2.95}$$

The readout gradient is typically parametrized using the readout bandwidth $\Delta\nu$ of the A/D. Consequently the increment in k-space in the time $1/\Delta\nu$ must equal $\Delta k$ (which is given by $1/[N\Delta x]$) and the amplitude of the FE gradient $G_{\text{FE}}$ can be calculated as

$$G_{\text{FE}} = \frac{2\pi\Delta\nu}{\gamma N \Delta x} \ . \tag{2.96}$$

It is important to note that typically, only the constant part of the readout gradient is used to sample data since otherwise the grid size in k-space $\Delta$k would not be equidistant anymore. Consequently, the gradient area of the ramp has to be included in the dephasing

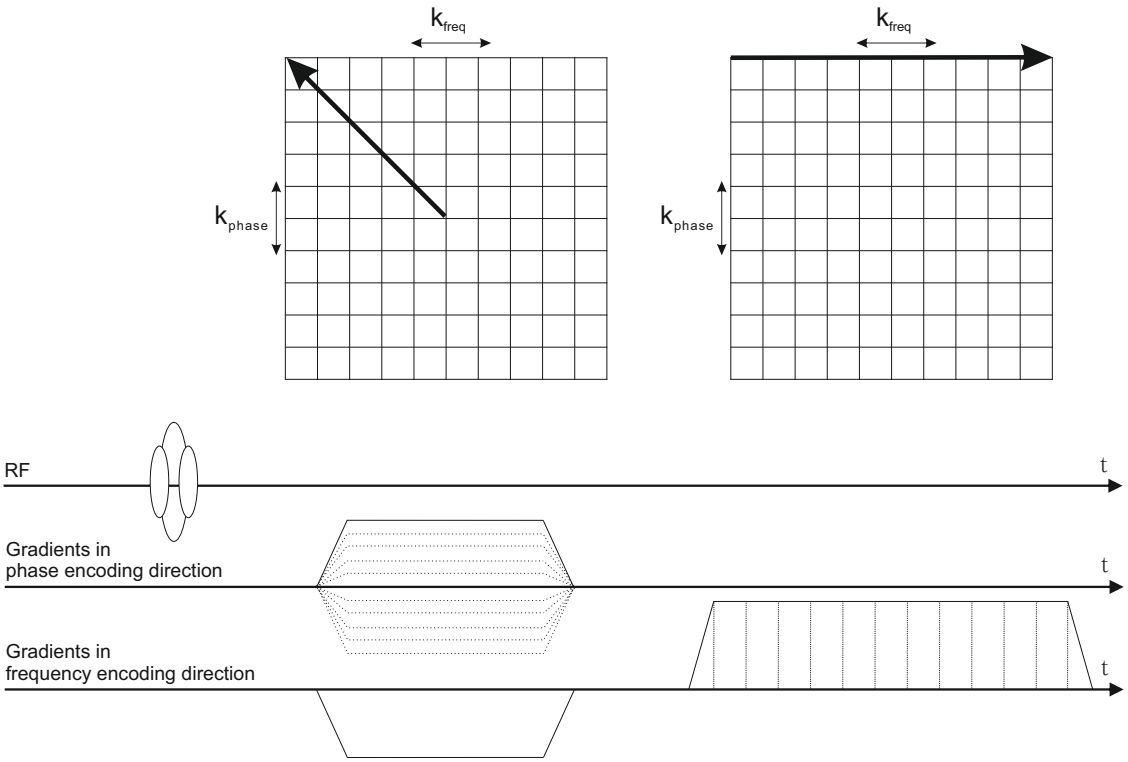


Figure 2.6.: Schematic illustration of one phase encoding step. After the excitation pulse, a dephasing gradient (FE direction) and a PE gradient to prepare the actual Cartesian readout. Next, one line in k-space is sampled while the FE gradient is activated. This procedure is repeated with different PE gradients until the full 2D k-space is covered.

gradient. However, very rapid imaging sequences use a technique called ramp sampling where almost the complete readout gradient is used to acquire data. In this case, the k-space data need to be regridded prior to IDFT [36, p. 506 ff.] or a non-uniform technique must be used [85].

### Partial Fourier

The Fourier transform has an important property for real valued functions. If a function $a(x)$, is real valued and $\hat{a}(x)$ is the corresponding Fourier transform of $a(x)$ then $\hat{a}(x)$ is a Hermitian function with

$$\hat{a}(-x) = \overline{\hat{a}(x)} \ . \tag{2.97}$$

That means in the case of MRI, if the image space is real valued then only half of the k-space needs to be sampled because the missing part can be calculated as the complex conjugate of the first half. Unfortunately, the NMR signal is generally not real valued. Phase variations $\phi(\vec{r})$ are for example caused by $B_0$ inhomogeneity, eddy currents or motion encoding (see

section 2.2.2). However, these phase variations $\phi(\vec{r})$ are most often smooth and therefore can be sufficiently described by low frequencies in k-space.

In Partial Fourier undersampling, only one half of k-space is fully sampled and the other half is only partially sampled. The degree of partial Fourier is typically described by the portion of the sampled data, e.g. 5/8 Partial Fourier. The missing part of the data is most simple replaced by zeros or otherwise, a Partial Fourier reconstruction algorithm is applied. Partial Fourier reconstruction techniques try to correct for $\phi(\vec{r})$ using the symmetrically sampled data and subsequently synthesize the missing data based on the conjugate symmetry [86, 87]. If $\phi(\vec{r})$ is sufficiently smooth, Partial Fourier results only in a SNR penalty since less data was sampled, e.g. the SNR of a 5/8 Partial Fourier acquisition is only $\sqrt{5/8} = 79\,\%$ compared to a full k-space sampling. However, if $\phi(\vec{r})$ cannot be well approximated by the symmetrically sampled part of the k-space, significant artifacts can arise. In DWI, velocity encoding of intracranial pulsatility [20] and subject motion can lead to very inhomogeneous phase pattern due to the high gradient moments of the diffusion sensitizing gradients (see section 2.2.2). Consequently, only moderate partial Fourier undersampling is usually used (e.g. default at GE scanners is $7/8$).

### 2.3.2. Pulse Sequences in Magnetic Resonance Imaging

A MRI pulse sequence is a series of RF-pulses, gradient pulses and readout windows. A pulse sequence can be used to create a large variety of different contrasts. Most widely used in MRI are $T_1$-weighted, $T_2$-weighted and proton density weighted contrasts. The first two contrasts are based on the relaxation times $T_1$ and $T_2$, where $T_1$-weighting results in a high signal originating from short $T_1$ species and $T_2$-weighting results in a high signal originating from long $T_2$ species. To the contrary in proton density imaging, the pulse sequence is designed such that the relaxation times have only a very weak influence on the signal and the contrast is mainly determined by the density of spins. There exist many more contrasts in MRI, most important for this thesis, the diffusion contrast (see sections 2.2.1, 2.2.2, 2.2.3) but also others such as susceptibility weighted contrast ($T_2^*$) [4], angiographic contrast [88], BOLD contrast ($T_2^*$ weighting) [5] and many more.

Apart from the desired contrast, MRI pulses sequence can be also categorized in two groups, namely Gradient Echo (GRE) and SE based sequences. In this section, a short description for both types is provided. Subsequently, the EPI readout technique is introduced, as it is most commonly used in DWI.

#### Gradient Echo Sequences

GRE is a class of rapid pulse sequences, which do not have a refocusing pulses to create a SE. The first GRE sequence was called Fast Low-Angle Shot (FLASH) [89] GRE, which substantially reduced the acquisition times, using low flip angles and short TRs. GRE sequences are widely used in MRI, especially for high resolution 3D volume imaging. Assuming a Cartesian readout scheme, a typical GRE sequence consists of a dephasing gradient in FE direction, a PE gradient, possibly a rephasing gradient in slice encoding direction (depending on what kind of RF-pulse is used) and a subsequent readout gradient to acquire one k-space line (see section 2.3.1). However, there are three types of GRE sequences differing in the way how the remaining transverse magnetization is handled.

In an unbalanced Steady State Free Precession (SSFP) sequence, the PE gradients are compensated after the readout and a constant spoiler gradient is applied. Because the gradient area of each TR interval is constant, a steady state of the magnetization is created. The signal evolution of an unbalanced SSFP sequence can be explained with the theory of Coherence Pathways (CPs) [90]. The magnetization which is dephased by the spoiler gradient is split into three CPs by the next RF-pulse: one which is not effected by the RF-pulse, one which is flipped into longitudinal direction by the RF-pulse and one which is refocused by the RF-pulse. Subsequent RF-pulses split each CP in three more and so on and so forth. This results in a very high number of CPs, all contributing to the measured signal. Consequently, an unbalanced SSFP is not purely $T_1$ weighted as CPs of previous excitations contribute some $T_2$ weighting as well. An unbalanced SSFP with a very large spoiler gradient can also be employed for DWI which is investigated in section 5.2.1.

In a Spoiled Gradient Echo (SPGR) sequence, the remaining transverse magnetization is perfectly spoiled and therefore the image can be purely $T_1$ weighted. In this case only longitudinal magnetization remains over subsequent excitations. After a certain number of excitations pulses, a longitudinal steady state is reached where the $T_1$ recovery within one TR interval is the same as the decrease of longitudinal magnetization by the RF-pulse. The optimal flip angle, where the traverse magnetization is maximized, is called Ernst angle $\alpha_{\mathrm{Ernst}}$ [91].

$$\alpha_{\mathrm{Ernst}} = \arccos(e^{\frac{-TR}{T_1}}). \tag{2.98}$$

A challenge of SPGR is the actual spoiling of the transverse magnetization after the readout, since otherwise the $T_1$ contrast would be contaminated by additional SEs and STEs of previous excitations. A commonly used spoiling technique is called RF-spoiling, where analogous to unbalanced SSFP the PE gradients are rephased and an additional constant spoiler gradient is applied with the result that the gradient area is constant for each TR interval. In addition, the phase of the RF-pulse is modulated following a certain algorithm such that an almost perfectly spoiled signal is created [92, 93]. Apart from the $T_1$ weighted contrast, SPGR sequences with longer TEs can also yield a $T_2^*$ weighting, which is used for example in susceptibility weighted imaging [4] or functional MRI [5].

A third GRE sequence is Balanced Steady State Free Precession (bSSFP) where the gradient area of all axis is zero during each TR interval resulting in a very different steady state compared to unbalanced SSFP [94]. A bSSFP exhibits the highest signal of all GRE with a contrast approximately proportional to $T_2/T_1$. In contrary to unbalanced SPGR and SPGR, the signal of bSSFP heavily depends on the off-resonance $\Delta B_0$ which can be described by the Frequency Response Function (FRF). The FRF describes the transverse magnetization as a function of the dephasing angle $\theta$ over one TR interval, defined as

$$\theta = \gamma \Delta B_0 \mathrm{TR} \ . \tag{2.99}$$

In Fig. 2.7 the examples of the FRF are plotted for flip angles ranging from $2°$ to $90°$ and relaxation times typical for WM in the human brain. The FRF for flip angles of $15°$, exhibits a significant drop of the signal at $\theta = -\pi$ $\theta = \pi$, which is called the stop band. However, for $\theta$ in between $-\pi$ and $\pi$, there is a plateau with high signal, which is called the pass band. Consequently, in case of too high $B_0$ inhomogeneity, bSSFP exhibits banding artifacts at locations where $\theta = -\pi$ or $\theta = \pi$. Nevertheless, bSSFP is a very rapid sequence with a strong SNR and it is fairly insensitive to motion due to the nulling of the gradient area in

each TR interval. Because of these properties, bSSFP is for example widely used in cardiac MRI [95].

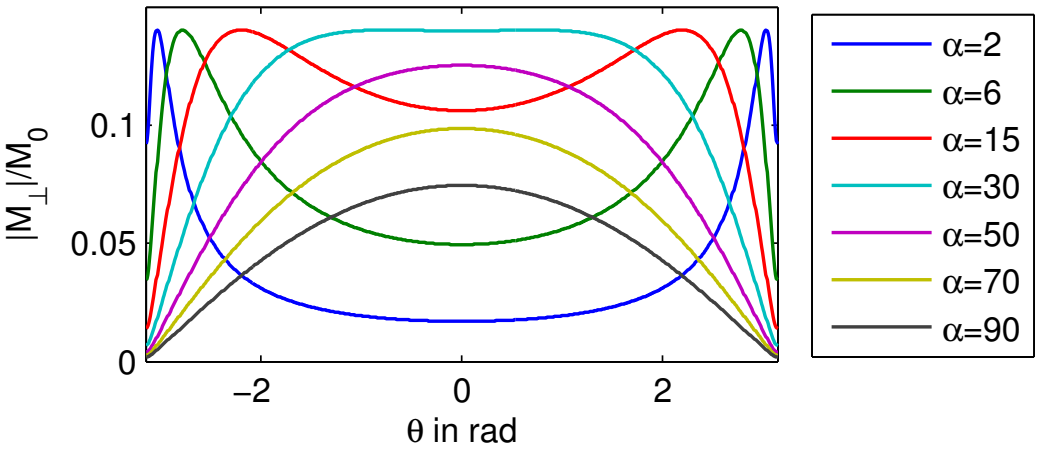


Figure 2.7.: FRF of a bSSFP sequence showing the absolute value of the normalized transverse magnetization $|M_\perp|/M_0$ as function of the dephasing angle $\theta$. The relaxation times, $T_1 = 1330\,\mathrm{ms}$, $T_2 = 110\,\mathrm{ms}$ and flip angles ranging from $2°$ to $90°$ were assumed.

Finally, there is a GRE based sequence, called Magnetization-Prepared Rapid Gradient-Echo Imaging (MP RAGE) which is not based on a steady state but uses an inversion prepulse to enhance the $T_1$ contrast [96]. MP RAGE is widely used in neuroimaging as it yields an excellent WM to GM contrast.

### Spin Echo Sequences

MRI pulse sequences which use one or more refocusing pulses belong to the class of SE sequences. In the most simple case of a single SE sequence, an excitation pulse with a flip angle of $90°$ is applied and after the time $\tau$ a refocusing pulse with a flip angle of $180°$ is used to form a SE at the time $\mathrm{TE} = 2\tau$ (see section 2.1.3) where one line in k-space is acquired (see section 2.3.1). In contrary to GRE sequences the signal at the TE is truly $T_2$ weighted because off-resonance effects are compensated by the refocusing pulse.

The major advantage of SE sequences is the flexibility to obtain all three main MRI contrasts, $T_1$, $T_2$ and proton density weighting. However, the disadvantage of single SE sequence as described before is the very low acquisition efficiency since each k-space line requires one SE preparation. Moreover a substantial waiting time between two consecutive excitation pulses is needed to allow the longitudinal magnetization to recover. Therefore SE sequences are usually used in the 2D mode and multiple slice locations are interleaved within a TR interval to increase the time for $T_1$ recovery. Nevertheless, the efficiency of a single SE sequence is still low. A significantly faster SE sequence is RARE, sometimes also called Turbo Spin Echo (TSE), where a train of refocusing pulse is employed to produce multiple consecutive SEs [97]. As illustrated in Fig. 2.8, at each SE a different line in k-space is encoded where the signal decays with $T_2$. The number of refocusing pulses or

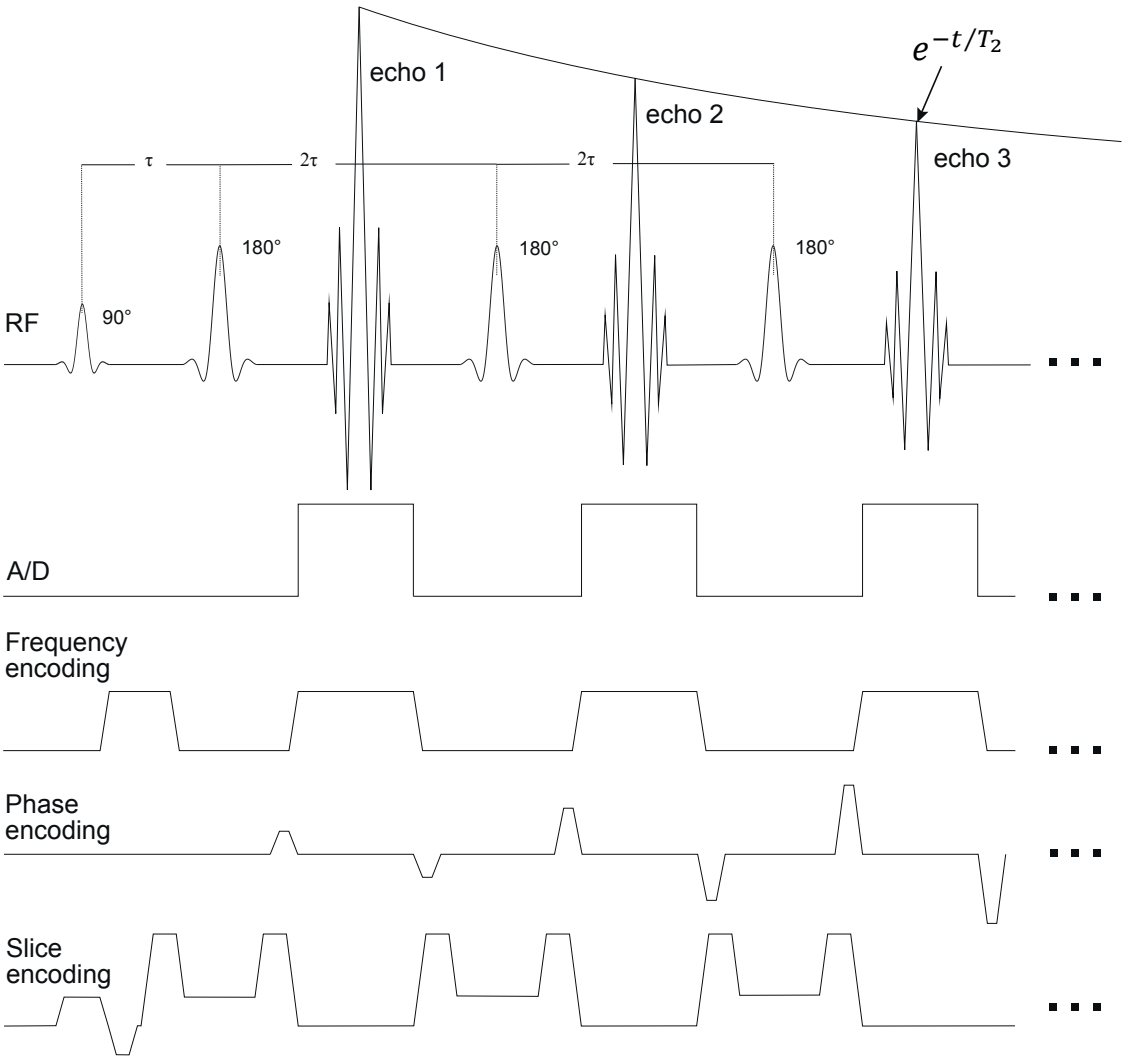


Figure 2.8.: Sequence diagram of a Rapid Acquisition with Relaxation Enhancement (RARE) sequence. After the excitation pulse, a train of refocusing pulses forms multiple SE where one k-space line is encoded at each echo respectively. The PE gradients are reversed after each echo, for the reason that the total gradient among all segments is constant. The gradients before and after the refocusing pulses, called crusher gradients, ensure that only magnetization which was initially flip into the transverse plane by the excitation pulse contributes to the measured signal.

the number of segments in RARE is typically called turbo factor, accounting for the fact that the acquisition time can be approximately reduced by this factor compared to a single SE sequence. There are three rules, suggested by Carr and Purcell [6] well as Meiboom and Gill [42], therefore named CMPG conditions, which increase the robustness of a RARE against $B_1$ inhomogeneity:

- **Condition 1:** The phase of the excitation pulse is shifted by $\pi/2$ with respect to the refocusing pulses.
- **Condition 2:** The time between consecutive refocusing pulses is constant and twice as long as the time between the excitation pulse and the first refocusing pulse.
- **Condition 3:** The phase that is being accumulated between two consecutive refocusing pulses is constant (therefore the gradient area of each segment must be constant).

RARE sequences are widely used in MRI due to their high flexibility regarding the image contrast. There are also 3D versions, usually using very long echo trains with a technique called echo stabilization, where the refocusing flip angle is modulated to obtain a more constant signal of the echoes [98].

#### Echo Planar Imaging

Echo Planar Imaging (EPI) is one of the fastest imaging techniques in MRI [99], capable to acquire a single 2D image within tenth of seconds. In EPI, a series of bipolar readout gradients is employed to generate a GRE train yielding a much faster sampling rate than the SE train of a RARE. The EPI readout technique can be used for almost all MRI contrasts including $T_1$, $T_2$ and $T_2^*$. Due to the very high acquisition speed, EPI set the stage for new MR applications, such as DWI or functional MRI. The biggest disadvantage of EPI is the very high sensitivity to off-resonance effects, such as $B_0$ inhomogeneity (see section 2.3.3), Eddy currents (see section 2.3.3) and chemical shifts, but also concomitant magnetic fields (see section 2.3.3) and system imperfections such as mismatched gradient group delays and gradient amplifier hysteresis [36]. Although there exist segmented k-space EPI techniques for 2D and for 3D, in DWI, most often a ST diffusion preparation with a subsequent single shot 2D EPI readout is used. The term single shot implies, that the complete image is encoded with a single EPI echo train. The reason why a single shot readout is preferable in DWI is the motion encoding of the diffusion sensitizing gradients which can lead to phase inconsistencies between k-space segments belonging to different diffusion preparations. However, alternative acquisition techniques for DWI are investigated in chapter 7.

In Fig. 2.9 an exemplary sequence diagram of a 2D single shot EPI sequence with a ST preparation is shown, based on the implementation on a MR750w (GE Healthcare, Milwaukee,WI). Below, all gradient pulses, RF-pulses and readout windows are explained in the chronological order given in Fig. 2.9:

- **RF1:** This is a nonspatial, frequency selective RF-pulse to excite only the fat in the imaging volume.
- **$G_y$sp1:** The spoiler gradient $G_y$sp1 is used to dephase the previously excited fat signal. Due to its different chemical shift compared to water, fat would result in

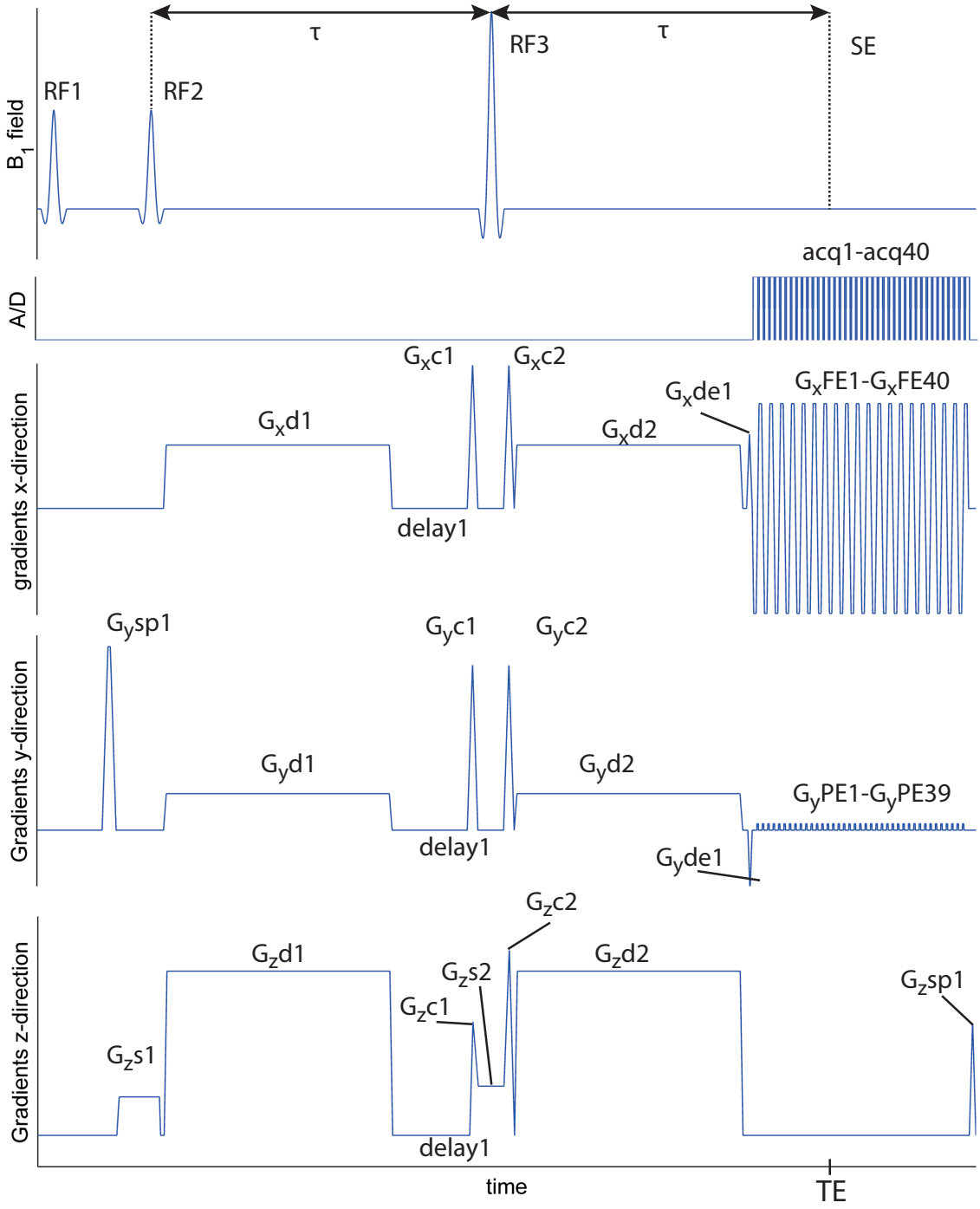


Figure 2.9.: Sequence diagram of a single shot 2D EPI sequence with a ST diffusion preparation. All gradients, RF-pulses and readout windows are marked and corresponding explanations can be found in the text next to this figure.

ghosting artifacts (see section 2.3.3) due to the EPI readout. The fat suppression technique shown here is called fat saturation but also other methods such as spectral, spatial water excitation [100] or Short Tau Inversion Recovery (STIR) [101] can be used.

- **RF2, $G_z$s1:** RF2 is a slice selective $90°$ excitation pulse with the corresponding slice selective gradient $G_z$s1.
- **$G_x$d1, $G_y$d1, $G_z$d1:** First diffusion weighting gradient of the ST preparation, simultaneously applied on all three gradient axes. The diffusion encoding direction corresponds to the vector addition of the $G_x$, $G_y$ and $G_z$ component.
- **delay1:** This delay is used to ensure, that the SE occurs when the k-space center is sampled during the readout.
- **$G_x$c1, $G_y$c1, $G_z$c1:** This is the first crusher gradient which is simultaneously applied on all axes. Crusher gradients are used to account for potential $B_1$ inhomogeneity. Together with the second crusher gradient $G_x$c2, $G_y$c2, $G_z$c2 it is ensured that only the CP that is being refocused contributes to the measures signal. The CP which is not affected by the RF-pulse is twice dephased by the crusher gradients and the CP rotated into the longitudinal direction does not contribute to the signal anyways. Further, new magnetization, which is flipped into the transverse plane by an imperfect refocusing pulse is dephased by the second crusher gradient. Note, that the size of $G_z$c1 is smaller than $G_z$c2 because the gradient area of the slice rephasing gradient and the gradient area of the first crusher gradient are added together.
- **$G_z$s2:** Slice selective gradient for the refocusing pulse. Note that, a symmetric refocusing pulse does not require a slice rephasing gradient.
- **$G_x$c2, $G_y$2, $G_z$c2:** The second crusher gradients after the refocusing pulse.
- **$G_x$d2, $G_y$d2, $G_z$d2:** Second diffusion weighting gradient of the ST preparation, simultaneously applied on all three gradient axes.
- **$G_x$de1, $G_y$de1:** Dephasing gradients in FE and PE direction. The trajectory of the dephasing gradients from the k-space center to the lower right corner is shown in Fig. 2.10. Note that partial Fourier in PE direction is used and therefore the area of the PE dephaser is smaller than the area of the FE dephaser.
- **$G_x$FE1-$G_x$FE40,acq1-acq40, $G_y$PE1-$G_y$PE39:** The actual EPI readout train consisting of the readout gradients $G_x$FE1-$G_x$FE40 where the polarity of gradients with an odd number is negative and with an even number is positive, the corresponding data acquisition windows acq1-acq40 and the small PE gradients $G_y$PE1-$G_y$PE39, called blips, which shift the position in k-space to the next line. The corresponding k-space trajectory is shown in Fig. 2.10. Note that in the given example, two undersampling techniques, Partial Fourier (see section 2.3.1) and parallel imaging are used. Parallel imaging allows for a for a coherent undersampling of the data—in this example only every second line is sampled—where the missing data is reconstructed using information about the sensitivities of a multi-coil receiver array [26, 102, 103]. Moreover ramp sampling is used to reduce the duration the readout gradients [104].

- **$G_z$sp1:** Spoiler gradient to dephase remaining transverse magnetization.

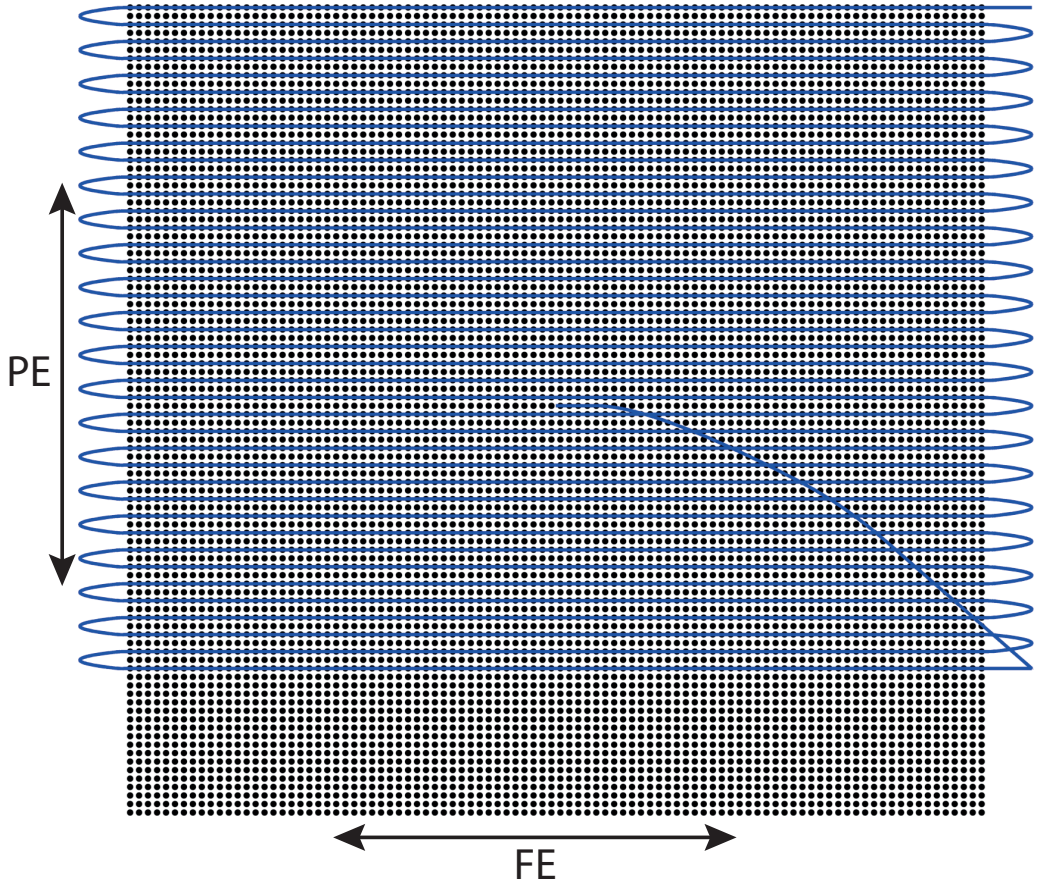


Figure 2.10.: k-space trajectory of the single shot 2D EPI sequence as shown in 2.9. Parallel imaging with an acceleration factor of 2, ramp sampling and partial Fourier in PE direction are used.

As shown in Fig. 2.9, the diffusion preparation takes a fairly long time, resulting in a significant $T_2$ weighting of the signal. This $T_2$ weighting is unwanted in DWI as it reduces the SNR. In MRI sequences with long echo trains, such as EPI or RARE, the weighting of the signal is dominated by the weighting of the k-space center. Therefore the TE is defined as the time when the k-space center is acquired. Consequently a diffusion weighted single shot 2D EPI, is highly optimized for a TE as short as possible, involving techniques such as Partial Fourier, parallel imaging and ramp sampling. However, these efforts are limited by the SNR loss due to the reduced sampling time—the SNR is proportional to the square root of the sampling time [105]—and in case of parallel imaging by the so called g-factor penalty on the SNR, which limits the amount of undersampling [26, 103]. The reduction of $T_2$ weighting in DWI is also one of the reasons why the maximal gradient strength of MRI scanners is continuously increasing [106]. Furthermore, ramp sampling and parallel imaging also have significant impact on the off-resonance artifacts in EPI images as they reduce the so called Echo Spacing (ESP) which is defined as the time between the echo

center of two consecutive readout gradients of the EPI train. Details can be found in section 2.3.3.

### 2.3.3. Sources of Artifacts in MRI

#### Convolution artifacts

An important property of the Fourier transform is that a convolution in one domain is equivalent to a simple multiplication in the other. The convolution of two functions $f(x)$ and $g(x)$ is defined as

$$f(x) * g(x) = \int_{-\infty}^{+\infty} f(x - x')g(x') \; dx' \;\; , \tag{2.100}$$

and the corresponding Fourier transform is defined as

$$\mathcal{F}\big(f(x) * g(x)\big) = \mathcal{F}\big(f(x)\big)\mathcal{F}\big(G(x)\big) \;\; . \tag{2.101}$$

In MRI, the k-space is usually sampled, for a given image resolution $\Delta x$, from $-1/(2\Delta x)$ to $1/(2\Delta x)$. Consequently the reconstructed image is a convolution of the true image with a sinc function (the Fourier transform of a rectangular sampling window). The side lobes of the sinc cause ringing artifacts, particularly near sharp edges, which is also called truncation artifacts or Gibbs ringing (after Josiah Willard Gibbs). Gibbs ringing is generally less pronounced for high resolution, because the frequency of the sinc function is increased and the lobes are narrower. Gibbs ringing artifacts can be also reduced using window functions with a smoother Fourier transform, which however, reduces the effective resolution.

In MRI sequences with a long readout train, such as RARE or EPI, the window function is dominated by $T_2$ or $T_2^*$ decay. As a result, these sequences typically suffer from additional blurring of the image and a reduced effective resolution, depending on the length of the echo train and the relaxation times of the tissue. 3D RARE sequences often exhibit a very long readout train, and therefore, echo stabilization techniques are used to obtain a more constant signal amplitude [98].

#### Aliasing artifacts

According to the Nyquist–Shannon sampling theorem, the sampling frequency $f_s$ must be twice as high as the difference between the highest frequency $f_{max}$ and the lowest $f_{min}$ in the signal [107, 108].

$$f_s \geq 2(f_{max} - f_{min}) \tag{2.102}$$

If this condition is violated, aliasing occurs because different frequencies of the signal become indistinguishable in the sampled data. In MRI the theorem can be formulated as

$$\frac{1}{\Delta k_x} \leq x_{max} - x_{min} \;\; , \tag{2.103}$$

where $x_{max}$ and $x_{min}$ are the spatial coordinates of the spins with furthest distance from each other. If this condition is violated, the signal originating from spins at different positions can become indistinguishable and overlap in image space. The area or the volume

which is covered by the Fourier encoding is called Field Of View (FOV) and corresponds to the inverse k-space grid size $\frac{1}{\Delta k_x}$. Spins that exceed the FOV on one end erroneously alias into the FOV on the opposite site.

It is important to note, that only spins that induce a signal in the receive coils can cause aliasing. Consequently, one method to avoid aliasing are spatially selective RF-pulses which excite only spins within the FOV. Moreover, many receive coils, e.g. phased array coils, exhibit a very narrow sensitivity profile. Thus, spins outside this sensitivity profile cannot cause aliasing. Furthermore, if a Cartesian readout scheme is used, $\Delta k_x$ in FE direction can be simply reduced by increasing the sampling frequency of the A/D without any loss of time or SNR, which is called oversampling. Therefore, aliasing is typically only a problem in PE direction. Finally, parallel imaging methods can be used to unalias voxels which violate the Nyquist–Shannon sampling theorem at the cost of potential g-factor penalty in SNR [26, 103].

In non-Cartesian readout schemes, such as spiral or radial, the points in k-space are not spaced equidistantly. As a result, aliasing artifacts of non-Cartesian readout schemes often look more similar to noise or blurring, rather than the coherent aliasing artifacts obtained for Cartesian readout schemes.

### $B_0$ inhomogeneity

Almost all in-vivo MRI systems with a field strength of more than $0.5\,\mathrm{T}$ rely on superconducting magnets. When the magnetic field is first ramped up, the root mean squared $B_0$ inhomogeneity can be up to $50\,\mathrm{ppm}$ of the static magnetic field strength [109] within the so called Diameter Spherical Volume (DSV). For a human scanner the DSV diameter is typically about $45\,\mathrm{cm}$ [109]. When the magnet is commissioned, there are typically two techniques to homogenize the magnetic field. On the one hand, ferromagnetic elements are strategically placed around the magnet which is called passive-shimming or ferroshimming. On the other hand, some MRI scanners are additionally equipped with superconducting shim coils to further improve homogeneity of the magnetic field. Typically the field homogeneity of the empty magnet finally reaches about $1.5\,\mathrm{ppm}$ within the DSV volume [109].

However, as soon as an object is placed in the magnet, the homogeneity of the magnetic field is perturbed by the magnetic response of the specific object. This magnetic responds can be described by the unitless volumetric susceptibility coefficient $\chi$. The magnetic field $\vec{B}_0$ that the spins experience during an MRI or NMR experiment differs from the static field $\vec{B}_{\text{empty}}$ of the empty magnet by the factor $(1+\chi)$.

$$\vec{B}_0 = \vec{B}_{\text{empty}}(1+\chi) \tag{2.104}$$

It can be seen from Eq. 2.104, that susceptibility induced $B_0$ inhomogeneity scales with the field strength of the magnet. In MRI, especially tissue–air interfaces can cause significant magnetic field perturbations since air is slightly paramagnetic ($\chi = 0.3\,\mathrm{ppm}$) while biological tissue is typically diamagnetic ($\chi = -9.2\,\mathrm{ppm}$). Although many modern MRI scanners are equipped with higher order shim coils, the spatial distribution of susceptibility induced magnetic field perturbations is usually too inhomogeneous to be fully corrected.

Regarding head imaging, especially air cavities, such as the sinuses, the nasal cavity, the ear channels or the jaw, cause significant $B_0$ inhomogeneity.

Basically, an inhomogeneous $B_0$ field results in an increased $T_2^*$ decay and a reduced SNR of the FID. In a bSSFP sequence, off-resonance can also cause banding artifacts as shown in Fig. 2.7. Additionally, some MRI sequences, such as spiral or EPI, suffer from severe blurring or geometrical distortions because of $B_0$ inhomogeneity. Since EPI is the most commonly used readout technique for DWI, off-resonance effects are described in more detailed below.

In EPI, geometrical distortions occur predominantly in PE direction [110]. The reason is, that the timespan between the acquisition of two consecutive k-space points in FE direction is far smaller than in PE direction (see Fig. 2.10). Off-resonance effects can be understood using the following example, assuming the k-space signal $S_k(k_x, k_y)$ that corresponds to the image space signal $S(x, y) = S_0\delta(x-x_0)\delta(y-y_0)$ of one spin at position $x_0$, $y_0$, where $k_x$ is the FE direction $k_y$ is the PE direction. Due to the off-resonance $\Delta B_0$, the k-space exhibits a phase gradient $m_{B0}k_y$ in PE direction because the PE lines are sampled consecutively in time and therefore, the spin accumulates phase. Now, $S_k(k_x, k_y)$ is calculated as the Fourier transform of $S(x, y)$.

$$S_k(k_x, k_y) = S_0 \int\int_{-\infty}^{+\infty} \delta(x - x_0)\delta(y - y_0)e^{-i2\pi(k_x x + k_y y + m_{B0}k_y)}\, dxdy \quad (2.105)$$

$$= S_0 e^{-i2\pi(k_x x_0 + k_y y_0 + m_{B0}k_y)} \ . \quad (2.106)$$

The effect of $m_{B0}$ can be corrected by the coordinate transform $y_0' = y_0 + m_{B0}$.

$$S_k(k_x, k_y) = S_0 e^{-i2\pi(k_x x_0 + k_y y_0')} \ , \quad (2.107)$$

This example demonstrates the effect of a phase gradient $m_{B0}$ in the acquired k-space data which causes a shift of the spins in image space. The shift can be quantified with the bandwidth per pixel $\Delta f_p$ which is defind as

$$\Delta f_p = \frac{1}{N \cdot \Delta t} \ , \quad (2.108)$$

where $\Delta t$ is the time between the sampling of two consecutive points in k-space and N is the corresponding matrix size. For the EPI case, $\delta t$ is equivalent to ESP. For example, assuming a matrix size of 100 and an ESP of $0.5\,\mathrm{ms}$, the corresponding bandwidth per pixel is $\Delta f_p = 20\,\mathrm{Hz}$. That means that a off-resonance of $\gamma\Delta B_0 = 20\,\mathrm{Hz}$ results in a shift of a voxel. For example at $3\,\mathrm{T}$, the off-resonance in the brain can easily exceed $100\,\mathrm{Hz}$ in some regions. It is important to note that these spatial shifts can also occur in FE direction. However, the effect is much less pronounced because $1/\Delta t$ corresponds to the receiver bandwidth which is typically several ten thousand Hz.

If the $B_0$ inhomogeneity $\Delta B_0(\vec{r})$ is spatially inhomogeneous, geometrical distortions occur because spins with different Larmor frequencies are shifted differently. Fig. 2.11a depicts an undistorted $T_2$ weighted slice of the brain in axial orientation. The corresponding fieldmap, given by $\gamma B_0(\vec{r})/(2\pi)$, is shown in Fig. 2.11b. The fieldmap exhibits multiple maxima originating from air cavities, including the nasal cavity (marked with 1), the ear channels (marked with 2) and the sinuses (marked with 3). Severe image distortions can

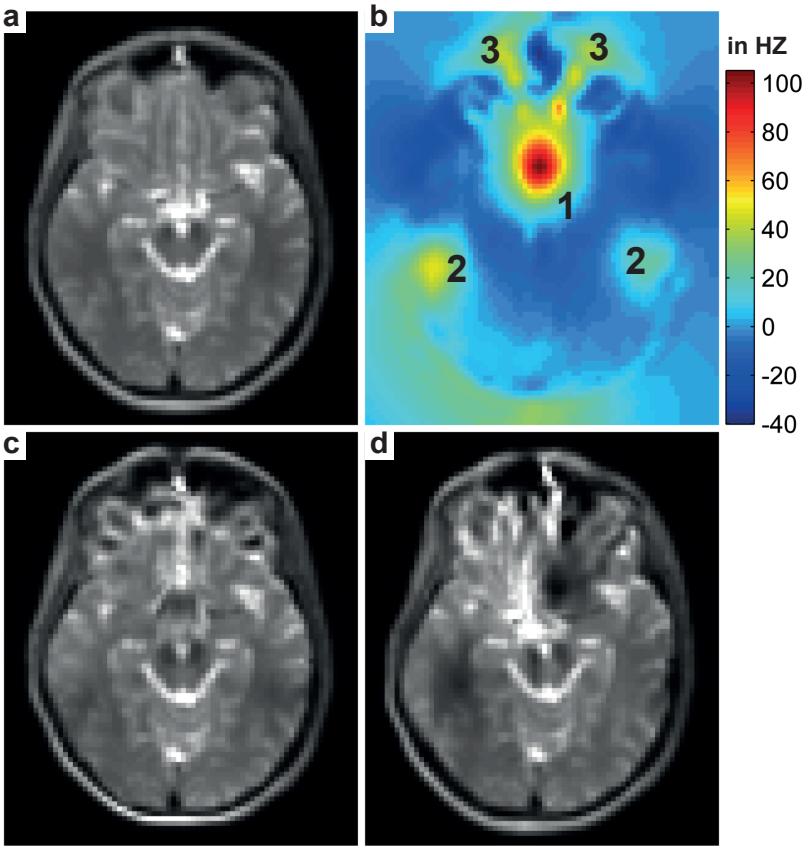


Figure 2.11.: EPI distortions of an axial slice assuming ESP = $0.6\,\mathrm{ms}$, matrix size in-plane $96 \times 96$, and an isotropic resolution of $2.5\,\mathrm{mm}$. **a**: Undistorted $T_2$ weighted image, **b**: Corresponding $B_0$ fieldmap to a, **c**: Image distortions assuming the PE direction is Anterior-Posterior (AP), **d**: Image distortions assuming the PE direction is Left-Right (LR).

be seen in the corresponding EPI images, for PE in AP direction (Fig. 2.11c), or in LR direction (Fig. 2.11d). In regions with a strong gradient in the fieldmap, image compression or image stretching can be observed in the PE direction. As a result, there are also significant fluctuations of the image intensity, because either the signal of multiple voxels is erroneously compressed to one voxel, or the signal in some regions is erroneously stretched over multiple voxels, leaving a hole with low intensity.

Several techniques have been proposed to correct for off-resonance induced EPI distortions, such as fieldmap based approaches [111], reverse gradient techniques [112, 113], or point spread function methods [114, 115]. Although geometrical accuracy can be significantly improved, especially with the latter to methods, regions of severe image compression are still challenging because the unwarping operation is not well conditioned. Geometrical distortions can also be reduced in the acquisition by keeping the effective ESP as short as possible. Particularly, the spatial resolution and the parallel imaging acceleration factor have a large impact on the geometrical distortions. On the one hand, higher spatial resolutions require longer readout gradients which lengthens the ESP. On the other

hand, the effective ESP can be shortened by the parallel imaging acceleration factor $r$, because only every $r$th line is sampled reducing the readout time and potential phase errors. However, shortening the ESP by using higher gradient strengths for the readout is usually technically but also physiologically limited due to peripheral nerve stimulation [116].

#### Eddy currents

According to Faraday's law of induction, all conductive materials respond to changes of the magnetic flux with an opposing field. This opposing field results from eddy currents which are, for example induced in the gradient coils itself, but also in elements of the receive coils or other conductive materials. In MRI, eddy currents are generated during the ramps of the gradient pulses and therefore, increase with higher gradient amplitudes and faster slewrates.

The spacial distribution of the eddy current field $\vec{B}_e(\vec{r}, t)$ is typically described in a Taylor expansion [36, p. 320].

$$\vec{B}_e(\vec{r}, t) = b_0(t) + \vec{r} \cdot \vec{G}_e + ... \tag{2.109}$$

The first term $b_0(t)$ is typically called $B_0$ eddy currents, the second term $\vec{G}_e$ is called linear eddy currents and all other terms are called higher order or nonlinear eddy currents.

The time evolution of eddy currents can be modeled in good approximation by an exponential decay [117]. However, on a commercial scanner, the decay constants can vary from a few microseconds up to multiple seconds depending on the resistance and inductance of the circuits, where the eddy currents are induced [36, p. 318-322]. Therefore, the time evolution of the eddy current field is a superposition of multiple exponential decays.

The increase and decrease of the gradient field generates eddy currents with opposite sign. Consequently, eddy currents arising from trapezoidal gradient pulses partially cancel, depending on the plateau time. Unfortunately in DWI, the plateau time of the diffusion weighting gradients is typically very long compared to the imaging gradients. Consequently, eddy currents arising from the ramp up of the gradient have partially decayed already, so that eddy currents from the ramp down cannot be fully eddy compensated. As a result, some eddy currents from the diffusion weighting gradients usually persist during the readout.

Eddy currents can cause image artifacts, particularly in sequences with long echo trains, such as EPI or RARE. For example in EPI, eddy currents arising from the alternating polarity of the readout gradients, can create a mismatch of odd and even lines in k-space, which results in ghosting artifacts. Moreover in DWI, the eddy currents originating from the diffusion weighting gradients generate an off-resonance field which can cause geometrical distortions in the same way as $B_0$ inhomogeneity (see section 2.3.3). There are three typical distortion patterns induced by eddy currents. On the one hand, a $B_0$ eddy current results only in a shift of the imaging object in PE direction. On the other hand, a linear eddy current in PE or FE direction cause shearing and scaling of the imaging object in PE direction, respectively. Moreover, these eddy current induced distortions highly depend on the diffusion encoding gradients, and therefore, can be different for each DWI.

Several techniques have been developed to reduce eddy currents. Most important are shielded gradient coils, which can reduce the eddy current amplitude by one to two orders of magnitude [118]. Furthermore, waveform preemphasis is a widely used technique,

where the waveform that is input to the gradient coil is modified such that subsequent eddy currents are canceled. Additionally, in some cases, the gradient amplitude can be derated in favor of a longer gradient pulse, which also reduces the eddy currents. Finally, some eddy current effects can be corrected in the post processing. For example, the mismatch between odd and even lines in EPI can be corrected using a reference scan, or eddy current induced geometrical distortions from the diffusion encoding gradients can be corrected with an affine registration on an undistorted image.

**Concomitant field terms**

In section 2.3.1, it is shown that the gradient coils of an MRI scanner generate a spatially varying $z$-component $B_z$ of the magnetic field $\vec{B}(\vec{r})$.

$$B_z = xG_x + yG_y + zG_z \ , \tag{2.110}$$

However, the Maxwell equations $\nabla \cdot \vec{B} = 0$ and $\nabla \times \vec{B} = 0$ (assuming free space, i.e. no sources are present) require that a spatial gradient of $B_z$ is accompanied by spatial gradients in the $B_x$ and $B_y$ component. Consequently, in the presence of a magnetic field gradient, the Larmor frequency is not given by $\gamma B_z$ but must be calculated as

$$\omega = \gamma\sqrt{B_x^2 + B_y^2 + B_z^2} \ . \tag{2.111}$$

Assuming gradient coils with a cylindrical symmetry, the Taylor series of $|\vec{B}(\vec{r})|$ until the second order [119] is given by

$$|\vec{B}(\vec{r})| = B_0 + xG_x + yG_y + zG_z + \frac{1}{2B_0}\Big(G_x^2z^2 + G_y^2z^2 + G_z^2\frac{x^2+y^2}{4} - G_xG_zxz - G_yG_zyz\Big). \tag{2.112}$$

The last terms in parentheses are called concomitant field terms which cause an additional, spatially varying phase shift when a gradient is applied. In contrary to $B_0$ inhomogeneity, the concomitant field scales with the inverse field strength $1/B0$ and therefore, are less of a problem at $3\,\mathrm{T}$. Moreover, in DWI of the brain, the FOV is typically rather small and the slice orientation is typically close to axial which significantly reduces the EPI distortions due to the concomitant field [120].

Similar to $B_0$ inhomogeneity, EPI distortions arising from the concomitant field can be corrected in the post processing. However, the concomitant field is independent of the imaging object, and therefore generally easier to handle than $B_0$ inhomogeneity [120].

# 3. Bias and precision analysis of DKI for different acquisition schemes

The content of this chapter was published in the scientific journal Magnetic Resonance in Medicine (MRM) and it was recently made available as early view [121]. The manuscript was entitled "Bias and precision analysis of DKI for different acquisition schemes".

## 3.1. Introduction

In section 2.2.5 the Diffusion Kurtosis Imaging (DKI) diffusion model is introduced which describes the non-Gausianity of diffusion in biological tissue [15]. Regarding the data acquisition for DKI, the most common approach is a multi-shell acquisition scheme comprising: one or more b=0-images, two to five concentric spherical shells in q-space, a fixed number of non-collinear diffusion directions per shell ranging from 15 (the minimum for the DKT) to 32 (9,20-22) and maximum b-values ranging from 2000 s/mm² to 3000 s/mm² [122]. Widely used is a 5-shell acquisition scheme, first introduced by Lu et al. [13], with a uniform b-value spacing of the shells, 30 non-collinear directions, and a total of 150 DWIs. However, Poot et al. showed an optimized DKI acquisition scheme based on a Cramér Rao lower bound analysis [123] which includes 3 shells with 25, 45, 70 directions and corresponding b-values of 700 s/mm², 1000 s/mm², 2800 s/mm² respectively [68]. Furthermore a general enhancement for multi-shell acquisition schemes has been reported by jointly maximizing the angular incoherence of the directions of all shells [124, 125]. Besides the multi-shell acquisition schemes, also DSI sampling schemes (see section 2.2.5) have been used for DKI [126]. To shorten the very long acquisition times of DSI a technique called Compressed Sensing Diffusion Spectrum Imaging (CS-DSI) was introduced which undersamples the Cartesian grid and uses a Compressed Sensing (CS) algorithm to reconstruct the full q-space [126, 127]. In addition to recovering the signal of only partially measured samples, CS can also be used to recover inaccurately sampled data, e.g. noise corrupted data [128]. This can be employed to address the low SNR of DWIs which represents a problem for DKI in two respects: First, it causes low precision of the derived scalar metrics and second, it causes a significant bias to the derived kurtosis metrics due to the Rician distribution of the noise, as processing is commonly done on magnitude data [68, 71, 129]. Several approaches have been carried out to counter these problems. A comparison between LLS fitting and WLLS showed that the precision of the estimation of the DKT can be increased without introducing additional bias if the weights for the WLLS fitting routine are carefully chosen [71]. Furthermore, Maximum Likelihood Estimation (MLE) has been used to significantly reduce the bias of the DKT [68, 70]. However, a crucial requirement for MLE is the knowledge of the correct noise amplitude, which is often non-uniform due to parallel imaging effects [129, 130]. As a result accuracy and precision of MLE estimators often suffer from incorrect estimation of the noise amplitude [71]. Additionally correction

for susceptibility induced imaging distortions, subject motion, or eddy current induced geometric deformations can alter the noise distribution.

Previous work extensively investigated the performance of conventional estimators like LLS and WLLS as well as more sophisticated estimators like MLE to fit the DKI model [68, 71, 129]. It has been found that a low SNR causes a positive bias of scalar DKI metrics like mean Kurtosis. In this work the most common estimator WLLS is used and the 3D distribution of the AKC in terms of bias and precision is analyzed. For this study Monte Carlo simulations are conducted using different voxel types as well as real data experiments involving complex averaging of multiple repetitions as ground truth. The correlation between the anisotropy of a voxel and the stability of the DKI model will be investigated because failed fits in DKI metrics are often seen in high FA regions like the corpus callosum [15, 123]. In addition different state-of-the-art acquisition schemes are systematically compared in terms of precision and resulting bias regarding the DKI model and the influence of denoising using averaging or CS is investigated.

## 3.2. Methods

### 3.2.1. Data Acquisition

DWI acquisitions were obtained from one healthy volunteers. The study protocol was in line with the Declaration of Helsinki and was approved by a local ethical review board. The data were acquired with a 3T GE MR750 scanner, with a maximum gradient strength of $50\,\mathrm{mT\,m^{-1}}$ (GE Healthcare, Milwaukee, WI) using a ST diffusion preparation and a single-shot 2D EPI readout train. The imaging volume was recorded with a matrix size of $96 \times 96 \times 16$ and an axial oriented $24 \times 24 \times 4\ \mathrm{cm^3}$ scan volume, covering the brain at the level of the corpus callosum. Further acquisition parameters were: isotropic resolution $2.5\,\mathrm{mm}$, TE = $80.7\,\mathrm{ms}$, TR = $1800\,\mathrm{ms}$, ESP = $0.592\,\mathrm{ms}$, effective readout bandwidth per pixel $1930\,\mathrm{Hz}$. A 32-channel head coil was used with parallel imaging factor 2 in the phase-encoding direction and Sensitivity Encoding (SENSE) reconstruction [26].

DWIs with 5 different acquisition schemes in q-space were obtained with a maximal b-value of $3000\,\mathrm{mm^2\,s^{-1}}$. Two versions of the 5-shell acquisition scheme based on Lu et al. (9) with 30 directions and corresponding b-values of $600\,\mathrm{mm^2\,s^{-1}}$, $1200\,\mathrm{mm^2\,s^{-1}}$, $1800\,\mathrm{mm^2\,s^{-1}}$, $2400\,\mathrm{mm^2\,s^{-1}}$ and $3000\,\mathrm{mm^2\,s^{-1}}$ were acquired. The first version features collinear directions for the 5 shells and is referred to as c5shell (Fig. 3.1a). In the second version the directions are distributed to maximize angular incoherence [125], referred to as mi5shell (Fig. 3.1b). Furthermore two versions of the 3-shell acquisition scheme from Poot. et al. [123] with 25, 40, and 75 directions for the three shells and corresponding b-values of $750\,\mathrm{mm^2\,s^{-1}}$, $1070\,\mathrm{mm^2\,s^{-1}}$ and $3000\,\mathrm{mm^2\,s^{-1}}$ were acquired. The first version features 3 shells where the directions for each shell are distributed homogeneously but there is no coupling between the shells, referred to as r3shell (Fig. 3.1c). In the second version the directions are distributed to maximize angular incoherence [125], referred to as mi3shell where 10 repetitions of this scheme were acquired. Finally an 11-cube DSI acquisition scheme with 514 DWIs on a spherically bounded Cartesian grid was acquired, referred to as fDSI. The DSI scheme was also used to derive a uniformly randomly undersampled DSI (uDSI) dataset comprising only 150 DWIs (Fig. 3.1d). Furthermore, a single-shell DTI

acquisition scheme with 60 directions and a maximum b-value of $1000\,\mathrm{mm^2\,s^{-1}}$ was acquired. Interspersed b=0-images every 20 DWIs were acquired for retrospective motion correction.

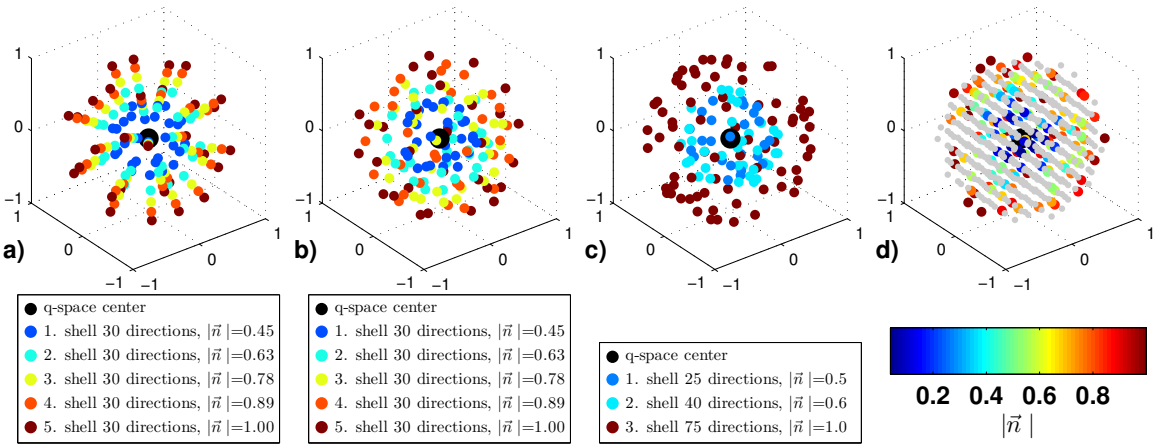


Figure 3.1.: DKI acquisition schemes in q-space. The vector $\vec{n} = \vec{q}/|\vec{q}_{max}|$ corresponds to $\vec{q}$ normalized by the maximum q-value among all acquisition scheme $|\vec{q}_{max}|$. The x, y, z axes correspond to the $n_x$, $n_y$, $n_z$ and the color bar shows the absolute value of $|\vec{n}|$. The corresponding b-value would be defined as: $|\vec{q}|^2$ times maximal b-value of the acquisition. (a) mi5shell, 5 shell acquisition scheme with 30 directions per shell, equidistant spacing of the shells in b-space, all 150 directions are arranged to maximize angular incoherence (b) c5shell, same as a) but directions are collinear (c) mi3shell, 3-shell acquisition scheme with increasing number of directions per shell and an optimized spacing for DKI, directions are arranged to maximize angular incoherence, the r3shell scheme is not shown as it looks very similar, (d) uniformly randomly uDSI scheme arranged on $11 \times 11 \times 11$ Cartesian grid in q-space with 150 sample points. The colored points are sampled with the corresponding q-value whilst the small grey points are not sampled (due to undersampling).

### 3.2.2. Data Preprocessing

All interspersed b=0-volumes were coregistred on the first b=0-volume using an affine transformation to compensate for motion during the acquisition. Subsequently all DWIs were corrected employing the same transformation parameters as those being used for the closest b0-images. As simulation results indicated an increase of bias if magnitude averaging is used, complex averaging of 9 repetitions of the mi3shell scheme was utilized to create a "bronze standard". Prior to averaging, phase correction of the DWIs were carried out following the method of Prah et al. [131] using a quadratic filter kernel of size 3. The magnitude of the complex averaged data was taken, as WLLS can only be applied to positive real valued data. The resulting bronze standard exhibits a significantly reduced bias and increased precision comparable to data with an SNR almost three times higher. However, the bronze standard is not a perfect ground truth for two reasons. On the one

hand, there is a remaining bias due to potentially imperfect phase correction and the absolute value operation after complex averaging. On the other hand, DKI itself exhibits a model error, as it does not provide a full description of the diffusion-weighted signal. Moreover, this model error also depends on the acquisition scheme. In addition to the 6 schemes already described in section data acquisition (c5shell, mi5shell, r3shell, mi3shell, fDSI, uDSI) two further datasets were derived. Firstly a magnitude average of 9 repetitions of the mi3shell scheme (the same data used for the bronze standard) referred to as mi3shell9ma and secondly a CS reconstruction of the uDSI scheme referred to as csDSI [126]. Details of the CS reconstruction are described below. Separation of intracranial volume from soft tissue was performed by an automated brain extraction algorithm (FSL, BET) [132]. Further, segmentation into WM, grey matter GM and CSF was approximated using an absolute thresholding approach on the MD and FA maps computed from the single-shell DTI dataset. All voxels with MD $> 1.8 \times 10^{-9}\,\mathrm{m^2\,s^{-1}}$ were considered as CSF, all voxels with MD $< 1.8 \times 10^{-9}\,\mathrm{m^2\,s^{-1}}$ and FA $< 0.2$ were considered as GM, and the remaining voxels were considered as WM [133, 134].

### 3.2.3. Undersampling and CS Reconstruction

Given the undersampled q-space signal y, CS-DSI computes the data x in the reciprocal propagator space (EAP) by solving

$$\min_x \left(\|Ax - y\|_2 + \lambda_{TV}\|\mathrm{TV(x)}\|_1 + \lambda_{WAV}\|\Psi_{WAV}x\|_1\right) \tag{3.1}$$

with $A = MF$ (where $M$ is the undersampling operator mask and $F$ is Fourier transform), TV and $\Psi_{WAV}$ the sparsifying transforms into total variation and wavelet domain, respectively, and $\lambda_{TV}$ and $\lambda_{WAV}$ the corresponding weights.

Eq. 3.1 can be solved using an iterative shrinkage-thresholding algorithm (ISTA) [127, 135]. In each iteration for a given iterate x the residual z between the sampled data $y$ and the $Ax$ is calculated.

$$z = y - Ax \tag{3.2}$$

Next a gradient descent is applied using the adjoint operator $A^H$ (which is identical to the inverse Fourier transform) to the residual $z$.

$$w = A^H z + x \tag{3.3}$$

Finally the next iterate $x'$ is calculated by applying the denoising operators $\eta_{TV}$ and $\eta_{WAV}$ on $w$.

$$x' = \eta_{WAV}\left[\eta_{TV}(w)\right] \tag{3.4}$$

The denoising operators $\eta_{TV}$ and $\eta_{WAV}$ are defined as

$$\eta_{TV}(w) = w - \sigma_{TV}\nabla\,\mathrm{TV}(w) \tag{3.5}$$

$$\nabla\,\mathrm{TV}(w) = -\,\mathrm{div}\left(\frac{\nabla w}{\|\nabla w\|}\right) \tag{3.6}$$

$$\eta_{WAV}(w) = {\Psi_{WAV}}^{-1}\,\mathrm{T}\left(\Psi_{WAV}w\right) \tag{3.7}$$

$$\mathrm{T}(w') = \begin{cases} w' - \mathrm{sgn}(w')\sigma_{WAV} & \text{if } |w'| \geq \sigma_{WAV} \\ 0 & \text{else} \end{cases} \tag{3.8}$$

where $\sigma_{TV}$ and $\sigma_{WAV}$ are weighting parameters that control the amount of denoising. A empirical optimization of the denoising parameters for DKI resulted in $\sigma_{TV} = 1$ and $\sigma_{WAV} = 0.2$

In this work a uniform random undersampling pattern comprising 150 q-space points out of 514 was used (Fig. 3.1). For the pattern generation, point symmetry of q-space was employed to sample at most one of the two central symmetric points to increase angular resolution. Before CS reconstruction each acquired DWI was copied to its antipodally symmetric counterpart in q-space. This ensures real valued data in the EAP due to Hermitian symmetry of q-space and it enforces the ISTA algorithm to check data consistency also for the virtual antipodally symmetric counterpart in each iteration. Furthermore random translations in the EAP space were used for each iteration to improve performance of the wavelet denoising [127].

### 3.2.4. DKI fitting

The DKI model was fitted using a WLLS routine that was implemented in Matlab (MathWorks, Natick, MA). The WLLS weights were chosen as the squared values of the predicted signal of a DKI fit obtained by a LLS estimator [71, 136]. To allow AKC values only within physically acceptable range, constraints #1 and #2 (see Eqs. 2.61 and 2.62) were imposed in all acquisition directions as described in section 2.2.5. The linearly constrained problem was solved using quadratic programming . The third constraint #3 (see Eq. 2.63), enforcing the signal to be monotonically decreasing for all acquisition directions was not used as it was found to not significantly improve the fit.

The average of the AKC was calculated in the scaled inherent coordinate system and is denoted MZ as described in section 2.2.5. The Radial Kurtosis ($AKC_{\perp}$) was calculated numerically in the scaled inherent coordinate system as the average AKC over 60 uniformly spaced directions pointing perpendicular to the main eigenvector of the $DT_{DKI}$. The Axial Kurtosis ($AKC_{||}$) was calculated as the AKC in the direction of the main eigenvector. The extrema, Minimum Kurtosis ($AKC_{min}$) and Maximum Kurtosis ($AKC_{max}$) were also calculated numerically, using 1024 uniformly distributed directions on a sphere.

### 3.2.5. Simulations

To assess the performance of the different acquisition schemes, Monte Carlo simulations, assuming Rician noise, were carried out. Three sets of $DT_{DKI}$ and DKT coefficients were derived from the real data acquisition to serve as inputs for the simulations as shown in Fig. 3.2a-c. For this purpose three different voxel types were defined empirically using the DTI model: a GM voxel with eigenvalues $\lambda_1$, $\lambda_2$, $\lambda_3$ from $0.5 \times 10^{-9}\,\mathrm{m^2\,s^{-1}}$ to $1.0 \times 10^{-9}\,\mathrm{m^2\,s^{-1}}$, a low-FA WM voxel with eigenvalues $\lambda_1$, $\lambda_2$ from $0.3 \times 10^{-9}\,\mathrm{m^2\,s^{-1}}$ to $0.7 \times 10^{-9}\,\mathrm{m^2\,s^{-1}}$ and $\lambda_3$ from $1.0 \times 10^{-9}\,\mathrm{m^2\,s^{-1}}$ to $1.5 \times 10^{-9}\,\mathrm{m^2\,s^{-1}}$, and a high-FA WM voxel with eigenvalues $\lambda_1$, $\lambda_2$ from $0.2 \times 10^{-9}\,\mathrm{m^2\,s^{-1}}$ to $0.5 \times 10^{-9}\,\mathrm{m^2\,s^{-1}}$ and $\lambda_3$ from $1.5 \times 10^{-9}\,\mathrm{m^2\,s^{-1}}$ to $2.5 \times 10^{-9}\,\mathrm{m^2\,s^{-1}}$. The definition of these thresholds ensured, that only very similar voxels are assigned to one of the 3 voxel types respectively. The DTI model was fitted to the single-shell dataset. All voxels corresponding to one of the three types were identified and a DKI fit was applied to those voxels using all DWIs (2454 volumes). Next, the coefficients

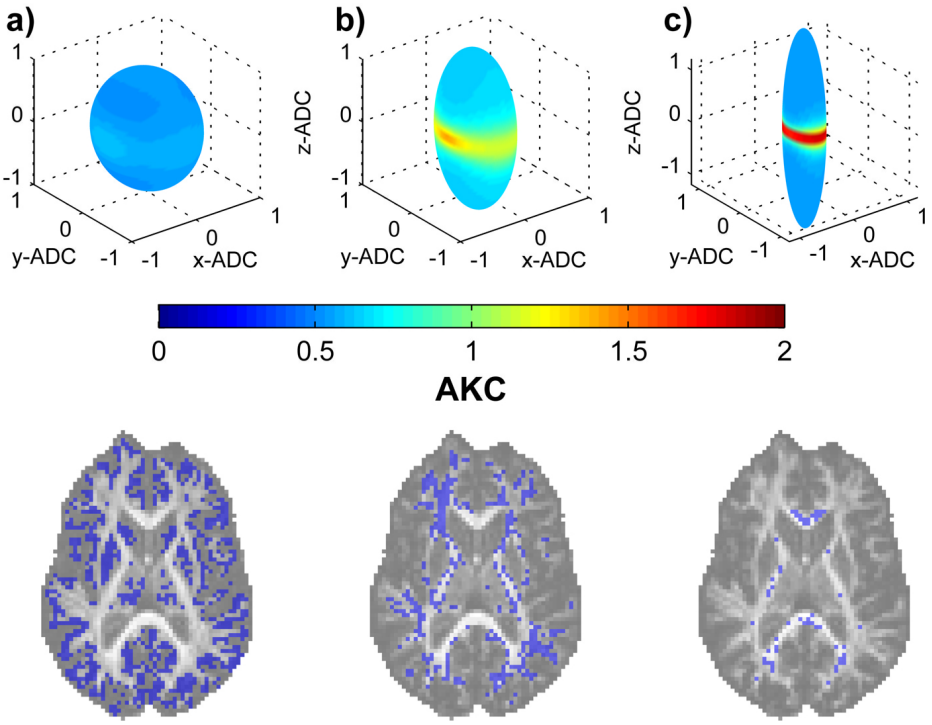


Figure 3.2.: Simulated DKI voxels. The DKI fits were transformed into principal eigenvector system of the DTI fit and averaged resulting in: (a) the GM voxel, (b) the low-FA WM voxel and (c) the high-FA WM voxel. Upper row: The 3D plots show the ADC using the spatial axes x, y, z and the AKC using the color-coding shown in the color bar. Lower row: In an exemplary FA map, the three voxel pools as defined in the simulation study are depicted. The corresponding scalar DTI and DKI metrics can be found in table 1.

of the $DT_{DKI}$ and the DKT were transformed into the principal eigenvector system of the $DT_{DKI}$ and averaged, resulting in three sets of $DT_{DKI}$ and DKT coefficients.

Out of the $DT_{DKI}$ and DKT coefficients, q-space data was synthesized for the same acquisition schemes described in data preprocessing section and altogether 4800 noise instances for 6 SNR levels ranging between 10 and 20 were created, where for each noise instance the $DT_{DKI}$ and DKT were randomly rotated to eliminate orientation effects. The fitting of the DKI model to the simulated data was done with the same WLLS routine and the same parameters as the real data. An overview of some DTI and DKI metrics of the simulated voxels is given in Table 3.1.

## 3.3. Results

### 3.3.1. Simulations

In Fig. 3.3, the different acquisition schemes are compared in terms of the bias of the AKC (Fig. 3.3a), and the bias of the resulting kurtosis metrics as a function of SNR (Fig. 3.3b-m).

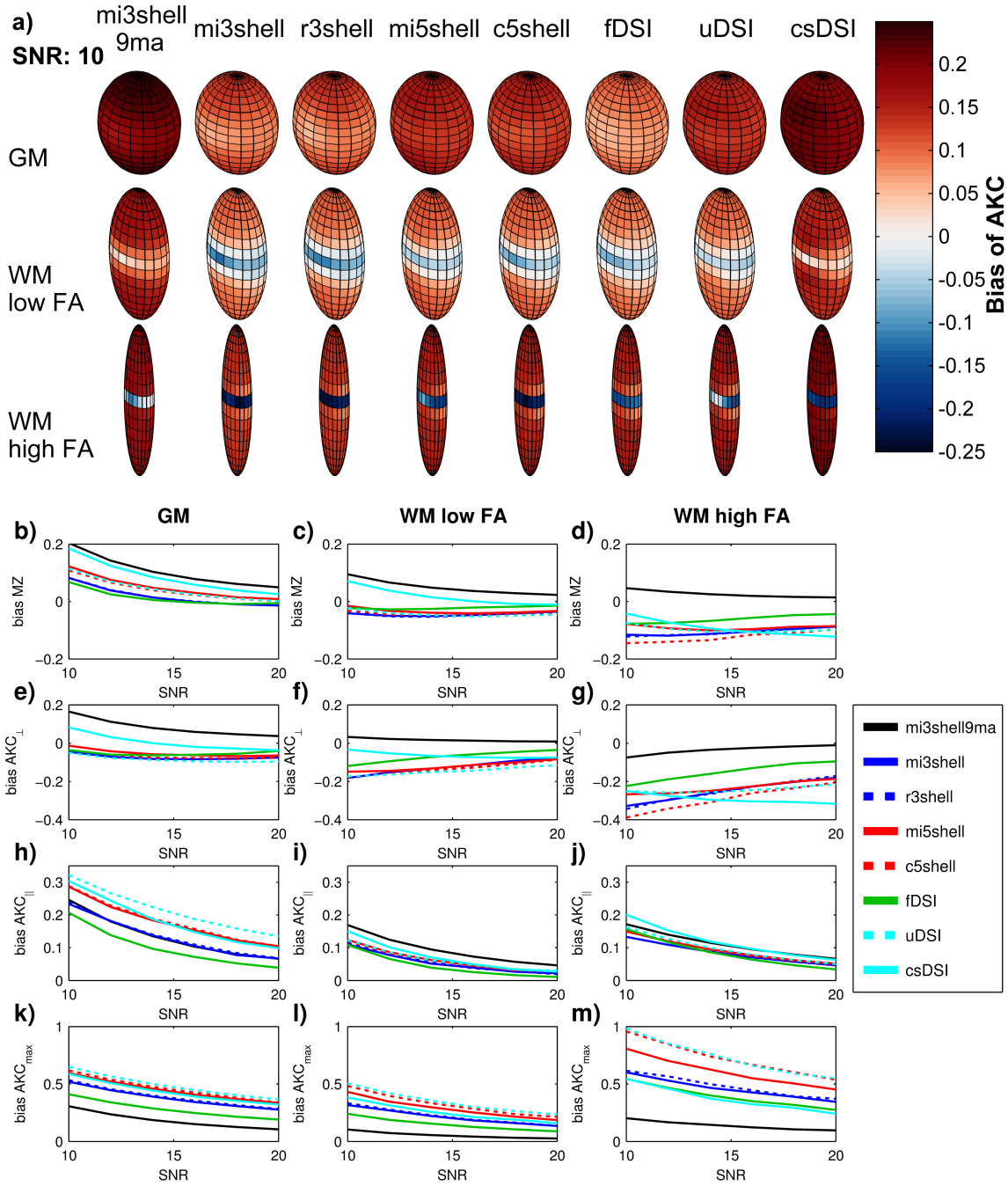


Figure 3.3.: Mean bias of 4800 noise instances for the simulated GM, low-FA WM and high-FA WM voxels as obtained using eight different acquisition schemes. (a) Surface plot of the bias for SNR $= 10$ where the spatial axes describe the eigenvectors of the DT, and the color reflects the bias of the AKC. (b-m) Diagrams of the bias for the scalar DKI metrics MZ, $AKC_{\perp}$, $AKC_{||}$, $AKC_{max}$ for 6 different SNR levels ranging from 10 to 20.

| | GM voxel | low FA voxel | high FA voxel |
|---|---|---|---|
| **MD** | $0.78 \times 10^{-9}$ m²/s | $0.77 \times 10^{-9}$ m²/s | $0.86 \times 10^{-9}$ m²/s |
| **FA** | 0.17 | 0.50 | 0.79 |
| **MZ** | 0.56 | 0.97 | 1.40 |
| **$AKC_{\perp}$** | 0.59 | 1.26 | 2.05 |
| **$AKC_{\parallel}$** | 0.54 | 0.65 | 0.53 |
| **$AKC_{min}$** | 0.52 | 0.65 | 0.53 |
| **$AKC_{max}$** | 0.62 | 1.43 | 2.15 |

Table 3.1.: Scalar DKI metrics $MD_{DKI}$, $FA_{DKI}$, MZ, $AKC_{\perp}$, $AKC_{||}$, $AKC_{min}$ and $AKC_{max}$ of the 3 simulated voxels as depicted in Fig. 3.2.

The bias, calculated as the mean of the difference between 4800 noise instances and the true value of the corresponding metric, varied strongly across the direction within the voxel, the voxel types and the different acquisition schemes. In Fig. 3.3a the angular dependency of the bias within the voxel is illustrated as a 3D surface plot for the lowest simulated SNR of 10. A strong anisotropy of the bias distribution for the low- and high-FA voxel can be observed. While the polar regions of the voxels exhibit an overestimation of the AKC, the equatorial regions show a nominal underestimation in some cases. In Fig. 3.3b-m the bias of the scalar DKI metrics is depicted in more detail. Regarding the GM voxel, MZ (Fig. 3.3b) is overestimated and, as expected, the bias decreases the higher the SNR. The metrics $AKC_{\perp}$ and $AKC_{||}$ (Fig. 3.3e,h) are not very well defined for the GM voxel and there is only a very small anisotropy in the AKC distribution of the ground truth (Fig. 3.2a). Fig. 3.3e,h show, however, that $AKC_{||}$ is heavily overestimated while $AKC_{\perp}$ is slightly underestimated except for the csDSI and the mi3shell9ma dataset. This tendency of overestimating $AKC_{||}$ and underestimating $AKC_{\perp}$ increases substantially (in accord with Fig. 3.3a) with higher FA (Fig. 3.3f-i). Actually, the bias on MZ (Fig. 3.3c,d) becomes more negative the higher the anisotropy because the negative bias of $AKC_{\perp}$ outweighs the positive bias of $AKC_{||}$. There is an apparent inconsistency between the results of Fig. 3.3a and Fig. 3.3b-m. For example, the GM voxel in Fig. 3.3a does not show any negative bias at all, but there are cases of negative $AKC_{\perp}$ in Fig. 3.3e. The reason for this is the different way in which the DKI metrics are calculated over the 4800 noise instances. For the plot in Fig. 3.3a, the orientation of the $DT_{DKI}$ is ignored because the random rotation of each noise instance is simply reversed before averaging. For the plots of Fig. 3.3b-m the orientation of the $DT_{DKI}$ is used to determine the parallel and the orthogonal directions of the fiber. Obviously, any misalignment of the $DT_{DKI}$ can increase the bias of $AKC_{||}$ and $AKC_{\perp}$. However, for experimental data the true orientation of the $DT_{DKI}$ will be unknown, and we should expect a bias behavior as shown in Fig. 3.3b-m. Based on the Monte Carlo simulation, comparison of the different acquisition schemes in terms of bias performance revealed a heterogeneous picture with no advantage for one specific scheme. Overall, the bias of the different schemes varies for the two most common DKI metrics MZ (Fig. 3.3b-d) and $AKC_{\perp}$ (Fig. 3.3e-g) by about 0.15 and 0.2 respectively. This corresponds to a relative error in MZ ranging between $11\,\%$ (high-FA voxel) and $26\,\%$ (GM voxel) and in $AKC_{\perp}$ between

14 % (high-FA voxel) and 35 % (GM voxel).

The 9 fold averaged mi3shell9ma dataset creates a significantly different bias compared to all other datasets, namely a strong overestimation of MZ and $AKC_{\perp}$ (Fig. 3.3b,e) for the GM voxel, an overestimation of MZ (Fig. 3.3c), yet almost no bias of $AKC_{\perp}$ (Fig. 3.3f) for the low-FA WM voxel, almost no bias for MZ (Fig. 3.3d) and slight negative bias of $AKC_{\perp}$ (Fig. 3.3g) for the high-FA WM voxel. Further, $AKC_{||}$ is generally overestimated. This can be explained by the averaging operation in image space, which changes the noise distribution prior to the nonlinear logarithmic operation and the subsequent WLLS fitting routine. The CS reconstruction of the csDSI dataset changes the bias compared to the uDSI dataset towards the bias of mi3shell9ma dataset. This is expected, as the data also undergo a denoising step in image space before the WLLS fitting. The impact of the maximized angular incoherence of the mi5shell and mi3shell datasets on the bias is rather small. Some deviations between mi5shell and the c5shell dataset can be observed for the high FA voxel where the angular resolution of the c5shell dataset may be too small (Fig. 3.3d,g). A comparison of the 3-shell and 5-shell schemes shows a very similar bias behavior. There is a slightly smaller bias of the 3-shell schemes for the GM voxel (Fig. 3.3b,h). The bias of $AKC_{max}$ (Fig. 3.3k-m) was positive for all data sets and noise levels. It increased with anisotropy and decreased with the number of sampling points in the corresponding data sets. The CS denoising of the csDSI dataset clearly reduced the bias of $AKC_{max}$ compared to the uDSI dataset and therefore increases stability. The 3-shell schemes and the csDSI performed similarly to one another but clearly better than the 5-shell and the uDSI schemes, especially for the two anisotropic voxel types. Moreover, maximization of angular incoherence reduced the bias of $AKC_{max}$ slightly for mi3shell and significantly for mi5shell, compared to their conventional counterparts r3shell and c5shell. In Fig. 3.4, the different acquisition schemes are compared in terms of the resulting precision as a function of the SNR. The precision is calculated as the Standard Diviation (SD) of 4800 noise instances for each acquisition scheme and each SNR level. In Fig. 3.4a, the angular dependency of the precision within the voxel is illustrated as a 3D surface plot for the lowest simulated SNR of 10. While the SD is very homogeneous for the GM voxel, the low-FA WM voxel generates a band around the equator with increased SD. The high-FA voxel reveals a very narrow band around the equator with an almost tenfold higher SD at the corresponding pole of the voxel. In general there is a significant decrease in precision for MZ (Fig. 3.4b-d) the more anisotropic the voxel is. The SD approximately doubles for the high-FA voxel relative to the GM voxel. In fact, the SD of $AKC_{\perp}$ (Fig. 3.4e-g) increases by as much as 400 %, while the SD of $AKC_{||}$ (Fig. 3.4h-j) is halved. Overall, the kurtosis tensor seems to be highly unstable for very anisotropic voxels such as the high-FA WM voxel. As a result, the AKC around the equatorial region dominates the precision also for MZ and causes the increased SD for anisotropic relative to isotropic voxels (Fig. 3.4b-d).

A comparison of the precision across the different acquisition schemes reveals the 3-shell as preferable among acquisition schemes with a comparable number of data points. Regarding MZ and the GM voxel (Fig. 3.4b), it is even slightly better than the full DSI dataset with more than 3 times as many data points. For the two anisotropic voxels (Fig. 3.4c,d) the SD of MZ is similar for the 3-shell and full DSI but still better than the 5-shell, uDSI and CS-DSI datasets. CS denoising reduces the SD compared to the uDSI dataset, i.e. it increases the stability of the kurtosis estimation. This effect, however, is more pronounced for the two anisotropic voxels as well as for the two directional metrics $AKC_{\perp}$ and $AKC_{||}$

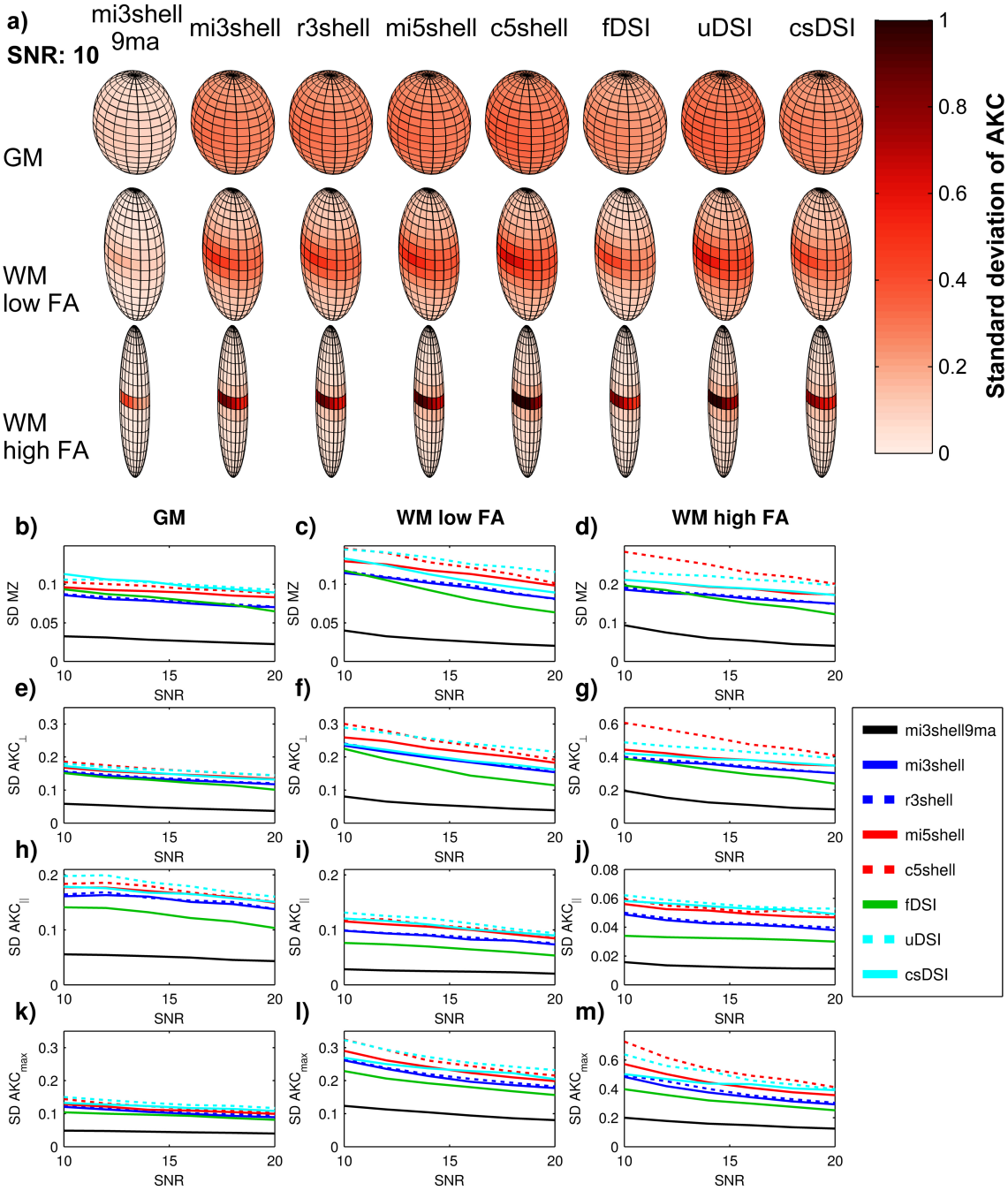


Figure 3.4.: Mean Standard Diviation (SD) of 4800 noise instances for the simulated GM, low-FA WM and high-FA WM voxels as obtained using eight different acquisition schemes (a) Surface plot of the SD for SNR = 10, where the spatial axes describe the eigenvectors of the DT, and the color reflects the SD of the AKC (b-m) Diagrams of the SD for the scalar DKI metrics MZ, $AKC_{\perp}$, $AKC_{||}$, $AKC_{max}$ for 6 different SNR levels ranging from 10 to 20.

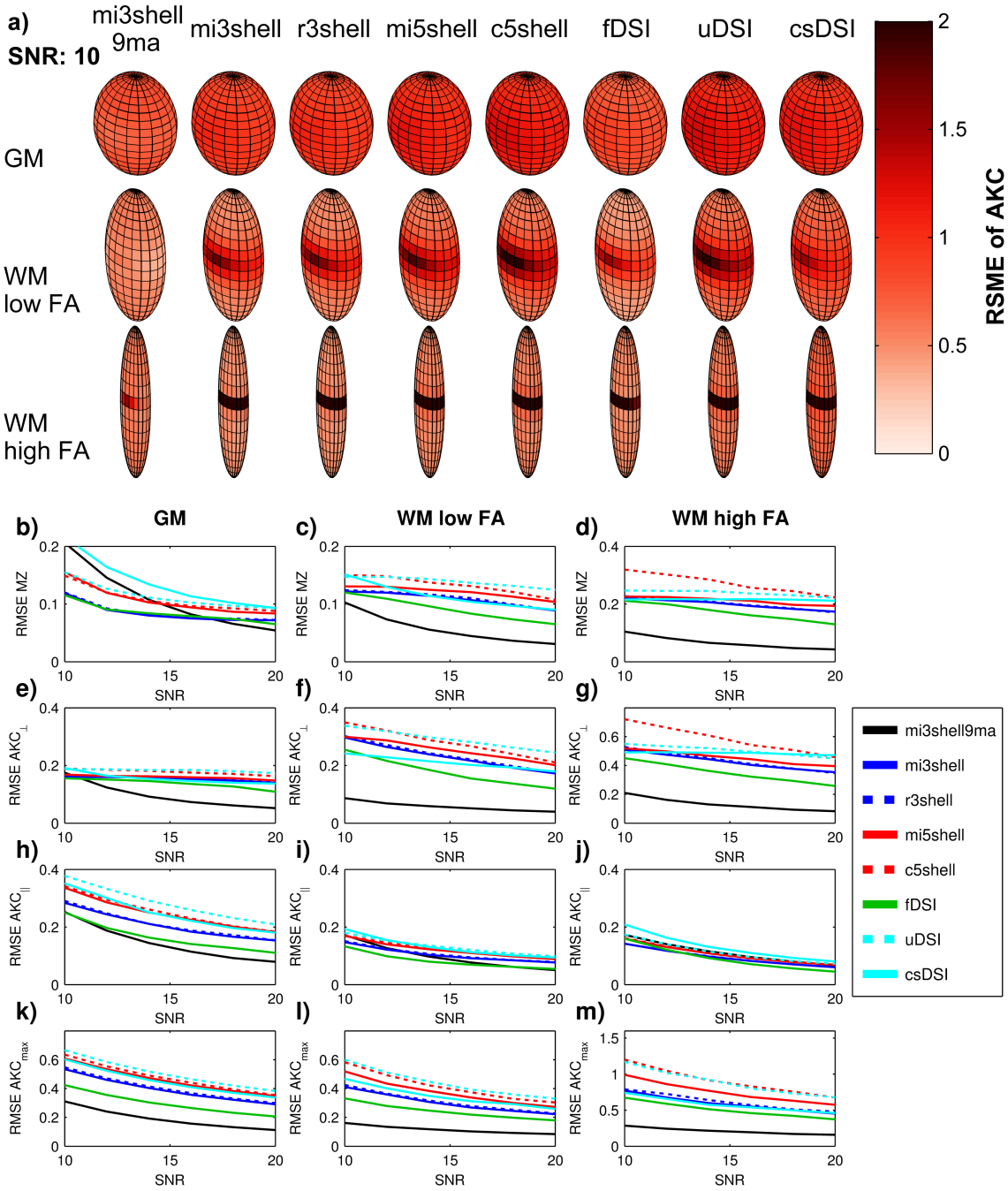


Figure 3.5.: RMSE of 4800 noise instances for the simulated GM, low-FA WM and high-FA WM voxels as obtained using eight different acquisition schemes (a) Surface plot of the RMSE for SNR = 10, where the spatial axes describe the eigenvectors of the DT, and the color reflects the SD of the AKC (b-m) Diagrams of the SD for the scalar DKI metrics MZ, $AKC_{\perp}$, $AKC_{||}$, $AKC_{max}$ for 6 different SNR levels ranging from 10 to 20.

(Fig. 3.4f,g,i,j). The maximization of angular incoherence generally increases precision of the DKI estimation, where the increase is more distinct for the anisotropic voxels. In summary, among all datasets having a comparable number of data points, the 3-shell schemes performed best in terms of precision, followed by csDSI and mi5shell on the second rank as well as the c5shell and uDSI dataset on the last rank. In Fig. 3.5, the different acquisition schemes are compared in terms of the resulting Root Mean Squared Error (RMSE) to evaluate the total error arising from the biased expectation value (Fig. 3.3) and the variance around this value (Fig. 3.4). The RMSE is highest in the equatorial regions of the anisotropic voxels (Fig. 3.5a). A comparison of Fig. 3.3a, 4a, 5a reveals the variance in these regions as the predominant contribution to the RSME. To the contrary the RMSE of the polar regions seems to be rather bias dominated. The dependency of the RMSE from the SNR is different for mi3shell9ma and csDSI compared the other datasets (Fig. 3.5b-j), as they exhibit a different noise distribution, and thus a different bias. As a result, the RMSE of metrics is bias dominated for low SNR and variance dominated for high SNR (Fig. 3.5b,c,e).

### 3.3.2. Volunteer experiments

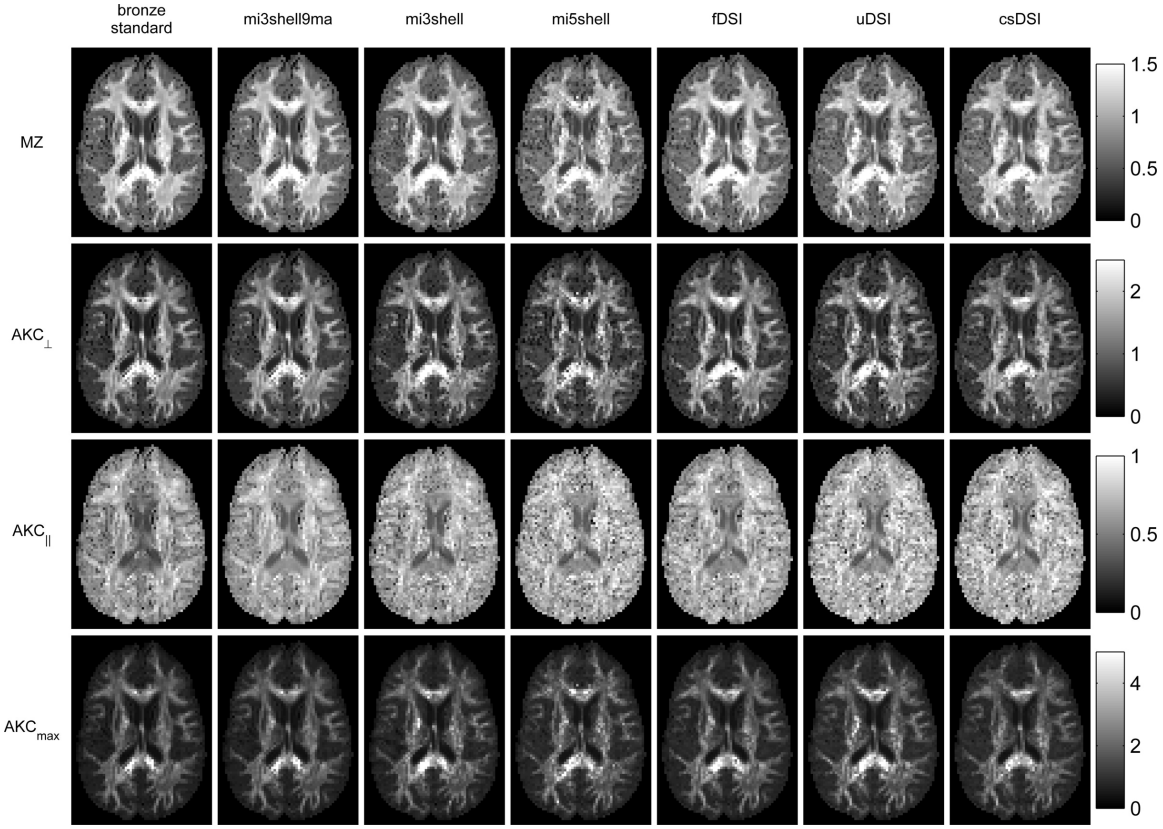


Figure 3.6.: Parametric DKI maps of a volunteer data including MZ, $AKC_{\perp}$, $AKC_{||}$ and $AKC_{max}$ for the six different acquisition schemes.

In Fig. 3.6 the parametric maps of the different kurtosis metrics of a representative slice

from the volunteer data sets are shown. In favor of clarity, only the maximum angular incoherence versions mi3shell and mi5shell of the multi shell schemes are shown, as r3shell and c5shell look very similar. Even though the bronze standard (mi3shell, 9 fold complex averaged) is based on 1400 DWIs, there are still some instabilities of MZ, $AKC_{\perp}$ and $AKC_{max}$ recognizable, in particular in regions with very high FA like the corpus callosum. This is expected as the Monte Carlo simulations indicated that the DKI model is highly unstable in areas of high anisotropy. Comparing the MZ and $AKC_{\perp}$ maps of the 4 datasets that have a comparable number of raw data points, the mi5shell and uDSI datasets appear noisier in particular in GM regions. The $AKC_{||}$ maps confirm this observation, exhibiting more outliers for the 5-shell and uDSI datasets. The GM/WM contrast of $AKC_{||}$ is rather low in all acquisition schemes. The extremal metric $AKC_{max}$ provides information about the stability of the DKT independent of a particular direction, because noise leads to a random overestimation of the AKC in an arbitrary direction, and AKC values above 3 are considered to be not physiologically plausible. CS reconstruction increases the stability of the DKT resulting in fewer outliers and a less bright appearance of $AKC_{max}$ compared to the uDSI dataset.

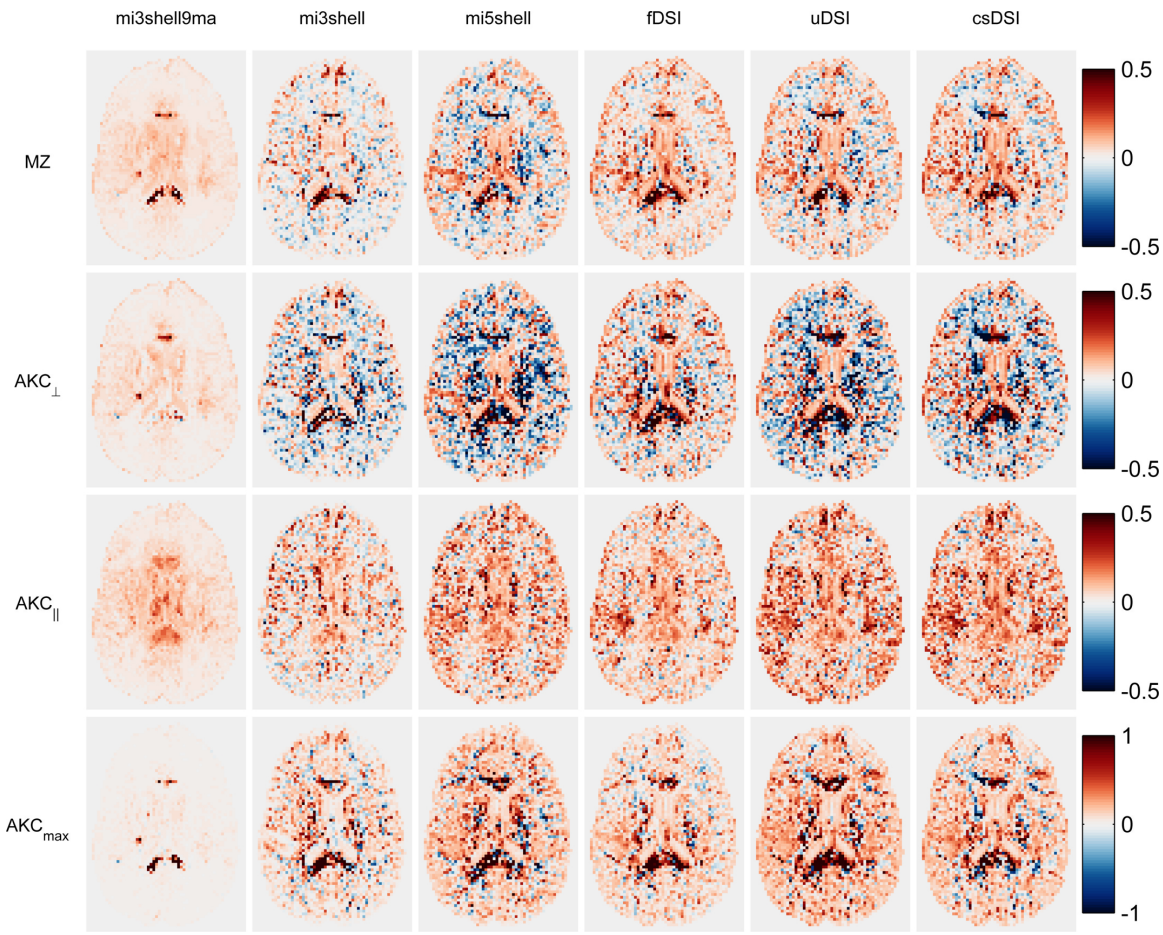


Figure 3.7.: Error maps of the scalar DKI metrics MZ, $AKC_{\perp}$, $AKC_{||}$ and $AKC_{max}$ relative to the bronze standard.

In Fig. 3.7, difference maps of the mi3shell9ma, mi3shell, mi5shell, fDSI, uDSI, and csDSI datasets with respect to the bronze standard are shown. The difference maps for the mi3shell9ma dataset are a special case, as the source data is identical with the bronze standard and only the post processing technique, complex averaging or magnitude averaging, is different. As a result, the noise of the two datasets is correlated and the difference reveals the bias of the WLLS estimator without being spoiled by the variance, assuming the bronze standard is true. A comparison with the simulation results in Fig. 3.3 show a very good agreement with a strong overestimation of $AKC_{||}$ in the center where the SNR is lowest. Assessment for the other datasets is more complicated as bias and variance are overlaid. Nevertheless, in agreement with the simulations, negative bias can be found in white matter regions for MZ and more predominant for $AKC_{\perp}$. To the contrary $AKC_{||}$ is heavily overestimated. Comparison of the acquisition schemes reveals lower bias in the mi3shell dataset. We hypothesize that this is mainly due to the identical acquisition scheme (not the identical data) used for the bronze standard and mi3shell, yielding an identical model error.

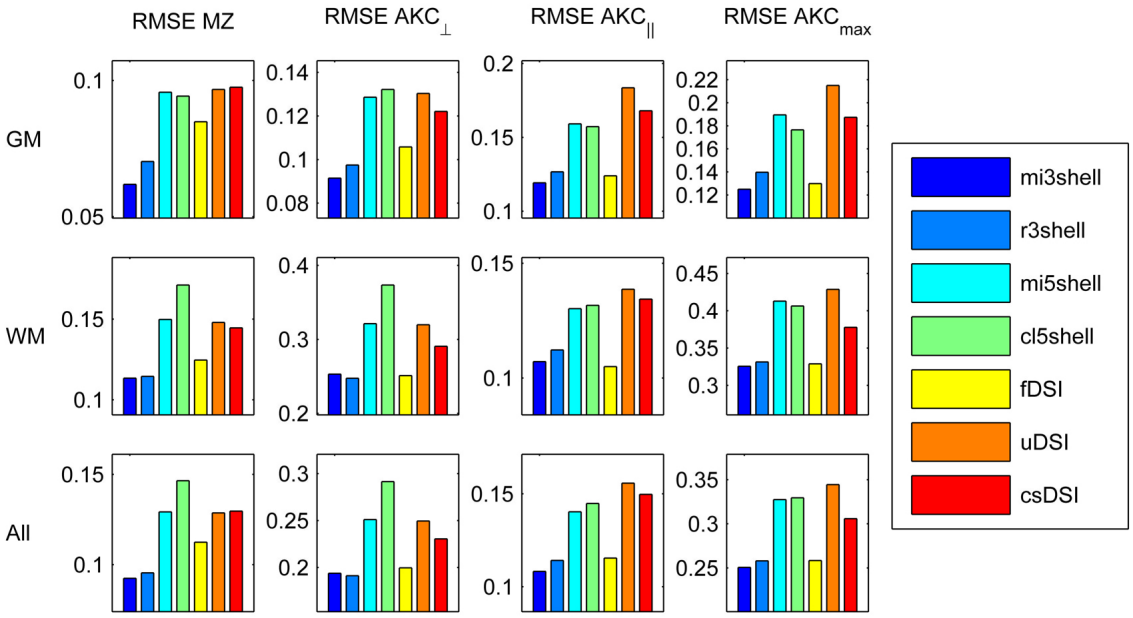


Figure 3.8.: ERMSE diagrams relative to the bronze standard for the GM, WM, full brain voxel compartments and the DKI metrics MZ, $AKC_{\perp}$, $AKC_{||}$ and $AKC_{max}$.

In Fig. 3.8 the RMSE of the different datasets relative to the bronze standard is shown. Although use of the RMSE has the weakness of mixing precision errors and bias errors, it allows a rough estimation of the performance of the different acquisition schemes. Compressed sensing reduced the RMSE particularly for $AKC_{\perp}$ and WM. Also maximizing the angular incoherency improved the RMSE. A comparison between all datasets shows the lowest RMSE for the mi3shell where even the fDSI dataset with 3 times more data exhibits a clearly higher RMSE. When focusing on the two most important metrics MZ and $AKC_{\perp}$, the csDSI dataset performes slightly better than the mi5shell and the c5shell performs the

worst. As discussed above, it is very likely that the RMSE evaluation favors the mi3shell, as the corresponding DKI model error is identical to the bronze standard. This explains why the mi3shell outperforms even the fDSI dataset.

## 3.4. Discussion

### Simulations

Monte Carlo simulations are a very powerful technique to investigate the noise behavior of DWI models and have been extensively used for DKI [68, 70, 71, 129]. In these cases the synthetic data was created using the bi-exponential diffusion model [137]. In the present work we derived $DT_{DKI}$ and DKT coefficients from real data experiments with a very high number of DWIs (2454) and averaging of similar voxels. According to our experience, this real data driven approach to create synthetic diffusion data is more suitable for anisotropic voxels. The analysis of the noise behavior of the DKI model should not be limited to mean kurtosis although this is the most commonly used DKI metric. The simulations demonstrated, that the precision and the bias of the AKC can be highly heterogeneous within a voxel. In contrast to previous work [68, 70, 71, 129] we also observed a negative bias of the AKC perpendicular to the fiber direction while the bias parallel to the fiber direction was always positive (Fig. 3.3). The precision of the fitted AKC also depends on the direction within the voxel and is significantly lower in the radial direction than in the axial direction. Overall, parametric maps of the DKI model have an inhomogeneous bias and precision depending on the voxel type and the SNR. This effect causes instabilities of the DKI model in high-FA regions such as the corpus callosum.

### Denoising

CS has proved its potential to significantly shorten the lengthy data acquisition of DSI [126, 127, 138]. It has been shown in this work, that the denoising inherent to the CS technique can also improve precision of the estimation of DKI metrics. However we also observed a substantial change of the bias including both increase and decrease when CS was used. Even averaging, as the simplest form of denoising, resulted in a substantial change of the bias. This behavior can be explained with the nonlinear logarithmic operation prior to solving the least squares equation in WLLS (or LLS). This implicates that all preprocessing steps that involve interpolation may affect the noise distribution and thus the bias when WLLS is used as estimator. Since the DKI model is particularly vulnerable to a low SNR with its effect on the bias, this should be taken into account when quantitatively comparing DKI metrics.

### b-value dependence of the DKI Model

The bias of a DKI metric is an accurate quantity in an idealized Monte Carlo Simulation, where the simulated voxel conforms perfectly to the DKI model. However in reality this is not the case. The measured diffusion-weighted signal is the ensemble average over a variety of microstructural configurations. Hence, the signal decay as a function of b will not perfectly match the DKI model. This aforementioned DKI model error strongly depends

on the chosen acquisition scheme, even if noise is neglected. The effect is well known from the DTI model, where ADC depends on the maximum b-value [73]. In the case of the DKI it is even more pronounced, as multiple b-values are used. Even if the maximum b-value is identical, a different distribution of the b-values in the radial direction may lead to different DKI model parameters because model errors may be more pronounced in certain b-value regimes. We conclude that this effect is the main reason for the significantly lower RMSE of the mi3shell scheme compared to other datasets, because the bronze standard was based on the same acquisition scheme.

**Acquisition schemes**

The simulation results as well as the real data experiments demonstrated that the 3-shell acquisition schemes (mi3shell, r3shell) of Poot et al. [123] is favorable in terms of precision. Further the use of the CS reconstruction generally improves precision of the DKI estimation compared to the uDSI dataset. Certainly DSI has the advantage of being more flexible and of providing a direct transformation into the propagator space with the use of the Fourier transform [63]. Moreover, the maximization of the angular incoherence of multi shell acquisition schemes also improves precision of the DKI estimation. Overall, the bias of the DKI metrics is less dependent on the acquisition scheme compared to previously discussed preprocessing steps such as denoising.

# 4. Phase Sensitive Reconstruction of Diffusion Weighted Images

The content presented in this chapter was submitted to the scientific journal Magnetic Resonance in Medicine (MRM) in October 5th 2015. The manuscript was entitled "Real Valued DWI using Decorrelated Phase Filtering" and it was accepted on December 24th 2015 [139]. However, the production process of the article was not finished when this thesis was submitted.

## 4.1. Introduction

More recent diffusion models, such as DKI [15], neurite orientation dispersion and density imaging [60], composite hindered and restricted model of diffusion [58], and AxCaliber [59] assume non-Gaussian diffusion because the motion of the water molecules is restricted or hindered by structures within the tissue. These models usually require b-values above $1000\,\mathrm{s\,mm^{-2}}$, extending beyond the validity range of the Gaussian diffusion model. Apart from modeling the diffusion in single voxels, DWI also considers the structural connectivity of the brain. Fiber tracking requires high spatial and angular resolution [140, 141] to resolve the fine structures of the human brain [106]. Several methods have been proposed to determine the Orientation Distribution Function (ODF) of the fibers within a voxel. These can be model-dependent techniques such as high angular-resolution diffusion imaging [56], or the model-free approach called DSI [63]. DSI needs particularly high b-values, typically above $6000\,\mathrm{s\,mm^{-2}}$, to reduce truncation effects when calculating the EAP (see section 2.2.5).

Unfortunately, increasing the diffusion weighting and spatial resolution significantly reduces the SNR of DWIs. While the intrinsic noise acquired by each channel of the MR hardware is Gaussian-centered around zero [105], DWI usually post-processes the magnitude of the complex MR signal only. Hence, the noise distribution alters to a noncentral chi distribution [142, 143] with a positive expectation value. In the case of a single channel acquisition or complex channel combination, the noncentral chi distribution reduces to the so-called Rician distribution [144, 145]. If the SNR is sufficiently high (i.e., > 5), the impact of the Rician distribution can be neglected, because the probability distribution can be well approximated by a Gaussian (Fig. 4.1a), providing a fairly accurate expectation value (Fig. 4.1b).

However, for SNRs significantly below 5, the non-Gaussian noise distribution introduces positive bias in the measured signal, and a noise floor even if the true signal is zero [21] (Fig. 4.1a, b). Hence, depending on the SNR of individual voxels, diffusion models that are fitted to the magnitude data tend to be biased as shown in the previous chapter 3 using the example of DKI. Furthermore, the magnitude data lose contrast in the low SNR

regime because the expectation value has lower dynamic range than the true value (Fig. 4.1c).

The bias, introduced by non-Gaussian noise in DWI, can be corrected by several techniques. These techniques can be roughly divided into two categories: those that directly modify the acquired DWIs [147–150] and those that account for the noise distribution in the fitting algorithm of the individual diffusion model [68, 129, 151]. However, both classes of techniques require precise knowledge of the noise parameter, which is challenging for multiple reasons [129]. First, the noise in MRI images is non-stationary if parallel imaging is used. Second, because of physiological noise, the temporal and local SNRs can be significantly different; therefore, the noise parameter is difficult to estimate in the time domain. Third, unlike thermal noise, physiological noise depends on the amplitude of the MR signal [152]. Consequently the noise in DWI also depends on the b-value. Finally, most of the post-processing steps, such as partial Fourier reconstruction, motion and eddy current correction, change the noise distribution in an unexpected way. Consequently, the uncertainty of the noise parameter estimation reduces the estimation accuracy and precision of the true DWI signal and the true parameters of the diffusion model, respectively.

It is important to note that the above correction techniques are magnitude based and may only cope with the bias. The contrast loss is not well-handled, simply because the full dynamic range of the complex signal is irretrievably lost when the absolute value has been computed. Alternatively, a Phase Correction (PC) real-valued data reconstruction can be used [24, 131, 153–161]. PC techniques try to estimate the true phase of the DWI that is not compromised by noise and subtract it from the complex DWI. Theoretically, the remaining imaginary part can be discarded as pure noise, while the real part contains all relevant image information. PC–DWI maintains the Gaussian noise distribution of the MR signal and introduces no bias, but remains challenging because the estimation of the true image phase is heavily spoiled by eddy currents and motion effects (both bulk motions and intracranial pulsatility) [20]. There are two general categories of PC techniques: those that assume smooth phase and estimate the true, noise free phase of the DWI by filtering [131, 153, 156, 158–161] and those employing an additional phase navigator [24, 154, 155, 157]. The latter are typically used for segmented k-space acquisitions. However, additional acquisition time [24, 155, 157] or significant oversampling of the k-space center [154] is needed.

The crucial step in filter-based approaches is the design of the filter itself. If the phase is sufficiently smooth, a larger filter provides a more accurate estimate of the true phase, resulting in a more Gaussian noise distribution and reducing the bias. However, the phase may not be slowly varying, especially during certain phases of the cardiac cycle when the pulsatile motion is maximized. In such cases, the PC fails and unwanted signal loss occurs. Previously reported PC techniques have limited the strength of filtering, e.g. the size of the filter kernel, which compromises between bias reduction and the robustness to local phase variations. In this study, a new PC method is proposed, which minimizes the smoothness requirements on the phase and maximizes the efficiency of the bias correction. Previously methods do not consider how the noise properties of the raw signal propagate through typical EPI reconstruction pipelines. Here, the method of Prah et al. [131] is improved, using a neighborhood correlation of the noise in the reconstructed complex image. Moreover, a data-driven outlier detection method is presented, which replaces the PC results of certain voxels with their corresponding magnitude values if the phase

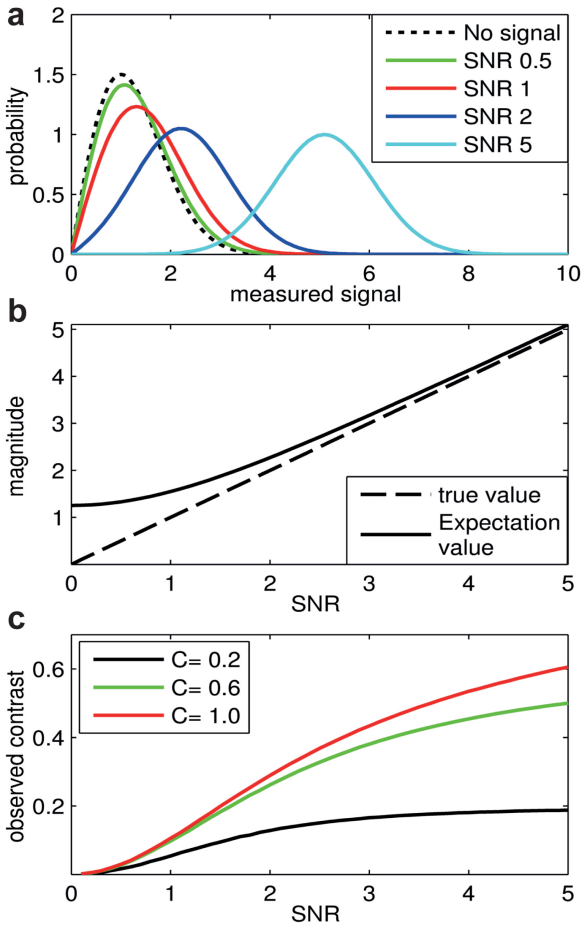


Figure 4.1.: Simulated properties of Rician distributed data. a: Noise distributions either for zero true signal or SNRs of 0.5, 1, 2, and 5; b: Comparison between the expectation value of Rician-distributed data and the true value; c: Michelson Contrast $C$ between signals $\alpha$ and $\beta$ with $C = (\alpha - \beta)/(\alpha + \beta)$ [146], $\alpha > \beta$ and SNR $=$ SNR($\alpha$). The contrast of the expectation value is compared with the contrast of the true signal assuming Rician noise. Note that the larger the contrast $C$, the smaller is signal $\beta$. This figure illustrates how the dynamic range of the expectation value of magnitude data narrows in low SNR situations.

is strongly inhomogeneous. The bias reduction and sensitivity to phase inhomogeneity of the new PC method are evaluated in Monte Carlo simulations. Based on healthy volunteer experiments, the robustness of the new method is demonstrated on the DWI data itself, the estimated DKI model parameters, and the model-free DSI technique. The vulnerability to phase errors, quality of the bias correction, and contrast in the DWIs are compared with those of Prah et al.'s [131] method and with traditional magnitude processing.

## 4.2. Methods

### 4.2.1. Noise propagation in the EPI reconstruction pipeline

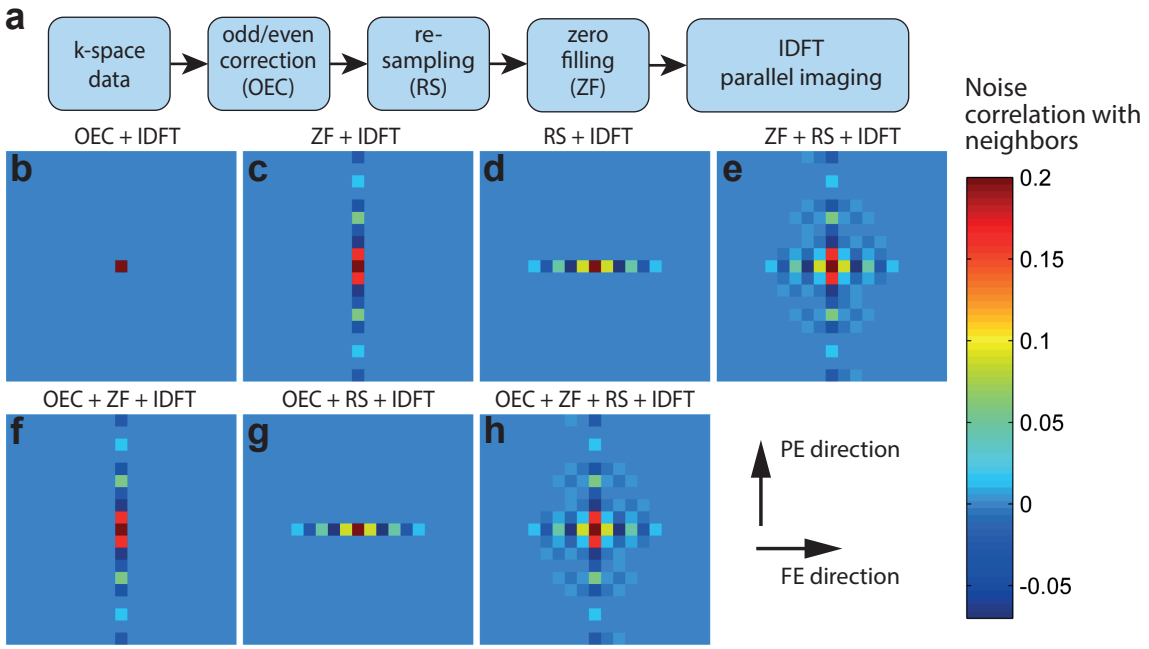


Figure 4.2.: Typical processing pipeline of diffusion weighted EPI data; b: Noise correlation kernel, assuming a k-space grid size of $256 \times 80$ (FE $\times$ PE). Other conditions are oversampling factor = 2, ramp sampling enabled, partial Fourier in the PE direction = 7/8, and final grid size in image space = $96 \times 96$.

Fig. 4.2 schematically depicts a typical processing pipeline for EPI data. Eddy currents and gradient amplifier delays introduce a mismatch between the odd and even k-space lines, yielding a zero-order phase term and a shift of the k-space center where the latter corresponds to a first order phase term in image space. Both the zero and the first order phase term are determined from reference scans and the k-space data is corrected by an IDFT in the FE direction, phase correction by a linear polynomial and subsequent DFT. To maintain the echo spacing as short as possible, ramp sampling is used. Hence, the k-space data require resampling to match the Cartesian grid. This step can also handle potential oversampling in FE direction, which is used to avoid aliasing. In typical DWI, the TE is minimized by partial Fourier in the PE direction and the data is most simply

reconstructed by zero filling. Finally, the actual image is resolved by IDFT in all Fourier-encoded dimensions. In the event of parallel imaging, the corresponding reconstruction must be conducted either in k-space prior to IDFT, e.g., GRAPPA (37), or in the image space after IDFT, e.g., SENSE (38).

Monte Carlo simulations were conducted to analyze the noise propagation through the EPI reconstruction pipeline assuming perfect amplifiers such that the noise between neighboring k-space points is perfectly uncorrelated. The following simulation parameters were used: 10000 noise instances, k-space grid size $256 \times 80$ (FE × PE), oversampling factor 2, ramp sampling enabled, 7/8-partial Fourier in the PE direction with zero filling, and final grid size in image space $96 \times 96$. The Odd/Even Correction (OEC) was performed with an arbitrary first-order polynomial in the FE direction. From the simulation results, the noise correlation kernel was calculated for different combinations of OEC, resampling and zero filling (Fig. 4.2b-h). No noise correlations were introduced by IDFT and OEC. Consequently, the correlation coefficient of the center voxel was unity (self-correlation) and of all other voxels was zero (Fig. 4.2b). IDFT is a linear, orthogonal transformation and thus cannot introduce correlations. OEC adds a phase gradient in image space which is independently performed on each voxel. On the other hand, zero filling and resampling, which are linear but non-orthogonal transforms, did introduce noise correlations in PE and FE direction respectively (Fig. 4.2c-h). However even if both, resampling and zero filling, were applied the diagonal neighbors were almost completely uncorrelated (Fig. 4.2e,h). If parallel imaging in image space is used [26], correlations among the aliased voxels are introduced but the correlations among directly neighboring voxels are not altered. Note that the noise correlation is shift invariant as the thermal noise is independent of position [105].

### 4.2.2. Decorrelated phase correction

For a perfect PC of a DWI, the true phase of the signal in each voxel must be known. Unfortunately, the measured signal is a superposition of the object signal and noise, compromising the estimation of the true phase. Thus, if one would simply subtract the measured phase from the signal, this would be identical to an absolute value operation, rendering the PC obsolete. To overcome this problem, Prah et al. suggested the following PC approach [131]:

- **Step 1:** Filter the complex DWIs using a kernel in image space.
- **Step 2:** Extract the phase of the filtered DWIs.
- **Step 3:** Subtract the phase of the filtered images from the original DWIs.
- **Step 4:** Post-process the real part of the data only.

The effectiveness of PC depends on the correlation of the estimated phase with the measured noise in the voxel. Referring to Fig. 4.2, larger boxcar kernels can reduce the influence of the center voxel and its highly correlated neighbors on the phase estimation and therefore reduce the resulting noise bias. Unfortunately, large filter kernels at the same time are more sensitive to local phase variations limiting their accuracy. In this study, the

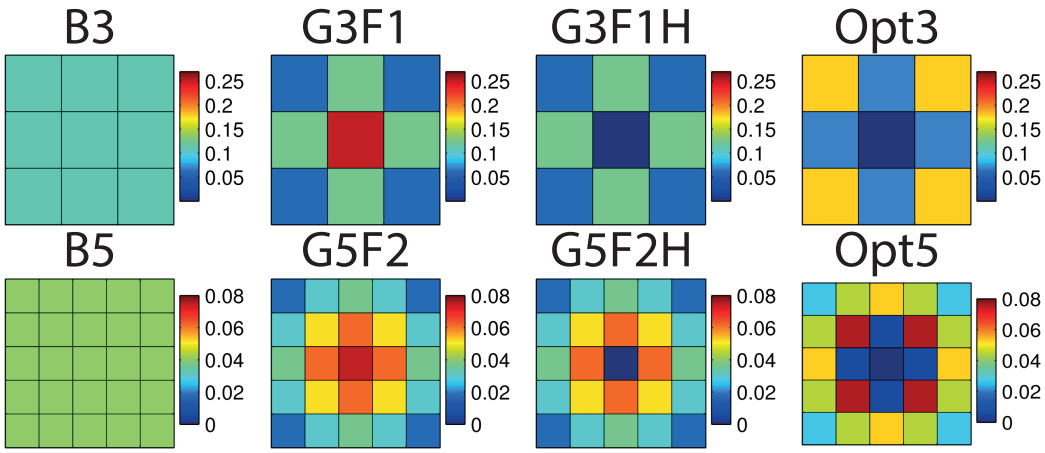


Figure 4.3.: Filter kernels used for estimating DWI phases: B3: size = 3 boxcar kernel, G3F1: size = 3 Gaussian kernel with a Full Width Half Maximum (FWHM) = 1 1/pixel, G3F1H: identical to G3F1 but with center set to zero (hole filter), Opt3: size = 3 kernel optimized with respect to the noise correlation (Fig. 4.2b), B5: size = 5 boxcar kernel, G5F2: size 5 Gaussian kernel with FWHM = 2 1/pixel, G5F2H: G5F2 but with the center set to zero (hole filter), Opt5: size = 5 kernel optimized with respect to the noise correlation (Fig. 4.2b).

performance of multiple existing kernels is evaluated, namely, boxcar kernels [131], Gaussian kernels, newly proposed Gaussian kernels with zero-weighted center voxel ("hole filter"), and empirically optimized, decorrelated kernels. For determination of the optimized filter kernels, the results from Fig. 4.2 were used to assign small weights to highly correlated neighbors and vice versa. An overview of the tested filter kernels and their corresponding abbreviations is depicted in Fig. 4.3.

### 4.2.3. Outlier detection and replacement

If the local phase in a DWI exceeds a certain level of inhomogeneity, the PC becomes corrupted and unwanted signal loss occurs. To detect these errors a simple thresholding method is derived:

- **Step 1:** Estimate the global noise amplitude $\sigma$.
- **Step 2:** Compute the difference maps $\Delta$MR of the magnitude and real-valued images smoothed by a $3 \times 3$ boxcar kernel.
- **Step 3:** Detect outliers by thresholding $\Delta$MR with $\sigma_T = k\sigma$ (where $k > 0$).
- **Step 4:** Replace detected outliers with the magnitude data.

After PC, the imaginary part should theoretically contain pure noise. Applying the robust estimator Median Absolute Deviation (MAD) to the imaginary part of all voxels in all DWIs, the global noise amplitude $\sigma$ is determined (step 1), corresponding to 1.4826 ×

MAD [162]. MAD offers a singular advantage: a signal erroneously assigned to the imaginary part under failed PC exerts less impact on the $\sigma$ estimation than on the standard deviation. In principle, a voxel-wise estimation of $\sigma$ is also possible, but global estimation seemed sufficient for our present purpose. The filtering of $\Delta$MR in step 2 is motivated by the clustering of errors in typical PC. Even when the local phase gradients exceed a certain limit, the corresponding second derivative remains smooth. On the contrary, noise is only weakly correlated among neighboring voxels, as discussed above. For the smoothed $\Delta$MR maps in the PC error detection (step 3), thresholds of $\sigma_T = 2\sigma$ and $\sigma_T = 2.5\sigma$ were chosen empirically. Assuming Gaussian noise, the probability that a voxel with zero true signal randomly exceeds $\sigma_T$ is approximately $4\,\%$for $\sigma_T = 2\sigma$ and $0.3\,\%$ for $\sigma_T = 2.5\sigma$. Because the likelihood of truly zero signals in all voxels within the kernel is very low, the probabilities of exceeding the thresholds by noise alone are rather smaller. If the threshold is exceeded, the real part of the voxel is replaced by the magnitude (step 4).

### 4.2.4. Simulating accuracy and robustness of the phase correction

The biases in the magnitude data and the real-valued data after PC with various filter kernels (see Fig. 4.3) were evaluated in Monte Carlo simulations. SNR levels were ranged from 0 to 3 at 0.1 intervals. The amplitude and phase of the true signal were assumed constant across the kernel size. Although this approach is highly simplified, it reasonably estimates the expected signal bias. In the simulations, 10000 noise instances were created, each of matrix size $256 \times 80$ (FE × PE). Correlated noise was introduced by applying the resampling matrix and by zero-filling 16 lines in the PE direction. The $96 \times 96$ matrix was subsequently subjected to IDFT. A constant signal was added to the correlated noise to match the desired SNR. PC under the different filter kernels was implemented, and the signal expectation value was computed as the mean of the real part taken over all voxel and noise instances. To ensure that the full filter kernel was applied to each voxel, the two-voxel-wide ribbon at the edge of the matrix was discarted.

To investigate potential errors arising from kernel filtering, additional simulations were conducted assuming a linear phase gradient and constant amplitude across the kernel size. This simplified approach cannot capture nonlinear phase variations but reasonably estimates the phase errors as functions of the SNR and phase gradient. 10000 noise instances were simulated for all filter kernels, 3 SNR levels (infinite, 5, and 1), and 20 phase gradients (ranging from zero to $\pi$/voxel). The orientation of the phase gradient was randomly rotated to cancel orientation effects. Finally, the RMSE of the estimated phase was calculated over all noise instances.

### 4.2.5. Data Acquisition

Diffusion-weighted imaging acquisitions were obtained from two healthy volunteers. The study protocol complied with the Declaration of Helsinki and was approved by a local ethical review board. The data were acquired with a $3\,\mathrm{T}$ GE MR750, maximum gradient strength $g_{max}$ of $50\,\mathrm{mT\,m^{-1}}$ (GE Healthcare, Milwaukee, WI), using a single-spin-echo ST diffusion preparation and a single-shot EPI readout train [48]. The first acquisition (ACQ1) comprised 10 repetitions of a 3-shell scheme suggested by Poot et al. [123] with 25, 35, and 70 directions per shell, and corresponding b-values of $750\,\mathrm{s\,mm^{-2}}$, $1070\,\mathrm{s\,mm^{-2}}$ and

$3000\,\mathrm{s\,mm^{-2}}$. The second acquisition (ACQ2) comprised 4 repetitions of an 11-cube DSI acquisition scheme with 514 DWIs [63] on a spherically bounded Cartesian grid and a maximum b-value of $8000\,\mathrm{s\,mm^{-2}}$.

DWIs were recorded with matrix sizes of $96 \times 96 \times 17$ (ACQ1) and $96 \times 96 \times 11$ (ACQ2), and axial-oriented scan volumes of $24 \times 24 \times 4.25$ DWIs were recorded with matrix sizes of $96 \times 96 \times 17$ (ACQ1) and $96 \times 96 \times 11$ (ACQ2), and axial-oriented scan volumes of $24 \times 24 \times 4.25\ \mathrm{cm}^3$ (ACQ1) and $24 \times 24 \times 2.75\ \mathrm{cm}^3$ (ACQ2) covering the brain at the corpus callosum level. Further acquisition parameters were isotropic resolution $2.5\,\mathrm{mm}$, TE = $80.7\,\mathrm{ms}$ (ACQ1) and TE = $105.1\,\mathrm{ms}$ (ACQ2), TR $1800\,\mathrm{ms}$ (ACQ1) and TR $1700\,\mathrm{ms}$ (ACQ2), ESP = $0.592\,\mathrm{ms}$ and ramp sampling (ramp up/down time $72\,\mu\mathrm{s}$, plateau time $368\,\mu\mathrm{s}$). A 32-channel head coil (MR Instruments Incorporated, Minneapolis, MN, USA) was used with a parallel imaging factor of 2 in the PE direction and SENSE reconstruction (39). Retrospective motion correction was computed from interspersed b = 0 images acquired every 20 DWIs. PC and outlier detection and replacement were applied prior to motion correction.

### 4.2.6. DKI fitting

To investigate the impact of real-valued data on the accuracy of quantitative DWI, the DKI model was adopted, which is heavily error-prone to Rician bias [68]. The DKI model was fitted to the real-valued data and to the magnitude data of acquisition ACQ1. LLS or WLLS estimators require two steps: the rejection of negative values, e.g. by replacing them with a fixed positive value, and a logarithmic operation. As these processes would destroy the Gaussian noise distribution, a Nonlinear Least Squares (NLS) [163] fitting routine was used for the real-valued data. The NLS was implemented in Matlab (MathWorks, Natick, MA) using an interior-point optimization algorithm [164], initialized by the solution of a LLS estimator running on magnitude data. Furthermore, to ensure a robust fitting, the ADC and the AKC were constrained to be positive in all acquisition directions to increase robustness of the fit [69, 71] (see constraints #1 and #2 in section 2.2.5). The average AKC was calculated in the scaled inherent coordinate system and is denoted MZ, following the nomenclature of [72] (see section 2.2.5 for details).

### 4.2.7. EAP calculation

The influence of PC on the EAP was determined from DSI acquisition ACQ2. To enforce Hermitian symmetry and real-valued signal of the EAP, each point in q-space was calculated as the average of the four acquired repetitions and their antipodally symmetric counterparts. The matrix size of the q-space was increased from 11 to 31 by zero-filling followed by 3D DFT, yielding the EAP. Finally, the results of the magnitude and real-valued data were compared by projecting the EAP onto the axial, coronal, and sagittal planes.

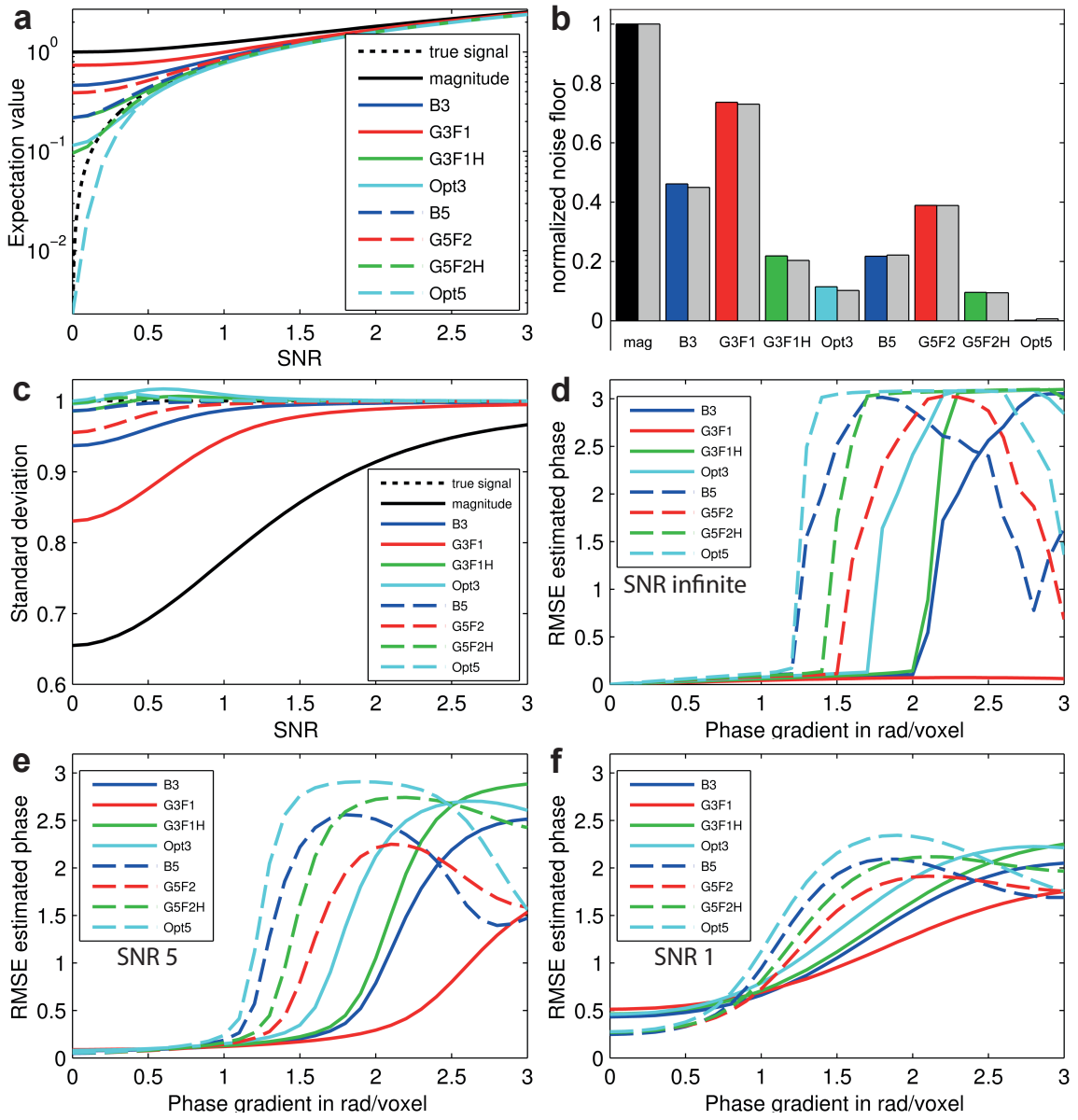


Figure 4.4.: Results of Monte Carlo simulations for evaluating bias reduction and vulnerability to local phase variations of the kernel-based PC: a: Logarithmic plot of the expectation values of magnitude and real-valued data versus SNR. Data are normalized by the expectation value of the magnitude data at zero true signal; b: Bar plot showing the expectation value of the noise floor (true signal is zero). Values are normalized by the expectation value of the magnitude data. The gray bars to the right are the averaged noise floors of ACQ1, derived for a small ribbon outside the brain in the FE direction; c: Standard deviations of magnitude and real-valued data versus SNR. The true SD of the added noise was 1; d–f: RMSEs of the estimated phases of different filter kernels versus the background phase gradient. Results are plotted for infinite SNR, SNR = 5, and SNR = 1.

## 4.3. Results

### 4.3.1. Simulations

Fig. 4.4 presents the simulation results of the magnitude and real-valued data using different phase filtering kernels. As anticipated, the expectation value of the real-valued data is lower than that of the magnitude data and closer to the true signal. The performance of the filtering kernels well agrees with the amount of remaining noise correlation. The expectation values begin diverging from the true signal at SNR $\approx 1.5$ for G3F1-filtered data, $\approx 1$ for B3 and G5F2 data, $\approx 0.5$ for B5 and G3F1H data, and $\approx 0.2$ for Opt3 and G5F2H data (Fig. 4.4a). Interestingly, the real-valued data filtered through Opt3, G5F2H, and particularly Opt5 are slightly negatively biased in the very low SNR regime. There are two opposing effects: the positive bias introduced by the remaining noise correlations and the false attenuation caused by the variance of the estimated phase. However, the negative bias is much smaller than the positive bias of the magnitude data. A major contributor to the DWI contrast is the level of the noise floor (Fig. 4.4b), defined as the expectation value of the true zero signals. The kernel B3 suggested by Prah et al. [131] reduces the noise floor to approximately $46\,\%$ of the magnitude data, while the G3F1H kernel with the same size reduces it to $21\,\%$. The optimized kernel Opt3 achieves $11\,\%$ of the nominal noise floor, indicating an almost fourfold improvement over B3. Finally, the perfectly decorrelated kernel Opt5 reduces the noise floor to almost zero. The gray bars to the right of the colored bars in Fig. 4.4b show the averaged noise floors of ACQ1, derived in a small ribbon outside the brain in FE direction. The very good agreement with the simulated results proves that the MR scanner generates near-perfect Gaussian noise and validates the simulation assumptions. Fig. 4.4c plots the SDs of the magnitude and real-valued data at different SNR levels. In the low SNR regime, the remaining noise correlation leads to a Rician-shaped distribution with a reduced SD, except in highly decorrelated kernels such as Opt3 and Opt5. In these cases, the SD slightly increases under the increased variance of the filtered phase (as mentioned above).

In the second Monte Carlo simulation, the impact of local phase variations on the accuracy of PC was investigated at different SNR levels (infinite, 5, and 1). The RMSE of the estimated phase is plotted in Fig. 4.4d-f. Note, that $\pi$ is the highest possible RMSE of the estimated phase. Under infinite SNR conditions, PC performs very accurately up to a certain value of the phase gradient, after which it immediately breaks down. The threshold itself depends on multiple factors but is dominated by the kernel size. In general, size 3 kernels perform better than size 5 kernels. A hole filter further reduces the threshold as it discards some of the meaningful phase information; namely, the phase value of the central voxel. Moreover, Gaussian kernels perform better than boxcar kernels probably because they possess circular symmetry. Therefore, each voxel is weighted proportionally to its distance from the central voxel. The simulations at lower SNR (Fig. 4.4e,f) yielded smoother profiles but showed similar overall behavior. In summary, the approximate thresholds of B3 (and G3F1H), Opt3, and Opt5 are about $2\,\mathrm{rad}$, $1.7\,\mathrm{rad}$ and $1.2\,\mathrm{rad}$, respectively. Recalling the results of the bias analysis (Fig. 4.4a, b), the noise floors of kernels B3, G3F1H, Opt3, and Opt5 (relative to the magnitude data) range from almost zero to about $46\,\%$. To present an uncluttered analysis, hereafter the experimental explorations are limited to these four kernels.

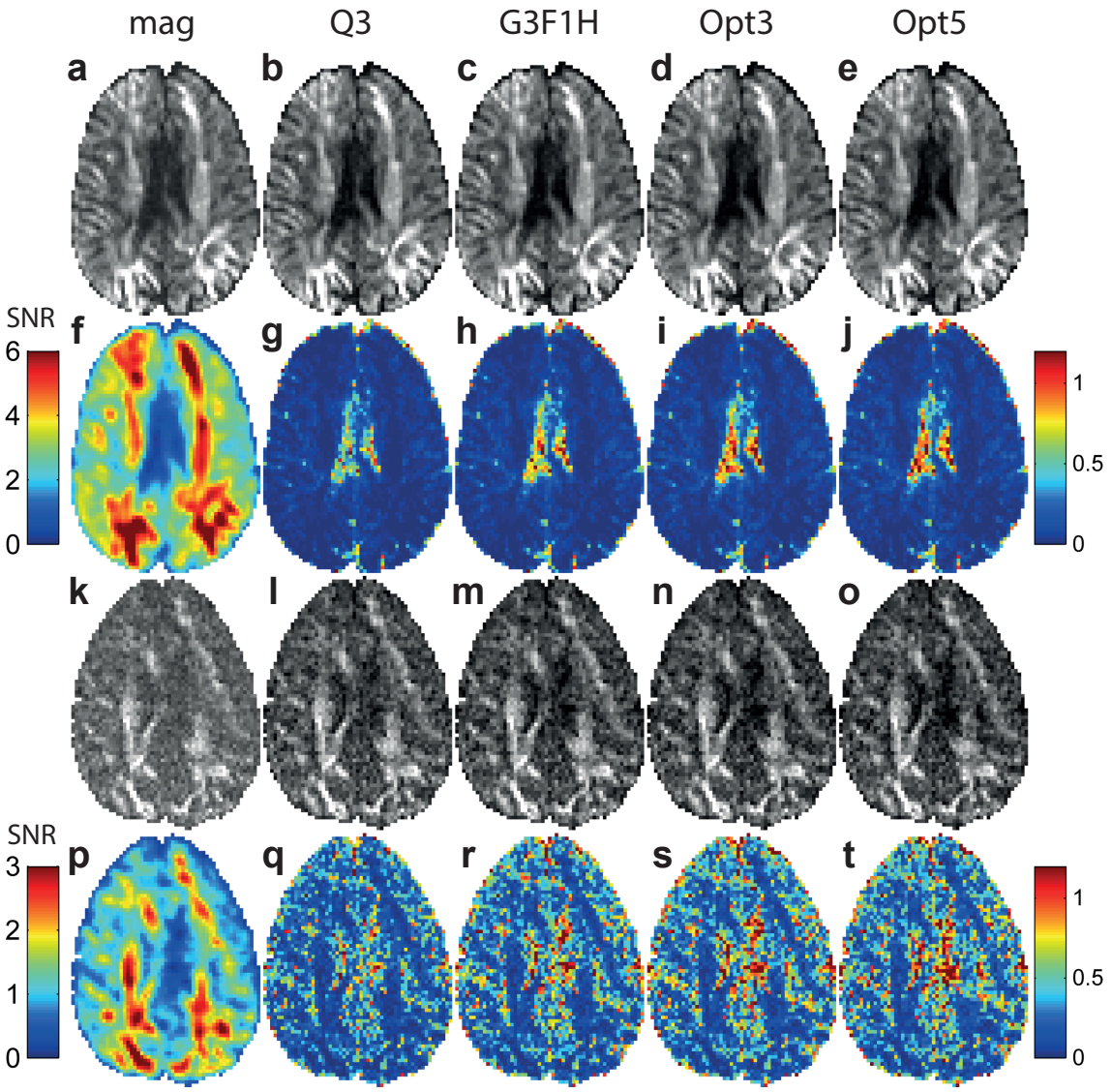


Figure 4.5.: Representative DWIs after PC. a–e: 10-fold average of a DWI with $b = 3000\,\mathrm{s\,mm^{-2}}$ from acquisition ACQ1, calculated from both magnitude and real-valued data for kernels B3, G3F1H, Opt3, and Opt5; f–i: ΔMR maps of b–e; j–n: 4-fold average of a DWI with $b = 8000\,\mathrm{s\,mm^{-2}}$ from acquisition ACQ2, calculated from both magnitude and real-valued data for kernels B3, G3F1H, Opt3, and Opt5; and o–r: ΔMR maps of k–n.

### 4.3.2. Volunteer experiments

Fig. 4.5 shows the averaged DWIs of ACQ1 and ACQ2, with b-values of $3000\,\mathrm{s\,mm^{-1}}$ and $8000\,\mathrm{s\,mm^{-1}}$, respectively, determined in both magnitude reconstruction and PC. It is important to note that averaging is not required for PC but is conducted only for visualizing the bias reduction. In ACQ1, some regions (particularly those containing CSF) appear darker in the PC DWIs (Fig. 4.5b–e) than in the magnitude DWIs (Fig. 4.5a). This is expected because the CSF signal rapidly decays with increasing $b$, reaching almost zero at $b = 3000\,\mathrm{s\,mm^{-1}}$. Further, the corresponding SNR map in Fig. 4.5f, indicates that the SNR in the CSF regions is very close to zero with the result that the Rician bias dominates (see Figs. 4.1 and 4.4). The bias reduction of our approach (especially in the CSF region) is demonstrated in the relative $\Delta$MR maps (Fig. 4.5f–i), defined as the difference between magnitude and real part after PC and divided by the magnitude. Consistent with the simulations, the intensity of the relative $\Delta$MR maps increases from kernel B3 to kernel Opt5. Similar trends are observed in ACQ2; here, however, the increased contrast in the DWIs (Fig. 4.5j–n) is even more significant, as the SNR is lowered by the longer TE and the higher b-value (Fig. 4.5m), increasing the proportion of the noise floor in the signal. Consequently, the relative $\Delta$MR maps exhibit much more complex patterns in ACQ2 (Fig. 4.5o–r) than in ACQ1.

A major problem of real-valued DWI is the unwanted signal loss arising from incorrect PC. For example, Fig. 4.6a shows a DWI from ACQ1 with a highly inhomogeneous phase profile (Fig. 4.6b). This phase pattern probably results from both pulsatile motion and a small left–right rotation of the subject's head during the diffusion encoding. Three regions with very high phase gradients are indicated by arrows. Within these regions, signal loss occurs in the real part (Fig. 4.6c), and bright spots appear in the relative $\Delta$MR maps (Fig. 4.6d). The phase gradient in the region marked with a yellow arrow (Fig. 4.6b) is approximately $2\,\mathrm{rad}$ per voxel. According to the simulations (Fig. reffig:PhaseCor4d–f), this gradient approximates the threshold level of B3 and G3F1H but is above that of Opt3 and Opt5. Consequently, the latter two kernels show the highest signal loss with Opt5 yielding by far the worst results. These errors are also evident in the imaginary part of the data (Fig. 4.6g), which exhibits obvious structure rather than pure noise. Outlier detection improves these results at both thresholds $\sigma_T = 2\sigma$ (Fig. 4.6f) and $\sigma_T = 2.5\sigma$ (Fig. 4.6g), where the pink areas indicate the regions of PC failure.

Fig. 4.7 maps the fraction of outliers across all DWIs. In general, there were fewer outliers in ACQ1 (Fig. 4.7b–i) than in ACQ2 (Fig. 4.7k–r) because of the lower SNR and the increased motion encoding in ACQ2. Overall, the number of outliers increased in the order B3 < G3F1H < Opt3 < Opt5, consistent with the simulation results. Typically, the outliers were concentrated in regions close to the ventricles, where intracranial pulsatility is likely to be highest. Even at the smaller threshold ($\sigma_T = 2\sigma$), the outlier fractions rarely exceeded $6\,\%$ for the most sensitive kernel Opt5. Therefore, this threshold was adopted in further analysis. Additional outlier maps using PC with filtering kernel Opt3 and $\sigma_T = 2\sigma$, showing all slices of ACQ1 and ACQ2 as well as a third data set with full brain coverage, can be found in Appendix A.1.

Besides analyzing the performance of PC on the actual DWI data, we also investigated the effect of PC on the estimation of DKI metrics. Panels a–e of Fig. 4.8 compare the MZ maps of the magnitude and real-valued data in the slices shown in Fig. 4.7a–i. Despite the

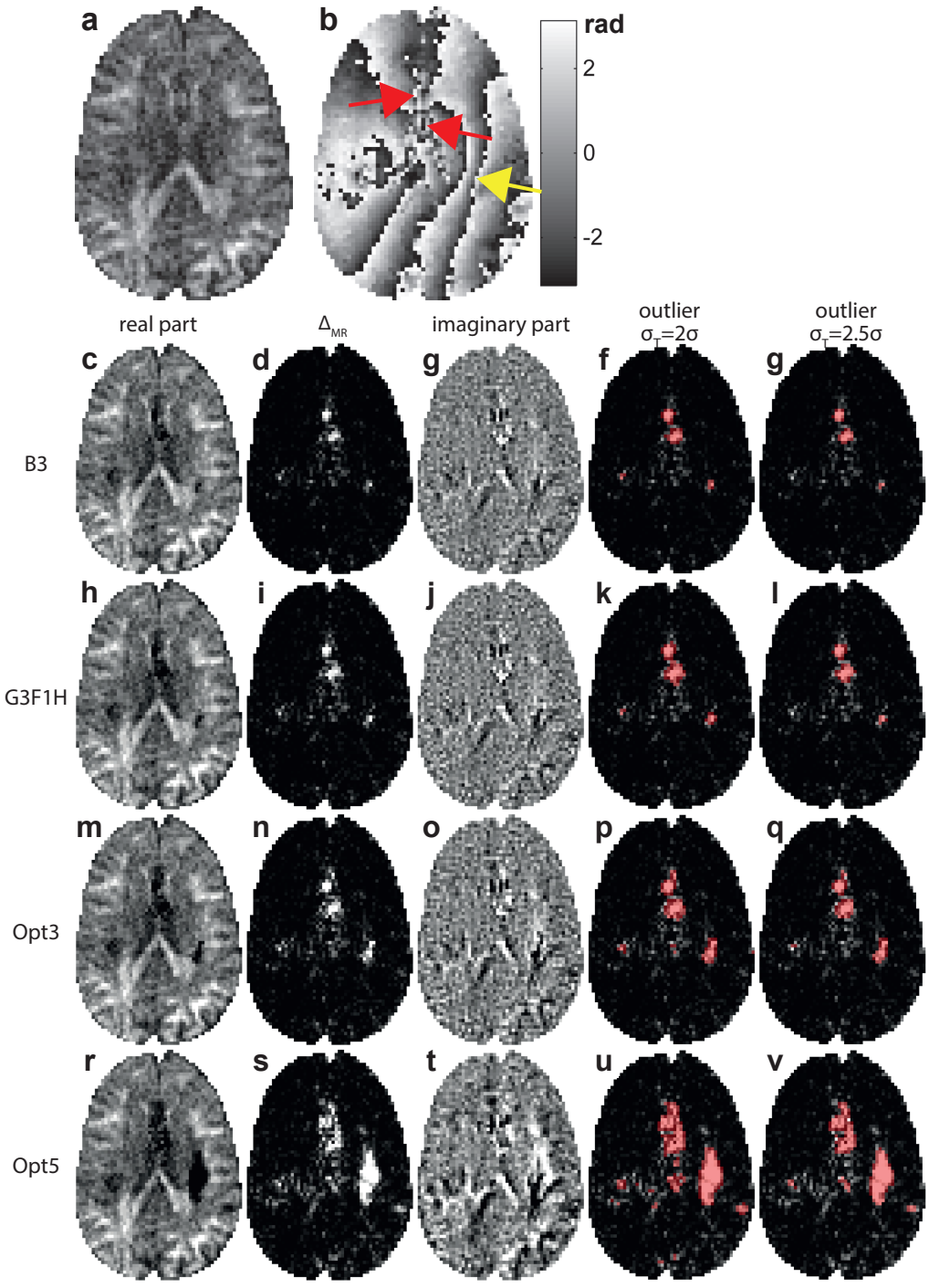


Figure 4.6.: Representative DWI with $b = 3000\,\mathrm{s\,mm^{-2}}$ from ACQ1, exhibiting very strong phase inhomogeneity. PC was conducted for kernels B3, G3F1H, Opt3, and Opt5: a: DWI magnitude; b: DWI phase; c, h, m, and r: Real part of the PC data; d, h, m, and r: corresponding ΔMR maps; g, j, o, and t: Imaginary part of the PC data; f, k, p, and u: Outliers marked in pink on smoothed ΔMR maps with $\sigma_T = 2\sigma$; g, l, q, and v: Outliers marked in pink on smoothed ΔMR maps with $\sigma_T = 2.5\sigma$.

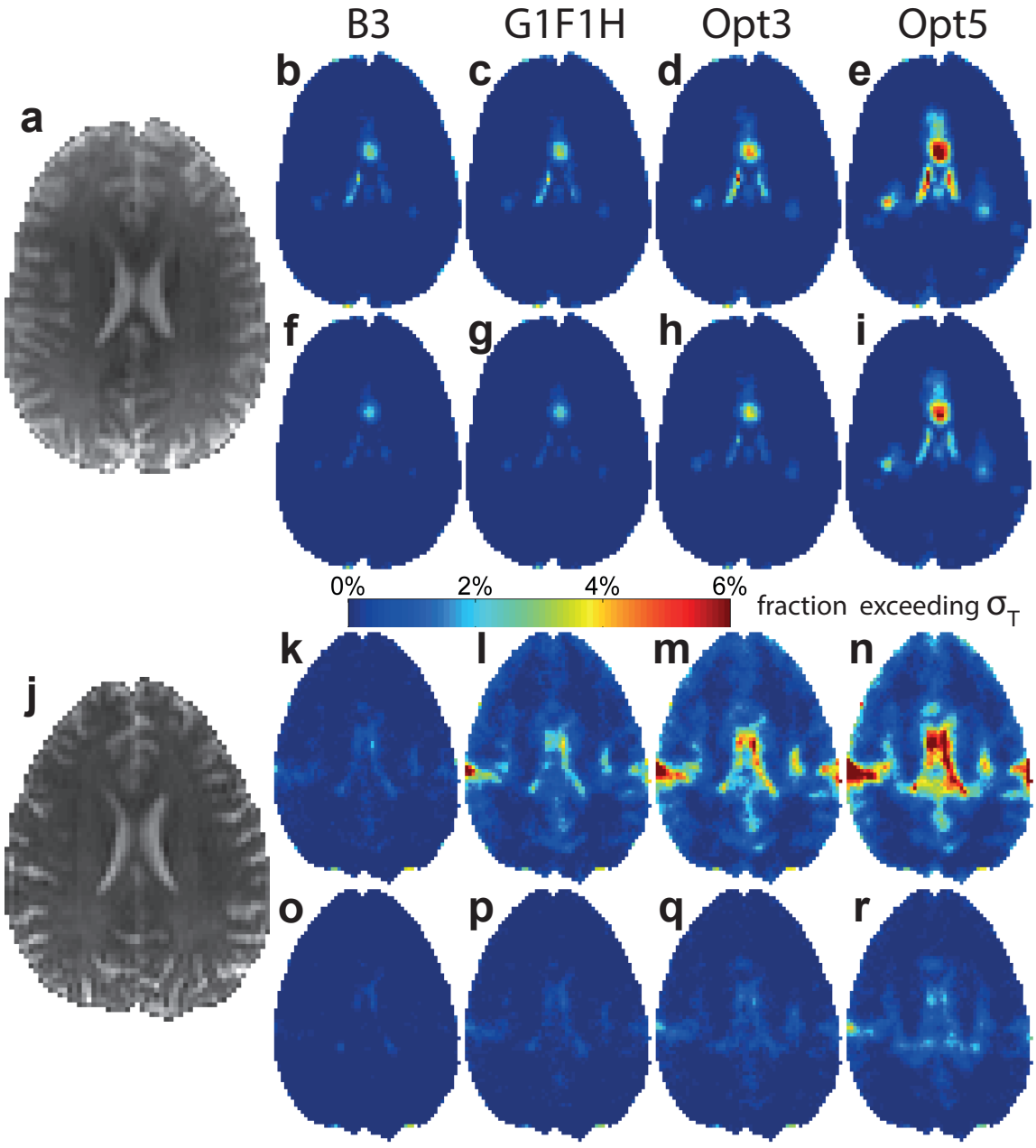


Figure 4.7.: Maps indicating the fraction of outliers exceeding threshold $\sigma_T$ among all DWIs for kernels B3, G3F1H, Opt3, and Opt5. The slices are those shown in Fig. 6. a–d: ACQ1, $\sigma_T = 2\sigma$; e–h: ACQ1, $\sigma_T = 2.5\sigma$; i–l: ACQ2, $\sigma_T = 2\sigma$; and m–o: ACQ2, $\sigma_T = 2.5\sigma$.

fact, that there is no appropriate ground truth provided, difference maps between magnitude and PC reconstruction reveal some significant changes (Fig. 4.8f-i). MZ seems generally overestimated and overestimation increases toward the center of the image which is consistent with recent reports [71, 129]. This result is plausible as the sensitivity of the receiver coil reduces in the central regions, lowering the SNR. The CSF seems highly overestimated in the ventricles which is also in agreement with recent reports [71, 129]. Theoretically, the kurtosis in the ventricles should approximate zero as CSF is a liquid; thus, it should diffuse in a Gaussian manner. Besides the ventricles, two additional areas (marked with red arrows) appear to be heavily overestimated. Comparisons with Fig. 4.8a–i reveal that these spots correspond to larger numbers of PC outliers. Panels j–m of Fig. 4.8 present the same MZ maps but with the outlier data replaced by the magnitude data. As unveiled in the corresponding difference maps (Fig. 4.8n–q), the spots marked in Fig. 4.8f–i are introduced by incorrect PC rather than Rician bias. This indicates good performance of the outlier correction and the applicability of PC to highly sensitive diffusion metrics such as kurtosis. Comparing Fig. 4.8n–q, a steady increase in the difference maps from B3 to Opt5 can be observed, mirroring the reduced Rician bias. However we cannot exclude, that a small portion of the apparent overestimation of MZ (Fig. 4.8n–q) is still caused by remaining errors in PC.

Finally, the performance of PC is evaluated on the DSI data acquired in ACQ2. Fig. 4.9a presents a colored fractional anisotropy map in the coronal plane. This map plots the ODF in each voxel, thus revealing the fiber orientation. Fig. 4.9b displays the axial, coronal, and sagittal projections of the EAP at five representative voxels (labeled V1–V5 in Fig. 4.9a). Overall, the real-valued data exhibit broader probability distributions than the magnitude data. This is a direct result of the enhanced contrast in the real-valued DWIs. The fiber crossings in V1 (axial and coronal), V2 (coronal and sagittal), and V3 (axial) are barely recognizable in the magnitude image but are well resolved in the real-valued images. The orientation of the corpus callosum in V4 is also much clearer in the real-valued images. The EAP distribution of voxel V5 in the CSF is much narrower in the magnitude data because the rapidly decaying CSF signal in q-space is significantly broadened by the noise floor. Judging from the similar axial and coronal orientation of the EAP in V4 and V5 under Opt3 and Opt5, real-valued data also better resolve the partial volume effects compared with the magnitude data.

## 4.4. Discussion

Compared with the method of Prah et al. [131], decorrelated phase correction significantly reduces the Rician bias, whereas it only slightly increases the sensitivity to local phase variations. The major advantage of kernel-based PC is its simple computation. The method completes within seconds on a standard computer, even when processing numerous DWIs. PC is applied directly after the EPI reconstruction and is invulnerable to noise distribution changes in post-processing, such as motion correction or non-stationary noise introduced by parallel imaging. While Prah et al.'s [131] approach with a boxcar filter kernel reduces the positive noise floor to approximately $46\,\%$ of the magnitude data, the proposed decorrelated filter kernel Opt3 reduces it to approximately $11\,\%$. Using the larger filter kernel Opt5, almost zero noise floor was reached, but at the cost of additional outliers.

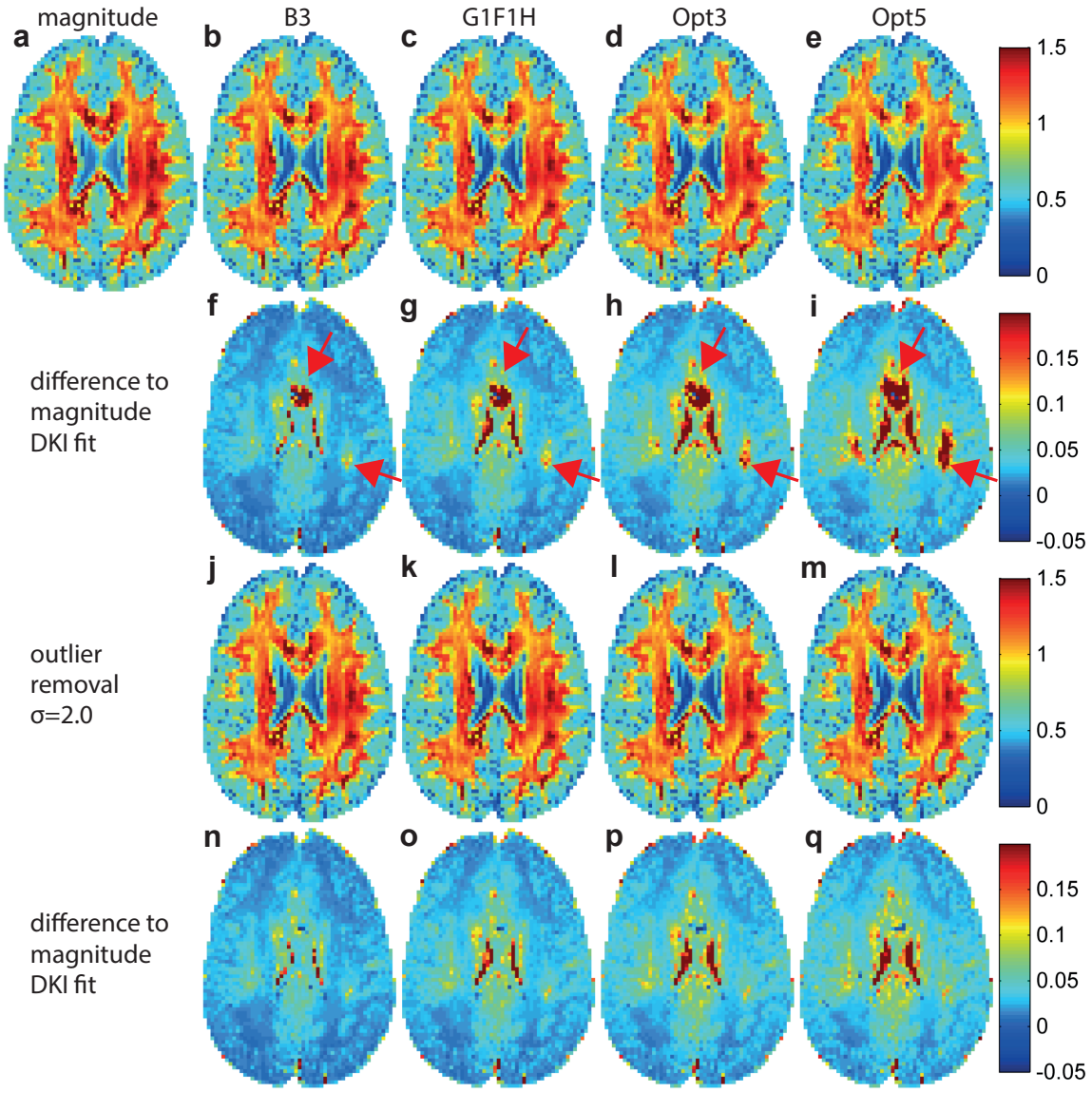


Figure 4.8.: a-e: Parametric MZ maps of the magnitude and real-valued data using kernels B3, G3F1H, Opt3, and Opt5. The slices are those shown in Figs. 6 and 7; f–i: MZ difference maps between magnitude and real-valued data; j–m: Parametric MZ maps of real-valued data with outlier replacement ($\sigma_T = 2\sigma$); n–q: MZ difference maps between magnitude data and real-valued data with outlier replacement ($\sigma_T = 2.5\sigma$).

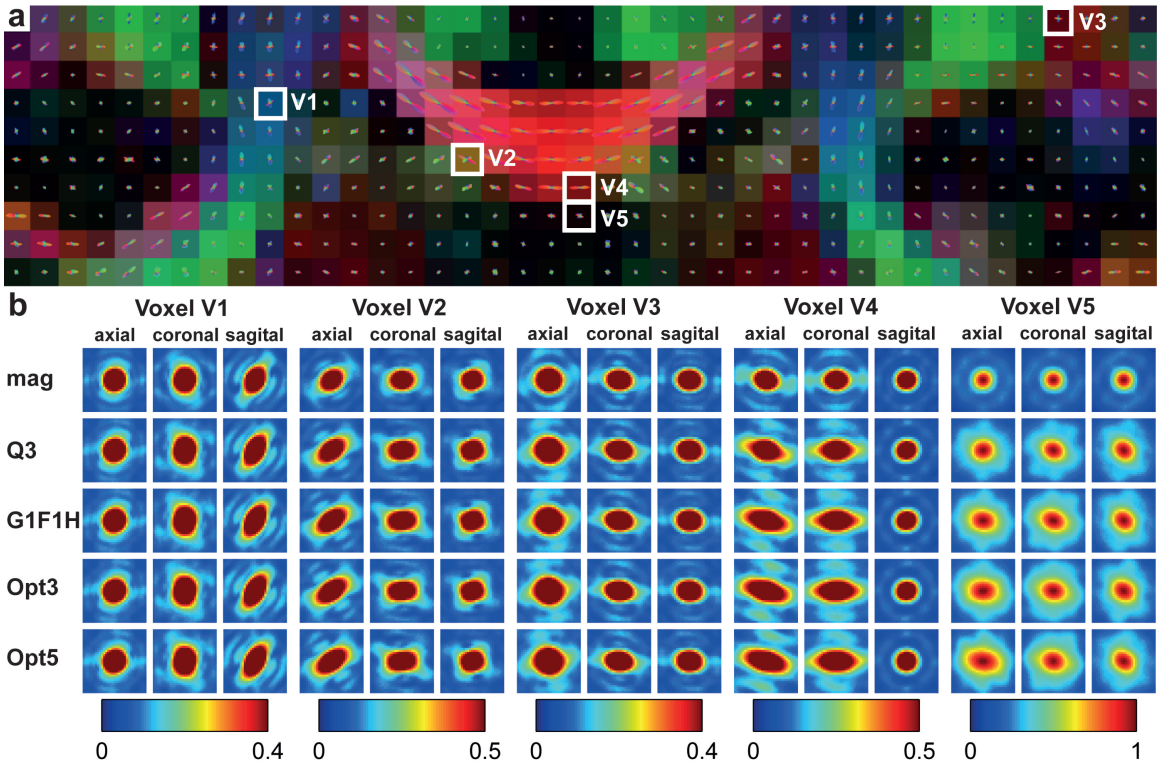


Figure 4.9.: a: FA map of a coronal slice of ACQ2. Fiber directions are indicated in the ODFs of each voxel. Five voxels (labeled V1–V5) are analyzed in detail. b: Projections of the absolute value of the EAP into the axial, coronal, and sagittal planes of voxels V1–V5, computed from magnitude and real-valued data using kernels B3, G3F1H, Opt3, Opt5, and outlier replacement ($\sigma_T = 2\sigma$).

This improvement was achieved by considering the noise correlations in the MR images, introduced by non-orthogonal transforms in the EPI processing pipeline. Consequently, the noise in each imaging voxel was correlated not only to itself but also to neighboring voxels. Because only linear transforms were employed, the object signal and the noise can be treated separately, and thus noise propagation was independent of the imaging object.

It is important to note that the decorrelated kernels Opt3 and Opt5 depend on the specific acquisition protocol and the specific EPI reconstruction chain. It was shown that resampling introduces noise correlations in FE direction and Partial Fourier in PE direction (see Fig. 4.2) while the odd/even correction and SENSE reconstruction have no impact on the local noise correlation. Using Monte Carlo simulations, a noise correlation pattern was computed and the optimized kernels were derived empirically such that small weights were assigned to highly correlated voxels and vice versa. However, the correlation pattern depends on the acquisition and reconstruction parameters and therefore the optimized kernels may need to be adapted to the individual case. Especially nonlinear partial Fourier reconstruction techniques (such as homodyne reconstruction [86], POCS [87]) and parallel imaging in k-space (e.g., GRAPPA [103]) may also have a significant impact on the correlation pattern. Nevertheless, reducing the weights of the center voxel of

the kernel, as well as of its direct neighbors, and increasing the weights of the diagonal neighbors seemed fairly general rules to reduce the bias.

The crucial challenge of PC is estimating the correct phase as errors lead to unwanted signal loss. However in recent studies, the impact of incorrect PC was not investigated in detail [131, 161]. In the present study, the influence of local phase gradients on the phase estimation accuracy was analyzed in Monte Carlo simulations. Phase estimation using a filter kernel proved highly robust, with no significant error, up to a certain threshold. Above this threshold, the phase estimation failed. In rare cases, failure of PC was also observed in the real data experiments ACQ1 and ACQ2, even under a size 3 kernel. To detect PC failure, a simple thresholding method was devised, based on smoothed $\Delta$MR maps. If a voxel in these maps exceeds a certain threshold $\sigma_T$, defined as a multiple of the global noise amplitude $\sigma$, it is considered an outlier. The fraction of the outliers among all DWIs was generally small but very spatially inhomogeneous. Outliers tended to be concentrated in small clusters, especially in regions close to the ventricles. Therefore it seems very likely that PC failure primarily occurs by motion encoding of intracranial pulsatility, which generates phase gradients exceeding the tolerance of the filter kernels. However, even for the perfectly decorrelated kernel Opt5, the outlier fraction in these regions never significantly exceeded $6\,\%$. In all voxels exceeding the threshold, the real value was replaced by the magnitude. There are two potential drawbacks when using the magnitude for outlier voxels, since the absolute value operation introduces a positive bias. On the one hand, incorrect phase estimation may be more pronounced in certain diffusion encoding directions resulting in an angular inhomogeneous noise bias and potentially false anisotropy measures. On the other hand, the noise bias may be spatially inhomogeneous across the image volume since incorrect phase estimation occurs more often in specific regions of the brain, e.g. next to the ventricles. However, it is important to note, that not replacing the real value by the magnitude, would cause a negative signal bias due to incorrect PC resulting in a much higher angular and spatial inhomogeneity. Even applying PC with the most robust kernels, e.g. size 3 boxcar or size 3 Gaussian, rather than using the magnitude seemed not favorable as there was still a remaining signal loss in some cases. Moreover among the detected outliers, there were many voxels having a SNR not prone to Rician bias whereas an error in PC may cause a severe underestimation of the signal. In conclusion, it seems that the magnitude replacement is so far the best method to handle potential outlier voxels.

There are two major benefits of real-valued data: more accurate fitting of diffusion models and increased contrast of DWIs in the low SNR regime. In this study, the former was demonstrated on the DKI model, which is highly vulnerable to Rician bias [68]. Although WLLS estimators are popular for their low computational cost, they are unsuitable for exponential models and real-valued data because the log transform of negative values is undefined. Consequently, we adopted an NLS estimator [163], which directly handles real-valued data and fully exploits the PC technique. The results are consistent with those of previous studies [68, 71], indicating that the AKC was overestimated due to Rician bias contributions. The AKC was reduced by NLS fitting of the PC data, particularly in the center of the brain where the SNR is minimized. However, in certain small regions of PC failure, the AKC was erroneously underestimated by the use of real-valued data. These regions matched those marked by the outlier detection. By replacing the values of all outlier voxels by their magnitudes, the erroneous underestimation of MZ could be eliminated.

The influence of PC data on the EAP was investigated using DSI data. The reduction of the noise floor in the DWIs resulted in a broadening of the EAP and increased angular resolution. Fiber crossings that were at most barely visible in the EAP of the magnitude data were better delineated in the real-valued data, and the delineation improved as the noise floor was lowered. Moreover, truncation artifacts in the EAP due the limited support of the discrete q-space signal were reduced by PC in some cases (especially CSF voxels). However, some advantages of the real-valued data were sacrificed because the magnitude of the EAP was computed in the last processing step as the EAP still contained a significant portion of negative signal after DFT due truncation effects. Windowing functions such as the Hanning filter could be applied prior to DFT to reduce these artifacts [63], but this would also blur the EAP. Thus, more sophisticated EAP reconstruction techniques, such as deconvolution [80], compressed sensing [126], and constrained spherical polar Fourier expansion [165], may realize the full potential of real-valued data.

Recent advances in Simultaneous Multi-Slice (SMS) have almost tripled the number of DWIs acquired per unit time (see also section 5). However, SMS increases the $T_1$ saturation and the g-factor penalty of parallel imaging [22, 23], thereby reducing the SNR of single DWIs (see Fig. 5.11 in section 5). Furthermore, the Human connectome project has set new standards in terms of image resolution pushing it to $1.5\,\mathrm{mm}$ and below [106, 166] which also significantly reduce the SNR per DWI. The greatest benefits of PC can be expected in the low SNR regime, where real-valued data significantly reduce the noise floor and increase the dynamic range. For the same reason, real-valued data increase the usefulness of higher b-values, allowing deeper insights into tissue microstructure.

# 5. Comparison of the SNR efficiency of Diffusion weighted Imaging sequences

The content presented in this chapter is based in parts on the master thesis of Benjamin Fürsich, entitled "Investigating the Applicability of Diffusion Weighted Steady State Free Precession MRI Pulse Sequences in Neuro-Imaging" which was supervised during the work on this dissertation [167]. The work of Benjamin Fürsich, however, was substantially extended by a novel DWSSFP signal model and comprehensive simulations. A journal paper of this work is in preparation.

## 5.1. Introduction

As mentioned in previous chapters, the data acquisition in DWI is most commonly based on a ST diffusion preparation [48] and a subsequent single-shot 2D EPI readout. Although commercially available, in vivo MRI scanners feature high performance gradients systems with a maximal gradient strength of up to $80\,\mathrm{mT\,m^{-1}}$ per axis, the diffusion encoding still requires a significant portion of time. As a result, DWIs often suffer from low SNR because the images are not only diffusion weighted but also heavily $T_2$ weighted due to a long TE. Significant efforts have been made to further improve the gradient hardware and the receive coils to increase the SNR [106, 166].

An alternative approach is the use of new diffusion weighted pulse sequences which sample the Magnetic Resonance (MR) signal more efficiently and, therefore, improve the SNR per unit time compared to a ST preparation with a 2D EPI readout. One option is the increase of the simultaneously excited volume and the use of a segmented k-space readout rather than a single shot trajectory. In this case, a larger amount of spins share the time consuming ST preparation and the image volume is constructed from multiple Fourier encoded segments. Unfortunately, the diffusion preparation does not only encode the incoherent motion of the spins as an attenuation of the signal's amplitude, but also encodes the coherent motion as a shift in the signal's phase (see section 2.2). Therefore, bulk motion and the intrinsic pulsatility of the brain cause a complex, individual phase pattern in image space for each diffusion preparation (see section 6). As a result, different k-space segments can exhibit phase inconsistencies resulting in signal loss when the segments are jointly reconstructed. Recently, three techniques have been proposed to overcome this problem.

In Simultaneous Multi-Slice Echo Planar Imaging (SMS-EPI), several spatially separated slices are excited simultaneously, using a multiband excitation pulse followed by a ST preparation and a single shot 2D EPI readout [168]. The signal originating from the different slices is separated using parallel imaging reconstruction techniques [22, 26, 103]. A second method is called Multi-Slab Echo Planar Imaging (MS-EPI), where a slab of several consecutive slices is excited and a 3D segmented k-space encoding scheme is used to sam-

ple the data [24, 169, 170]. A 2D phase navigator is acquired to correct for phase variations between the different k-space segments.

A third technique, called DWSSFP, uses a different type of diffusion preparation, based on the rapid application of RF-pulses and diffusion weighting gradient pulses, resulting in a steady-state of the signal [171, 172]. Promising results have been reported in vivo and particularly ex vivo with excellent detection of anisotropy and improved SNR over conventional 2D EPI [25, 173–178].

All three techniques have large potential to improve the SNR efficiency of DWI but they are also accompanied by several disadvantages. For example, unaliasing the simultaneously excited slices in SMS-EPI can cause g-factor penalties and, therefore, the acceleration factor in slice direction is limited [23]. MS-EPI suffers from slab boundary effects due to imperfect RF-pulses [27] and DWSSFP has to deal with motion induced phase errors [25].

To weigh the pros and cons of the different techniques, a comparison of the expectable SNR efficiency is needed. In this study, a framework is provided to analyze the SNR efficiency of the different DWI sequences with respect to conventional 2D EPI. This framework is applied to a typical DWI setup assuming typical relaxation times for WM and GM as well as state of the art scanner hardware. In recent studies, individual techniques, such as SMS-EPI [23] or MS-EPI [179] were compared with conventional 2D EPI. However, a general analysis of the SNR efficiency of all mentioned sequences for a whole brain DWI acquisition and a wide range of resolutions and b-values is missing.

Moreover, the signal model of a pulsed DWSSFP sequence is investigated in depth as it is a requirement for an accurate comparison of the SNR efficiency. Quantifying diffusion using DWSSFP is challenging because in contrast to the ST diffusion preparation, the signal model of DWSSFP is highly complex, even when assuming nonrestricted Gaussian diffusion. The signal can be described as the sum of multiple Coherence Pathways (CPs) where each CP has a well defined b-value [180]. Unfortunately, the contribution of each CP to the overall signal depends on the relaxation parameters $T_1$ and $T_2$ as well as on the sequence parameters TR and flip angle. Nevertheless, the quantification of the ADC has been reported, either by additional mapping of $T_1$ and $T_2$ [174, 177, 178, 181] or by using the double-echo approach [182].

Kaiser et al. [171] derived the first analytical solution describing the diffusion sensitivity of DWSSFP assuming a constant gradient and nonrestricted Gaussian diffusion. This solution is represented by a Fourier integral that is further simplified by the assumption of symmetric Fourier coefficients. Wu and Buxton generalized the model of Kaiser et al. to the case of pulsed gradients [172]. However, Freed et al. reported that the assumption of symmetric Fourier coefficients can lead to a highly inaccurate description of the signal [183], particularly for short TRs and low flip angles [177, 183]. Therefore, Freed et al. derived an accurate solution accounting for the correct coupling between positive and negative Fourier modes. However, constant gradients were assumed again. To use the model of Freed et al., the pulsed gradient were approximated by a constant gradient with the same gradient area per TR [177]. In addition, a completely different approach, the two-transverse approximation, was reported by Buxton, where only CPs with two periods in the transverse plane are considered to contribute to the signal [181].

None of the described models is capable of calculating the accurate solution for the pulsed DWSSFP sequence because either the coupling between positive and negative Fourier modes is not accounted for correctly or the pulsed gradient is approximated by a

constant gradient. It was also noted in a recent DWSSFP review paper that "the issue of accuracy of the Kaiser model in vivo has not been explored in depth" [180]. In this work, the error of each model is investigated for recently reported in vivo and ex vivo imaging scenarios using Random Walk Simulation (RWS) as ground truth. Moreover, an accurate signal model is presented by combining the approaches of Wu and Buxton [172] and Freed et al. [183].

## 5.2. Theory and Methods

### 5.2.1. Analytic Models of a Diffusion-Weighted Steady State Free Precession Sequence

In contrast to the ST preparation where the signal is spoiled after each TR (Fig. 5.1a), the signal model of DWSSFP uses a steady state of the magnetization. In Fig. 5.1b, the signal curve of a DWSSFP sequence is shown for two successive TR intervals. The DWSSFP features two different signal components, one immediately after the RF pulse, called $S_{FID}$, and one right before the RF pulse, called $S_{echo}$, where both components are separated by the diffusion weighting gradient. $S_{FID}$ decreases with $T_2^*$, whereas $S_{echo}$ typically increases as it is being refocused—$T_2$ decay and the refocusing of the static background field effects work against each other where the refocusing effect usually dominates. Although the $S_{FID}$ signal is generally higher, it has lower sensitivity to diffusion [181]. Consequently, $S_{echo}$ is used in diffusion experiments. Note that it is not possible to reduce the amplitude of the diffusion gradient to zero to receive a non-diffusion-weighted signal because $S_{FID}$ and $S_{echo}$ would overlap in this case resulting in a bSSFP sequence (see section 2.3.2).

Modeling the DWSSFP signal is substantially more complex compared to the ST preparation. $S_{echo}$ is a superposition of multiple SE and STE, which can be described by the theory of CPs [90]. The diffusion sensitivity of each CP can be calculated with the theory of Stejskal and Tanner [48], using the corresponding mixing time $\Delta$ of the CP as well as the amplitude $G$ of the diffusion encoding gradient and its duration $\tau$. Also CPs with multiple consecutive ST preparations are possible and the diffusion effects add up. Unfortunately, the contribution of each CP to $S_{echo}$ depends on the relaxation times $T_1$ and $T_2$ of the underlying tissue. As a result, the diffusion sensitivity is a function of the diffusion gradient parameters $G$ and $\tau$, the sequence parameters TR and flip angle $\alpha$ as well as the relaxation times $T_1$ and $T_2$, making the conventional b-value concept inapplicable.

#### The model of Kaiser et al.

Kaiser et al. [171] derived the first analytical solution for the DWSSFP signal in the presence of a constant magnetic field gradient by solving the Bloch–Torrey equations (see section 2.2.2) [38, 45]. This model is referred herein as the KBE model. Assuming Gaussian diffusion, the general solution can be written as a Fourier series with symmetric Fourier

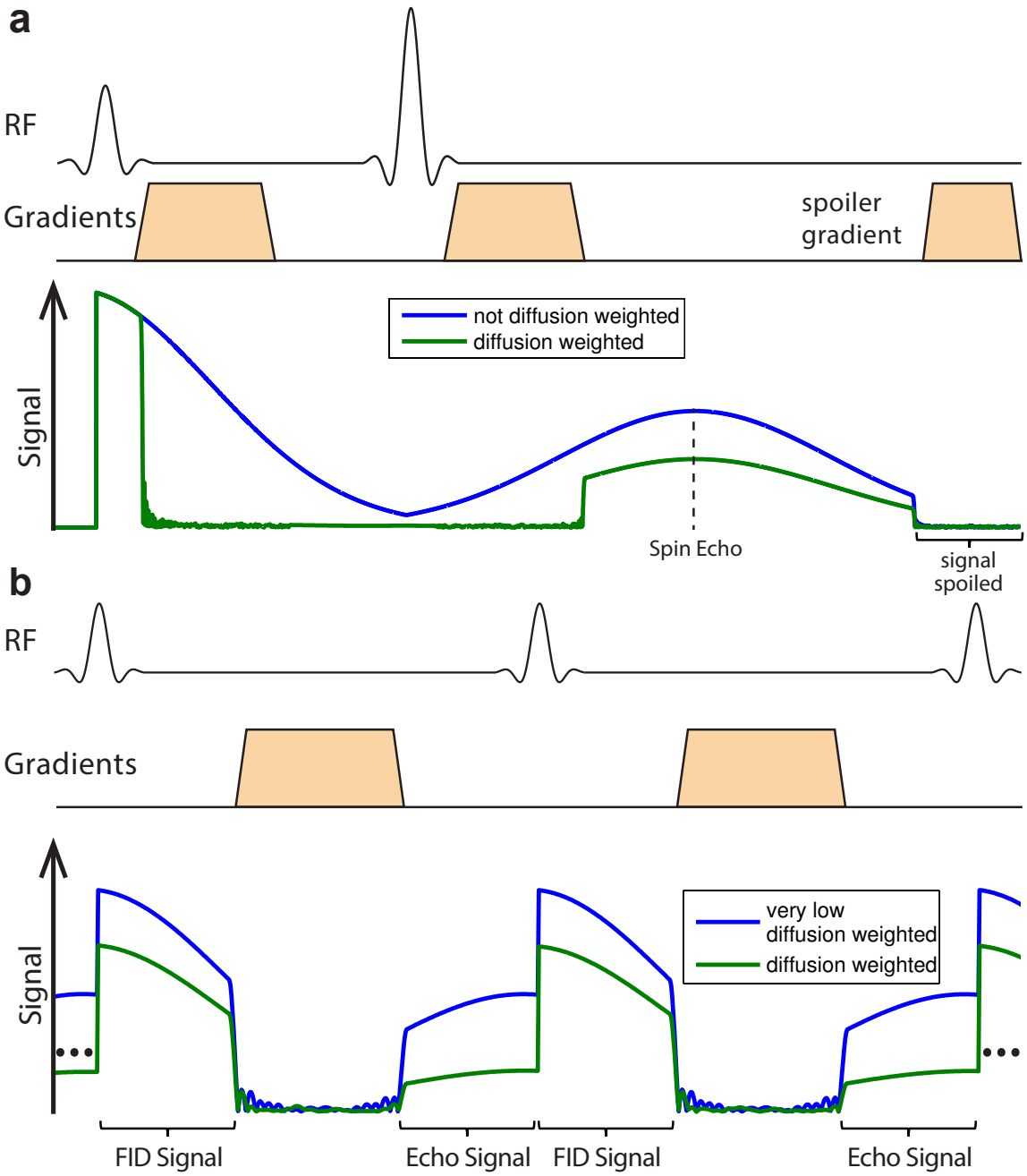


Figure 5.1.: Sequence diagram and signal evolution of **a**: the ST diffusion preparation, and **b**: the DWSSFP. No imaging gradients are shown.

coefficients.

$$M_x(\theta,t) = -\sum_{k=-\infty}^{+\infty} b_k E_{2,k}(t)\sin\left[\left(k+\frac{t}{\mathrm{TR}}\right)\theta\right] \tag{5.1}$$

$$M_y(\theta,t) = \sum_{k=-\infty}^{+\infty} b_k E_{2,k}(t)\cos\left[\left(k+\frac{t}{\mathrm{TR}}\right)\theta\right] \tag{5.2}$$

$$M_z(\theta,t) = M_0 + \sum_{k=-\infty}^{+\infty} c_k E_{1,k}(t)\cos k\theta \tag{5.3}$$

The damping terms $E_{1,k}(t)$ and $E_{2,k}(t)$ are defined as

$$E_{1,k}(t) = \exp\left(-\frac{t}{T1}-\frac{1}{3}Dg^2\gamma^2(\mathrm{TR})^2k^2t\right)\ , \tag{5.4}$$

$$E_{2,k}(t) = \exp\left(-\frac{t}{T2}-\frac{1}{3}Dg^2\gamma^2(\mathrm{TR})^3\left[3k^2\frac{t}{\mathrm{TR}}+3k\left(\frac{t}{\mathrm{TR}}\right)^2+\left(\frac{t}{\mathrm{TR}}\right)^3\right]\right)\ , \tag{5.5}$$

where $b_k$ and $c_k$ are the corresponding Fourier coefficients to the Fourier mode $k$, $\theta$ is the precession angle over one TR, and $g$ is the amplitude of the constant gradient. In practical imaging conditions, the voxel size is typically in the millimeter range and the diffusion weighting gradient is sufficiently strong to uniformly distribute the precession angle $\theta$ from 0 to $2\pi$ [172, 184]. Furthermore, typically only $S_{FID}$ ($t = 0$) and $S_{echo}$ ($t = TR$) are of interest because at all other times the signal is additionally dephased by the diffusion weighting gradient. Evaluating Eqs. 5.1 and 5.2 using the assumptions of practical imaging conditions results in

$$S_{FID,KBE} = \frac{1}{2\pi}\int_0^{2\pi} M_y(\theta,0)\,d\theta = b_0\ , \tag{5.6}$$

$$S_{echo,KBE} = \frac{1}{2\pi}\int_0^{2\pi} M_y(\theta,\mathrm{TR})\,d\theta = b_1E_{2,k}(t)\ . \tag{5.7}$$

Note that the integral over $M_x(\theta,0)$ and $M_x(\theta,\mathrm{TR})$ from 0 to $2\pi$ is zero for all coefficients $b_k$ and, therefore, only $M_y(\theta,0)$ and $M_y(\theta,\mathrm{TR})$ contributes to $S_{FID}$ and $S_{echo}$ respectively. The phases of $S_{FID}$ and $S_{echo}$ depend on the orientation of the $B_1$ field in the rotating reference frame, or in other words, the phase of the RF pulse. In this example, $B_1$ points to the x direction. For clarity, the description of all signal models investigated in this study are restricted to $S_{FID}$ and $S_{echo}$, where the additional index denotes the name of the model.

It is described in [171], that the Fourier coefficients $b_k$ can be calculated by a recursion equation assuming that the positive and negative modes decay equally in the presence of diffusion. Solving this recursion equation (not shown, see [171]) yields the coefficients $b_{-1}$ and $b_0$

$$b_0 = \frac{M_0\big(1-E_{1,0}(\mathrm{TR})\big)\big(1-F_1E_{2,-2}(\mathrm{TR})\big)\sin\alpha}{(r-F_1s)} \tag{5.8}$$

$$b_{-1} = \frac{M_0\big(1-E_{1,0}(\mathrm{TR})\big)\big(F_1-E_{2,0}(\mathrm{TR})\big)\sin\alpha}{(r-F_1s)} \tag{5.9}$$

where

$$r = 1 - E_{1,0}(\mathrm{TR})\cos\alpha + E_{2,0}(\mathrm{TR})E_{2,-1}(\mathrm{TR})\big(\cos\alpha - E_{1,0}(\mathrm{TR})\big) \ , \tag{5.10}$$

$$s = E_{2,-2}(\mathrm{TR})\big(1 - E_{1,0}(\mathrm{TR})\cos\alpha\big) + E_{2,-1}\big(\cos\alpha - E_{1,0}(\mathrm{TR})\big) \ , \tag{5.11}$$

and

$$F_1 = K - \sqrt{K^2 - L} \tag{5.12}$$

with

$$K = \frac{1 - E_{1,1}(\mathrm{TR})\cos\alpha - E_{2,0}(\mathrm{TR})E_{2,-1}(\mathrm{TR})\big(E_{1,1}(\mathrm{TR}) - \cos\alpha\big)}{E_{2,-2}(\mathrm{TR})(\cos\alpha + 1)(1 - E_{1,1}(\mathrm{TR})} \ , \tag{5.13}$$

$$L = \frac{E_{2,0}(\mathrm{TR})}{E_{2,-2}(\mathrm{TR})} \ . \tag{5.14}$$

Eqs. 5.6–5.14 present a fairly complex but easy to compute closed form solution of the KBE model yielding $S_{FID,KBE}$ and $S_{echo,KBE}$.

**The model of Wu and Buxton**

Wu and Buxton generalized the KBE approach to pulsed gradients [172]. This model is referred herein as the WB model. At time $\epsilon$ after each RF-pulse, a gradient pulse of amplitude $G$ and duration $\tau$ is applied. In the derivation of Wu and Buxton, the TR is divided into three segments: segment one is $t = [0..\epsilon]$, segment two is $t = [\epsilon..\epsilon + \tau]$, and segment three is $t = [\epsilon + \tau..\mathrm{TR}]$. Continuity constraints are imposed at the boundaries of each segment to derive a solution similar to the KBE model. It is shown in [172] that $S_{FID,WB}$ and $S_{echo,WB}$ equal

$$S_{FID,KBE} = b_{0,WB} \ , \tag{5.15}$$

$$S_{echo,KBE} = b_{-1,WB}E^{WB}_{2,k}(\mathrm{TR}) \ , \tag{5.16}$$

where

$$E^{WB}_{1,k}(t) = \exp\Big(-\frac{t}{T_1} - D(\gamma\tau G)^2k^2t\Big) \tag{5.17}$$

$$E^{WB}_{2,k}(t) = H_{2,k}\exp\Big(-\frac{t}{T_2} - D(\gamma\tau G)^2(k+1)^2t\Big) \tag{5.18}$$

$$H_{2,k} = \exp\Big(D(\gamma\tau G)^2[\tau(k + \frac{2}{3}) + \epsilon(2k+1)]\Big) \tag{5.19}$$

The calculation of $b_{-1,WB}$ and $b_{0,WB}$ is identical to the KBE model but the damping terms $E^{WB}_{1,k}(\mathrm{TR})$ and $E^{WB}_{2,k}(\mathrm{TR})$ must be used instead of $E_{1,k}(t)$ and $E_{2,k}(t)$ for Eqs. 5.6–5.14. The full derivation of the WB model can be found in [172] and a simplified solution for $\epsilon = 0$ in [181].

**The model of Freed et al.**

Freed et al. reported that the assumption of the symmetry for the Fourier coefficients $b_k$ is wrong [183] and leads to significant errors at low $\alpha$ and short TRs. Thus, a different recursion equation was derived to account for the correct coupling between positive and negative Fourier modes. This model is referred to as FR model. Like the KBE model, the FR model assumes a constant gradient with the amplitude $g$. According to [183], $S_{FID,FR}$ and $S_{echo,FR}$ are given by

$$S_{FID,FR} = b_{0,FR} \ , \tag{5.20}$$

$$S_{echo,FR} = b_{-1,FR} E_{2,k}(TR) \ . \tag{5.21}$$

The damping terms $E_{1,k}(t)$ and $E_{2,k}(t)$ are identical with the KBE model but the Fourier coefficients $b_{k,FR}$ and are computed using a different recursion equation. Solving this recursion equation (not shown, details can be found in [183]), yields the new coefficients $b_{-1,FR}$ and $b_{0,FR}$

$$b_{0,FR} = \frac{-\sin\alpha M_0\big(1 - E_{1,0}(TR)\big)}{A_{k=0} + E_{2,-1}(TR) C_{k=0} r_1} \ , \tag{5.22}$$

$$b_{-1,FR} = -r_1 b_{0,FR} \ , \tag{5.23}$$

where

$$A_k = \frac{1}{2}\big(E_{1,0}(TR) - 1\big)\big(1 + \cos\alpha\big) \ , \tag{5.24}$$

$$B_k = \frac{1}{2}\big(E_{1,0}(TR) + 1\big)\big(1 - \cos\alpha\big) \ , \tag{5.25}$$

$$C_k = A_k + B_k \ . \tag{5.26}$$

The term $r_1$ is given in a truncated continued fraction notation

$$r_1 = \frac{x_1}{E_{2,-1}(TR) B_{k=0}} + \frac{E_{2,0}(TR) C_{k=1}}{B_{k=1}} \tag{5.27}$$

where $x_1$ is the truncated continued fraction

$$x_1 = \cfrac{n_1}{d_1 + \cfrac{n_2}{d_2 ... + \cfrac{n_l}{d_l + e_l}}} \ , \tag{5.28}$$

with $n_k$ is the numerator

$$n_k = \frac{-E_{2,-k}(TR) E_{2,k-1}(TR) A_k^2 B_{k-1}}{B_k} \ , \tag{5.29}$$

$d_k$ is the denominator

$$d_k = \big(A_k - B_k\big) + \frac{E_{2,-k-1}(TR) E_{2,k}(TR) B_k C_{k+1}}{B_{k+1}} \tag{5.30}$$

and $e_k$ is the extra term

$$e_k = -\frac{E_{2,k}(TR) E_{2,-k-1}(TR) B_k C_{k+1}}{B_{k+1}} \ . \tag{5.31}$$

In agreement with [177, 183], the truncation of Eq. 5.28 at $l = 6$ resulted in a very accurate estimate of $x_1$ up to several decimal places.

**Combining the KBE, WB, and FR models**

With the generalization of the KBE model to pulsed gradients, Wu and Buxton introduced the new damping terms $E_{1,k}^{\text{WB}}(\text{TR})$ and $E_{2,k}^{\text{WB}}(\text{TR})$ to account for the length $\tau$, amplitude $G$, and the position $\epsilon$ of the gradient pulse [172]. On the other hand, Freed et al. derived a different recursion equation to account for the correct coupling between the positive and negative Fourier modes [183]. Both improvements are independent of each other. Consequently, it seems natural to combine both approaches, i.e. solving the recursion equation derived from Freed et al. with the damping terms suggested by Wu and Buxton. This newly proposed model is referred to as the KWF model where $\text{S}_{\text{FID,KWF}}$ and $\text{S}_{\text{echo,FR}}$ are given by

$$\text{S}_{\text{FID,KWF}} = b_{0,\text{KWF}} \ , \tag{5.32}$$

$$\text{S}_{\text{echo,KWF}} = b_{-1,\text{KWF}} E_{2,k}^{\text{WB}} \ . \tag{5.33}$$

The coefficients $b_{0,\text{KWF}}$ and $b_{-1,\text{KWF}}$ can be calculated with Eqs. 5.22–5.33 but using the damping terms $E_{1,k}^{\text{WB}}$ and $E_{2,k}^{\text{WB}}$. The complete model is presented in appendix A.2.

**The two-transverse periods approximation**

Buxton derived a fairly simple approximation for $\text{S}_{\text{echo}}$ based on a partition analysis, referred to as the 2TP model [181]. Assuming that the main contribution to $\text{S}_{\text{echo}}$ results primarily from CPs having only two transverse periods, $\text{S}_{\text{echo,2TP}}$ can be calculated as

$$S_{\text{echo,2TP}} = M_{\text{SE}} + M_{\text{STE}} \ , \tag{5.34}$$

with

$$M_{\text{SE}} = \left( \frac{Q_1 M_0 (1 - K_1)(K_2)^2 \sin\alpha}{1 - K_1 \cos\alpha} \right) \left( \frac{1 - cos\alpha}{2} \right) \ , \tag{5.35}$$

$$M_{\text{STE}} = \frac{(Q_1)^2 M_0 (1 - K_1) K_1 (K_2)^2 (\sin\alpha)^3}{2(1 - K_1 \cos\alpha)(1 - Q_1 K_1 \cos\alpha)} \ , \tag{5.36}$$

where $M_{\text{SE}}$ and $M_{\text{STE}}$ correspond to the signal originating from SEs or STEs with two transverse periods, respectively. The terms $K_1$, $K_2$, and $Q_1$ are given by

$$K_1 = \exp\left( -\frac{\text{TR}}{T_1} \right) \ , \tag{5.37}$$

$$K_2 = \exp\left( -\frac{\text{TR}}{T_2} \right) \ , \tag{5.38}$$

$$Q_1 = \exp\Big( -\text{TR}(\gamma G \tau)^2 D \Big) \ . \tag{5.39}$$

### 5.2.2. Random Walk Simulation

A Random Walk Simulation (RWS) was implemented to investigate the accuracy of the different analytical models of the DWSSFP signal as well as its sensitivity to coherent motion.

For that purpose, $N$ spins were randomly positioned within an artificial voxel, where each spin $n$ had a position vector $\vec{x}_n$ and a magnetization vector $\vec{M}_n$, as shown in Fig. 5.2. After each time step $\Delta t = 100\,\mu s$, $\vec{M}_n$ is updated to account for the $T_1$ and $T_2$ relaxation, dephasing by the diffusion weighting gradient, and rotation by the RF pulses. The rotation of $\vec{M}_n$ is assumed instantaneous. The position of each spin is updated to account for coherent and incoherent motion. Nonrestricted, Gaussian diffusion, which is a sort of incoherent motion, was implemented by an individual shift $\Delta\vec{x}_n$ of the spins' position $\vec{x}_n$. The coefficients of the vectors $\Delta\vec{x}_n$ were randomly generated following a Gaussian probability distribution with the standard deviation $\sigma_{\text{RWS}}$ given by

$$\sigma_{\text{RWS}} = \sqrt{2D\Delta t} \ , \tag{5.40}$$

with the result that the mean squared displacement $\langle \Delta\vec{x}_n^2 \rangle$ (see section 2.2.1) equals

$$\langle \Delta\vec{x}_n^2 \rangle = 6D\Delta t \ . \tag{5.41}$$

Basically, also anisotropic incoherent motion, as defined in the DTI model, could be simulated with the RWS by assigning individual $\sigma_{\text{RWS}}$ to each spatial axis. However, in the present work, the analysis was restricted to isotropic diffusion. Moreover, coherent motion was implemented in the RWS assuming a motion trajectory $\vec{x}(t)$ which described the time evolution of the center of mass of all spins. The motion trajectory $\vec{x}(t)$ was split into discrete shifts $\Delta\vec{x}(t)$ which were simultaneously applied to all spins at each time step $\Delta t$.

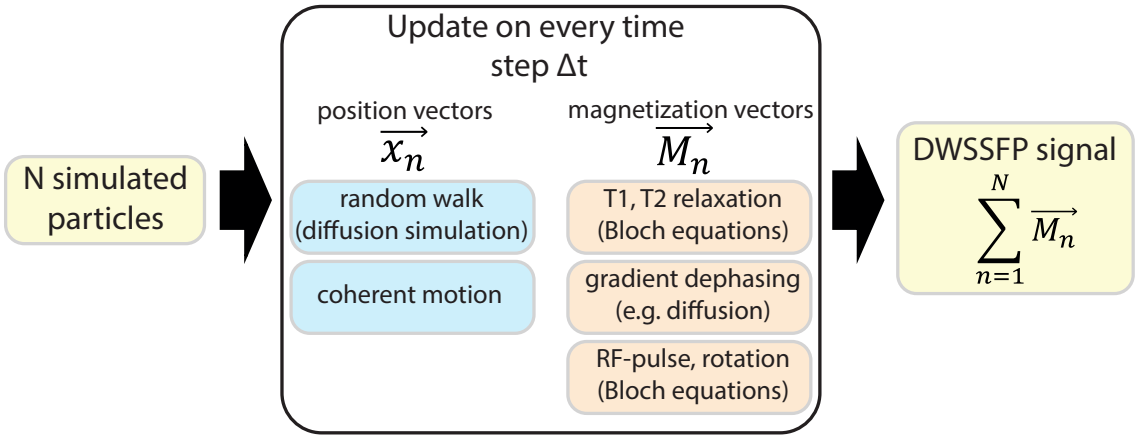


Figure 5.2.: Flow chart of the random walk simulation. $N$ particles are simulated, each with a position vector $\vec{x}_n$ and a magnetization vector $\vec{M}_n$. Every iteration $\vec{x}_n$ is updated allowing for incoherent motion (diffusion) and coherent motion and $\vec{M}_n$ is updated allowing for relaxation, rotation (RF pulses), and dephasing (gradients pulses).

**Random walk simulation to investigate the impact of intracranial pulsatility**

Motion trajectories of the thalamus region, which were reported by Soelinger et al. [185], were used to investigate the influence of intracranial pulsatility on the steady state of the

DWSSFP signal. The RWS signal was computed for a time period of $4\,\mathrm{s}$ with $N = 100000$ spins, assuming a constant heart rate of $60\,\mathrm{bpm}$. The other simulation parameters were: $G = 35\,\mathrm{mT\,m^{-1}}$, $\tau = 8\,\mathrm{ms}$, $\alpha = 30°$, TR $= 25\,\mathrm{ms}$, $T_1 = 830\,\mathrm{ms}$, $T_2 = 80\,\mathrm{ms}$ and $D = 0.7 \times 10^{-9}\,\mathrm{m^2\,s^{-1}}$. Three different simulation runs with the diffusion weighting gradients pointing in AP, LR and Superior-Inferior (SI) direction were conducted.

**Random walk simulation to investigate the accuracy of analytical DWSSFP models**

The transient phase of the DWSSFP signal was assumed to last from $t = 0$ to $t = 5T_1$, and 200 TRs past the transient phase were simulated. The signal of the RWS, i.e., $S_{FID,RWS}$ and $S_{Echo,RWS}$ was calculated as the average of $\vec{M}_n$ over $N = 1000000$ spins, directly after the RF-pulse ($S_{FID,RWS}$) or directly before the RF-pulse ($S_{echo,RWS}$). Furthermore, $S_{FID,RWS}$ and ($S_{echo,RWS}$) were averaged over all 200 TRs past the transient phase to increase the numerical stability.

### 5.2.3. Comparison of the analytical DWSSFP models

The analytical models, described in section 5.2.1, were investigated for three parameter sets used in recent publications (Table 5.1). The first set S1 was used by Miller et al. for ex vivo whole brain imaging [174], the second set S2 was used by Bieri et al. for in vivo ADC quantification of the knee cartilage [177], and the third set S3 was used by O'Halloran et al. for in vivo whole-brain imaging [25]. In the simulations, either $D$ is varied from $0\,\mathrm{m^2\,s^{-1}}$ to $2 \times 10^{-9}\,\mathrm{m^2\,s^{-1}}$ or $\alpha$ is varied from 2° to 178° assuming all other parameters to be fixed. To apply the KBE and FR models to pulsed gradients, the approximation suggested by Bieri et al. [177] was used, where the pulsed gradient is replaced by a constant gradient (constant gradient approximation) of the same gradient area ($\tau G = \mathrm{TR}g$). Note that the position $\epsilon$ of the diffusion gradient pulse does not affect $S_{FID}$ or $S_{echo}$ as the mixing time for each CP is independent of $\epsilon$. The accuracy of signal $S_{ana}$, predicted by the analytical models was evaluated first by direct comparison to the ground truth signal $S_{RWS}$, second by the relative error $\delta S$, defined as

$$\delta S = \frac{S_{ana} - S_{RWS}}{S_{RWS}} \tag{5.42}$$

and third, using the relative error of the diffusion sensitivity $\delta\sigma$

$$\delta S = \frac{\sigma_{ana} - \sigma_{RWS}}{\sigma_{RWS}} \tag{5.43}$$

with

$$\delta\sigma_{ana} = \log\left(\frac{S_{ana}}{S_{ana}(G=0)}\right), \tag{5.44}$$

$$\delta\sigma_{RWS} = \log\left(\frac{S_{RWS}}{S_{RWS}(G=0)}\right), \tag{5.45}$$

where $S_{ana}(G = 0)$ or $S_{RWS}(G = 0)$ is the signal of the DWSSFP sequence having the same parameters as $S_{ana}$ or $S_{RWS}$ but with $D$ set to zero. Note, this is only possible in a

| | S1 | S2 | S3 |
|---|---|---|---|
| $T_1$ | 340 ms | 1200 ms | 1100 ms |
| $T_2$ | 45 ms | 50 ms | 75 ms |
| TR | 42 ms | 15 ms | 26.5 ms |
| α | 37° | 14° | 37 ° |
| G | 40 mT/m | 40 mT/m | 40 mT/m |
| τ | 16.7 ms | 2.5 ms | 6.5 ms |
| $\tilde{q}$ | 668 mT ms $m^{-1}$ | 100 mT ms $m^{-1}$ | 260 mT ms $m^{-1}$ |
| D | 0.1 × $10^{-9}$ $mm^2/s$ | 1.5 × $10^{-9}$ $mm^2/s$ | 0.7 × $10^{-9}$ $mm^2/s$ |

Table 5.1.: Overview over the parameter sets S1, S2, and S3 which are investigated in this study to determine the accuracy of the analytical models of the DWSSFP signal. The tissue and sequence parameters are denoted as follows: relaxation times $T_1$ and $T_2$, repetition time TR, flip angle $\alpha$, amplitude of the gradient pulse $G$, duration of the gradient pulse $\tau$, diffusion weigthing $\tilde{q}$ given by $G\tau$ and diffusion coefficient $D$.

simulation environment and in practice a very small diffusion gradient is used to obtain an almost non-diffusion weighted image. The definition used for the diffusion sensitivity $\sigma$ is similar to the definition of the b-value for a ST preparation. However, as already mentioned, in contrast to the ST preparation, the diffusion sensitivity of DWSSFP also depends on $T_1$, $T_2$, $\alpha$, and TR (see definition of the effective b-value in the next section).

### 5.2.4. Comparison of the SNR efficiency of DWI sequences

#### The signal to noise ratio in MRI

According to Edelstein et al. [105], the SNR per voxel in an MRI image can be defined as

$$\mathrm{SNR} = \Psi_s \rho V \sqrt{N \cdot T_{\mathrm{acq}}}\, S_{\mathrm{NMR}} \ . \tag{5.46}$$

where $\rho$ is the proton density, $V$ is the voxel volume, $N$ is the number of shots (excitations) used to encode the MRI image, $T_{\mathrm{acq}}$ is sampling time per shot, $S_{\mathrm{NMR}}$ is the normalized NMR signal depending on the sequence parameters as well as the relaxation parameters of the scanned tissue, and $\Psi_s$ is the so called system SNR in units of $\mathrm{Hz}^{1/2}\mathrm{mm}^{-1}$. The factor $\Psi_s$ includes all hardware related impact factors such as the quality factor of the coil, the local sensitivity of the coil or the coil array, amplifiers, temperature and more. It is important to note, that in Eq. 5.46 a uniform encoding of k-space is assumed. In case of non-Cartesian encoding schemes, the SNR also depends on the k-space trajectory, the scanned object and the reconstruction technique [186].

#### Relative SNR efficiency

When comparing the SNR efficiency of different DWI sequences, it seems sensible to assume the same system SNR $\Psi_s$, voxel volume $V$, spin density $\rho$ and relaxation times $T_1$ and $T_2$. According to Eq. 5.46, this leaves three impact factors on the SNR, namely $N$, $T_{\mathrm{acq}}$ and $S_{\mathrm{NMR}}$ which can vary between the sequences. However, not only the SNR of an image

is important but also the time needed to acquire it. Therefore, the SNR per scan scan time SNR/$T_{\text{scan}}$ is a very useful quantity to describe the efficiency of a sequence. As the accurate SNR for a specific parameter set $V$, $\rho$, $T_1$ and $T_2$ is not known, a normalized quantity is derived to compare the efficiency of different sequences.

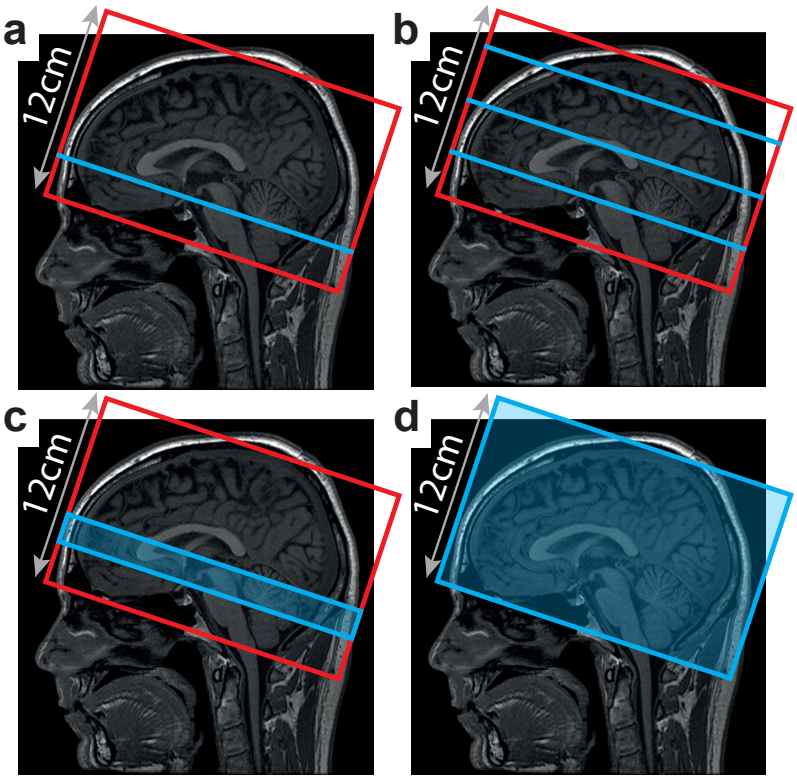


Figure 5.3.: Scan volume (red) and simultaneously excited volume (blue) for **a**: 2D EPI, **b**: SMS-EPI, **c**: MS-EPI and **d**: DWSSFP.

A substantial difference between 2D EPI, SMS-EPI, MS-EPI and DWSSFP is the simultaneously exited volume $V_{\text{exc}}$ as illustrated in Fig. 5.3. In case of MS-EPI, a slab of $N_{\text{slab}}$ slices is simultaneously exited and $N_{\text{slab}}$ phase encoding steps in slice direction are needed to Fourier encode the slab volume. Consequently, the SNR and also the SNR/$T_{\text{scan}}$ will be increased by a factor of $\sqrt{N_{\text{slab}}}$ compared to a 2D EPI because the sampling time per volume (or per spin) is 6 times longer. It is important to note, that the overall scan time is not increased in this case since the TR, given by the time interval of two consecutive RF-pulses exciting the same volume, is reduced at the same time by a factor of $N_{\text{slab}}$. This is the reason why 3D sequences are typically more efficient than 2D sequences. Similarly, in SMS-EPI the TR can be reduced by the multiband factor MB and the gained time can be used to acquire MB repetitions, increasing the SNR/$T_{\text{scan}}$ by a factor of $\sqrt{\text{MB}}$. However, in case of SMS-EPI the SNR of a single DWI is not increased. The influence of the simultaneously exited volume $V_{\text{exc}}$ (the blue area in Fig. 5.3) on $\eta$ can be accounted for by introducing the volume efficiency $v$

$$v = \frac{V_{\text{exc}}}{V_{\text{scan}}} \ , \tag{5.47}$$

where $V_{\text{scan}}$ corresponds to the complete volume covered by the DWI scan (the red area in Fig. 5.3).

The proportion of the sampling time spent on acquiring data and the TR can also vary between the different sequences. If $T_{\text{acq}}$ is the duration of the readout window of one shot, the sampling efficiency $\chi$ can be defined as

$$\chi = \sqrt{\frac{N \cdot T_{\text{acq}}}{\text{TR}}} \ . \tag{5.48}$$

Finally, the normalized SNR efficiency $\eta$ can be written as the product of $v$, $\chi$ and $S_{\text{NMR}}$, where each of the factors can range between zero and unity. Assuming all spins are in thermal equilibrium, $S_{\text{NMR}} = 1$ corresponds to the signal measured directly after application of a $90°$ excitation pulse.

$$\eta = v\chi S_{\text{NMR}} \tag{5.49}$$

The focus in this work is the potential gain in SNR efficiency compared to conventional 2D EPI. Thus, the relative SNR efficiency $\eta_{\text{rel}}$ is defined as

$$\eta_{\text{rel}} = \frac{\eta}{\eta_{\text{2DEPI}}} \ , \tag{5.50}$$

where $\eta_{\text{2DEPI}}$ is the SNR efficiency corresponding to a 2D EPI sequence.

Apart from $\eta$, the SNR of a single image is also important in DWI because most often the magnitude of the complex signal is processed. Thus, a higher SNR results in less bias due to non-Gaussian noise distribution [21] (see also chapters 3 and 4). The SNR of a single image is proportional to $\eta$ except for SMS-EPI because the efficiency gain is achieved by magnitude averaging of multiple repetitions or by acquiring DWIs with a higher number of directions and b-values. Unfortunately, this does not reduce the aforementioned bias. Therefore, relative SNR (rSNR) is defined identical to $\eta_{\text{rel}}$ but divided by $\sqrt{\text{MB}}$ if SMS-EPI is used.

#### Scan parameters for the simulation and optimization

To compare the different sequences, a fixed maximal gradient strength $G = 50\,\text{mT}\,\text{m}^{-1}$ was assumed which corresponds to a modern MRI scanner like the 3 T GE MR750 (GE Healthcare, Milwaukee, WI). Two different tissue types were considered, White Matter (WM) with ($T_1 = 1330\,\text{ms}$, $T_2 = 110\,\text{ms}$), and Gray Matter (GM) ($T_1 = 830\,\text{ms}$, $T_2 = 80\,\text{ms}$). The thickness of the scan volume was set to $120\,\text{mm}$ (Fig. 5.3) which is typically large enough to cover the full brain.

Fig. 5.4a presents the timing of the simulated EPI sequence used in the SNR efficiency comparison. The duration of RF-pulses, fat saturation and spoiler gradients were selected according to the implementation of a DWI EPI sequence on a 33 T MR750. The duration of the readout section of the EPI sequences was set to a fixed value of $T_{\text{acq,EPI}} = 30\,\text{ms}$ in which a full slice or a full phase encoding step in slice direction has to be acquired. A substantially longer readout time is usually not favorable as off-resonance effects and $T_2^*$ signal decay can lead to significant image artifacts (see section 2.3.3). To achieve high resolutions in that time frame, parallel imaging may need to be used [26, 103]. The delay time $T_{\text{delay,EPI}}$

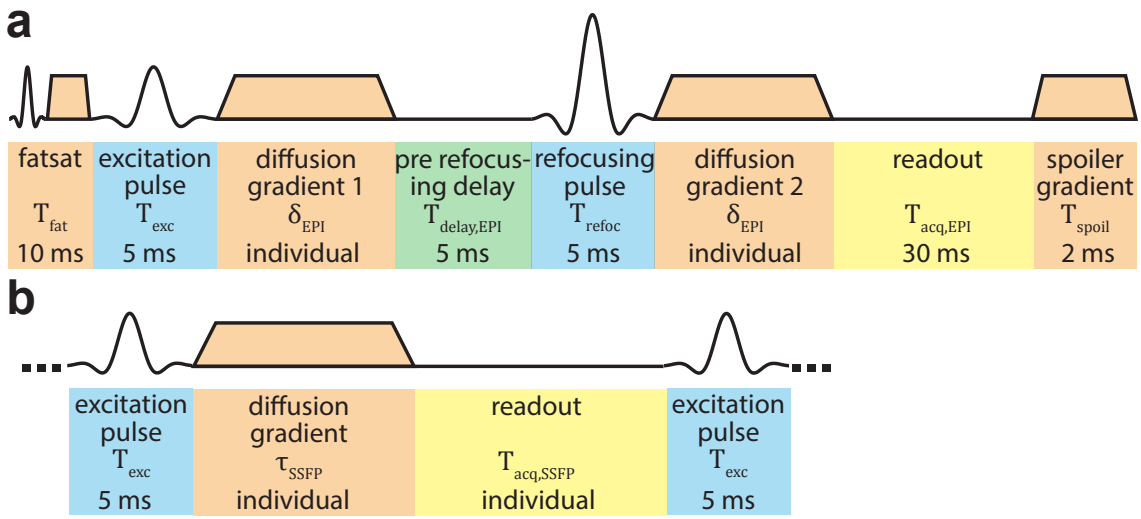


Figure 5.4.: Sequence timing of **a**: the EPI sequences and **b**: the DWSSFP sequence. 2D-EPI, SMS-EPI and MS-EPI share the same timing. The duration of sequence elements marked with "individual" is optimized for a specific resolution and b-value.

between the first diffusion weighting gradient and the refocusing was set to $5\,\mathrm{ms}$ which is a typical value to ensure, that the k-space center is acquired at the time the SE occurs. Although $T_{\mathrm{delay,EPI}}$ may be adjusted to the image resolution, Partial Fourier and parallel imaging acceleration factors, here a fixed value was used for simplicity. The duration of the diffusion gradients $\delta$ was calculated based on the formula of Stejskal–Tanner assuming rectangular gradient pulses [48] (also see section 2.2.3).

For all three EPI sequences, 2D EPI, SMS-EPI and MS-EPI the same timing for the ST preparation and readout module was assumed. The implementation of SMS-EPI and MS-EPI may be longer due to more complicated RF-pulses or phase navigators needed to correct for phase inconsistencies between different k-space segments. However, in this work, the best possible scenario was assumed to evaluate the capabilities of the new sequences. Potential drawbacks will be discussed later.

A DWSSFP is less common for in vivo imaging of the brain and, thus, the sequence timing was kept rather simple (Fig. 5.4b). One TR includes only a RF-pulse, a diffusion weighting gradient and a readout segment. In a more realistic scenario, navigators would be necessary to correct for motion induced phase variations [25].

The signal $S_{\mathrm{NMR,EPI}}$ of the EPI sequences with ST preparation was calculated assuming a spoiled SE sequence with a $90°$ excitation pulse and a $180°$ refocusing pulse [187].

$$S_{\mathrm{NMR,EPI}} = M_0 \left(1 - 2\exp\left(\frac{\frac{1}{2}\mathrm{TE} - \mathrm{TR}}{T_1}\right) + \exp\left(\frac{-\mathrm{TR}}{T_1}\right)\right)\exp\left(\frac{-\mathrm{TE}}{T_2}\right) \tag{5.51}$$

The SNR efficiency $\eta$ of a SE EPI sequence is optimized as follows. The sampling efficiency $\chi$ is constant since the duration of the ST preparation and the readout section is fixed but the volume effiency $v$ can be increased by increasing the simultaneously excited volume $V_{\mathrm{exc}}$. However, at the same time, $S_{\mathrm{NMR,EPI}}$ is reduced as the shorter TR results in an

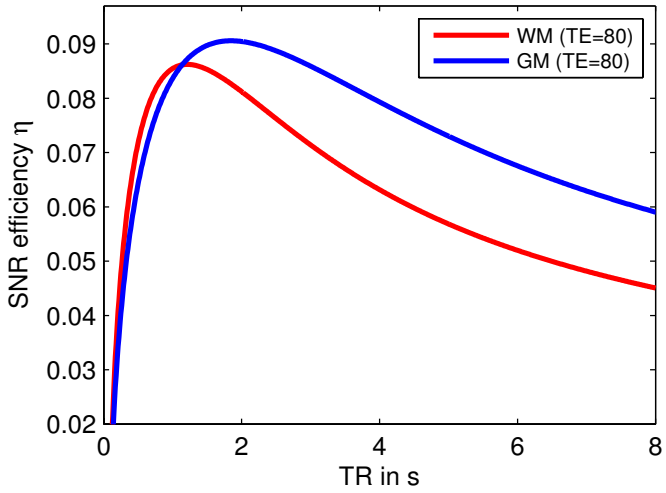


Figure 5.5.: SNR efficiency of a spoiled SE for WM and GM as a function of the TR, assuming a TE of $80\,\mathrm{ms}$.

increased $T_1$ saturation. Fig. 5.5 demonstrates that an optimal TR $\approx 1.4T_1$ exists, where $\eta$ is maximized. Two different cases were simulated for MS-EPI, a first version where the slab thickness was chosen such that the aforementioned optimal TR is reached and a second version with TR $= 4\,\mathrm{ms}$ because this TR was reported to be a good compromise between SNR efficiency and slab boundary artifacts [27]. To avoid discretization effects, noninteger values for the number of slices per slab were allowed. Regarding SMS-EPI, the simulation was restricted to MB $= 3$ and MB $= 4$ as higher multiband factors are problematic due to g-factor penalties [22].

| $b_{eff}$ in s/mm² | 999 | 2000 | 3003 | 3993 | 4998 | 5990 | 6987 | 8006 |
|---|---|---|---|---|---|---|---|---|
| τ in ms | 6,1 | 9,6 | 13,2 | 16,6 | 20,3 | 23,5 | 26,2 | 28,7 |
| $T_{acq,SSFP}$ in ms | 14,0 | 15,0 | 16,0 | 17,0 | 18,0 | 19,0 | 20,5 | 21,0 |
| TR in ms | 25,1 | 29,6 | 34,2 | 38,6 | 43,3 | 47,5 | 51,7 | 54,7 |
| α in ° | 30 | 30 | 31 | 31 | 33 | 34 | 35 | 36 |
| $S_{NMR,SSFP}$ | 0,060 | 0,055 | 0,050 | 0,046 | 0,042 | 0,039 | 0,036 | 0,034 |
| η | 0,045 | 0,039 | 0,034 | 0,031 | 0,027 | 0,025 | 0,023 | 0,021 |

Table 5.2.: Overview over the optimized DWSSFP parameters for WM.

The optimization of the DWSSFP is more complicated because the diffusion sensitivity depends in addition to the diffusion gradient ($G$, $\tau$) also on $\alpha$ and TR, as well as tissue relaxation times $T_1$ and $T_2$. Thus, a traditional b-value is not well defined. However, an effective b-value $b_{\mathrm{eff}}$ that reflects the diffusion sensitivity for a distinct tissue type can be defined as

$$b_{\mathrm{eff}} = \frac{S_{\mathrm{SSFP}}(G, \tau, \alpha, \mathrm{TR}, T_1, T_2, D)}{S_{\mathrm{SSFP}}(G, \tau, \alpha, \mathrm{TR}, T_1, T_2, D = 0)} \tag{5.52}$$

where $S_{\text{SSFP}}(G, \tau, \alpha, \text{TR}, T_1, T_2, D)$ corresponds to the diffusion weigthed DWSSFP signal and $S_{\text{SSFP}}(G, \tau, \alpha, \text{TR}, T_1, T_2, D = 0)$ is the signal of the same sequence but with $D$ set to zero [176]. As already mentioned, setting $D$ to zero is only possible in a simulation environment and in practice, a very small diffusion gradient has to be used to obtain an almost non-diffusion weighted image. The optimal DWSSFP sequence parameters were determined empirically by calculating $S_{\text{SSFP}}(G, \tau, \alpha, \text{TR}, T_1, T_2, D)$ and $S_{\text{SSFP}}(G, \tau, \alpha, \text{TR}, T_1, T_2, D = 0)$ with the KWF model for a wide range of parameters: $\tau$ from $1\,\text{ms}$ to $30\,\text{ms}$ in intervals of $0.1\,\text{ms}$, $T_{\text{acq,EPI}}$ from $5\,\text{ms}$ to $30\,\text{ms}$ in intervals of $0.5\,\text{ms}$ and $\alpha$ from $5°$ to $90°$ in intervals of $1°$. The parameter set yielding the highest SNR efficiency $\eta$ and matching the wanted $b_{\text{eff}}$ $\pm 1\,\%$ was selected. The optimized DWSSFP parameters for WM and GM and $b_{\text{eff}}$ between $1000\,\text{s}\,\text{mm}^{-2}$ and $8000\,\text{s}\,\text{mm}^{-2}$ can be found in table 5.2 and 5.3 respectively. The efficiencies of all sequences were investigated for b-values, or in case of DWSSFP effective b-values, ranging from $300\,\text{s}\,\text{mm}^{-2}$ to $8000\,\text{s}\,\text{mm}^{-2}$ in intervals of $200\,\text{s}\,\text{mm}^{-2}$ and for slice thicknesses ranging from $0.5\,\text{mm}$ to $3\,\text{mm}$ in intervals of $0.1\,\text{mm}$.

| $b_{\text{eff}}$ in s/mm² | 998 | 2005 | 2997 | 3993 | 4998 | 5993 | 6988 | 7985 |
|---|---|---|---|---|---|---|---|---|
| τ in ms | 5,0 | 7,9 | 11,0 | 14,2 | 17,3 | 20,7 | 23,5 | 25,8 |
| $T_{\text{acq,SSFP}}$ in ms | 16,5 | 17,5 | 19,5 | 20,0 | 22,0 | 23,0 | 24,5 | 26,5 |
| TR in ms | 26,5 | 30,4 | 35,5 | 39,2 | 44,3 | 48,7 | 53,0 | 57,3 |
| α in ° | 28 | 27 | 28 | 28 | 28 | 30 | 31 | 32 |
| $S_{\text{NMR,SSFP}}$ | 0,062 | 0,059 | 0,055 | 0,052 | 0,048 | 0,046 | 0,043 | 0,041 |
| η | 0,049 | 0,044 | 0,041 | 0,037 | 0,034 | 0,031 | 0,029 | 0,028 |

Table 5.3.: Overview over the optimized DWSSFP parameter for GM.

## 5.3. Results

### 5.3.1. Accuracy of analytic DWSSFP models

Fig. 5.6 presents simulation results, comparing the DWSSFP signal predicted by the analytical models and the RWS for the three parameter sets S1, S2 and S3 (Table 5.1). $D$ is ranging from $0\,\text{m}^2\,\text{s}^{-1}$ to $2 \times 10^{-9}\,\text{m}^2\,\text{s}^{-1}$ while all other parameters are held constant. As the diffusion sensitivity of $S_{\text{FID}}$ (Fig. 5.6a–c) is much smaller than $S_{\text{echo}}$ (Fig. 5.6d–f), the analysis is focused on the latter. Overall, the KWF model seems accurate as $\delta S_{\text{echo}}$ (Fig. 5.6g–i) and $\delta\sigma_{\text{echo}}$ (Fig. 5.6j–l) are very low, and the remaining errors are most likely caused by the variance of the RWS. However, the accuracy of all other analytical models strongly depends on the sequence and tissue parameters.

The WB model seems very accurate for S1 with $\delta S_{\text{echo}}$ and $\delta\sigma_{\text{echo}}$ (Fig. 5.6g,j) of almost zero because the higher modes are strongly attenuated by the damping terms $E_{1,k}^{\text{WB}}(\text{TR})$ and $E_{2,k}^{\text{WB}}(\text{TR})$ (Eqs. 5.17 and 5.18) owing to the small $T_2/\text{TR}$ of 0.9 and the strong diffusion weighting ($\tilde{q} = 668\,\text{mT}\,\text{ms}\,\text{m}^{-1}$) in S1. Consequently, the false assumption in the WB model that positive and negative modes decay equally affects S1 only slightly. Solely in the case of very small $D$, $E_{1,k}^{\text{WB}}(\text{TR})$ and $E_{2,k}^{\text{WB}}(\text{TR})$ decrease, and hence, $S_{\text{echo}}$ (Fig. 5.6g)

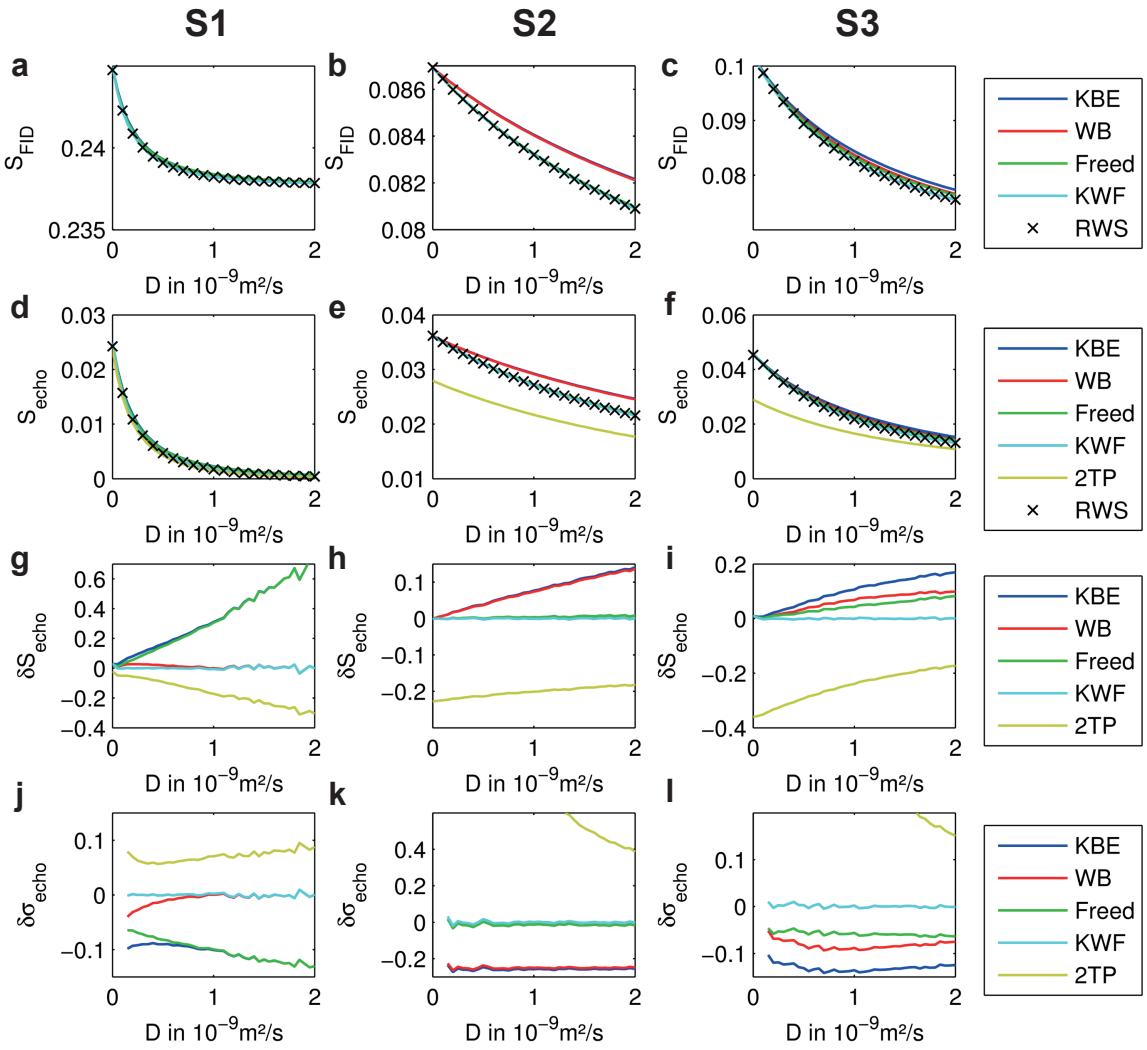


Figure 5.6.: Simulation results comparing the RWS signal with the analytical models for parameter sets S1 to S3, with $D$ ranging from $0\,\mathrm{m^2\,s^{-1}}$ to $2 \times 10^{-9}\,\mathrm{m^2\,s^{-1}}$. **a–c**: $S_{FID}$ **d–f**: $S_{echo}$ **g–h**: $\delta S_{echo}$, the relative error of $S_{echo}$. **i–k**: $\delta\sigma_{echo}$, the relative error of the diffusion sensitivity $\sigma_{echo}$.

is slightly overestimated and $\sigma_{\text{echo}}$ is underestimated (Fig. 5.6j). In S1, the KBE and FR models overestimate $S_{\text{echo}}$ with $D$ (Fig. 5.6g) and consistently underestimate $\sigma_{\text{echo}}$ at about $10\,\%$ (Fig. 5.6j). This is attributed to the constant gradient approximation that leads to particularly high errors in the b-value for short CPs. However, the short CPs dominate the signal of S1 because of the small $T_2/\text{TR}$ and the strong diffusion weighting. This attenuates the longer CPs. For the same reason, the approximate 2TP model performs very well, even better than the KBE and FR models (Fig. 5.6g,j), because CPs with more than two transverse periods are suppressed.

The situation is inverted for S2 because of the greater $T_2/\text{TR} \approx 3.3$, the lower diffusion weighting ($\tilde{q} = 100\,\text{mT}\,\text{ms}\,\text{m}^{-1}$), and lower $\alpha = 14°$. This leads to the coupling of modes [183] and lower signal portion for short CPs. Consequently, the errors owing to the constant gradient approximation are negligible and the FR and KWF models are very accurate, whereas the KBE and WB models overestimate $S_{\text{echo}}$ with $D$ (Fig. 5.6h) and consistently underestimate $\sigma_{\text{echo}}$ at about $20\,\%$ (Fig. 5.6k).

Finally, S3 lies between S1 and S2 with $T_2/\text{TR} \approx 2.8$, $\alpha = 37°$, and a moderate diffusion weighting of $\tilde{q} = 260\,\text{mT}\,\text{ms}\,\text{m}^{-1}$. Consequently both sources of error, the constant pulse approximation and the coupling of the modes, contribute equally to the error of the signal, leaving only the KWF model being accurate (Fig. 5.6i,l). The 2TP model seems unsuitable for both S2 and S3 as $\delta\sigma_{\text{echo}}$ significantly exceeds $20\,\%$.

Figure 5.7 shows the simulation results for $\alpha$ between $2°$ to $178°$ and fixed values for all other sequence and tissue parameters in Table 5.1. The differences in $S_{\text{FID}}$ (Fig. 5.7a–c) between models are very small for all given parameter sets and the analysis is limited to $S_{\text{echo}}$ again (Fig. 5.7d–f). The KWF model seems accurate for the full range of $\alpha$ with almost zero $\delta S_{\text{echo}}$ (Fig. 5.7g–i) and $\delta\sigma_{\text{echo}}$ (Fig. 5.7j–l). In general, low $\alpha$ seems to increase the coupling of the modes, which leads to the large errors of the KBE and WB models, but it decreases the effect of the constant gradient approximation resulting in small errors for the FR model (Fig. 5.7g–l). On the contrary, for high $\alpha$, the coupling of the modes is negligible but the constant gradient approximation leads to significant errors. The 2TP model is only sufficiently accurate in the very low $\alpha$ regime because the contributions of CPs with more than two transverse periods significantly increase with $\alpha$ (Fig. 5.7d–l).

### 5.3.2. Motion sensitivity of the DWSSFP signal

The intrinsic motion sensitivity is the biggest challenge of a DWSSFP sequence for in vivo application. Therefore, the RWS was used to investigate the disruption of the steady state caused by intracranial pulsatility in the thalamus region as reported in [185]. In Fig. 5.8, $S_{\text{echo}}$ is plotted with and without the influence of coherent motion assuming $b_{\text{eff}} = 1500\,\text{s}\,\text{mm}^{-2}$ and diffusion encoding directions LR (Fig. 5.8a), AP (Fig. 5.8b) and SI (Fig. 5.8c). In case the diffusion encoding gradient points in LR direction, $S_{\text{echo}}$ is only slightly reduced when comparing the plots with motion and without motion (Fig. 5.8a). However, in AP and SI direction, $S_{\text{echo}}$ is substantially fluctuating and the amplitude is in average reduced by about $30\,\%$ and $40\,\%$, respectively (Fig. 5.8b,c). The potential signal loss of the DWSSFP sequence is not included in the subsequent efficiency comparison because it strongly depends on the specific brain region and the selected sequence parameters.

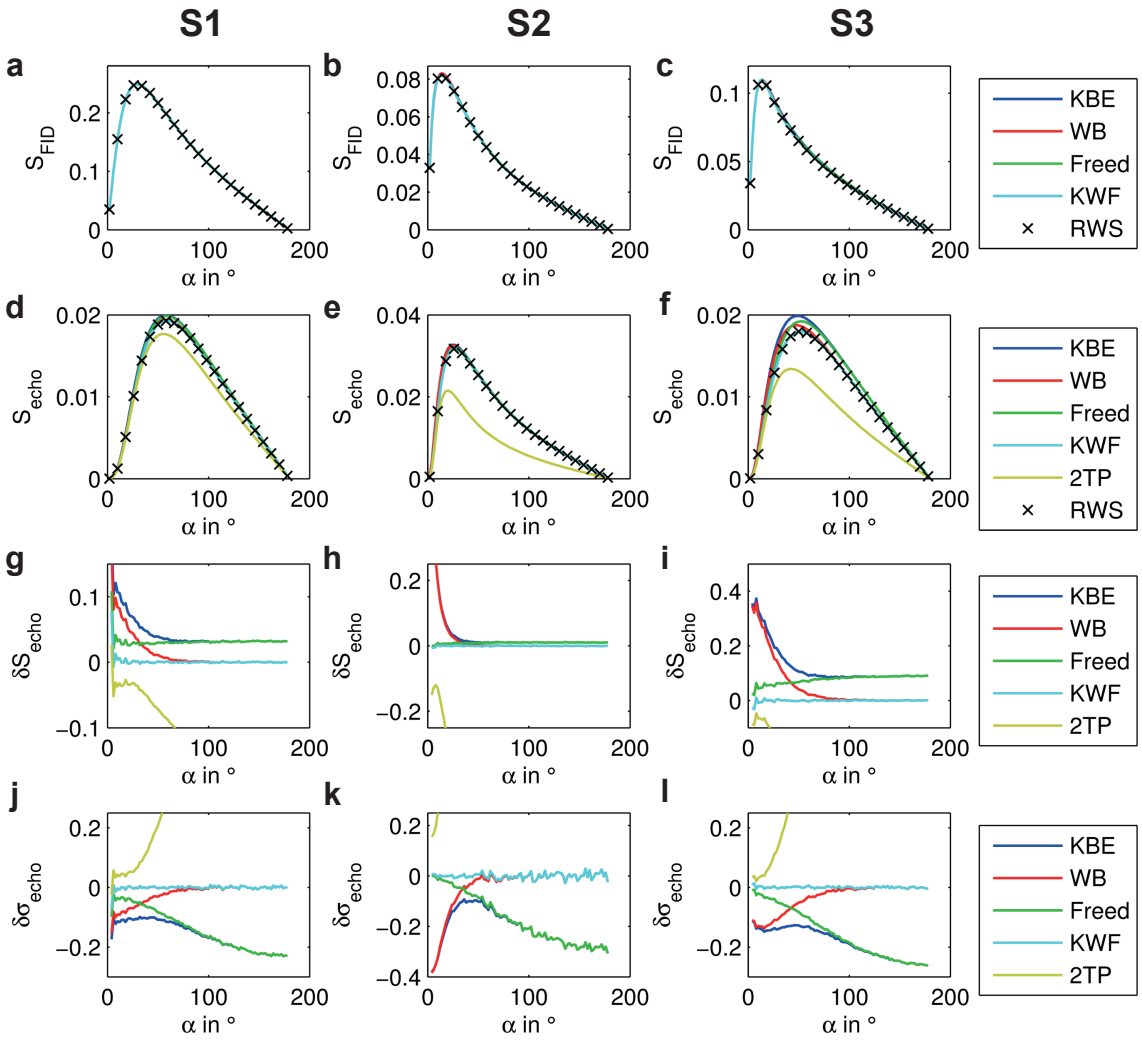


Figure 5.7.: Simulation results comparing the RWS signal with the analytical models for parameter sets S1 to S3, with $\alpha$ ranging from 2° to 178°. **a–c**: $S_{FID}$ **d–f**: $S_{echo}$ **g–h**: $\delta S_{echo}$, the relative error of $S_{echo}$. **i–k**: $\delta\sigma_{echo}$, the relative error of the diffusion sensitivity $\sigma_{echo}$.

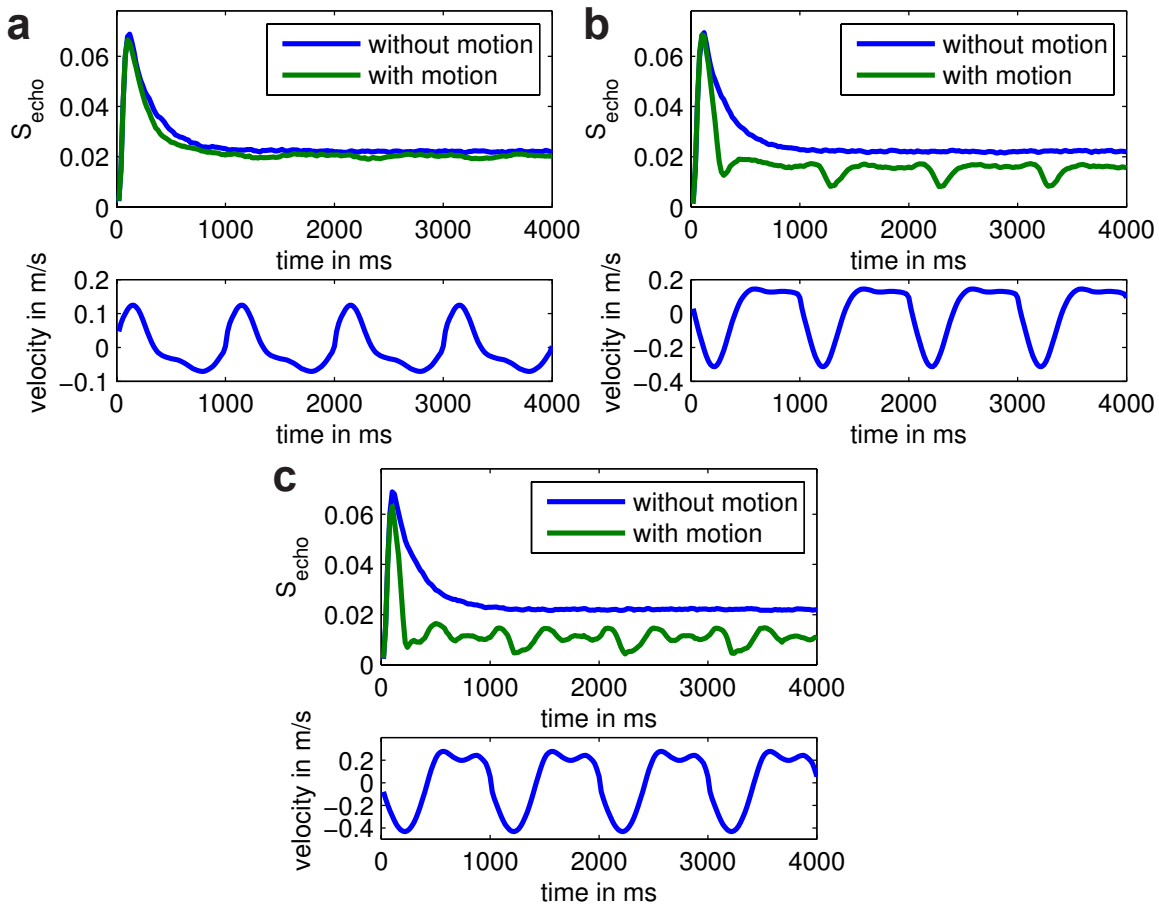


Figure 5.8.: RWS simulation results of $S_{echo}$ as a function of the time assuming pulsatile brain motion of the thalamus as reported in [185]. Parameters for the RWS were: $\alpha = 30°$, TR $= 25\,\mathrm{ms}$, $\alpha = 30°$, $T_1 = 830\,\mathrm{ms}$, $T_2 = 80\,\mathrm{ms}$, $G = 35\,\mathrm{mT\,m^{-1}}$, $\tau = 8\,\mathrm{ms}$, $b_{\mathrm{eff}} = 1500\,\mathrm{s\,mm^{-2}}$ and a heartbeat of $60\,\mathrm{bpm}$. **a**: Diffusion encoding in LR direction, **b**: Diffusion encoding in AP direction, and **c**: Diffusion encoding in SI direction.

### 5.3.3. Efficiency comparison of DWI sequences

Fig. 5.9a depicts the relative SNR efficiency $\eta_{\mathrm{rel}}$ over the simulated parameter space of all slice thicknesses and all b-values assuming WM as the underlying tissue. For all EPI sequences, $\eta_{\mathrm{rel}}$ increases steadily with decreasing slice thickness and increasing b-value. The reason is the prolonged TR and the reduced $T_1$ saturation which either results from a higher number of shots needed to cover the volume or from the longer diffusion encoding time. The behavior of the DWSSFP is similar for different slice thicknesses but different regarding $b_{\mathrm{eff}}$ because $\eta_{\mathrm{rel}}$ peaks at roughly $b_{\mathrm{eff}} = 2000\,\mathrm{s\,mm^{-2}}$, and then, slightly decreases for higher $b_{\mathrm{eff}}$. A comparison of $\eta_{\mathrm{rel}}$ among the sequences reveals MS-EPI with TR $= 1160\,\mathrm{ms}$ as the most efficient sequence. This is plausible because the TR was optimized for the best possible $\eta$ that a spoiled SE sequence can achieve (see Fig. 5.5).

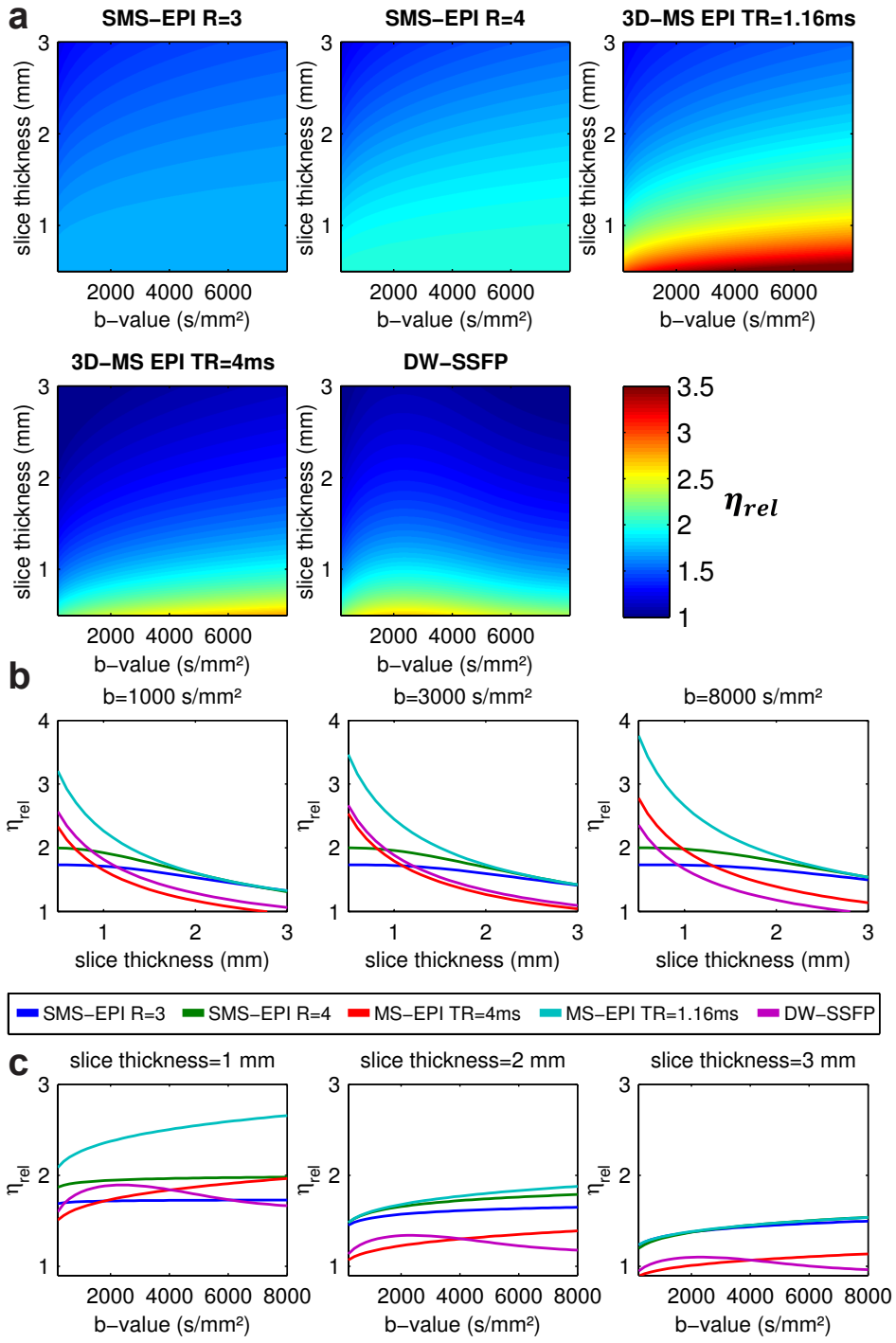


Figure 5.9.: Relative SNR efficiency gain $\eta_{\text{rel}}$ of SMS-EPI (MB $= 3$ and 4), MS-EPI (TR $=$ $1.16\,\text{ms}$ and $4\,\text{ms}$), and DWSSFP assuming tissue parameters typically observed in WM ($T_1 = 830\,\text{ms}$, $T_2 = 80\,\text{ms}$, $D = 0.7 \times 10^{-9}\,\text{m}^2\,\text{s}^{-1}$). **a**: Color plots of $\eta_{\text{rel}}$ as a function of the slice thickness and the b-value, **b**: Line plots of $\eta_{\text{rel}}$ for $b_{\text{eff}} = 1000\,\text{s}\,\text{mm}^{-2}$, $b_{\text{eff}} = 3000\,\text{s}\,\text{mm}^{-2}$ and $b_{\text{eff}} = 8000\,\text{s}\,\text{mm}^{-2}$ as a function of the slice thickness, **c**: Line plots of $\eta_{\text{rel}}$ for slice thicknesses of $1\,\text{mm}$, $2\,\text{mm}$ and $3\,\text{mm}$ as a function of the b-value.

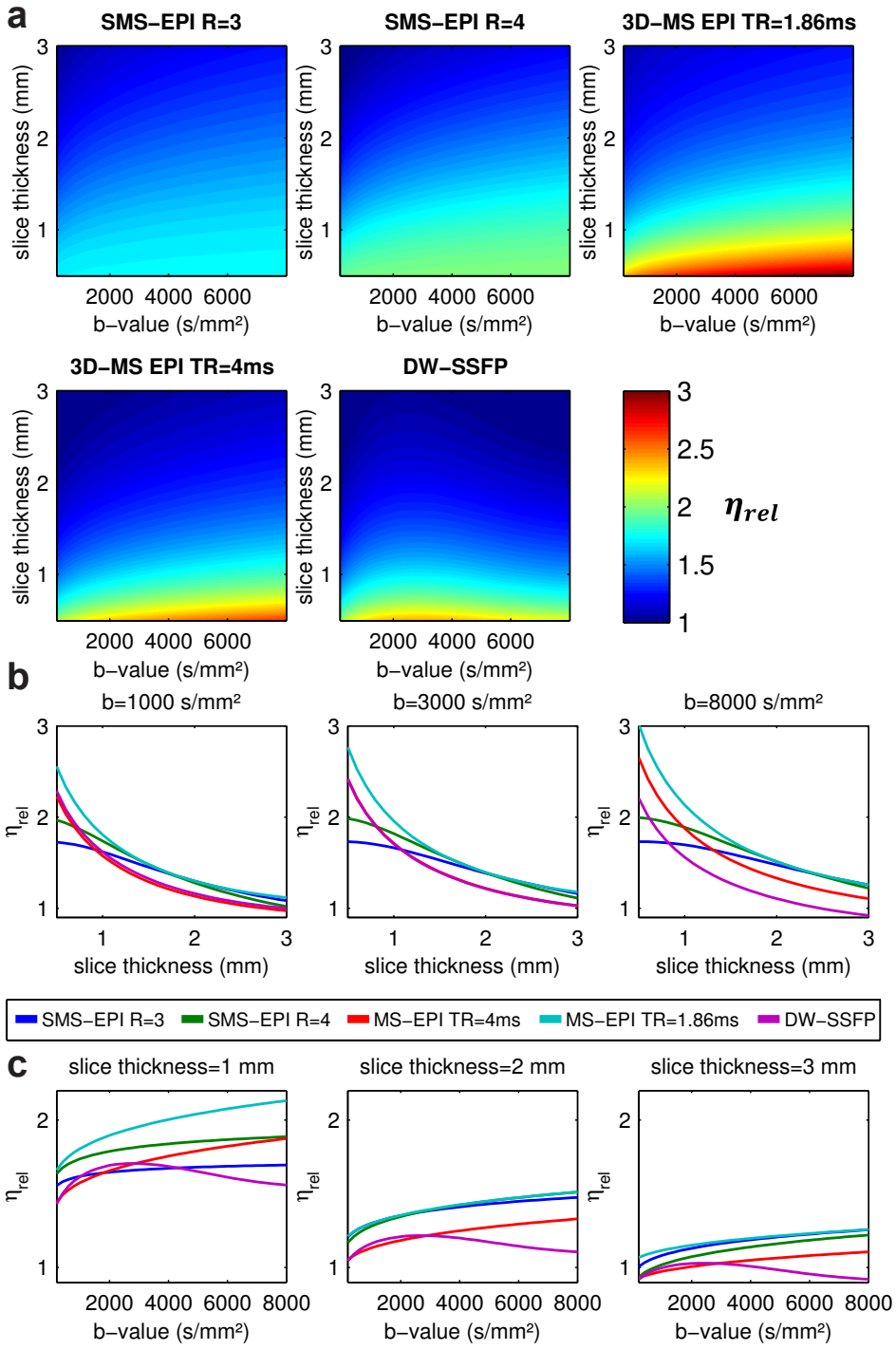


Figure 5.10.: Relative SNR efficiency gain $\eta_{\text{rel}}$ of SMS-EPI (MB $=$ 3 and 4), MS-EPI (TR $=$ 1.86 ms and 4 ms), and DWSSFP assuming tissue parameters typically observed in GM ($T_1 = 1330\,\text{ms}$, $T_2 = 110\,\text{ms}$, $D = 0.75 \times 10^{-9}\,\text{m}^2\,\text{s}^{-1}$). **a**: Color plots of $\eta_{\text{rel}}$ as a function of the slice thickness and the b-value, **b**: Line plots of $\eta_{\text{rel}}$ for $b_{\text{eff}} = 1000\,\text{s}\,\text{mm}^{-2}$, $b_{\text{eff}} = 3000\,\text{s}\,\text{mm}^{-2}$ and $b_{\text{eff}} = 8000\,\text{s}\,\text{mm}^{-2}$ as a function of the slice thickness, **c**: Line plots of $\eta_{\text{rel}}$ for slice thicknesses of 1 mm, 2 mm and 3 mm as a function of the b-value.

For a detailed comparison, $\eta_{\text{rel}}$ is plotted in Fig. 5.9b as a function of the slice thickness for different b-values. These plots correspond to vertical lines in Fig. 5.9a at $b_{\text{eff}} = 1000\,\text{s}\,\text{mm}^{-2}$, $3000\,\text{s}\,\text{mm}^{-2}$ and $8000\,\text{s}\,\text{mm}^{-2}$. Overall, the results for all three b-values seem very similar and the slice thickness has by far the greatest impact. SMS-EPI (MB $= 3, 4$) and MS-EPI (TR $= 1160\,\text{ms}$) provide a very similar performance for a slice thickness between from $2\,\text{mm}$ to $3\,\text{mm}$. However for slice thicknesses smaller than $2\,\text{mm}$ SMS-EPI (MB $= 3, 4$) quickly reaches the maximum possible $\eta_{\text{rel}}$ of $\sqrt{\text{MB}}$. DWSSFP and MS-EPI (TR $= 4000\,\text{ms}$) exhibit an essentially lower $\eta_{\text{rel}}$ at high slice thicknesses than SMS-EPI (MB $= 3, 4$) and MS-EPI (TR $= 1160\,\text{ms}$). However for slice thicknesses lower than about $1\,\text{mm}$, DWSSFP and and MS-EPI (TR $= 4000\,\text{ms}$) outperform both SMS-EPI sequences, because they don't have an intrinsic limit of $\eta_{\text{rel}}$. In Fig. 5.9c $\eta_{\text{rel}}$ is plotted as a function of the b-value corresponding to three horizontal lines in the color plots of Fig. 5.9a at slice thicknesses $1\,\text{mm}$, $2\,\text{mm}$ and $3\,\text{mm}$. Basically, the previous observations are confirmed. SMS-EPI (MB $= 3$, 4) and MS-EPI (TR $= 1160\,\text{ms}$), provide almost identical performance at $3\,\text{mm}$ because $T_1$ saturation limits the potential gain in SNR efficiency. At $2\,\text{mm}$ slice thickness, SMS-EPI (MB $= 4$) and MS-EPI are still very similar, but SMS-EPI (MB $= 3$) falls behind especially at higher b-values. Finally, at $1\,\text{mm}$ slice thickness, MS-EPI (TR $= 1160\,\text{ms}$) exhibits its full potential with $\eta_{\text{rel}}$ reaches about 2.8 at high b-values whereas all other sequences achieve at most $\eta_{\text{rel}} = 2$.

Fig. 5.10 shows the same analysis as Fig. 5.9 but for GM tissue instead of WM tissue. The conclusions are very similar compared to WM. However, the possible benefit of the new DWI sequences are generally smaller because of the longer $T_1$ of GM and therefore, stronger saturation effects. Consequently, the optimal TR for a spoiled gradient echo is about $1.86\,\text{ms}$ for GM compared to TR $= 1.16\,\text{ms}$ for WM.

Fig. 5.11 depicts the rSNR as a function of the b-value or the slice thickness. The results demonstrate that the rSNR does not increase for SMS-EPI. On the contrary, in case of large slice thicknesses, the rSNR is even smaller than one, indicating a lower SNR than conventional 2D EPI. This can be explained by the increased $T_1$ saturation due to the shorter TR. However for small slice thicknesses below 2 mm this effect is negligible and the rSNR yields almost 1. Overall this saturation effect is more pronounced in GM (Fig. 5.11d-e) than in WM (Fig. 5.11a-c) due to the longer $T_1$ of GM.

### 5.3.4. Discussion

#### Analytic DWSSFP models

The errors of different analytical models for pulsed DWSSFP sequences were evaluated for three recently published parameter sets S1, S2 and S3 [25, 174, 177] using a RWS simulation as ground truth. Previously reported models are very accurate in some parameter regimes, e.g. the WB model for low $T_2/\text{TR}$ (parameter set S1) and high $\alpha$, or the FR model for high $T_2/\text{TR}$ and low $\alpha$ (parameter set S2). However, none of the existing models was found accurate for parameter set S3. The proposed KWF model, which combines the improvements of Wu and Buxton [172] and Freed et al. [183] to the original KBE model [171], yielded accurate solutions for all three parameter sets. Despite the lack of theoretical proof of the accuracy of the KWF model, the simulation results of the three scenarios suggest that the KWF model generally is the accurate analytical solution to predict the signal of

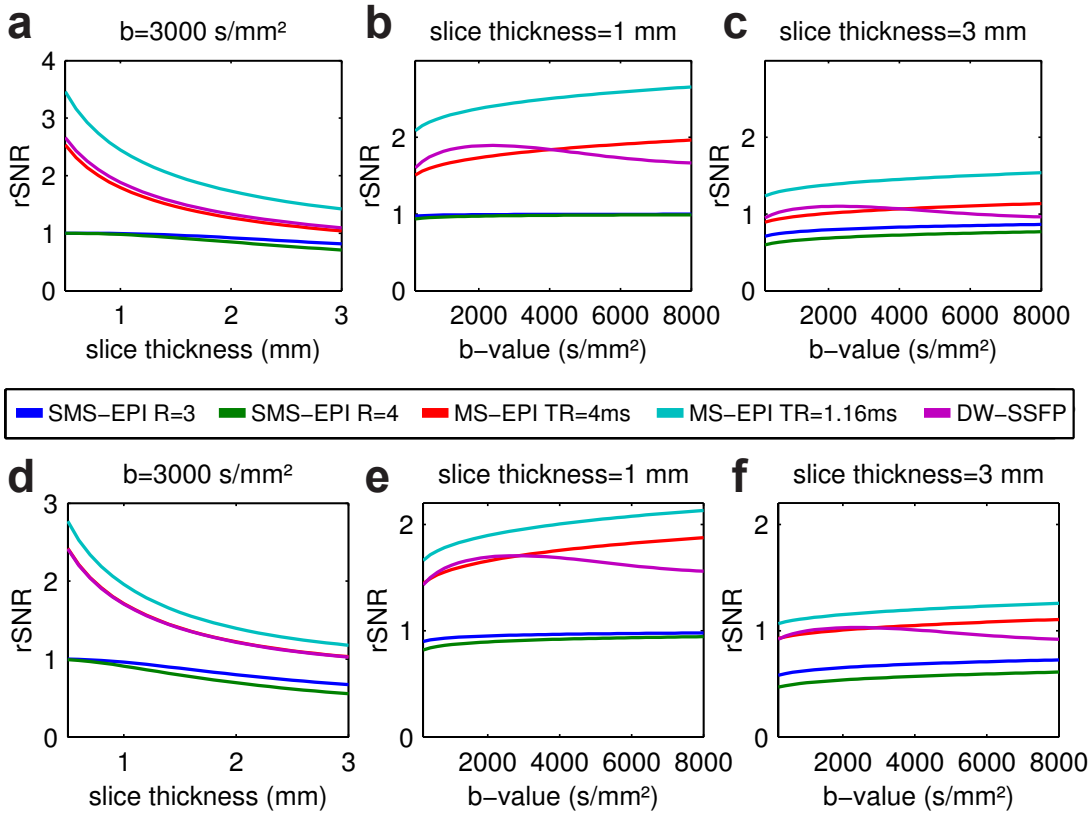


Figure 5.11.: Relative SNR gain, rSNR, of SMS-EPI (MB $= 3$ and 4), MS-EPI (TR = $1.86\,\mathrm{ms}$ and $4\,\mathrm{ms}$), and DWSSFP. **a**: rSNR at $b = 3000\,\mathrm{s\,mm^{-2}}$ as a function of the slice thickness for WM, **b**: rSNR at at a slice thickness of $1\,\mathrm{mm}$ as a function of the b-value for WM, **c**: rSNR at at a slice thickness of $3\,\mathrm{mm}$ as a function of the b-value for WM, **d**: rSNR at $b = 3000\,\mathrm{s\,mm^{-2}}$ as a function of the slice thickness for GM, **e**: rSNR at at a slice thickness of $1\,\mathrm{mm}$ as a function of the b-value for GM, and **f**: rSNR at at a slice thickness of $3\,\mathrm{mm}$ as a function of the b-value for GM.

the pulsed DWSSFP sequence. The approximate 2TP solution, suggested by Buxton [181], was overall the least accurate model with significant errors at high $\alpha$. However, the 2TP model can be sufficiently accurate at very low $\alpha$ and high $T_2/\mathrm{TR}$ (e.g. parameter set S1). Moreover, 2TP is computationally very simple and contrary to the other models presented here, the 2TP model can also be used for non-Gaussian diffusion signals where each CP is handled as an ST preparation [173].

### Efficiency comparison of DWI sequences

A framework was presented to compare SNR efficiencies of DWI sequences with different types of diffusion preparations, e.g. conventional ST preparation or a diffusion weighted steady state, but also with different readout techniques such as 2D, SMS, multi-slab or 3D. The framework was used to compare the SNR efficiency gains of several recently reported

DWI sequences, i.e. MS-EPI, SMS-EPI and DWSSFP, over conventional 2D EPI. For the comparison, a modern MR scanner with a maximum gradient strength of $50\,\mathrm{mT\,m^{-1}}$ was assumed, as well as a fixed value of $12\,\mathrm{cm}$ for the FOV in slice encoding direction, which is typically sufficient to cover the human brain. Two significant impact factors on the potential SNR efficiencies gains were identified, namely the b-value and the slice thickness, because both directly influence the TR and therefore the $T_1$ saturation.

Overall the slice thickness or the resolution—most often isotropic voxels are used in DWI—had a substantially larger impact on the SNR efficiency gain than the b-value. For moderate slice thicknesses between $2\,\mathrm{mm}$ and $3\,\mathrm{mm}$, SMS-EPI with MB $= 3$ and MB $= 4$ achieved similar results like MS-EPI with optimal TR. However, at slice thicknesses substantially below $2\,\mathrm{mm}$, the SNR efficiency gain of SMS-EPI is limited to $\sqrt{\mathrm{MB}}$. A further increase of MB is difficult, because SMS-EPI relies on parallel imaging reconstruction to separate the simultaneously excited slices, which can cause a g-factor penalty in SNR. Modern multi-channel receive coils and controlled aliasing using blipped CAIPIRINHA [23, 188] can reduce the g-factor to almost one for MB $= 3$ and an in-plane acceleration of 2 [22]. However, MB higher than 4 seems challenging in DWI as the potential gain in SNR efficiency may be overcompensated by the g-factor penalty. Another disadvantage of SMS-EPI is the limited possibility to apply parallel imaging in-plane, since the g-factors resulting from SMS and Fourier encoding add up. Consequently, very high resolution are difficult to reach and may require segmented k-space acquisition schemes [189].

At slice thicknesses of $1.5\,\mathrm{mm}$ and below, MS-EPI may be an interesting alternative. With an optimal TR, MS-EPI clearly outperformed SMS-EPI and achieved gains in SNR efficiency of 2 and higher, which is in good agreement with recent reports based on simulations and real data experiments [24, 179]. In MS-EPI, the different slices of a slab are separated by Fourier encoding, resulting in no additional g-factor compared to SMS-EPI. Therefore higher in-plane acceleration factors may be used to achieve higher resolutions with less distortions because the effective ESP is reduced (see section 2.3.3). However, the crucial challenge of MS-EPI is the excitation profile of the slab. Even optimized RF-pulses cause unwanted excitation of neighboring slabs and insufficient signal at the edges of the slabs resulting in so called slab boundary artifacts due to inhomogeneous $T_1$ saturation [179]. Because slab boundary artifacts are more severe for short TRs, the optimal case of TR $= 1.4T_1$ may be difficult to reach. Several techniques have been reported to correct the slab profile in the post processing, such as slab profile encoding [27], bandpass filtering or adjusted slab weighting [179]. Nevertheless, for very thin slices around $1\,\mathrm{mm}$, MS-EPI with a TR $= 4000\,\mathrm{ms}$ may be an interesting option. On the one hand, the SNR efficiency gains exceeded those of SMS-EPI and on the other hand, slab boundary artifacts in WM or GM seem negligible according to Van et al. [27].

A second challenge of MS-EPI are phase inconsistencies between different k-space segments. To avoid a potential signal cancellation, additional 2D phase navigator images are acquired after the readout of the actual DWI data. However, recalling the inhomogeneity of the image phase of DWIs that was observed in chapter 4 and 6 (e.g. Fig. 4.6), it seems questionable whether a 2D phase navigator can acquire sufficient information to reliably correct for phase variations in very thick slabs. Therefore, the possible SNR efficiency gain of MS-EPI may be also limited by the slab thickness. Alternatively, cardiac reordering and online reacquisition of DWIs that exhibit significant phase vaiations, could be used to minimize phase inconsistencies between different k-space segments [170].

The DWSSFP sequence generally achieved similar SNR efficiency gains as MS-EPI with TR $= 4000\,\mathrm{ms}$. However the motion sensitivity is an even bigger challenge for DWSSFP because it is a 3D sequence which requires also a 3D phase navigator and additionally the steady state can be disrupted by coherent motion. The latter was investigated in this work for the thalamus region in the human brain using a random walk simulation and motion parameters reported by Söllinger et al. [185]. While the steady state was very stable for diffusion encoding in LR direction, significant signal loss in AP and SI direction was observed. Consequently, erroneous signal loss due to coherent motion could be easily confused with an anisotropic diffusion. Further, this signal loss may also be spatially inhomogeneous as pulsation motion of the brain is more pronounced in certain regions (see chapter 6). It is important to note, that the signal loss due to the disruption of the steady state and signal loss due to phase inconsistencies of different k-space segments are different effects. While phase inconsistencies of different k-space segments can be addressed by phase navigators, the signal loss due to disruption of the steady state is irretrievable because multiple CPs have accumulated different phases and destructive interference occurs already at the time of the data acquisition. O'Halloran et al. proposed a real time correction for first order phase terms in image space by measuring the signal with a 3D navigator and applying a corresponding correction gradient prior to the next RF-pulse [190]. However, this method can be used only to address rigid body motion rather than pulsatile brain motion which is highly nonlinear. Further, several post processing strategies were developed to account for motion induced signal loss including, 3D navigators, cardiac reordering and binning and low pass filtering yielding DTI results comparable to EPI acquisitions [25, 190]. Unfortunately, the k-space center was heavily oversampled in these cases, reducing the SNR efficiency far below the results that were presented in this work. Taking into account the highly complex reconstruction and the still not fully solved problem of the motion sensitivity, DWSSFP seems not favorable for in vivo DWI of the brain compared to the other novel DWI sequences such as SMS-EPI or MS-EPI. On the other hand, excellent DWI results of DWSSFP have been reported ex-vivo where motion is not an issue and the relaxation times are more favorable for this sequence type [176].

# 6. Measurement of the brain pulsatility using DWI

The content presented in this chapter is based in parts on two conference abstracts which were submitted to the 23rd Annual Meeting of the ISMRM 2015 and the 21st Annual Meeting of the OHBM 2015 [160, 191]. These conference abstracts were awarded the "Summa Cum Laude Award" and "Merit Award", respectively.

## 6.1. Introduction

It was pointed out in the previous chapter that data processing in DWI is most often based on the magnitude of the complex MR signal, and the inherent phase of the signal is discarded as it is considered to be spoiled by different sources. However, one of these sources for a non-zero phase of DWIs is the pulsatile motion of the brain itself [185], which is encoded by the diffusion sensitizing gradients.

Changes in the biomechanical properties of the brain, typically accompanied by changes of the brain pulsatility, however, are of potential importance for disorders such as peripheral vascular disease, dementia, brain tumor or traumatic brain injury [20]. Therefore, measuring the brain pulsatility can be a valuable tool to assess the stage of these disorders. Three primary techniques can be used to measure the brain pulsatility [20]: continuous intracranial pressure monitoring, transcranial Doppler ultrasound and MRI. The first is an invasive technique, which requires placement of pressure sensors in the brain. While Doppler ultrasound techniques are typically restricted to 2D images, MRI can also provide 3D information of the brain pulsatility.

Velocity encoding is a well-known technique in the field of MRI [192], however, it is usually used for the measurement of blood flow, featuring a much higher velocity than brain pulsatility. In Söllinnger et al. [185], a technique called cine displacement encoding was used to measure the brain pulsatility, which, however, can take more than half an hour.

Here, a new technique is proposed to process the complex signal of DWIs in order to extract a meaningful phase, which allows for inferring information of the pulsation of the brain. This novel approach enables joint examination of the brain's microstructure and pulsatile motion, without increasing scan time as compared to regular DWI.

## 6.2. Methods

### 6.2.1. Phase filtering pipeline to extract pulsatile brain motion

The signal's phase $\phi$ of a DWI originates from multiple sources and can be described as a sum of a constant offset $\phi_0$, the susceptibility induced phase $\phi_\chi$, the eddy current induced

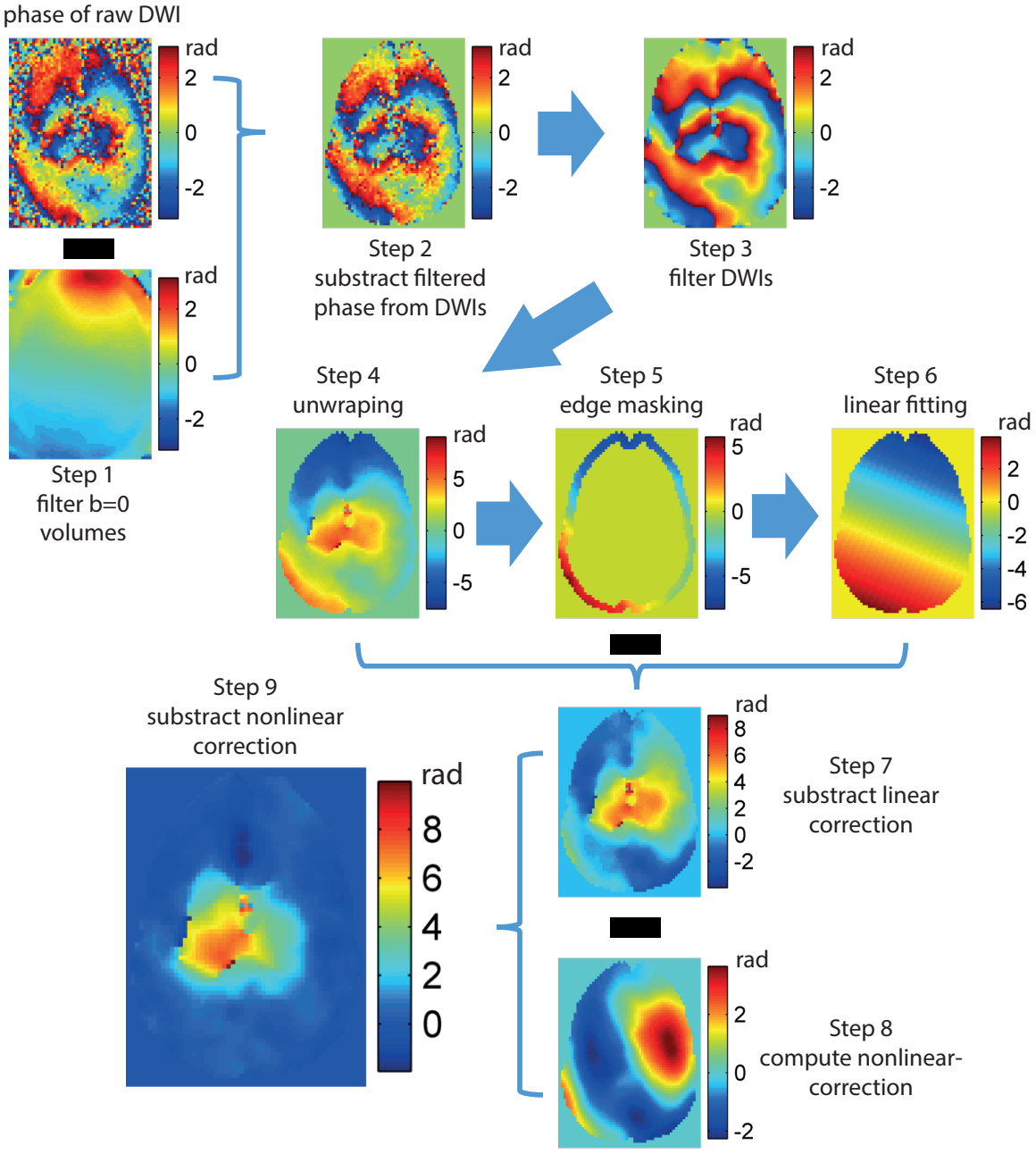


Figure 6.1.: Schematic description of the proposed phase filtering technique to extract information of the pulsatile motion of the brain from DWIs. In step 1 and 2 constant phase components which are independent of the diffusion encoding, such as $\phi_0$ and $\phi_\chi$, are filtered out. After smoothing the DWIs (Step 3) and unwrapping the phase (Step 4), linear phase components caused by (linear) eddy currents or rigid body motion, are filtered out. Finally nonlinear eddy currents are accounted for by steps 8 and 9, leaving only phase components originating from nonlinear motion.

phase, split in a linear term $\phi_{\text{eddy,lin}}$ and a nonlinear term $\phi_{\text{eddy,nl}}$, and motion induced phase, split in a rigid motion term $\phi_{\text{motion,rigid}}$ and a nonrigid motion term $\phi_{\text{motion,nonrigid}}$ (note that the eddy current term $\phi_{\text{eddy,lin}}$ accounts for $B_0$ eddy currents and linear eddy currents with respect to section 2.3.3).

$$\phi = \phi_0 + \phi_\chi + \phi_{\text{eddy,lin}} + \phi_{\text{eddy,nl}} + \phi_{\text{motion,rigid}} + \phi_{\text{motion,nonrigid}} \tag{6.1}$$

The constant offset $\phi_0$, is primarily caused by the RF-pulse, which imparts a phase onto the spins while they are flipped into the transverse plane, but also amplifier delays and different signal transit times in the receive coils can contribute. Susceptibility differences in the tissue, or tissue–air interfaces, result in different local Larmor frequencies (see section 2.3.3). However, these differences in the local Larmor frequency are constant in time, and thus the phase component $\phi_\chi$ is typically negligible because the ST diffusion preparation is based on a Spin Echo (SE) and off-resonance effects cancel. The terms $\phi_{\text{eddy,lin}}$ and $\phi_{\text{eddy,nl}}$ account for linear and nonlinear eddy currents which are generated by the diffusion encoding gradients (see section 2.3.3). The eddy current field is not constant but decays exponentially in time. Therefore, off-resonance effects due to eddy currents do not fully cancel in a SE. Furthermore, the eddy current field depends on the diffusion encoding gradient and therefore, the terms $\phi_{\text{eddy,lin}}$ and $\phi_{\text{eddy,nl}}$ vary between the DWIs. Moreover, rigid body motion but also non rigid motion, such as brain pulsatility, is encoded by the diffusion sensitizing gradients, resulting in the phase terms $\phi_{\text{motion,rigid}}$ and $\phi_{\text{motion,nonrigid}}$.

Fig. 6.1 schematically depicts a phase filtering technique which aims to extract the phase component $\phi_{\text{motion,nonrigid}}$, which is assumed to be caused primarily by pulsatile motion of the brain. This phase filtering technique involves the following steps:

- **Step 1:** Smoothing of all b=0 volumes with a 3D size 3 boxcar kernel.
- **Step 2:** Subtract the phase of the closest filtered b=0 volume from the DWIs. This step removes the phase components $\phi_0$ and $\phi_\chi$.
- **Step 3:** Smoothing of all DWIs with a 2D size 3 boxcar kernel.
- **Step 4:** Unwrapping of the phase using a robust, best path algorithm suggested by Abdul-Rahman et al. [193].
- **Step 5:** Masking a three voxel wide ribbon at the edge of the brain.
- **Step 6:** Fitting a 2D first order polynomial to the masked and unwrapped phase.
- **Step 7:** Subtract the phase pattern that was calculated from the polynomial fit in step 6, from the unwrapped phase of the DWIs. This step removes the phase components $\phi_{\text{eddy,lin}}$ and $\phi_{\text{motion,rigid}}$.
- **Step 8:** Smoothing of the phase maps with a 3D size 5 boxcar kernel and computing the nonlinear component $\phi_{\text{eddy,nl}}$ by fitting the phase of each voxel with a 3D second order polynomial in q-space.
- **Step 9:** Subtract the nonlinear phase component $\phi_{\text{eddy,nl}}$ from the phase of the DWIs after linear correction (Step 7) yielding the phase maps $\phi_{\text{motion,nonrigid}}$. This step removes the phase component $\phi_{\text{eddy,nl}}$.

The phase components $\phi_0$ and $\phi_\chi$ are typically very smooth and constant for all $b = 0$ volumes and all DWIs. Thus, $\phi_0$ and $\phi_\chi$ can can be easily removed using the $b = 0$ volumes (steps 1 and 2), which are not affected by motion encoding og the gradients gradients. The DWIs are smoothed (step 3) to increase the robustness of the unwrapping algorithm (step 4). In step 5, a small ribbon at the edge of the brain is masked, where no or only very little pulsatile motion of the brain is expected. The phase values of the voxels, belonging to the masked area, are used to apply a 2D first order polynomial fit in image space (Step 6). The zero order term of this polynomial either accounts for a $B_0$ shift due to eddy currents or translational motion of the head which is encoded by the diffusion sensitizing gradients. In case of translational motion, the displacement vector of all spins is the same, and hence, the corresponding phase shift spins is the same for all voxels too. The first order terms of the polynomial corresponds to a phase gradient which can either originate from linear eddy currents or from rotational motion of the head. Note, that rigid motion is a combination of translational motion and rotational motion. To better understand the motion encoding of a rotation, let $\mathbf{R}$ be the rotation matrix by an angle $\theta$ about the $x$ axis

$$\mathbf{R} = \begin{bmatrix} 1 & 0 & 0 \\ 0 & \cos\theta & -\sin\theta \\ 0 & \sin\theta & \cos\theta \end{bmatrix} \quad . \tag{6.2}$$

Moreover, let $x$, $y$ and $z$ be the coordinates of a spin before the rotation. Now, the displacement vector $\Delta\vec{r}$ of the rotation can be calculated as

$$\Delta\vec{r} = \begin{pmatrix} x \\ y \\ z \end{pmatrix} - \mathbf{R} \begin{pmatrix} x \\ y \\ z \end{pmatrix} = \begin{pmatrix} 0 \\ y(1-\cos\theta) + z\sin\theta \\ -y\sin\theta + z(1-\cos\theta) \end{pmatrix} \quad . \tag{6.3}$$

Typical rotation angles of a subject during the scan do not exceed a few degrees. Therefore, the small-angle approximation ($\sin\theta = \theta$ and $\cos\theta = 1$) can be applied and Eq. 6.3 simplifies to

$$\Delta\vec{r} = \begin{pmatrix} 0 \\ z\theta \\ -y\theta \end{pmatrix} \quad . \tag{6.4}$$

Now a ST preparation is assumed, parametrized by the diffusion weighting gradient $\vec{G}$ with the duration $\delta$, and mixing time $\Delta$. If the subject performs a rotational movement in between the diffusion encoding gradients, each voxel is displaced by $\Delta\vec{r}$. The corresponding phase shift $\Delta\phi_{\text{rot}}$ can be calculated as

$$\Delta\phi_{\text{rot}} = \gamma\delta\vec{G} \cdot \Delta\vec{r} = \gamma\delta\theta \left(G_y z - G_z y\right) \quad . \tag{6.5}$$

It can be seen in Eq. 6.5 that the phase shift $\Delta\phi_{\text{rot}}$ resulting from rotational motion corresponds to a phase gradient in image space.

According to Eq. 6.1, only the phase components $\phi_{\text{eddy,nl}}$ and $\phi_{\text{motion,nonrigid}}$ are left after the linear phase correction in step 7. To estimate $\phi_{\text{eddy,nl}}$ (step 8), the assumption is used, that pulsatile brain motion is nearly periodic and the predominant cause of $\phi_{\text{motion,nonrigid}}$. Therefore, $\phi_{\text{motion,nonrigid}}$ cancels in average as will be shown next. Let $\vec{r}_P(t)$ be a periodic motion trajectory and let $\vec{g}^*_{ST}(t)$ be the effective gradient trajectory corresponding to a ST

preparation (see section 2.37). Recalling the solution of the Bloch–Torrey equation, which describes the effect of coherent motion (see Eq. 2.42), the phase shift $\Delta\phi_P$ can be calculated as

$$\phi_P(t_0) = \gamma \int_{t_0}^{t_0+\Delta+\delta} \vec{g}^*_{ST}(t')\vec{r}_P(t')\, dt' \ , \tag{6.6}$$

where $t_0$ is the time at the beginning of the first diffusion weighting gradient. In the time between the two gradient pulses, from $t = t_0 + \delta$ to $t = t_0 + \Delta$, there is no active gradient in a ST preparation. Therefore, the formulation in Eq. 6.6 can be split in two integrals.

$$\phi_P(t_0) = \gamma \int_{t_0}^{t_0+\delta} \vec{g}^*_{ST}(t')\vec{r}_P(t')\, dt' + \gamma \int_{t_0+\Delta}^{t_0+\Delta+\delta} \vec{g}^*_{ST}(t')\vec{r}_P(t')\, dt' \tag{6.7}$$

The second gradient pulse is identical to the first gradient pulse but has the opposite effective polarity (the true polarity is the same but the refocusing pulse changes the sign of the effective polarity). As a result, Eq. 6.7 can be rewritten to

$$\phi_P(t) = \gamma \int_{t_0}^{t_0+\delta} \vec{g}^*_{ST}(t') \left[\vec{r}_P(t') - \vec{r}_P(t'+\Delta)\right]\, dt' \ . \tag{6.8}$$

It can be seen from Eq. 6.8, that the temporal mean of $\phi_P(t)$ must be zero because the temporal means of $\vec{r}_P(t')$ and of $\vec{r}_P(t'+\Delta)$ are identical. Consequently, if one acquires a sufficient number of DWIs at a random time with respect to the periodicity of $\vec{r}_P(t')$, the phase contributions due periodic motion cancel in average. Note that this is only the case, if cardiac gating is not used because otherwise $\vec{r}_P(t)$ and $\vec{g}^*_{ST}(t)$ would not be independent of each other (also see the next section 6.2.2).

An empirical model is used to estimate the phase components $\phi_{\text{eddy,nl}}$ originating from nonlinear eddy currents, assuming that deviations from the model, which are caused by $\phi_{\text{motion,nonrigid}}$, cancel in average. Let $q_x$, $q_y$ and $q_z$ be the q-space coordinates of a ST preparation as defined in section 2.2.5. The phase $\phi_{\text{eddy,nl}}$ of the signal in each voxel originating from nonlinear eddy currents is modeled with a 3D second order polynomial in the q-space domain, given by

$$\phi_{\text{eddy,nl}} = C_1 q_x + C_2 q_y + C_3 q_z + C_4 q_x q_y + C_5 q_x q_z + C_6 q_y q_z + C_7 q_x^2 + C_8 q_y^2 + C_9 q_z^2 \tag{6.9}$$

where $C_1$ to $C_9$ corresponds to the nine coefficients of the polynomial. Although this approach results in a fairly high number of free parameters, i.e. nine times the voxel count, the problem is still well conditioned as long as the number of volumes in the DWI acquisition is sufficiently high. Moreover the phase $\phi_{\text{eddy,nl}}$ is expected to be rather smooth. Therefore, to impose smoothness of the coefficient maps $C_1$ to $C_9$ and to increase robustness of the fit, the phase is smoothed with a 3D size 5 boxcar kernel prior to the fitting of the polynomial. A positive side effect of this smoothing operation is, that the phase values of neighboring slices are included into the fit of each voxel too. Each slice is typically acquired in a single shot 2D EPI acquisition, and thus, all voxels within this slice share the same ST preparation and the same motion encoding at the same time in the cardiac cycle. However, if no cardiac gating is used, the ST preparation of a neighboring slice likely happens at a different time in the cardiac cycle. That is why including voxels from neighboring slices into the fit on the one hand decreases resolution of coefficient maps $C_1$ to

$C_9$, but on the other hand increases statistical certainty that phase components originating from pulsatile brain motion cancel in average.

The phase $\phi_{\text{eddy,nl}}$ is synthesized for each voxel in each DWI using coefficients $C_1$ to $C_9$. Finally in step 9, $\phi_{\text{eddy,nl}}$ is subtracted from the linearly corrected phase in step 7, resulting in the phase maps $\phi_{\text{motion,nonrigid}}$. In brain imaging, it is assumed that the predominant source of $\phi_{\text{motion,nonrigid}}$ is the pulsatile brain motion.

### 6.2.2. Quantitative metrics

In conventional MR flow measurement techniques, multiple images with the same flow sensitizing gradients, e.g. a bipolar gradient, are acquired at different times of the cardiac cycle. However, in a typical diffusion acquisition scheme, the directions are distributed such that angular incoherence is maximized [125]. Further, cardiac gating is most often not used, and the DWIs are therefore randomly distributed over the cardiac cycle (the random distribution is also a requirement for step 8 as described in the previous section).

Although the motion encoding direction for each DWI is different and the time of the cardiac cycle when the DWIs are acquired is unknown, the Mean Absolute Velocity (MAV) can be calculated as follows. Assuming that the motion trajectory between the beginning of the first gradient pulse and the end of the second gradient pulse can be well approximated by a linear term, each phase $\phi_{\text{motion,nonrigid}}$ can be associated with a velocity $v_P$ using the first order magnetic moment $M_1$ of the ST preparation of each DWI respectively (see section 2.2.2).

$$v_P = \frac{\phi_{\text{motion,nonrigid}}}{M_1} \ . \tag{6.10}$$

It is important to note, that $v_P$ is the projected velocity, into the direction of the diffusion encoding gradient $\vec{G}$ and the true velocity vector $\vec{v}$ is unknown. Assuming an acquisition with $N$ DWIs and $v_P(n)$ is the projected velocity for the $n$th volume, MAV is given by

$$\text{MAV} = \frac{\xi}{N} \sum_{n=1}^{N} |v_P(n)| \ . \tag{6.11}$$

The correction factor $\xi$ compensates for the random orientation between $\vec{G}$ and $\vec{v}$. $\xi$ can be derived as follows. Let $\vec{n}$ be a unit vector given in spherical coordinates

$$\vec{n} = \begin{pmatrix} \sin\theta cos\varphi \\ \sin\theta \sin\varphi \\ cos\theta \end{pmatrix} \ . \tag{6.12}$$

Assuming that $\vec{n}$ is randomly rotated around a second unit vector with fixed orientation, e.g. in positive $x$ direction, such that the projection of $\vec{n}$ is given by

$$\begin{pmatrix} \sin\theta cos\varphi \\ \sin\theta \sin\varphi \\ cos\theta \end{pmatrix} \cdot \begin{pmatrix} 1 \\ 0 \\ 0 \end{pmatrix} \ . \tag{6.13}$$

Now $\xi$ can be calculated as

$$\xi = \frac{4\pi}{\int_0^{\pi} \int_0^{2\pi} |\sin\theta \cos\varphi \sin\theta| \; d\theta d\varphi} = 2 \; . \tag{6.14}$$

Note that there is no loss of generality by assuming a fixed orientation of the second unit vector, because the surface integral in Eq. 6.14 covers the full sphere anyways.

The directionality of the brain pulsatility is investigated as well. A set of 60 unit vectors $\vec{u}_m$, which are uniformly spaced on the surface of a sphere, are used to determine the main direction of the pulsatile motion. For each vector $\vec{u}_m$, all $|v_P(n)|$ are weighted by the projection of $\vec{G}_n$ of the $n$th DWI onto $\vec{u}_m$, and averaged, yielding $\phi_m$.

$$\phi_m = \frac{1}{N} \sum_{n=1}^{N} |v_P(n)| \vec{u}_m \cdot \frac{\vec{G}_n}{|\vec{G}_n|} \tag{6.15}$$

Finally, the direction corresponding to the largest $\phi_m$ value is assumed to be the main direction of the pulsatile motion in each voxel.

### 6.2.3. Data acquisition

DWI acquisitions were obtained from an oil phantom and one healthy volunteer. The data were acquired with a 3T GE MR750 scanner, with a maximum gradient strength of $50\,\mathrm{mT\,m^{-1}}$ (GE Healthcare, Milwaukee, WI) using a ST diffusion preparation and a single-shot 2D EPI readout train. The imaging volume was recorded with a matrix size of $96 \times 96 \times 16$ and an axial oriented $24 \times 24 \times 4$ cm$^3$ scan volume, covering the brain at the level of the corpus callosum. Further acquisition parameters were: isotropic resolution $2.5\,\mathrm{mm}$, TE = $80.7\,\mathrm{ms}$, TR = $1800\,\mathrm{ms}$, ESP = $0.592\,\mathrm{ms}$. A 32-channel head coil was used with parallel imaging factor 2 in the phase-encoding direction and SENSE reconstruction [26].

A diffusion encoding scheme with five shells and 30 collinear directions directions per shell was used as illustrated in section 3, Fig. 3.1. Ten repetitions of this diffusion encoding scheme were acquired for the volunteer scan and one repetition for the phantom scan.

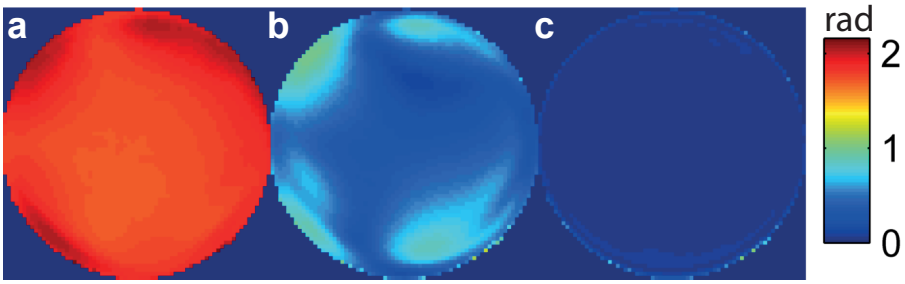


Figure 6.2.: Standard Diviation (SD) maps of the signal's phase, calculated for each voxel over all DWIs for the a representative slice of the phantom acquisition. **a**: before linear correction (step 4), **b**: after linear correction (stepp 7) and **c**: after nonlinear correction (step 9).

## 6.3. Results

In Fig. 6.2, the phase variation between the different DWIs of the phantom scan was investigated using Standard Diviation (SD) maps. The SD of the phase was calculated voxel by voxel over all DWIs before the linear correction at step 3 (Fig. 6.2a), after the linear correction in step 7 (Fig. 6.2b), and after the nonlinear correction in step 9 (Fig. 6.2c). The SD was substantially reduced by the linear correction. However, there were some fairly well defined regions where the phase still seemed to deviate between the DWIs (Fig. 6.2b). After the nonlinear correction step 9 the remaining regions with increased SD completely vanished (Fig. 6.2c), which indicates, that phase components originating from nonlinear eddy currents can be accurately described by the proposed model (see Eq. 6.9).

Fig. 6.3 depicts the same SD maps as shown Fig. 6.2, for 14 slices of the volunteer experiment. Before the linear correction, the SD was ranging from about $3\,\mathrm{rad}$ to $5\,\mathrm{rad}$ and there was no maximum in the center where pulsatile brain motion is expected to be highest (Fig. 6.3a). The picture changed significantly after the linear correction step 4 (Fig. 6.3b). Overall the SD was substantially reduced, and the highest SD could then be observed in the center around the ventricles. Moreover, the passage from one slice to the following one, was much smoother, which is expected because brain pulsatility does not stop or change at a certain slice. However, the phase still appeared to be spoiled, especially at the edges of the brain, where pulsatile motion is not anticipated. After application of the nonlinear phase correction step 9, the SD at the edges of the brain reduced to almost zero and the origin of the brain pulsatility seemed to be very well defined at the center of the brain.

Fig. 6.4 depicts maps of the coefficients $C_1$ to $C_9$ of the nonlinear phase correction for one slice of the in vivo acquisition. The larger image in each subfigure corresponds to a joint reconstruction of all 10 repetitions. To the contrary, the smaller coefficient maps in the subfigures, numbered from 1 to 10, were computed separately for each repetition to investigate the repeatability of the nonlinear phase correction. The coefficient maps $C_1$ to $C_3$ (Fig. 6.4a-c), which correspond to the linear terms $q_x$, $q_y$ and $q_z$, seemed very stable over all repetitions, especially coefficient map $C_1$ and $C_3$ (Fig. 6.4a,c). The maps for $C_1$ and $C_3$ both exhibit a diagonal symmetry while $C_2$ seemed to have a horizontal or vertical symmetry. This is remarkable, because the gradient coils in $x$ and $y$ direction are based on the same design (Golay pair design [35, p. 844]), while the gradient coil in $z$ direction is different (Maxwell pair design [35, p. 842]). On the other hand a quantitative comparison reveals that $C_1$ and $C_2$ have a very similar range between -1 and 1 while $C_3$ ranges from -2 to 2.

The coefficient maps $C_4$ to $C_6$ corresponding to the crossterms $q_xq_y$, $q_xq_z$ and $q_yq_z$ are presented in Fig. 6.4d-f. Overall the coefficient maps are slightly less stable compared to $C_1$ to $C_3$, but the same pattern can be still clearly recognized in each repetition. $C_4$ and $C_6$ exhibit a very similar patter with negative coefficients in the left and positive in the right and $C_5$ exhibits a pattern with positive values a the top and negative values below.

Finally the coefficient maps $C_7$ to $C_9$ belonging to the quadratic terms $q_x^2$, $q_y^2$ and $q_z^2$ are depicted in Fig. 6.4g-i. Only $C_7$ seems stable over all repetitions while there were significant variations for $C_8$ and particularly for $C_9$, also repetitive pattern can still be found. Moreover, the coefficients $C_7$ are distributed between about -4 to 4 which is the highest range among all coefficients.

Overall, the nonlinear correction seems to work fairly well, because the same pattern in

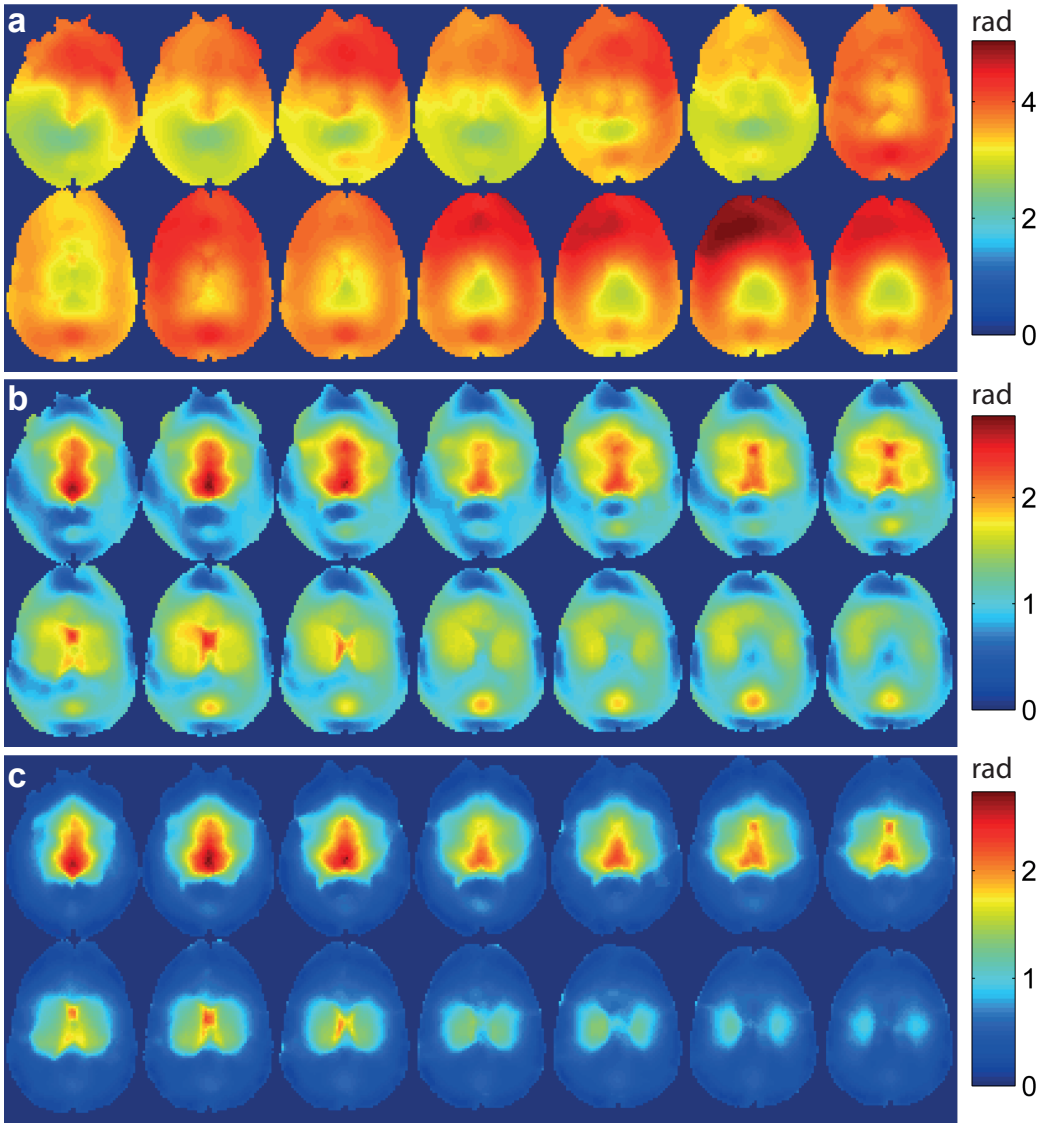


Figure 6.3.: Standard deviation maps of the signal's phase, calculated for each voxel over all DWIs, for 14 slices of the in-vivo acquisition. **a**: before linear correction (step 4), **b**: after linear correction (stepp 7) and **c**: after nonlinear correction (step 9).

the coefficient maps are found for different repetitions. The shape of these patterns does not indicate, that they originate from pulsatile brain motion or any other type of motion. However, pulsatile brain motion seems to slightly distort the estimation of the coefficients in some cases, leading to variations between the different repetitions. These distortions can found especially in the center of the brain where pulsatile brain motion is expected to be highest.

Fig. 6.5a presents MAV maps of one slice of the in vivo acquisition. Again, the larger map to the left is computed using all 10 repetitions jointly and the smaller maps to the right, numbered 1 to 10, are computed for each repetition separately. The maps show an

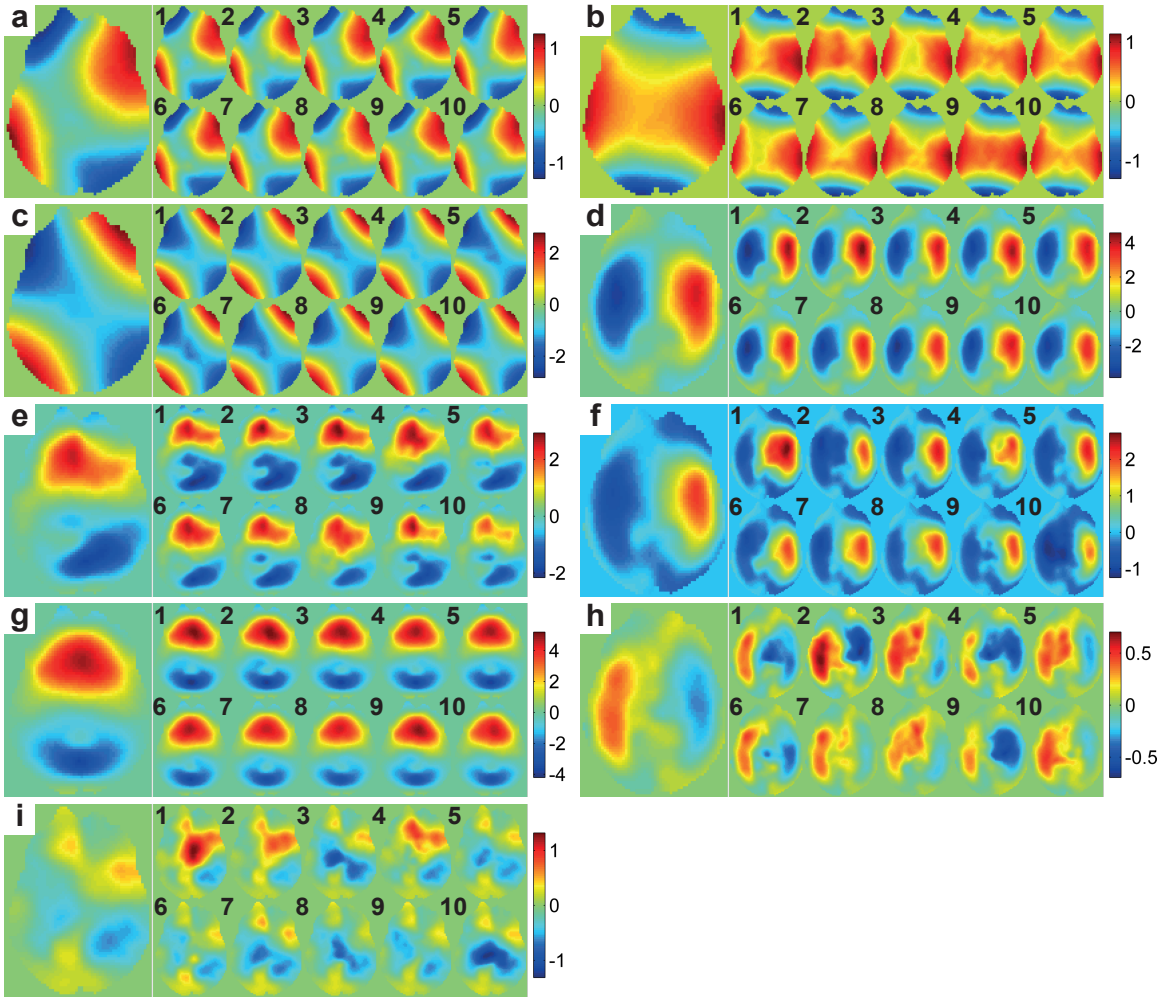


Figure 6.4.: Maps showing the fitted coefficients $C_1$ to $C_9$ for one slice of the in-vivo acquisition. The coefficients $C_1$ to $C_9$ are used to compute the phase components $\phi_{\text{eddy,nl}}$, which are caused by nonlinear eddy currents. The larger image in the left of each subfigure was calculated using all 10 repetitions jointly, while only one repetition was used for the smaller images as indicated by the numbers 1 to 10. **a**: $C_1$ ($q_x$), **b**: $C_2$ ($q_y$), **c**: $C_3$ ($q_z$), **d**: $C_4$ ($q_x q_y$), **e**: $C_5$ ($q_x q_z$), **f**: $C_6$ ($q_y q_z$), **g**: $C_7$ ($q_x^2$), **h**: $C_8$ ($q_y^2$), and **i**: $C_9$ ($q_z^2$).

area of higher MAV values, which is shaped similar to a pentagon. In the center of this pentagon, the MAV is highest and varies over the repetitions from about $0.4\,\mathrm{mm\,s^{-1}}$ to $0.6\,\mathrm{mm\,s^{-1}}$. This variation is likely caused by a nonuniform distribution of the DWIs over the cardiac cycle. Therefore, in some repetitions, the active period of pulsatile brain motion may be weighted to high, and in other repetitions to low. On the other hand, the shape of the aforementioned pentagon seems very stable and there are little features which are consistent in all repetitions. For example, there is a little buggle at the corner to the left, which can be observed in all repetitions. Also, the lower side edge is consistently bent innerwards. Moreover, below the lower edge of the pentagon is a little maximum which

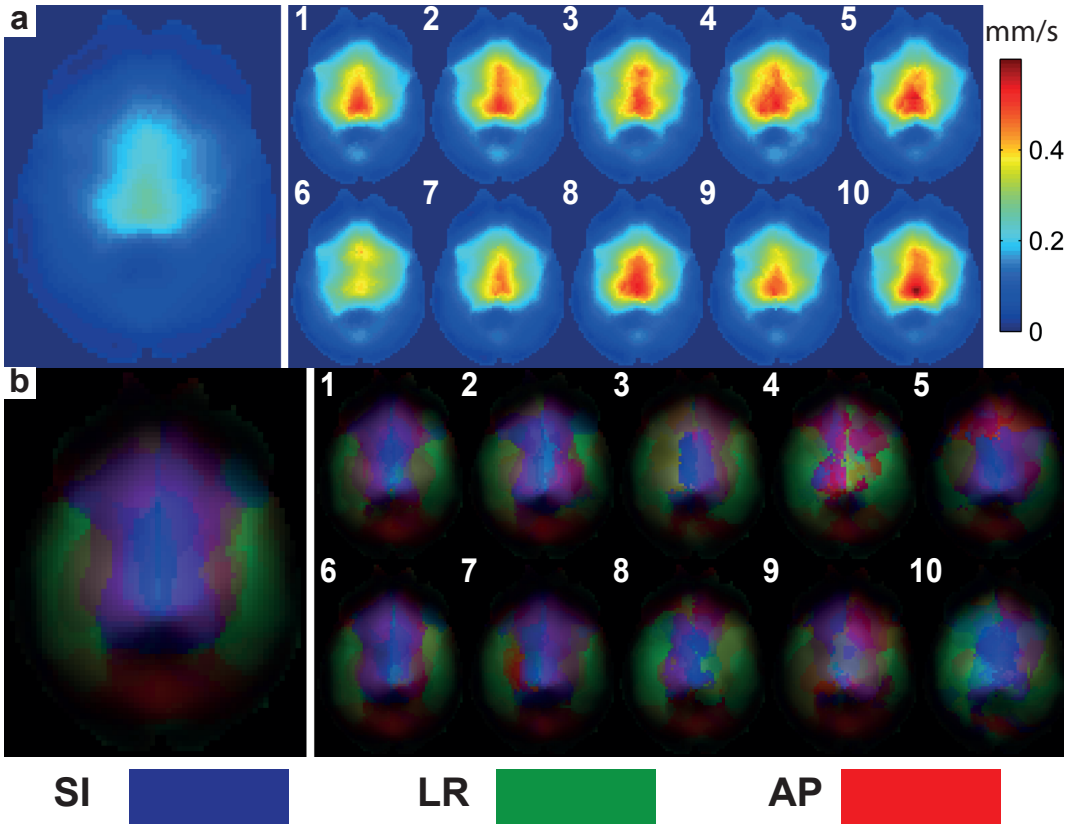


Figure 6.5.: **a**: MAV maps of the brain for one slice of the in-vivo acquisiton. Left, using a joint reconstruction of all 10 repetitions (1500 DWIs), right right using each repetition (150 DWIs) separately, as indicated by the numbers 1 to 10. **b**: Directional velocity maps of the brain for one slice of the in-vivo acquisiton. The intensity encodes MAV and the color encodes the direction as indicated by the colorbars below. Left, using a joint reconstruction of all 10 repetitions (1500 DWIs), right right using each repetition (150 DWIs) separately, as indicated by the numbers 1 to 10.

appears in all repetitions.

The MAV maps also exhibit a clear left–right symmetry which is expected because of the symmetry of the human brain. This symmetry can be observed in the directional velocity maps in 6.5b as well. The stability over the repetitions is significantly worse for the directional maps compared to the MAV maps. Especially in repetitions 4 and 9, the directional maps seem to be distorted with respect to the joint reconstruction. Despite the lower stability, the directionality of the measured brain pulsatility seems overall plausible. While motion in SI direction dominates in the center, at the left and the right edge, the predominant direction is LR. The aforementioned small spot below the lower edge of the pentagon, seems to be caused by motion in AP direction. It is not clear yet, whether this maximum originates from pulsatile brain motion, or maybe from scanner vibrations, which would also be plausible at the back of the head.

## 6.4. Discussion

A novel filtering technique was presented to extract quantitative information of the pulsatile motion of the brain from DWIs. Several phase components, which are superimposed with the phase originating from pulsatile brain motion, are sequentially removed, such as constant offsets, susceptibility induced phase, bulk motion induced phase, as well as linear and nonlinear eddy currents. The SD over the phase of all DWIs was used to investigate the spatial distribution of the phase variations. With each filtering step, the phase variations reduced significantly except for the regions around the ventricles, where pulsatile motion is expected to be highest [185].

In contrary to cine displacement encoding techniques [185] which are cardiac gated and sample the cardiac cycle equidistantly in time, DWIs are typically randomly distributed over the cardiac cycle. The randomness was exploited for estimating nonlinear eddy currents, where the assumption that phase contributions due to pulsatile motion cancel in average, was used. Since the accurate time of the cardiac cycle was not known, the novel metric MAV was introduce to quantify pulsatile motion. The computed MAV maps appear qualitatively similar compared to the results from Söllinger et al. [185], where a cine displacement encoding techniques was used. Also quantitatively, the MAV seem plausible compared to those results [185]. However, both techniques would need to be applied to the same subject for an accurate quantitative comparison. So far, the results are very encouraging but more data needs to be acquired to fully validate the proposed filtering technique.

An opened question is the origin of the phase patterns $\phi_{\text{eddy,nl}}$ which are assumed to result from nonlinear eddy currents (see Fig. 6.4). Although the proposed nonlinear correction seems to work well to estimate these phase patterns, their structure is actually too small to be caused from the gradient coils or other conductive material in the body of the scanner. Eddy currents in elements of the receive coils may be one explanation because, because the receive coil is placed very close to the head. However, the fairly high coefficients $C_7$, which describes the quadratic term $q_x^2$, contradict the assumption of eddy currents because according to the Lenz's rule, opposing changes of the magnetic field should induced opposing eddy currents. On the other hand, the quadratic term $q_x^2$ is reminiscent of the concomitant field (see section 2.3.3). However, phase terms originating from the concomitant field of the diffusion encoding gradients should fully cancel out in a ST preparation. Therefore, further research is needed to clarify the origin of these nonlinear phase patterns. Especially more experiments with static oil phantoms may be useful because of the low diffusivity of carbon hydrogen chains compared to water. Therefore, the eddy current effects of the gradients could be investigated independent from diffusion effects.

An advantage of the proposed filtering technique is that it works with conventional DWI data. Therefore, the microstructure of the brain and the brain pulsatility can be investigated jointly. There is, however, a lower limit for the number of DWIs, which are required for the nonlinear phase correction. For acquisition with less than about 100 DWIs, the requirement, that the phase induced by pulsatile motion cancels, may be not fulfilled. An alternative to increase robustness of the filtering technique, is to record the cardiac cycle during the measurement such that each DWI can be associated with the accurate time of the cardiac cycle. This knowledge could be incorporated into the estimation of nonlinear eddy current induced phase as well as the estimation of the MAV maps or more sophisti-

cated models of the brain pulsatility.

In conclusion, DWIs offer more information than magnitude based models provide. The feasibility to quantify the pulsatile motion of the brain using conventional DWI data was demonstrated in this work. In future work, more sophisticated models of the pulsatile brain motion may allow to derive also bio-mechanical features such as elasticity [194].

# 7. Conclusion

The work presented in this thesis contributes to the advancement of Diffusion Weighted Imaging (DWI) in the areas of data acquisition, data preprocessing and data quantification. In particular the problematic of low Signal to Noise Ratio (SNR) in DWI was addressed. Conventional magnitude processing leads to an overestimation of the signal's amplitude at low SNR. Consequently, estimated diffusion model parameters are systematically biased which reduces the comparability of quantitative DWI metrics. Moreover, magnitude processing also reduces the contrast of DWIs at low SNR which, for example, hampers the estimation of fiber orientation or the identification of fiber crossings in the human brain.

In chapter 3, the impact of low SNR on the estimation of Diffusion Kurtosis Imaging (DKI) model parameters was extensively investigated assuming a Weighted Linear Least Squares (WLLS) fitting algorithm. The results were published as a full paper, entitled "Bias and precision analysis of DKI for different acquisition schemes" in Magnetic Resonance in Medicine [121]. It was reported by Veraart et al., that magnitude processing generally results in an overestimation of the Apparent Kurtosis Coefficient (AKC) [68, 71, 129]. However, the results presented here indicated that the bias of the AKC can be highly heterogeneous and dependent on the tissue type and the orientation of the diffusion encoding gradient. Negative and positive bias were observed in both, simulation and in-vivo experiments. The impact of the diffusion encoding scheme on the AKC estimation accuracy seemed rather small in the simulation results. However, in in vivo experiments, the estimated AKC seemed to depend on the diffusion encoding scheme, even if the maximum b-value was the same. It was concluded that this behavior is predominantly caused by imperfections of the DKI model, which are more pronounced in certain b-value regions. Consequently, the model induced error not only depends on the maximum b-value, which is for example the case in Diffusion Tensor Imaging (DTI) [73], but also on the distribution of the b-values in radial direction. Moreover, the diffusion encoding scheme had a large impact on the precision of the DKI model parameters. Overall, a 3-shell scheme, suggested by Poot et al. [123], performed best but also an undersampled Diffusion Spectrum Imaging (DSI) acquisition with subsequent Compressed Sensing (CS) reconstruction [126] provided a good precision of the parametric DKI maps. It was further shown that denoising methods performed on magnitude data, such as CS or even simple averaging, can substantially change the signal bias. In conclusion, an accurate quantification of the DKI model based on magnitude data seemed difficult and motivated the development of a preprocessing method to obtain real valued data.

In chapter 4, a novel Phase Correction (PC) technique was adopted which avoids magnitude processing and significantly reduces the noise induced bias in DWI. The results were published as a full paper, entitled "Real Valued Diffusion-Weighted Imaging Using Decorrelated Phase Filtering" in Magnetic Resonance in Medicine [139]. PC in DWIs is generally challenging because the motion encoding of intracranial pulsatility can result in spatially very inhomogeneous phase pattern, which hampers the estimation of the signal's

true phase in each voxel. Recently, Prah et al. demonstrated that real-valued diffusion-weighted images can be obtained by using a spatial box-car filter to estimate the phase distribution of the complex images and apply a corresponding transformation to shift the signal to the real part [131]. The bias reduction of Prah et al's technique scales with the kernel size which is unfortunately at the expense of a significantly increased sensitivity to local phase variations that can lead to unwanted signal loss. In this thesis, Prah et al.'s approach was extended using improved filter kernels that consider the spatial noise correlations that are introduced in the image reconstruction chain, e.g. by regridding or Partial Fourier. Compared to Prah et al.'s technique, the performance of size 3 kernels could be improved by a factor of 4, and an optimized size 5 kernel even achieved virtually zero bias. Additionally, an outlier estimation method was proposed where voxels with potentially incorrect PC are identified in their majority and the real value is replaced by the magnitude value. The necessity of such an outlier detection and correction technique for quantitative DWI was demonstrated on parametric maps of the DKI model. Incorrect PC resulted in a local, erroneous underestimation of MZ, which could have been easily confused with pathology. However, when the real values of detected outlier voxels were replaced with the magnitude, these erroneous underestimations completely vanished. A very promising application of PC is DSI, as the SNR is typically very low because high b-values are required [63]. Compared to magnitude processing, PC achieved a better delineation of features in the Ensemble Average Propagator (EAP), e.g. fiber crossings, and the delineation improved as the noise floor was lowered. Overall, the proposed phase correction technique can significantly improve the quality of DWI data yielding both, a better contrast and a more accurate estimation of diffusion model parameters.

In chapter 5, a comprehensive framework was presented to systematically compare the SNR efficiency of different DWI sequences. This framework was used to evaluate the SNR efficiency of recently reported DWI sequences, i.e. Multi-Slab Echo Planar Imaging (MS-EPI), Simultaneous Multi-Slice Echo Planar Imaging (SMS-EPI) and Diffusion-Weighted Steady State Free Precession (DWSSFP), for brain imaging. In this comparison, a modern MR scanner with a maximum gradient strength of $50\,\mathrm{mT\,m^{-1}}$ was assumed. For the given setup, the slice thickness had the largest impact on the SNR efficiency because the Repetition Time (TR) increases with the number of slices. The spoiled sequences with Stejskal Tanner (ST) diffusion preparation reached the highest SNR efficiency at about $1.4T_1$. If the TR drops below this value, the SNR efficiency is reduced due to $T_1$ saturation. For moderate slice thicknesses between $2\,\mathrm{mm}$ and $3\,\mathrm{mm}$, SMS-EPI achieved comparable results to MS-EPI with an optimal TR. However, the maximum efficiency gain of SMS-EPI is intrinsically limited to the square root of the multiband acceleration factor MB. Unfortunately, MB factors higher than three are problematic because the separation of the simultaneously excited slices causes a g-factor penalty which may exceed potential gains in SNR efficiency [22, 23]. Simulation results in this work indicated that for slice thicknesses significantly below $2\,\mathrm{mm}$, MS-EPI may be a valuable alternative because it does not rely on parallel imaging in the reconstruction process. A publication of this work is currently in preparation.

Apart from SMS-EPI and MS-EPI, the potential of the pulsed DWSSFP was evaluated for in vivo application on the brain. At first, the accuracy of DWSSFP signal models, that were reported in literature, was evaluated for different parameter sets using random walk simulations as ground truth. Since none of these models predicted the DWSSFP signal

correctly for all parameters sets, a new, accurate model was proposed. A random walk simulation was also used to investigate the motion sensitivity of DWSSFP based on the pulsatility profile of the thalamus region in the brain as reported in Söllinger et al. [185]. It was found that the pulsatile motion of the brain can substantially disrupt the steady state, causing an unwanted signal loss. In addition, the calculated SNR efficiency of DWSSFP was generally smaller than MS-EPI and outperformed SMS-EPI only for slice thicknesses significantly smaller than $1\,\mathrm{mm}$. Therefore, it was concluded that MS-EPI and SMS-EPI are favorable over DWSSFP for in vivo DWI of the brain. However, encouraging results of DWSSFP have been reported for in vivo DWI of the knee cartilage [177, 182], and most important, for ex vivo DWI of the brain [174, 176].

In chapter 6, a novel phase filtering method was proposed that extracts the signal's phase of DWIs that originates from the pulsatile motion of the brain. It was motivated by the fact that magnitude processing not only yields distorted values of the diffusion weighted signal [21], but also discards potentially valuable information about the brain pulsatility [20]. Intermediate results of this work were submitted to the 23rd Annual Meeting of ISMRM 2015 and the 21st Annual Meeting of the OHBM 2015 where it received a "Summa Cum Laude Award" and a "Merit Award", respectively [160, 191]. For quantitative evaluation of the brain pulsatility, the novel metric Mean Absolute Velocity (MAV) was introduced, which describes the mean velocity of the brain tissue. The results were very encouraging and a comparison of the MAV maps with literature results seemed qualitatively and quantitatively plausible [185]. The major advantage of the proposed filtering technique is that it works with conventional DWI data. Therefore, the microstructure of the brain and the brain pulsatility can be investigated jointly. In future work, this technique may be used for extracting also bio-mechanical features such as elasticity from DWI data [194].

In summary, this thesis contributed to the data acquisition in DWI with a systematic comparison of the SNR efficiency of different diffusion preparation and readout approaches. Also, the diffusion encoding scheme was investigated to maximize the estimation accuracy and precision of DKI model parameters. In the area of data preprocessing, a novel PC technique was adopted that substantially reduces the signal bias and increases the image contrast. Moreover, a compressed sensing algorithm was optimized for denoising the DWI data to increase the precision of subsequent processing steps. In the field of data quantification, different fit routines for the DKI model were implemented and analyzed. On top of this, a new phase filtering technique was proposed which allows for quantifying not only the diffusivity of the tissue from DWI data, but also the brain pulsatility. The methods that were adopted in this thesis increase the data quality and quantity in DWI, pushing the limits of this fascinating technology to explore human brain.

# A. Appendix

## A.1. Phase correction - additional outlier maps

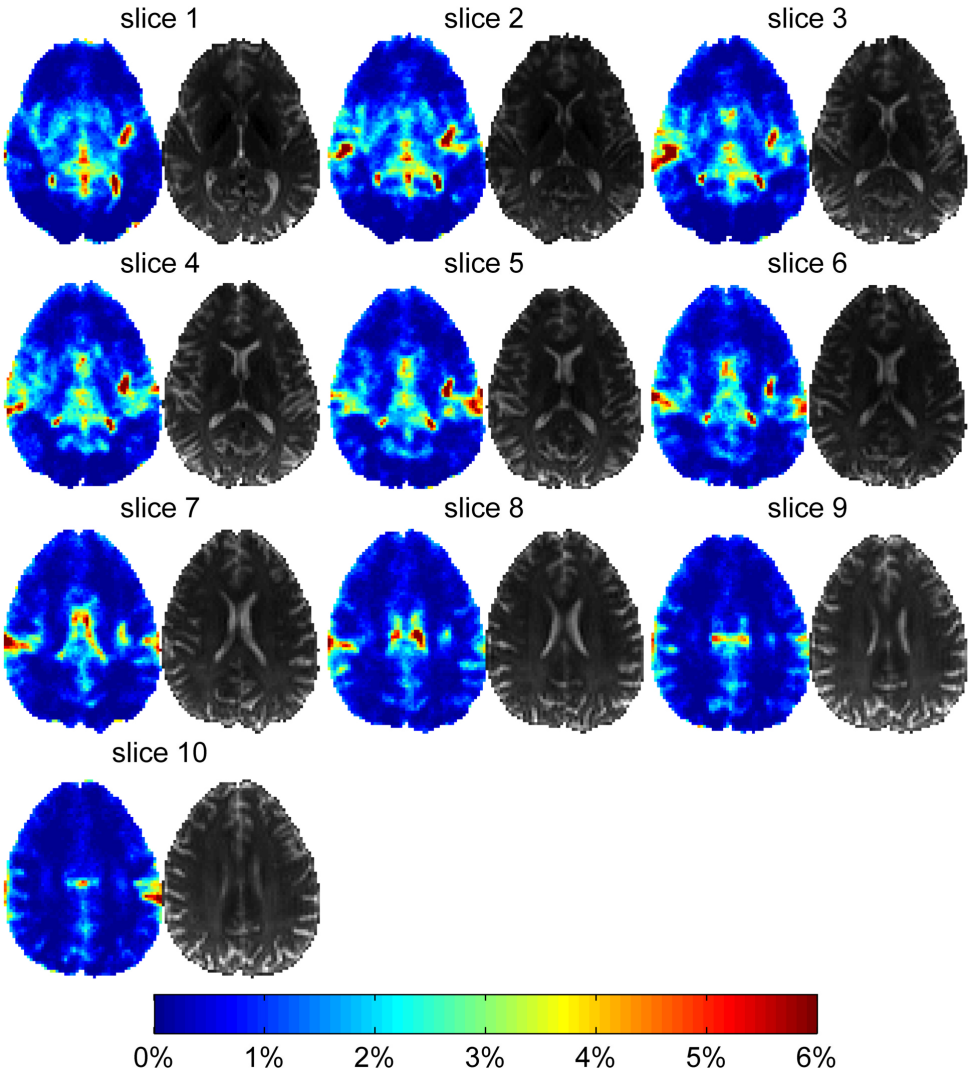


Figure A.1.: Maps indicating the fraction of outliers exceeding threshold $\sigma_T = 2\sigma$ among all DWIs for kernel Opt3 and all slices in ACQ2.

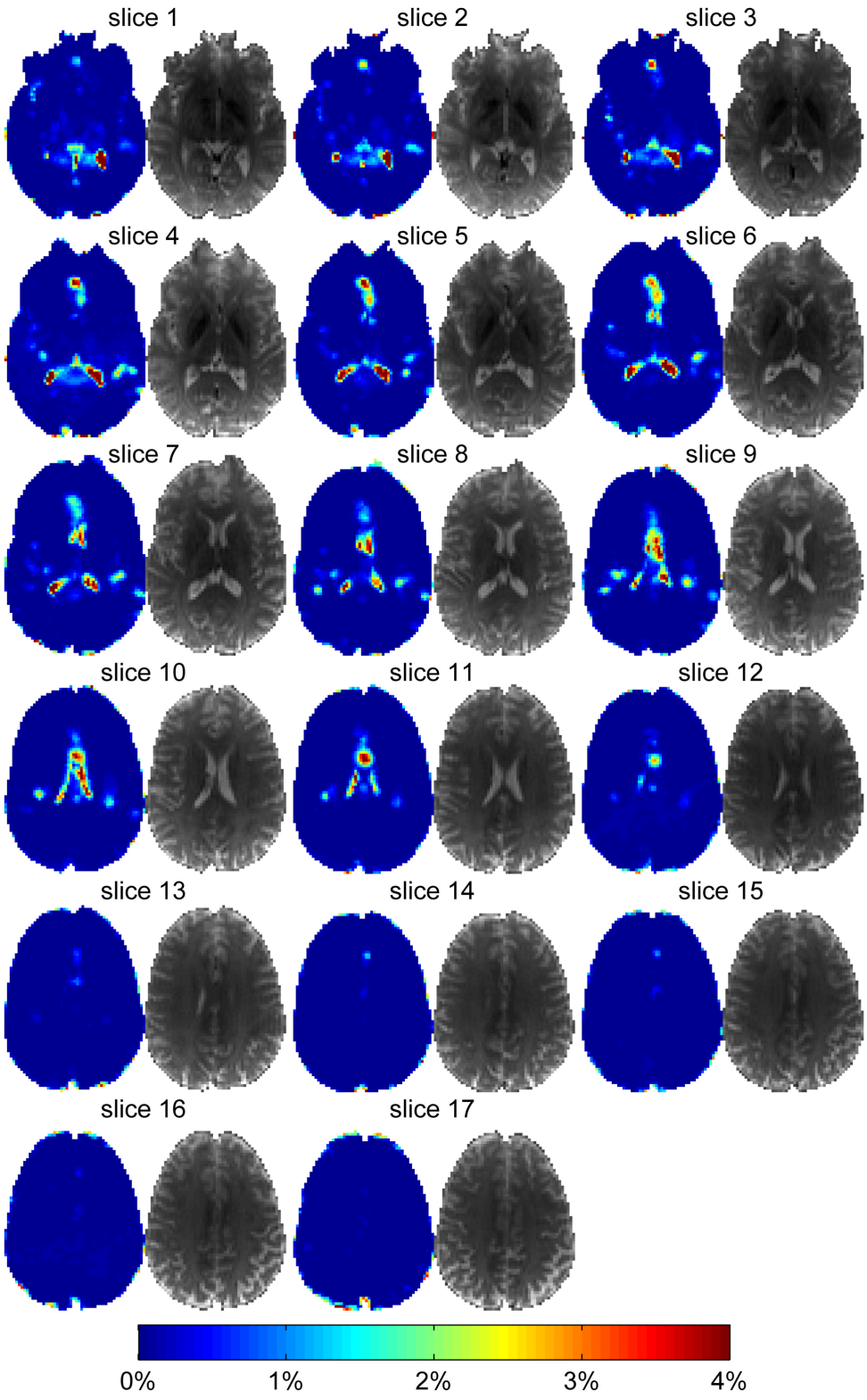


Figure A.2.: Maps indicating the fraction of outliers exceeding threshold $\sigma_T = 2\sigma$ among all DWIs for kernel Opt3 and all slices in ACQ1.

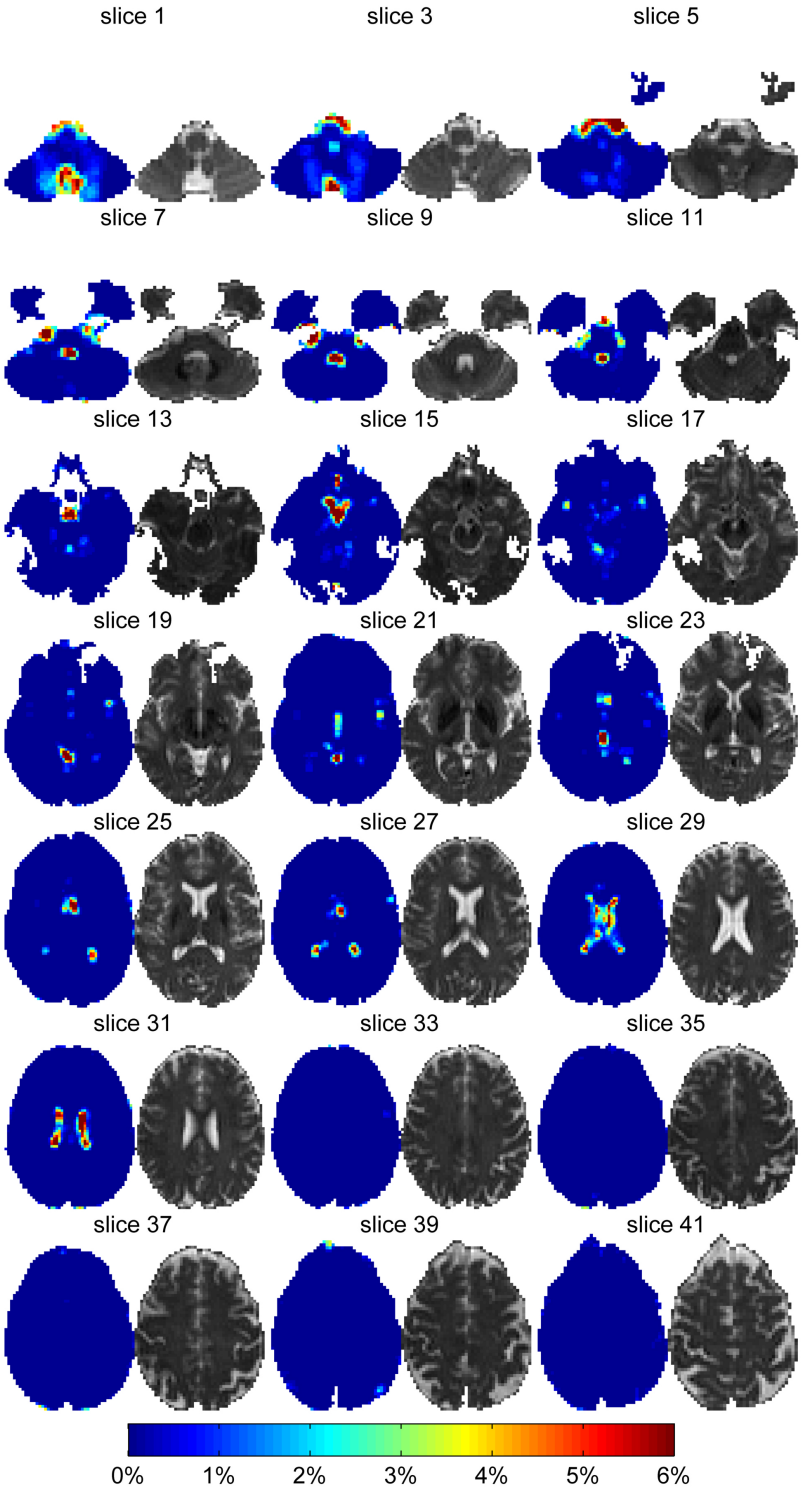


Figure A.3.: Maps indicating the fraction of outliers exceeding threshold $\sigma_T = 2\sigma$ among all DWIs for kernel Opt3. The underlying dataset is a full DSI acquisition, with $2.5\,\mathrm{mm}$ isotropic resolution, maximum b-value of $3000\,\mathrm{s\,mm^{-2}}$ and full brain coverage.

## A.2. The KWF model

The following equations describe the novel KWF model as suggested in chapter 5. According to Kaiser et al. the general solution of the DWSSFP signal with can be written as a Fourier series. The KWF model uses the same approach.

$$M_x(\theta,t) = -\sum_{k=-\infty}^{+\infty} b_k E_{2,k}(t) \sin\left[\left(k+\frac{t}{\mathrm{TR}}\right)\theta\right] \tag{A.1}$$

$$M_y(\theta,t) = \sum_{k=-\infty}^{+\infty} b_k E_{2,k}(t) \cos\left[\left(k+\frac{t}{\mathrm{TR}}\right)\theta\right] \tag{A.2}$$

$$M_z(\theta,t) = M_0 + \sum_{k=-\infty}^{+\infty} c_k E_{1,k}(t) \cos k\theta \tag{A.3}$$

The damping terms $E_{1,k}^{\mathrm{KWF}}(t)$ and $E_{2,k}^{\mathrm{KWF}}(t)$ for pulsed diffusion gradients can be calculated following the approach of Wu and Buxton [172].

$$E_{1,k}^{\mathrm{KWF}}(t) = \exp\left(-\frac{t}{T_1} - D(\gamma\tau G)^2 k^2 t\right) \tag{A.4}$$

$$E_{2,k}^{\mathrm{KWF}}(t) = H_{2,k}\exp\left(-\frac{t}{T_2} - D(\gamma\tau G)^2 (k+1)^2 t\right) \tag{A.5}$$

$$H_{2,k} = \exp\left(D(\gamma\tau G)^2[\tau(k+\frac{2}{3}) + \epsilon(2k+1)]\right) \tag{A.6}$$

$\mathrm{S_{FID}}$ ($t=0$) and $\mathrm{S_{echo}}$ ($t=\mathrm{TR}$) can be derived from Eqs. A.2 and A.1 using the assumptions of practical imaging conditions as shown in section 5.2.1.

$$\mathrm{S_{FID,KWF}} = \frac{1}{2\pi}\int_0^{2\pi} M_y(\theta,0)\,d\theta = b_0 \ , \tag{A.7}$$

$$\mathrm{S_{echo,KWF}} = \frac{1}{2\pi}\int_0^{2\pi} M_y(\theta,\mathrm{TR})\,d\theta = b_1 E_{2,k}(t) \ . \tag{A.8}$$

Freed et al. suggested a recursion equation (not shown, details can be found in [183]) to obtain the coefficients $b_{-1,\mathrm{KWF}}$ and $b_{0,\mathrm{KWF}}$.

$$b_{0,\mathrm{KWF}} = \frac{-\sin\alpha M_0\big(1-E_{1,0}(\mathrm{TR})\big)}{A_{k=0}+E_{2,-1}(\mathrm{TR})C_{k=0}r_1} \ , \tag{A.9}$$

$$b_{-1,\mathrm{KWF}} = -r_1 b_{0,\mathrm{KWF}} \ , \tag{A.10}$$

where

$$A_k = \frac{1}{2}\big(E_{1,0}(\mathrm{TR})-1\big)\big(1+\cos\alpha\big) \ , \tag{A.11}$$

$$B_k = \frac{1}{2}\big(E_{1,0}(\mathrm{TR})+1\big)\big(1-\cos\alpha\big) \ , \tag{A.12}$$

$$C_k = A_k + B_k \ . \tag{A.13}$$

The term $r_1$ is given in a truncated continued fraction notation

$$r_1 = \frac{x_1}{E_{2,-1}(\mathrm{TR})B_{k=0}} + \frac{E_{2,0}(\mathrm{TR})C_{k=1}}{B_{k=1}} \tag{A.14}$$

where $x_1$ is the truncated continued fraction

$$x_1 = \frac{n_1}{d_1 + \dfrac{n_2}{d_2 ... + \dfrac{n_l}{d_l + e_l}}} \ , \tag{A.15}$$

with $n_k$ is the numerator

$$n_k = \frac{-E_{2,-k}(\mathrm{TR}) E_{2,k-1}(\mathrm{TR}) A_k^2 B_{k-1}}{B_k} \ , \tag{A.16}$$

$d_k$ is the denominator

$$d_k = \left(A_k - B_k\right) + \frac{E_{2,-k-1}(\mathrm{TR}) E_{2,k}(\mathrm{TR}) B_k C_{k+1}}{B_{k+1}} \tag{A.17}$$

and $e_k$ is the extra term

$$e_k = -\frac{E_{2,k}(\mathrm{TR}) E_{2,-k-1}(\mathrm{TR}) B_k C_{k+1}}{B_{k+1}} \ . \tag{A.18}$$

The simulation results in chapter 5 indicated, that the KWF model is accurate solution of the Bloch–Torrey equation [45] assuming a steady state with pulsed diffusion gradients (pulsed DWSSFP).

# Abbreviations List

**1D** one-dimensional.

**2D** two-dimensional.

**3D** three-dimensional.

**A/D** Analog-Digital-Converter.

**ADC** Apparent Diffusion Coefficient.

**AKC** Apparent Kurtosis Coefficient.

**AKC$_{\perp}$** Radial Kurtosis.

**AKC$_{max}$** Maximum Kurtosis.

**AKC$_{min}$** Minimum Kurtosis.

**AKC$_{||}$** Axial Kurtosis.

**AP** Anterior-Posterior.

**BOLD** Blood Oxygenation Level Dependent.

**bSSFP** Balanced Steady State Free Precession.

**CHARMED** Composite Hindered and Restricted Model of Diffusion.

**CP** Coherence Pathway.

**CS** Compressed Sensing.

**CS-DSI** Compressed Sensing Diffusion Spectrum Imaging.

**CSF** Cerebrospinal Fluid.

**DFT** Discrete forward Fourier Transformation.

**DKI** Diffusion Kurtosis Imaging.

**DKT** Diffusion Kurtosis Tensor.

**DSI** Diffusion Spectrum Imaging.

**DSV** Diameter Spherical Volume.

**DT** Diffusion Tensor.

**DTI** Diffusion Tensor Imaging.

**DWI** Diffusion Weighted Imaging.

**DWSSFP** Diffusion-Weighted Steady State Free Precession.

**EAP** Ensemble Average Propagator.

**EPI** Echo Planar Imaging.

**ESP** Echo Spacing.

**FA** Fractional Anisotropy.

**FE** Frequency Encoding.

**FID** Free Induction Decay.

**FLAIR** Fluid Attenuated Inversion Recovery.

**FLASH** Fast Low-Angle Shot.

**FOV** Field Of View.

**FRF** Frequency Response Function.

**FWHM** Full Width Half Maximum.

**GM** Gray Matter.

**GRE** Gradient Echo.

**HARDI** High Angular Resolution Diffusion-weighted Imaging.

**IDFT** Inverse Discrete forward Fourier Transformation.

**LLS** Linear Least Squares.

**LR** Left-Right.

**MAD** Median Absolute Deviation.

**MAV** Mean Absolute Velocity.

**MB** Multiband acceleration factor for SMS-EPI.

**MD** Mean Diffusivity.

**ME** Ellipsoidal average AKC.

**MK** Spherical average AKC.

**MLE** Maximum Likelihood Estimation.

**MP RAGE** Magnetization-Prepared Rapid Gradient-Echo Imaging.

**MR** Magnetic Resonance.

**MRI** Magnetic Resonance Imaging.

**MS-EPI** Multi-Slab Echo Planar Imaging.

**MSD** Mean Squared Displacement.

**MZ** Average AKC in the scaled inherent coordinate system.

**NLS** Nonlinear Least Squares.

**NMR** Nuclear Magnetic Resonance.

**NODDI** Neurite Orientation Dispersion and Density Imaging.

**ODF** Orientation Distribution Function.

**OEC** Odd/Even Correction.

**PC** Phase Correction.

**PE** Phase Encoding.

**RARE** Rapid Acquisition with Relaxation Enhancement.

**RF-pulse** Radio Frequency Pulse.

**RMSE** Root Mean Squared Error.

**RWS** Random Walk Simulation.

**SAR** Specific Absorption Rate.

**SD** Standard Diviation.

**SE** Spin Echo.

**SENSE** Sensitivity Encoding.

**SI** Superior-Inferior.

**SLR** Shinnar Le Roux algorithm.

**SMS** Simultaneous Multi-Slice.

**SMS-EPI** Simultaneous Multi-Slice Echo Planar Imaging.

**SNR** Signal to Noise Ratio.

**SPGR** Spoiled Gradient Echo.

**SSFP** Steady State Free Precession.

**ST** Stejskal Tanner.

**STE** Stimulated Echo.

**STIR** Short Tau Inversion Recovery.

**TE** Echo Time.

**TR** Repetition Time.

**TSE** Turbo Spin Echo.

**uDSI** undersampled DSI.

**WLLS** Weighted Linear Least Squares.

**WM** White Matter.

# Bibliography


[1] Lauterbur PC. Image Formation by Induced Local Interactions: Examples Employing Nuclear Magnetic Resonance. Nature 1973;242:190–191. 1

[2] Filippi M, Rocca MA. MR imaging of multiple sclerosis. Radiology 2011;259:659–81. 1

[3] Tokuda O, Harada Y, Shiraishi G, et al. MRI of the anatomical structures of the knee: the proton density-weighted fast spin-echo sequence vs the proton density-weighted fast-recovery fast spin-echo sequence. The British Journal of Radiology 2012;85:e686–e693. 1

[4] Haacke EM, Xu Y, Cheng YC, Reichenbach JR. Susceptibility weighted imaging (SWI). Magn Reson Med 2004;52:612–8. 1, 33, 34

[5] Ogawa S, Lee TM, Kay AR, Tank DW. Brain magnetic resonance imaging with contrast dependent on blood oxygenation. Proc Natl Acad Sci U S A 1990;87:9868–9872. 1, 33, 34

[6] Carr HY, Purcell EM. Effects of Diffusion on Free Precession in Nuclear Magnetic Resonance Experiments. Phys Rev 1954;94:630–638. 1, 15, 18, 37

[7] Le Bihan D, Breton E, Lallemand D, Grenier P, Cabanis E, Laval-Jeantet M. MR imaging of intravoxel incoherent motions: application to diffusion and perfusion in neurologic disorders. Radiology 1986;161:401–407. 1

[8] Brown R. A brief account of microscopical observations made in the months of June, July and August, 1827, on the particles contained in the pollen of plants; and on the general existence of active molecules in organic and inorganic bodies, 1828. 1, 14

[9] Basser PJ, Mattiello J, LeBihan D. Estimation of the effective self-diffusion tensor from the NMR spin echo. J Magn Reson B 1994;103:247–54. 2, 21

[10] Basser PJ, Mattiello J, LeBihan D. MR diffusion tensor spectroscopy and imaging. Biophys J 1994;66:259–67. 2

[11] Schaefer PW, Grant PE, Gonzalez RG. Diffusion-weighted MR Imaging of the Brain. Radiology 2000;217:331–345. 2

[12] Tuch DS, Reese TG, Wiegell MR, Wedeen VJ. Diffusion MRI of complex neural architecture. Neuron 2003;40:885–95. 2, 20

[13] Lu H, Jensen JH, Ramani A, Helpern JA. Three-dimensional characterization of non-gaussian water diffusion in humans using diffusion kurtosis imaging. NMR Biomed 2006;19:236–47. 47

[14] Alexander DC. Axon radius measurements in vivo from diffusion MRI: a feasibility study. In Computer Vision, 2007. ICCV 2007. IEEE 11th International Conference on. 2007; 1–8. 2, 20

[15] Jensen JH, Helpern JA, Ramani A, Lu H, Kaczynski K. Diffusional kurtosis imaging: the quantification of non-gaussian water diffusion by means of magnetic resonance imaging. Magn Reson Med 2005;53:1432–40. 2, 20, 22, 47, 48, 63

[16] Saygin ZM, Norton ES, Osher DE, et al. Tracking the Roots of Reading Ability: White Matter Volume and Integrity Correlate with Phonological Awareness in Prereading and Early-Reading Kindergarten Children. The Journal of Neuroscience 2013;33:13251–13258. 2

[17] Barbeau EB, Lewis JD, Doyon J, Benali H, Zeffiro TA, Mottron L. A greater involvement of posterior brain areas in interhemispheric transfer in autism: fMRI, DWI and behavioral evidences. Neuroimage Clin 2015;8:267–80.

[18] Frisoni GB, Fox NC, Jack CR, Scheltens P, Thompson PM. The clinical use of structural MRI in Alzheimer disease. Nat Rev Neurol 2010;6:67–77.

[19] Fitzsimmons J, Kubicki M, Shenton ME. Review of functional and anatomical brain connectivity findings in schizophrenia. Curr Opin Psychiatry 2013;26:172–87. 2

[20] Wagshul ME, Eide PK, Madsen JR. The pulsating brain: A review of experimental and clinical studies of intracranial pulsatility. Fluids Barriers CNS 2011;8:5–5. 2, 3, 33, 64, 109, 125

[21] Jones DK, Basser PJ. "Squashing peanuts and smashing pumpkins": how noise distorts diffusion-weighted MR data. Magn Reson Med 2004;52:979–93. 2, 63, 95, 125

[22] Setsompop K, Cohen-Adad J, Gagoski BA, et al. Improving diffusion MRI using simultaneous multi-slice echo planar imaging. Neuroimage 2012;63:569–580. 3, 81, 83, 97, 107, 124

[23] Setsompop K, Gagoski BA, Polimeni JR, Witzel T, Wedeen VJ, Wald LL. Blipped-controlled aliasing in parallel imaging for simultaneous multislice echo planar imaging with reduced g-factor penalty. Magn Reson Med 2012;67:1210–1224. 3, 81, 84, 107, 124

[24] Engström M, Skare S. Diffusion-weighted 3D multislab echo planar imaging for high signal-to-noise ratio efficiency and isotropic image resolution. Magn Reson Med 2013;70:1507–1514. 3, 64, 84, 107

[25] O'Halloran RL, Aksoy M, Van AT, Bammer R. 3D isotropic high-resolution diffusion-weighted MRI of the whole brain with a motion-corrected steady-state free precession sequence. Magn Reson Med 2013;70:466–78. 3, 84, 92, 96, 105, 108

[26] Pruessmann KP, Weiger M, Scheidegger MB, Boesiger P. SENSE: sensitivity encoding for fast MRI. Magn Reson Med 1999;42:952–62. 3, 39, 40, 42, 48, 67, 83, 95, 115

[27] Van AT, Aksoy M, Holdsworth SJ, Kopeinigg D, Vos SB, Bammer R. Slab profile encoding (PEN) for minimizing slab boundary artifact in three-dimensional diffusion-weighted multislab acquisition. Magn Reson Med 2015;73:605–13. 3, 84, 97, 107

[28] Rabi II, Zacharias JR, Millman S, Kusch P. A New Method of Measuring Nuclear Magnetic Moment. Phys Rev 1938;53:318–318. 7

[29] Landé A. Termstruktur und Zeemaneffekt der Multipletts. Z Physik 1923;19:112–123. 8

[30] Madelin G, Regatte RR. Biomedical applications of sodium MRI in vivo. J Magn Reson Imaging 2013;38:511–529. 9

[31] Ardenkjær-Larsen JH, Fridlund B, Gram A, et al. Increase in signal-to-noise ratio of > 10,000 times in liquid-state NMR. Proc Natl Acad Sci U S A 2003;100:10158–10163. 9

[32] Zeeman P. The Effect of Magnetisation on the Nature of Light Emitted by a Substance. Nature 1897;55:347–347. 9

[33] Einstein A. Strahlungs-Emission und -Absorption nach der Quantentheorie. Deutsche Physikalische Gesellschaft 1916;18:318–323. 11, 15

[34] Rabi II, Ramsey NF, Schwinger J. Use of Rotating Coordinates in Magnetic Resonance Problems. Reviews of Modern Physics 1954;26:167–171. 11

[35] Haacke E, Brown R, Thompson M, Venkatesan R. Magnetic Resonance Imaging: Physical Principles and Sequence Design. Wiley, 1999. 11, 13, 116

[36] Bernstein M, King K, Zhou X. Handbook of MRI Pulse Sequences. Elsevier Science, 2004. 12, 30, 32, 37, 45

[37] Shinnar M, Bolinger L, Leigh JS. The synthesis of soft pulses with a specified frequency response. Magn Reson Med 1989;12:88–92. 12, 28

[38] Bloch F. Nuclear Induction. Phys Rev 1946;70:460–474. 13, 85

[39] Hahn EL. Spin Echoes. Phys Rev 1950;80:580–594. 13, 18

[40] Hahn EL, Maxwell DE. Chemical Shift and Field Independent Frequency Modulation of the Spin Echo Envelope. Phys Rev 1951;84:1246–1247. 13

[41] Burstein D. Stimulated echoes: Description, applications, practical hints. Concept Magnetic Res 1996;8:269–278. 13

[42] Meiboom S, Gill D. Modified Spin-Echo Method for Measuring Nuclear Relaxation Times. Review of Scientific Instruments 1958;29:688–691. 15, 37

[43] Boxerman JL, Hamberg LM, Rosen BR, Weisskoff RM. MR contrast due to intravascular magnetic susceptibility perturbations. Magn Reson Med 1995;34:555–66. 15

[44] Fick A. Ueber Diffusion. Annalen der Physik 1855;170:59–86. 15

[45] Torrey HC. Bloch Equations with Diffusion Terms. Phys Rev 1956;104:563–565. 16, 17, 18, 85, 131

[46] Abragam A. The Principles of Nuclear Magnetism. Clarendon Press, 1961.

[47] Callaghan P. Translational Dynamics and Magnetic Resonance: Principles of Pulsed Gradient Spin Echo NMR. OUP Oxford, 2011. 17, 18, 26

[48] Stejskal EO, Tanner JE. Spin Diffusion Measurements: Spin Echoes in the Presence of a Time Dependent Field Gradient. J Chem Phys 1965;42:288–292. 18, 69, 83, 85, 96

[49] Mattiello J, Basser PJ, Lebihan D. Analytical Expressions for the b Matrix in NMR Diffusion Imaging and Spectroscopy. Journal of Magnetic Resonance, Series A 1994; 108:131–141. 20

[50] Alexander AL, Lee JE, Lazar M, Field AS. Diffusion Tensor Imaging of the Brain. Neurotherapeutics : the journal of the American Society for Experimental NeuroTherapeutics 2007;4:316–329. 20, 23

[51] Charles N. Diffusion and related transport mechanisms in brain tissue. Reports on Progress in Physics 2001;64:815. 20

[52] Le Bihan D. Molecular diffusion, tissue microdynamics and microstructure. NMR Biomed 1995;8:375–86. 20

[53] Beaulieu C. The basis of anisotropic water diffusion in the nervous system - a technical review. NMR Biomed 2002;15:435–55. 20, 22

[54] Johansen-Berg H, Behrens T. Diffusion MRI: From Quantitative Measurement to In vivo Neuroanatomy. Elsevier Science, 2013. 21

[55] Tournier JD, Mori S, Leemans A. Diffusion tensor imaging and beyond. Magn Reson Med 2011;65:1532–1556. 21, 22, 27

[56] Tuch DS, Reese TG, Wiegell MR, Makris N, Belliveau JW, Wedeen VJ. High angular resolution diffusion imaging reveals intravoxel white matter fiber heterogeneity. Magn Reson Med 2002;48:577–582. 21, 22, 63

[57] Hosey T, Williams G, Ansorge R. Inference of multiple fiber orientations in high angular resolution diffusion imaging. Magn Reson Med 2005;54:1480–9. 21

[58] Assaf Y, Basser PJ. Composite hindered and restricted model of diffusion (CHARMED) MR imaging of the human brain. Neuroimage 2005;27:48–58. 22, 63

[59] Assaf Y, Blumenfeld-Katzir T, Yovel Y, Basser PJ. AxCaliber: a method for measuring axon diameter distribution from diffusion MRI. Magn Reson Med 2008;59:1347–54. 22, 63

[60] Zhang H, Schneider T, Wheeler-Kingshott CA, Alexander DC. NODDI: practical in vivo neurite orientation dispersion and density imaging of the human brain. Neuroimage 2012;61:1000–16. 22, 63

[61] Ferizi U, Schneider T, Witzel T, et al. White matter compartment models for in vivo diffusion MRI at 300mT/m. Neuroimage 2015;118:468–83. 22, 26

[62] Callaghan PT. Principles of Nuclear Magnetic Resonance Microscopy. Clarendon Press, 1993. 22

[63] Wedeen VJ, Hagmann P, Tseng WY, Reese TG, Weisskoff RM. Mapping complex tissue architecture with diffusion spectrum magnetic resonance imaging. Magn Reson Med 2005;54:1377–86. 22, 27, 62, 63, 70, 81, 124

[64] Basser PJ, Pierpaoli C. Microstructural and physiological features of tissues elucidated by quantitative-diffusion-tensor MRI. J Magn Reson B 1996;111:209–19. 23

[65] Pierpaoli C, Basser PJ. Toward a quantitative assessment of diffusion anisotropy. Magn Reson Med 1996;36:893–906.

[66] Thomason ME, Thompson PM. Diffusion imaging, white matter, and psychopathology. Annu Rev Clin Psychol 2011;7:63–85. 23

[67] Song SK, Sun SW, Ramsbottom MJ, Chang C, Russell J, Cross AH. Dysmyelination revealed through MRI as increased radial (but unchanged axial) diffusion of water. Neuroimage 2002;17:1429–36. 23

[68] Veraart J, Van Hecke W, Sijbers J. Constrained maximum likelihood estimation of the diffusion kurtosis tensor using a Rician noise model. Magn Reson Med 2011; 66:678–86. 24, 47, 48, 61, 64, 70, 80, 123

[69] Tabesh A, Jensen JH, Ardekani BA, Helpern JA. Estimation of tensors and tensor-derived measures in diffusional kurtosis imaging. Magn Reson Med 2011;65:823–36. 25, 70

[70] Ghosh A, Milne T, Deriche R. Constrained diffusion kurtosis imaging using ternary quartics and MLE. Magn Reson Med 2014;71:1581–91. 24, 25, 47, 61

[71] Veraart J, Sijbers J, Sunaert S, Leemans A, Jeurissen B. Weighted linear least squares estimation of diffusion MRI parameters: strengths, limitations, and pitfalls. Neuroimage 2013;81:335–46. 25, 47, 48, 51, 61, 70, 77, 80, 123

[72] Qi L, Han D, Wu EX. Principal invariants and inherent parameters of diffusion kurtosis tensors. J Math Anal Appl 2009;349:165–180. 25, 70

[73] Hui ES, Cheung MM, Qi L, Wu EX. Towards better MR characterization of neural tissues using directional diffusion kurtosis analysis. Neuroimage 2008;42:122–134. 25, 62, 123

[74] Qi L, Wang Y, Wu EX. -eigenvalues of diffusion kurtosis tensors. Journal of Computational and Applied Mathematics 2008;221:150–157. 25

[75] King MD, Houseman J, Roussel SA, van Bruggen N, Williams SR, Gadian DG. q-Space imaging of the brain. Magn Reson Med 1994;32:707–13. 27

[76] Mitra PP. Multiple wave-vector extensions of the NMR pulsed-field-gradient spin-echo diffusion measurement. Physical Review B 1995;51:15074–15078. 27

[77] Bar-Shir A, Avram L, Ozarslan E, Basser PJ, Cohen Y. The effect of the diffusion time and pulse gradient duration ratio on the diffraction pattern and the structural information estimated from q-space diffusion MR: experiments and simulations. J Magn Reson 2008;194:230–6. 27

[78] Bracewell R. The Fourier Transform and Its Applications 3rd edition. McGraw Hill, 2000. 27, 30

[79] Canales-Rodriguez EJ, Lin CP, Iturria-Medina Y, Yeh CH, Cho KH, Melie-Garcia L. Diffusion orientation transform revisited. Neuroimage 2010;49:1326–39. 27

[80] Canales-Rodríguez EJ, Iturria-Medina Y, Alemán-Gómez Y, Melie-García L. Deconvolution in diffusion spectrum imaging. Neuroimage 2010;50:136–149. 27, 81

[81] Bottomley PA, Roemer PB. Homogeneous tissue model estimates of RF power deposition in human NMR studies. Local elevations predicted in surface coil decoupling. Ann N Y Acad Sci 1992;649:144–59. 28

[82] Ahn CB, Kim JH, Cho ZH. High-Speed Spiral-Scan Echo Planar NMR Imaging-I. Medical Imaging, IEEE Transactions on 1986;5:2–7. 31

[83] Pipe JG. Motion correction with PROPELLER MRI: application to head motion and free-breathing cardiac imaging. Magn Reson Med 1999;42:963–9.

[84] Zhang S, Block KT, Frahm J. Magnetic resonance imaging in real time: advances using radial FLASH. J Magn Reson Imaging 2010;31:101–9. 31

[85] Fessler JA, Sutton BP. Nonuniform fast Fourier transforms using min-max interpolation. Signal Processing, IEEE Transactions on 2003;51:560–574. 32

[86] Noll DC, Nishimura DG, Macovski A. Homodyne detection in magnetic resonance imaging. IEEE Trans Med Imaging 1991;10:154–63. 33, 79

[87] Haacke EM, Lindskogj ED, Lin W. A fast, iterative, partial-fourier technique capable of local phase recovery. Journal of Magnetic Resonance (1969) 1991;92:126–145. 33, 79

[88] Parker DL, Tsuruda JS, Goodrich KC, Alexander AL, Buswell HR. Contrast-enhanced magnetic resonance angiography of cerebral arteries. A review. Invest Radiol 1998;33:560–72. 33

[89] Haase A, Frahm J, Matthaei D, Hanicke W, Merboldt KD. FLASH imaging. Rapid NMR imaging using low flip-angle pulses. Journal of Magnetic Resonance (1969) 1986;67:258–266. 33

[90] Hennig J. Echoes—how to generate, recognize, use or avoid them in MR-imaging sequences. Part II: Echoes in imaging sequences. Concept Magnetic Res 1991;3:179–192. 34, 85

[91] Ernst RR, Anderson WA. Application of Fourier Transform Spectroscopy to Magnetic Resonance. Review of Scientific Instruments 1966;37:93–102. 34

[92] Crawley AP, Wood ML, Henkelman RM. Elimination of transverse coherences in FLASH MRI. Magn Reson Med 1988;8:248–60. 34

[93] Epstein FH, Mugler JP, Brookeman JR. Spoiling of transverse magnetization in gradient-echo (GRE) imaging during the approach to steady state. Magn Reson Med 1996;35:237–245. 34

[94] Freeman R, Hill HDW. Phase and intensity anomalies in fourier transform NMR. Journal of Magnetic Resonance (1969) 1971;4:366–383. 34

[95] Saeed M, Van TA, Krug R, Hetts SW, Wilson MW. Cardiac MR imaging: current status and future direction. Cardiovascular Diagnosis and Therapy 2015;5:290–310. 35

[96] Mugler JP, Brookeman JR. Three-dimensional magnetization-prepared rapid gradient-echo imaging (3D MP RAGE). Magn Reson Med 1990;15:152–157. 35

[97] Hennig J, Nauerth A, Friedburg H. RARE imaging: A fast imaging method for clinical MR. Magn Reson Med 1986;3:823–833. 35

[98] Le Roux P, Hinks RS. Stabilization of echo amplitudes in FSE sequences. Magn Reson Med 1993;30:183–90. 37, 41

[99] Mansfield P. Multi-planar image formation using NMR spin echoes. Journal of Physics C: Solid State Physics 1977;10:L55. 37

[100] Meyer CH, Pauly JM, Macovski A, Nishimura DG. Simultaneous spatial and spectral selective excitation. Magn Reson Med 1990;15:287–304. 39

[101] Bydder GM, Young IR. MR imaging: clinical use of the inversion recovery sequence. J Comput Assist Tomogr 1985;9:659–75. 39

[102] Sodickson DK, Manning WJ. Simultaneous acquisition of spatial harmonics (SMASH): fast imaging with radiofrequency coil arrays. Magn Reson Med 1997; 38:591–603. 39

[103] Griswold MA, Jakob PM, Heidemann RM, et al. Generalized autocalibrating partially parallel acquisitions (GRAPPA). Magn Reson Med 2002;47:1202–10. 39, 40, 42, 79, 83, 95

[104] Chen DQ, Marr RB, Lauterbur PC. Reconstruction from NMR Data Acquired with Imaging Gradients Having Arbitrary Time Dependence. Medical Imaging, IEEE Transactions on 1986;5:162–164. 39

[105] Edelstein WA, Glover GH, Hardy CJ, Redington RW. The intrinsic signal-to-noise ratio in NMR imaging. Magn Reson Med 1986;3:604–618. 40, 63, 67, 93

[106] Setsompop K, Kimmlingen R, Eberlein E, et al. Pushing the limits of in vivo diffusion MRI for the Human Connectome Project. Neuroimage 2013;80:220–33. 40, 63, 81, 83

[107] Nyquist H. Certain Topics in Telegraph Transmission Theory. American Institute of Electrical Engineers, Transactions of the 1928;47:617–644. 41

[108] Shannon CE. Communication In The Presence Of Noise. Proceedings of the IEEE 1998;86:447–457. 41

[109] Koch KM, Rothman DL, de Graaf RA. Optimization of static magnetic field homogeneity in the human and animal brain in vivo. Progress in nuclear magnetic resonance spectroscopy 2009;54:69–96. 42

[110] Munger P, Crelier GR, Peters TM, Pike GB. An inverse problem approach to the correction of distortion in EPI images. Medical Imaging, IEEE Transactions on 2000; 19:681–689. 43

[111] Jezzard P, Balaban RS. Correction for geometric distortion in echo planar images from B0 field variations. Magn Reson Med 1995;34:65–73. 44

[112] Chang H, Fitzpatrick JM. A technique for accurate magnetic resonance imaging in the presence of field inhomogeneities. IEEE Trans Med Imaging 1992;11:319–29. 44

[113] Andersson JLR, Skare S, Ashburner J. How to correct susceptibility distortions in spin-echo echo-planar images: application to diffusion tensor imaging. Neuroimage 2003;20:870–888. 44

[114] Robson MD, Gore JC, Constable RT. Measurement of the point spread function in MRI using constant time imaging. Magn Reson Med 1997;38:733–40. 44

[115] Zeng H, Constable RT. Image distortion correction in EPI: comparison of field mapping with point spread function mapping. Magn Reson Med 2002;48:137–46. 44

[116] Ham CL, Engels JM, van de Wiel GT, Machielsen A. Peripheral nerve stimulation during MRI: effects of high gradient amplitudes and switching rates. J Magn Reson Imaging 1997;7:933–7. 45

[117] Jehenson P, Westphal M, Schuff N. Analytical method for the compensation of eddy-current effects induced by pulsed magnetic field gradients in NMR systems. Journal of Magnetic Resonance (1969) 1990;90:264–278. 45

[118] Mansfield P, Chapman B. Active magnetic screening of coils for static and time-dependent magnetic field generation in NMR imaging. Journal of Physics E: Scientific Instruments 1986;19:540. 45

[119] Bernstein MA, Zhou XJ, Polzin JA, et al. Concomitant gradient terms in phase contrast MR: analysis and correction. Magn Reson Med 1998;39:300–8. 46

[120] Du YP, Joe Zhou X, Bernstein MA. Correction of concomitant magnetic field-induced image artifacts in nonaxial echo-planar imaging. Magn Reson Med 2002;48:509–15. 46

[121] Sprenger T, Sperl JI, Fernandez B, et al. Bias and precision analysis of diffusional kurtosis imaging for different acquisition schemes. Magn Reson Med 2016;n/a–n/a. 47, 123

[122] Jensen JH, Helpern JA. MRI quantification of non-Gaussian water diffusion by kurtosis analysis. NMR Biomed 2010;23:698–710. 47

[123] Poot DH, den Dekker AJ, Achten E, Verhoye M, Sijbers J. Optimal experimental design for diffusion kurtosis imaging. IEEE Trans Med Imaging 2010;29:819–29. 47, 48, 62, 69, 123

[124] Koay CG, Özarslan E, Johnson KM, Meyerand ME. Sparse and optimal acquisition design for diffusion MRI and beyond. Med Phys 2012;39:2499–2511. 47

[125] Caruyer E, Lenglet C, Sapiro G, Deriche R. Design of multishell sampling schemes with uniform coverage in diffusion MRI. Magn Reson Med 2013;69:1534–1540. 47, 48, 114

[126] Menzel MI, Tan ET, Khare K, et al. Accelerated diffusion spectrum imaging in the human brain using compressed sensing. Magn Reson Med 2011;66:1226–33. 47, 50, 61, 81, 123

[127] Sperl JI, Tan ET, I MM, et al. Combined Approximate Message Passing for Total Variation Minimization and Randomly Translated Wavelet Denoising - Improved Compressed Sensing for Diffusion Spectrum Imaging. In In Proc. of the 20th Annual Meeting of ISMRM. 2012; 2238. 47, 50, 51, 61

[128] Jin J, Yang B, Liang K, Wang X. General image denoising framework based on compressive sensing theory. Comput Graph 2014;38:382–391. 47

[129] Veraart J, Rajan J, Peeters RR, Leemans A, Sunaert S, Sijbers J. Comprehensive framework for accurate diffusion MRI parameter estimation. Magn Reson Med 2013; 70:972–84. 47, 48, 61, 64, 77, 123

[130] Robson PM, Grant AK, Madhuranthakam AJ, Lattanzi R, Sodickson DK, McKenzie CA. Comprehensive quantification of signal-to-noise ratio and g-factor for image-based and k-space-based parallel imaging reconstructions. Magn Reson Med 2008; 60:895–907. 47

[131] Prah DE, Paulson ES, Nencka AS, Schmainda KM. A simple method for rectified noise floor suppression: Phase-corrected real data reconstruction with application to diffusion-weighted imaging. Magn Reson Med 2010;64:418–429. 49, 64, 66, 67, 68, 72, 77, 80, 124

[132] Smith SM. Fast robust automated brain extraction. Hum Brain Mapp 2002;17(3):143–155. 50

[133] Chabriat H, Pappata S, Poupon C, et al. Clinical severity in CADASIL related to ultrastructural damage in white matter: in vivo study with diffusion tensor MRI. Stroke 1999;30:2637–43. 50

[134] Samann PG, Knop M, Golgor E, Messler S, Czisch M, Weber F. Brain volume and diffusion markers as predictors of disability and short-term disease evolution in multiple sclerosis. AJNR Am J Neuroradiol 2012;33:1356–62. 50

[135] Daubechies I, Defrise M, De Mol C. An iterative thresholding algorithm for linear inverse problems with a sparsity constraint. Comm Pure Appl Math 2004;57:1413–1457. 50

[136] Salvador R, Peña A, Menon DK, Carpenter TA, Pickard JD, Bullmore ET. Formal characterization and extension of the linearized diffusion tensor model. Hum Brain Mapp 2005;24:144–155. 51

[137] Niendorf T, Dijkhuizen RM, Norris DG, van Lookeren Campagne M, Nicolay K. Biexponential diffusion attenuation in various states of brain tissue: implications for diffusion-weighted imaging. Magn Reson Med 1996;36:847–57. 61

[138] Bilgic B, Setsompop K, Cohen-Adad J, Wedeen V, Wald LL, Adalsteinsson E. Accelerated diffusion spectrum imaging with compressed sensing using adaptive dictionaries. Med Image Comput Comput Assist Interv 2012;15:1–9. 61

[139] Sprenger T, Sperl JI, Fernandez B, Haase A, Menzel MI. Real Valued Diffusion-Weighted Imaging Using Decorrelated Phase Filtering. Magn Reson Med 2015;accepted/in production. 63, 123

[140] Mori S, Crain BJ, van Zijl PC. 3D brain fiber reconstruction from diffusion MRI. In In Proceedings of International Conference on Functional Mapping of the Human Brain. 1998; . 63

[141] Basser JB. Fiber-tractography via diffusion tensor MRI. In In Proceedings of International Society for Magnetic Resonance in Medicine. 1998; . 63

[142] Aja-Fernandez S, Tristan-Vega A, Hoge WS. Statistical noise analysis in GRAPPA using a parametrized noncentral Chi approximation model. Magn Reson Med 2011;65:1195–206. 63

[143] Tristan-Vega A, Aja-Fernandez S, Westin CF. Least squares for diffusion tensor estimation revisited: propagation of uncertainty with Rician and non-Rician signals. Neuroimage 2012;59:4032–43. 63

[144] Gudbjartsson H, Patz S. The Rician Distribution of Noisy MRI Data. Magn Reson Med 1995;34:910–914. 63

[145] Sijbers J, den Dekker AJ, Van Audekerke J, Verhoye M, Van Dyck D. Estimation of the Noise in Magnitude MR Images. Magn Reson Med 1998;16:87–90. 63

[146] Michelson A. Studies in Optics. Dover Publications, 1995. 65

[147] McGraw T, Vemuri BC, Chen Y, Rao M, Mareci T. DT-MRI denoising and neuronal fiber tracking. Med Image Anal 2004;8:95–111. 64

[148] Manjón JV, Coupé P, Concha L, Buades A, Collins DL, Robles M. Diffusion Weighted Image Denoising Using Overcomplete Local PCA. PLoS ONE 2013;8:e73021.

[149] Wirestam R, Bibic A, Latt J, Brockstedt S, Stahlberg F. Denoising of complex MRI data by wavelet-domain filtering: application to high-b-value diffusion-weighted imaging. Magn Reson Med 2006;56:1114–20.

[150] Aja-Fernandez S, Niethammer M, Kubicki M, Shenton ME, Westin CF. Restoration of DWI data using a Rician LMMSE estimator. IEEE Trans Med Imaging 2008;27:1389–403. 64

[151] Landman B, Bazin PL, Prince J. Diffusion Tensor Estimation by Maximizing Rician Likelihood. Proceedings / IEEE International Conference on Computer Vision IEEE International Conference on Computer Vision 2007;1–8. 64

[152] Triantafyllou C, Polimeni JR, Wald LL. Physiological noise and signal-to-noise ratio in fMRI with multi-channel array coils. Neuroimage 2011;55:597–606. 64

[153] Riek JK, Totterman SM, Tekalp AM, Smith WE, Kwok E. Flow compensation in MRI using a phase-corrected real reconstruction. Magn Reson Med 1993;30:724–31. 64

[154] Liu C, Moseley ME, Bammer R. Simultaneous phase correction and SENSE reconstruction for navigated multi-shot DWI with non-cartesian k-space sampling. Magn Reson Med 2005;54:1412–22. 64

[155] Miller KL, Pauly JM. Nonlinear phase correction for navigated diffusion imaging. Magn Reson Med 2003;50:343–53. 64

[156] Holdsworth SJ, Aksoy M, Newbould RD, et al. Diffusion tensor imaging (DTI) with retrospective motion correction for large-scale pediatric imaging. J Magn Reson Imaging 2012;36:961–71. 64

[157] Atkinson D, Counsell S, Hajnal JV, Batchelor PG, Hill DL, Larkman DJ. Nonlinear phase correction of navigated multi-coil diffusion images. Magn Reson Med 2006; 56:1135–9. 64

[158] Sperl JI, Tan ET, Sprenger T, et al. Phase Sensitive Reconstruction in Diffusion Spectrum Imaging Enabling Velocity Encoding and Unbiased Noise Distribution. In In Proc. of the 21st Annual Meeting of ISMRM. 2013; 2054. 64

[159] Menzel MI, Sprenger T, Tan ET, et al. Robustness of Phase Sensitive Reconstruction in Diffusion Spectrum Imaging. In In Proc. of the 23rd Annual Meeting of ISMRM. 2015; 5744.

[160] Sprenger T, Sperl JI, Fernandez B, Haase A, Menzel MI. Real valued diffusion weighted imaging using decorrelated kernel based phase correction. In 21st Annual Meeting of the Organization for Human Brain Mapping. 2015; 1795. 109, 125

[161] Eichner C, Cauley SF, Cohen-Adad J, et al. Real diffusion-weighted MRI enabling true signal averaging and increased diffusion contrast. Neuroimage 2015;122:373–384. 64, 80

[162] Rousseeuw PJ, Croux C. Alternatives to the Median Absolute Deviation. Journal of the American Statistical Association 1993;88:1273–1283. 69

[163] Koay CG, Chang LC, Carew JD, Pierpaoli C, Basser PJ. A unifying theoretical and algorithmic framework for least squares methods of estimation in diffusion tensor imaging. J Magn Reson 2006;182:115–125. 70, 80

[164] Byrd RH, Gilbert JC, Nocedal J. A trust region method based on interior point techniques for nonlinear programming. Mathematical Programming 2000;89:149–185. 70

[165] Caruyer E, Deriche R. Diffusion MRI signal reconstruction with continuity constraint and optimal regularization. Med Image Anal 2012;16:1113–20. 81

[166] Sotiropoulos SN, Jbabdi S, Xu J, et al. Advances in diffusion MRI acquisition and processing in the Human Connectome Project. Neuroimage 2013;80:125–43. 81, 83

[167] Fürsich B. Investigating the Applicability of Diffusion Weighted Steady State Free Precession MRI Pulse Sequences in Neuro-Imaging. Thesis, 2014. 83

[168] Feinberg DA, Reese TG, Wedeen VJ. Simultaneous echo refocusing in EPI. Magn Reson Med 2002;48:1–5. 83

[169] Van AT, Karampinos DC, Sutton BP. High Resolution 3D Multi-slab Multi-shot Spin Echo Diffusion-Weighted Imaging. In In Proc. of the 18th Annual Meeting of ISMRM. 2010; . 84

[170] Frost R, Miller KL, Tijssen RH, Porter DA, Jezzard P. 3D multi-slab diffusion-weighted readout-segmented EPI with real-time cardiac-reordered K-space acquisition. Magn Reson Med 2014;72:1565–79. 84, 107

[171] Kaiser R, Bartholdi E, Ernst RR. Diffusion and field gradient effects in NMR Fourier spectroscopy. J Chem Phys 1974;60:2966–2979. 84, 85, 87, 105

[172] Wu EX, Buxton RB. Effect of diffusion on the steady-state magnetization with pulsed field gradients. Journal of Magnetic Resonance (1969) 1990;90:243–253. 84, 85, 87, 88, 90, 105, 130

[173] McNab JA, Miller KL. Sensitivity of diffusion weighted steady state free precession to anisotropic diffusion. Magn Reson Med 2008;60:405–13. 84, 106

[174] McNab JA, Jbabdi S, Deoni SCL, Douaud G, Behrens TEJ, Miller KL. High resolution diffusion-weighted imaging in fixed human brain using diffusion-weighted steady state free precession. Neuroimage 2009;46:775–785. 84, 92, 105, 125

[175] Miller KL, Stagg CJ, Douaud G, et al. Diffusion imaging of whole, post-mortem human brains on a clinical MRI scanner. Neuroimage 2011;57:167–181.

[176] Miller KL, McNab JA, Jbabdi S, Douaud G. Diffusion tractography of post-mortem human brains: Optimization and comparison of spin echo and steady-state free precession techniques. Neuroimage 2012;59:2284–2297. 98, 108, 125

[177] Bieri O, Ganter C, Welsch GH, Trattnig S, Mamisch TC, Scheffler K. Fast diffusion-weighted steady state free precession imaging of in vivo knee cartilage. Magn Reson Med 2012;67:691–700. 84, 89, 92, 105, 125

[178] Foxley S, Jbabdi S, Clare S, et al. Improving diffusion-weighted imaging of post-mortem human brains: SSFP at 7T. Neuroimage 2014;102, Part 2:579–589. 84

[179] Engstrom M, Martensson M, Avventi E, Skare S. On the signal-to-noise ratio efficiency and slab-banding artifacts in three-dimensional multislab diffusion-weighted echo-planar imaging. Magn Reson Med 2015;73:718–25. 84, 107

[180] McNab JA, Miller KL. Steady-state diffusion-weighted imaging: theory, acquisition and analysis. NMR Biomed 2010;23:781–793. 84, 85

[181] Buxton RB. The diffusion sensitivity of fast steady-state free precession imaging. Magn Reson Med 1993;29:235–43. 84, 85, 88, 90, 106

[182] Bieri O, Ganter C, Scheffler K. Quantitative in vivo diffusion imaging of cartilage using double echo steady-state free precession. Magn Reson Med 2012;68:720–9. 84, 125

[183] Freed DE, Scheven UM, Zielinski LJ, Sen PN, Hürlimann MD. Steady-state free precession experiments and exact treatment of diffusion in a uniform gradient. J Chem Phys 2001;115:4249–4258. 84, 85, 89, 90, 100, 105, 130

[184] Buxton RB, Richard Fisel C, Chien D, Brady TJ. Signal intensity in fast NMR imaging with short repetition times. Journal of Magnetic Resonance (1969) 1989;83:576–585. 87

[185] Soellinger M, Rutz AK, Kozerke S, Boesiger P. 3D cine displacement-encoded MRI of pulsatile brain motion. Magn Reson Med 2009;61:153–62. 91, 100, 102, 108, 109, 120, 125

[186] K B, M B, L DJ, M G. Estimating SNR efficiency in non-Cartesian trajectories: Cartesian is to apples as BLADE is to schnitzel. In In Proceedings of the Joint Annual Meeting of the ISMRM-ESMRMB. 2009; 1880. 93

[187] Perman WH, Hilal SK, Simon HE, Maudsley AA. Contrast manipulation in NMR imaging. Magn Reson Med 1984;2:23–32. 96

[188] Breuer FA, Blaimer M, Heidemann RM, Mueller MF, Griswold MA, Jakob PM. Controlled aliasing in parallel imaging results in higher acceleration (CAIPIRINHA) for multi-slice imaging. Magn Reson Med 2005;53:684–91. 107

[189] Frost R, Jezzard P, Douaud G, Clare S, Porter DA, Miller KL. Scan time reduction for readout-segmented EPI using simultaneous multislice acceleration: Diffusion-weighted imaging at 3 and 7 Tesla. Magn Reson Med 2014;n/a–n/a. 107

[190] O'Halloran R, Aksoy M, Aboussouan E, Peterson E, Van A, Bammer R. Real-time correction of rigid body motion-induced phase errors for diffusion-weighted steady-state free precession imaging. Magn Reson Med 2015;73:565–576. 108

[191] Sprenger T, Sperl JI, Fernandez B, Haase A, Menzel MI. Measuring the pulsation of the brain using a phase sensitive reconstruction of DWIs. In 21st Annual Meeting of the Organization for Human Brain Mapping. 2015; 2197. 109, 125

[192] Morse OC, Singer JR. Blood Velocity Measurements in Intact Subjects. Science 1970; 170:440–441. 109

[193] Abdul-Rahman HS, Gdeisat MA, Burton DR, Lalor MJ, Lilley F, Moore CJ. Fast and robust three-dimensional best path phase unwrapping algorithm. Appl Opt 2007; 46:6623–35. 111

[194] Mariappan YK, Glaser KJ, Ehman RL. MAGNETIC RESONANCE ELASTOGRAPHY: A REVIEW. Clinical anatomy (New York, NY) 2010;23:497–511. 121, 125